# Measurement of atmospheric neutrino oscillations and search for sterile neutrino mixing with IceCube DeepCore

D i s s e r t a t i o n

zur Erlangung des akademischen Grades

d o c t o r r e r u m n a t u r a l i u m
( Dr. rer. nat.)
im Fach Physik

eingereicht an der

Mathematisch-Naturwissenschaftlichen Fakultät
der Humboldt-Universität zu Berlin

von

**M.Sc. Andrii Terliuk**

Präsidentin der Humboldt-Universität zu Berlin:

Prof. Dr.-Ing. Dr. Sabine Kunst

Dekan der Mathematisch-Naturwissenschaftlichen Fakultät:

Prof. Dr. Elmar Kulke

---

Gutachter: 1. Prof. Dr. Marek Kowalski
2. Priv.-Doz. Dr. Walter Winter
3. Prof. Dr. Stefan Söldner-Rembold

Tag der mündlichen Prüfung: 10. Juli 2018

**Abstract**

Neutrino oscillations, a phenomenon that can change the flavour of neutrinos after their propagation through space, are a proof of non-zero neutrino masses and are an indication of new physics beyond the Standard Model. This work presents the first measurement of the atmospheric neutrino oscillations using six years of IceCube DeepCore data taken between May 2011 and May 2017. It extends the previously available event selection to include new event signatures and to use an extended energy range. This work discusses the techniques used for simulation of neutrino interactions, event selection, reconstruction, and the statistical treatment of data and systematic uncertainties. The best estimates for the neutrino mixing parameters are $\Delta m^2_{32} = 2.54^{+0.11}_{-0.12} \cdot 10^{-3}$ eV$^2$ and $\sin^2\theta_{23} = 0.51 \pm 0.05$ (68% C.L.), which are currently among the most precise measurements obtained with atmospheric neutrinos.

In addition, this work tests the standard three-flavour paradigm by introducing one sterile neutrino with a mass on the order of 1 eV. The search for sterile neutrino effects in atmospheric neutrino oscillations is performed with three years of data taken between May 2011 and May 2014. The results are consistent with the standard three-neutrino oscillation picture, leading to limits on the allowed sterile neutrino mixing of $|U_{\mu 4}|^2 < 0.11$ and $|U_{\tau 4}|^2 < 0.15$ (90% C.L.) for $\Delta m^2_{41} = 1$ eV$^2$. Currently, the limit for $|U_{\tau 4}|^2$ is the most stringent in the World.

**Zusammenfassung**

Neutrinooszillation, ein Phänomen, das den Neutrino-Flavour nach ihrer Ausbreitung durch den Weltraum verändern kann, ist ein Beweis für nicht-verschwindende Neutrinomassen und ein Hinweis auf eine neue Physik außerhalb des Standardmodells. Diese Arbeit präsentiert die erste Messung zu atmosphärischen Neutrinooszillationen, die sechs Jahre zwischen Mai 2011 und Mai 2017 des IceCube DeepCore Experiment umfasst. Sie erweitert die bisher verfügbare Ereignisauswahl um eine neue Ereignissignatur und einen großeren Energiebereich. Diese Arbeit beschreibt die Methoden, die für die Simulationen der Wechselwirkungen der Neutrinos, die Ereignisauswahl, die Rekonstruktion und die statistische Behandlung von Messdaten und systematischen Messunsicherheiten benutzt werden. Die beste Abschätzung für die Neutrino-Mischungsparameter ist $\Delta m^2_{32} = 2.54^{+0.11}_{-0.12} \cdot 10^{-3}$ eV$^2$ und $\sin^2\theta_{23} = 0.51 \pm 0.05$ (68% C.L.) und gehört zurzeit zu den präzisesten Messungen atmosphärischer Neutrinos.

Darüber hinaus wird in dieser Arbeit das Standard-Drei-Flavour-Modell überprüft, indem ein steriles Neutrino mit einer Masse in der Größenordnung von 1 eV eingeführt wird. Die Suche nach Effekten steriler Neutrinos auf atmosphärischen Neutrinooszillationen wird auf drei Jahren Daten, genommen zwischen Mai 2011 und Mai 2014, durchgeführt. Die Ergebnisse stimmen mit dem Standard-Modell der Drei-Neutrino-Oszillation überein, was zu den Obergrenzen für sterilen Neutrino-Mischungsparameter $|U_{\mu 4}|^2 < 0.11$ und $|U_{\tau 4}|^2 < 0.15$ (90% C.L.) für $\Delta m^2_{41} = 1$ eV$^2$ führt. Dieser Ergebnis ist derzeit die stringenste Obergrenze für $|U_{\tau 4}|^2$.

# Contents

# Chapter 1

# Introduction

The proposal of a light and neutral particle, currently known as the neutrino, as an explanation for the shape of beta-decay spectra in 1930 [1] and its discovery in 1956 [2] opened a new page for nuclear and particle physics. Currently, three neutrino flavours are known: electron, muon and tau neutrinos. The discovery of neutrino oscillations, transitions between different neutrino types, in solar [3] and atmospheric neutrinos [4] confirmed that they have non-zero masses. Massive neutrinos are not explained within the Standard Model of Particle Physics [5] and are one of the most convincing signs of new physics.

Neutrino oscillations are phenomenologically explained by the mixture of the neutrinos present in the Standard Model and their mass state counterparts. These oscillations are observed for solar, atmospheric, accelerator and reactor neutrinos. For atmospheric neutrinos, neutrino oscillations lead to a suppression of the muon neutrino flux for neutrinos crossing the Earth. This effect is used to extract the fundamental neutrino mixing parameters.

The IceCube Neutrino Observatory [6] is the first cubic-kilometre Cherenkov neutrino detector. It is located at the geographic South Pole and comprises 5160 optical sensors. DeepCore, a more densely instrumented sub-detector, has a neutrino detection energy threshold of approximately 5 GeV. The DeepCore data are used for studies of fundamental neutrino properties and lead to some of the most precise measurements of neutrino mixing parameters obtained with atmospheric neutrinos [7, 8].

This work discusses one of the studies that measure atmospheric neutrino oscillations. It extends a previously available event sample to use new event signatures and the extended energy range. This work presents the first oscillation study that uses six years of IceCube data taken between May 2011 and May 2017. Its results provide one of the most precise measurements of the mixing parameters $\Delta m^2_{32}$ and $\sin^2\theta_{23}$ obtained with atmospheric neutrinos.

Anomalous neutrino transitions were observed in the data of several accelerator [9, 10], reactor [11] and radiochemical [12, 13] neutrino experiments. The reasons for these deviations are still unknown. One of the possible ways to explain the anomalies is the introduction of sterile neutrinos. Such hypothetical particles do

not interact via weak interactions, but they can be mixed with active neutrinos of the Standard Model and would lead to additional oscillation effects for atmospheric neutrinos. This work tests the three-neutrino paradigm introducing a single sterile neutrino family with a mass of around 1 $eV/c^2$. Its mixing with the muon and tau states is probed using three years of the IceCube DeepCore atmospheric neutrino data. The study provides stringent limits for the allowed sterile neutrino mixing, especially for its mixing to the tau neutrino state.

In this work, Chapter 2 introduces the reader to neutrinos, their properties in the Standard Model, their interactions and sources. The neutrino oscillation phenomenology for the standard and sterile neutrino oscillations and the recent experimental results are discussed in Chapter 3. Chapter 4 describes the principles of neutrino detection in ice and introduces the IceCube Neutrino Observatory.

The data analysis techniques used in this work are discussed in Chapter 5. This includes an overview of the simulation production, event reconstruction, event selection, statistical methods and treatment of the systematic uncertainties used in this work.

Chapter 6 presents the procedure and the results of the standard atmospheric neutrino oscillation measurement. The search for the sterile neutrino mixing is discussed in Chapter 7. Chapter 8 compares the results obtained in this work to the measurements and limits provided by other experiments and discusses potential future improvements to the sensitivity to neutrino mixing. Finally, a summary of this work is presented in Chapter 9.

# Chapter 2

# Neutrinos in the Standard Model

This chapter describes neutrinos and their place in the Standard Model. It starts with a short overview of the neutrino history. It is followed by information about the Standard Model, electroweak interactions and the properties of neutrinos. Then it discusses the neutrino-nucleon interactions relevant to this work. Finally, this chapter gives an overview of the neutrino sources with an emphasis on atmospheric neutrinos.

## 2.1 Neutrino prediction and discovery

The history of neutrinos dates back to the end of the nineteenth century, when radioactivity was discovered and systematically studied by Henri Becquerel, Marie and Pierre Curie, Ernest Rutherford, James Chadwick and others. The energy spectra of alpha particles and gamma rays were measured as mono-energetic lines, as is expected from a classical two-body decay. However, the spectrum of electrons in beta decay was found to be continuous, despite having only two visible particles in the final state.

At that time, the continuous beta spectrum could not be fit within energy and momentum conservation laws. Various hypotheses were proposed to explain the electron energy distribution, such as a statistical nature or outright violation of the energy and momentum conservation laws [14]. In 1930, Wolfgang Pauli proposed [1] a hypothetical third particle to explain observed electron spectra in beta-decays. This particle, later named the *neutrino*, should have a mass smaller than 1% of the proton mass, and a spin of $\frac{1}{2}$. Such a new particle fit well with the observed beta decay spectra, using the theory developed by Enrico Fermi in 1934 [15]. However, the predicted neutrino interaction cross-sections were as low as $10^{-44}$ cm$^2$, so they were impossible to detect at that time.

The first detection of neutrinos came approximately 20 years later. In 1952, George Rodeback and James Allen measured a nuclear recoil in the $^{37}$Ar electron capture reaction, where the result was consistent with the neutrino hypothesis [16]. In 1956, the first direct detection of neutrinos was performed by Clyde Cowan and

Frederick Reines [2], who used a nuclear reactor to observe the inverse beta decay

$$\bar{\nu}_{\mathrm{e}} + \mathrm{p} \rightarrow \mathrm{e}^{+} + \mathrm{n}, \tag{2.1}$$

where neutrons were captured with Cadmium, and the resulting positrons were detected by their annihilation photons. Such neutrino events have a characteristic signature, which was only observed when the reactor was running.

Later Raymond Davis Jr. proved that electron neutrinos and antineutrinos are not the same particles [17] by searching for the reaction

$$\bar{\nu}_{\mathrm{e}} + {}^{37}\mathrm{Cl} \rightarrow \mathrm{e}^{-} + {}^{37}\mathrm{Ar} \tag{2.2}$$

at the Brookhaven reactor, where no signal was found. Later, the Homestake Experiment confirmed that this reaction is possible for electron neutrinos by detection of solar neutrinos.

Muon neutrinos were discovered in 1962 at the experiment performed by Leon Lederman, Melvin Schwartz and Jack Steinberger at the Brookhaven accelerator [18]. The interactions of muon neutrinos producing muons

$$\begin{aligned} \nu_{\mu} + n &\rightarrow \mu^{-} + p, \\ \bar{\nu}_{\mu} + p &\rightarrow \mu^{+} + n, \end{aligned} \tag{2.3}$$

were observed, while the rate of reactions producing electrons

$$\begin{aligned} \nu_{\mu} + n &\rightarrow e^{-} + p, \\ \bar{\nu}_{\mu} + p &\rightarrow e^{+} + n \end{aligned} \tag{2.4}$$

was found to be at the background level. If $\nu_{\mu}$ and $\nu_{e}$ were actually the same particle, both reactions would be observed at the same rate.

The discovery of a third neutrino generation, $\nu_{\tau}$, was reported by the DONUT experiment [19] in 2000. It was looking for tau neutrinos produced by prompt decays of charmed bosons, generated by the beam dump of the Tevatron accelerator. They were detected using the scattering of tau neutrinos on nuclei

$$\nu_{\tau} + N \rightarrow \tau^{-} + X, \tag{2.5}$$

which were identified by charged tau leptons produced in the interactions of such neutrinos.

These three currently known neutrino flavours, $\nu_{e}$ , $\nu_{\mu}$ and $\nu_{\tau}$, are part of the Standard Model, discussed in the next section.

## 2.2 The Standard Model

The Standard Model (SM) [20–22] of particle physics is a relativistic quantum field theory that describes the interactions between elementary particles. It is a gauge

Table 2.1: A list of bosons in the Standard Model, their masses (taken from [23]), electric charges and their roles in the Standard Model.

| **Boson name** | **Mass** | **Charge (e)** | **Role in the SM** |
|---|---|---|---|
| photon ($\boldsymbol{\gamma}$) | 0 | 0 | EM force carrier |
| W boson ($\boldsymbol{W^{\pm}}$) | $80.385 \pm 0.015$ GeV | $\pm 1$ | weak force carriers |
| Z boson ($\boldsymbol{Z^0}$) | $91.1876 \pm 0.0021$ GeV | 0 | |
| gluon ($\boldsymbol{g}$) | 0 | 0 | strong force carrier |
| Higgs boson ($\boldsymbol{H^0}$) | $125.09 \pm 0.25$ GeV | 0 | particle mass gen. |

theory based on the local symmetry groups $\mathrm{SU(3)_C} \otimes \mathrm{SU(2)_L} \otimes \mathrm{U(1)_Y}$, where C, L and Y denote colour, left-handed chirality and weak hypercharge, respectively.

There are three interaction types in the Standard Model: strong, weak and electromagnetic (EM). The strong interactions are driven by $\mathrm{SU(3)_C}$ colour symmetry and are separated from the other two interaction types. The EM and weak interactions, forming together the electroweak interaction, are generated by $\mathrm{SU(2)_L} \otimes \mathrm{U(1)_Y}$ gauge groups. In the Standard Model, fundamental forces are mediated by gauge bosons, particles with a spin of 1, and arise from the corresponding gauge symmetries. A number of gauge bosons is equal to a number of generators in the corresponding group. Therefore, the strong interaction is carried by 8 types of gluons ($\boldsymbol{g}$), the weak interaction is mediated by three bosons ($\boldsymbol{W^{\pm}}$ and $\boldsymbol{Z^0}$), and the EM interaction is mediated by photons ($\boldsymbol{\gamma}$). Unlike gauge bosons, the Higgs boson has the spin of 0 and arises not from the gauge symmetries, but from spontaneous electroweak symmetry breaking. It is responsible for the generation of the elementary particle masses in the SM. The list of bosons, their masses and their roles in the SM are listed in Table 2.1.

Twelve fermions, particles with a spin of $\frac{1}{2}$, form the matter content of the Standard Model. Six of those particles are called quarks. They participate in all three interactions and are the building blocks of nucleons and other hadrons. Quarks are grouped into three generations by their mass. The other six particles are leptons. Three of them, electron, muon and tau, are charged and take part in electromagnetic and weak interactions. The other three leptons are neutrinos, which have no electric charge and take part only in the weak interactions. The list of fermions in the SM and their basic properties are given in Table 2.2. Neutrinos and their weak interactions are the primary focus of this work and are covered in more detail in the following sections.

The Standard Model is a comprehensive theory of particle physics, but it cannot describe some of the observed effects. Currently, gravity and Dark Matter are not covered by the SM. The discovery of neutrino oscillations, possible only if neutrinos have masses, contradicts their zero masses in the Standard Model. More information about neutrino oscillations is given in Chapter 3 of this work.

Table 2.2: A list of fermion particles in the Standard Model, their masses, electric charges $Q$, lepton numbers $L$ and their interaction types. Additionally, the flavour related lepton numbers $L_\ell$ are given for leptons. The values are taken from [23].

| | **1st generation** | **2nd generation** | **3rd generation** |
|---|---|---|---|
| **Quarks** | up ($\boldsymbol{u}$) | charm ($\boldsymbol{c}$) | top ($\boldsymbol{t}$) |
| | $m_u = 2.3$ MeV | $m_c = 1.28$ GeV | $m_t = 173.2$ GeV |
| | $Q = 2/3,\ L = 0$ | $Q = 2/3,\ L = 0$ | $Q = 2/3,\ L = 0$ |
| | EM, weak, strong | EM, weak, strong | EM, weak, strong |
| | down ($\boldsymbol{d}$) | strange ($\boldsymbol{s}$) | bottom ($\boldsymbol{b}$) |
| | $m_d = 4.8$ MeV | $m_s = 95$ MeV | $m_b = 4.2$ GeV |
| | $Q = -1/3,\ L = 0$ | $Q = -1/3,\ L = 0$ | $Q = -1/3,\ L = 0$ |
| | EM, weak, strong | EM, weak, strong | EM, weak, strong |
| **Leptons** | electron ($\boldsymbol{e}$) | muon($\boldsymbol{\mu}$) | tau ($\boldsymbol{\tau}$) |
| | $m_e = 0.511$ MeV | $m_\mu = 105.6$ MeV | $m_\tau = 1.78$ GeV |
| | $Q = -1,\ L = 1$ | $Q = -1,\ L = 1$ | $Q = -1,\ L = 1$ |
| | $L_e = 1,\ L_\mu = L_\tau = 0$ | $L_\mu = 1,\ L_e = L_\tau = 0$ | $L_e = L_\mu = 0,\ L_\tau = 1$ |
| | EM, weak | EM, weak | EM, weak |
| | electron neutrino ($\boldsymbol{\nu_e}$) | muon neutrino ($\boldsymbol{\nu_\mu}$) | tau neutrino ($\boldsymbol{\nu_\tau}$) |
| | $m_{\nu_e} < 2$ eV | $m_{\nu_\mu} < 2$ eV | $m_{\nu_\mu} < 2$ eV |
| | $Q = 0,\ L = 1$ | $Q = 0,\ L = 1$ | $Q = 0,\ L = 1$ |
| | $L_e = 1,\ L_\mu = L_\tau = 0$ | $L_\mu = 1,\ L_e = L_\tau = 0$ | $L_e = L_\mu = 0,\ L_\tau = 1$ |
| | weak | weak | weak |

## 2.3 Electroweak interactions

The electroweak interaction is generated by the product $\mathrm{SU(2)_L} \otimes \mathrm{SU(1)_Y}$ in the Standard Model. The $\mathrm{SU(2)_L}$ group conserves weak isospin and affects only left-handed components of the chiral representation of the fields. The right and left components are obtained by the operators

$$\begin{aligned} \hat{P}_R &= \frac{1}{2}(1+\gamma^5),\ \psi_R = \hat{P}_R\psi, \\ \hat{P}_L &= \frac{1}{2}(1-\gamma^5),\ \psi_L = \hat{P}_L\psi, \end{aligned} \tag{2.6}$$

where $L$ and $R$ represent the left-handed and the right-handed parts of the fields. Group $\mathrm{U(1)_Y}$ conserves the weak hypercharge $Y = 2(Q - T_3)$, where $Q$ is electric charge and $T_3$ is the projection of the weak isospin.

As mentioned before, the electroweak interactions can be split into two large classes:

- EM interactions have a long range, since their carrier, the photon, has zero mass.

- Weak interactions are carried by $W^{\pm}$ and $Z^0$ bosons. The large mediator masses cause this force to have a short range of about $10^{-18}$ m.

The weak interactions carried by $W^{\pm}$ bosons are called charged current (CC) interactions, as electric charges are transferred between the interacting particles. In these interactions neutrinos are converted into the corresponding charged leptons. The left part of Figure 2.1 depicts the CC interaction vertex of neutrinos. The corresponding part of the electroweak Lagrangian can be written [5] as

$$\mathcal{L}_I^{CC} = -\frac{g}{\sqrt{2}} \sum_{\ell=e,\mu,\tau} \left( W_\mu^+ \bar{\nu}_{\ell L} \gamma^\mu \ell_L + W_\mu^- \bar{\ell}_L \gamma^\mu \nu_{\ell L} \right), \tag{2.7}$$

where $\nu_{\ell L}$ and $\ell_L$ are the left-handed components of neutrino and lepton fields, respectively; $W^{\pm}$ are the fields of $W^{\pm}$-bosons.

A key characteristic of Equation (2.7) is that it only affects the left-handed (right-handed) part of the fields for particles (antiparticles), respectively. In the SM, neutrinos have only left-handed components. This plays an important role in the angular distribution of particles produced through neutrino interactions, as discussed in Section 2.5.

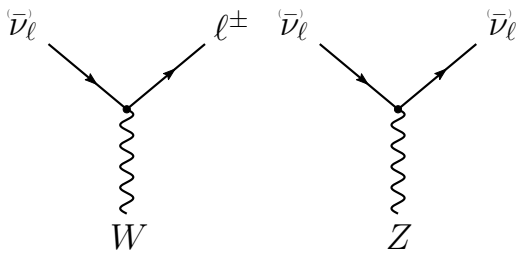


Figure 2.1: Feynman diagrams of neutrino charged current (left) and neutral current (right) interactions.

Neutral current (NC) interactions are carried by $Z^0$ bosons and the corresponding part of the electroweak Lagrangian can be formulated as

$$\mathcal{L}_I^{NC} = -\frac{g}{2c_W} \sum_{\ell=e,\mu,\tau} \left( \bar{\nu}_{\ell L} \gamma^\mu \nu_\ell - (1 - 2s_W^2) \bar{\ell}_L \gamma^\mu \ell_L + 2s_W^2 \bar{\ell}_R \gamma^\mu \ell_R \right) Z_\mu^0, \tag{2.8}$$

where $c_W$ ($s_W$) is the cosine (sine) of the Weinberg angle $\theta_W$, the mixing angle between SU(2) and U(1) sectors of the SM. The NC interactions occur via exchange of $Z^0$ bosons and do not convert neutrinos into charged leptons. The appearance of the right-handed components of the charged lepton fields in NC interactions is caused by the mixing between SU(2) and U(1) in the SM.

## 2.4 Neutrino properties

**Quantum numbers and number of generations**

There are three neutrino *flavours* in the Standard Model: $\nu_e$, $\nu_\mu$ and $\nu_\tau$. They are defined by the type of the associated charged leptons produced in the CC interactions. Each type carries empirically assigned lepton charge $L_\ell$, where $\ell$ denotes $e$, $\mu$ or $\tau$. Neutrinos have no electric charge and, therefore, do not interact electromagnetically. Also, neutrinos do not participate in the strong interaction, as do not carry any colour information.

The NC part of electroweak Lagrangian in Equation (2.8) is flavour-independent and is used to determine the total number of neutrino families. The decay width of the $Z$-boson depends on the number of neutrino species participating in the weak interaction. The most precise measurement was performed in experiments at LEP [24], where the number of neutrino families $N_\nu = 2.9840 \pm 0.0082$ was found, which is consistent with the three generations covered by the Standard Model. It is important to note that this number is only valid for neutrinos with masses much smaller than the mass of $Z$-boson and does not constrain the existence of heavy neutrinos or neutrinos that do not interact via the standard weak interaction, such as hypothetical right-handed neutrinos.

**Helicity and chirality**

Helicity, $h$, is a quantum property of particles and is defined by a projection of the spin into the momentum of a particle. A particle can be in states $h = +1$ when its spin and momentum are aligned or $h = -1$ when they are anti-parallel. If a particle is massless, as in case of neutrinos in the SM, the different chiral components of a fermion field are independent and describe states with different helicity. The right-handed particles and left-handed antiparticles have helicity equal +1. On the other hand, the left-handed particles and right-handed antiparticles have helicity of –1.

The helicity of neutrinos was determined by Maurice Goldhaber *et al.* [25], where it was found to be $h = -1$. In the Standard Model, neutrinos have zero mass and, therefore, helicity and chirality are both conserved for neutrinos.

**Neutrino mass**

Neutrinos are massless in the SM. However, the effects of massive neutrinos are observed in neutrino oscillations, as discussed in Chapter 3. They are affected by the differences between neutrino masses, but not the absolute mass scale, which has not yet been obtained from direct measurements. An explanation of non-zero neutrino masses and their smallness compared to the masses of other particles requires an addition of right-handed neutrinos or introduction of new symmetries into the SM [5, 14]. Current best limits on the neutrino mass in the direct searches are given by the measurements [26, 27] of the end point of the tritium decay spectrum

$$^3\mathrm{H} \rightarrow {}^3\mathrm{He} + \mathrm{e}^- + \bar{\nu}_\mathrm{e}, \tag{2.9}$$

where the most stringent limits are

$$\begin{aligned} \mathrm{m}_{\bar{\nu}_\mathrm{e}} &< 2.2 \text{ eV} \qquad \text{(Mainz)}, \\ \mathrm{m}_{\bar{\nu}_\mathrm{e}} &< 2.1 \text{ eV} \qquad \text{(Troitsk)}. \end{aligned} \tag{2.10}$$

The KATRIN experiment [28] should soon begin data-taking and will reach a sensitivity of 200 meV.

In addition, cosmological observations provide stringent limits on a sum of the neutrino masses as low as $\sum m_\nu < 0.12$ eV/c$^2$ (95% C.L.) [23]. A more detailed overview of the cosmological neutrino mass measurements can be found in the literature [23].

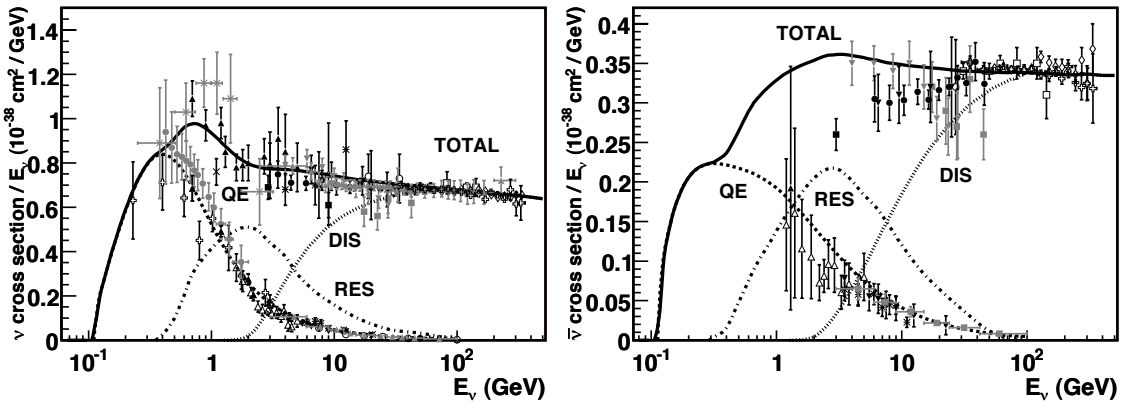


Figure 2.2: Total inclusive neutrino-nucleon cross-section as a function of neutrino energy for neutrinos (left) and antineutrinos (right). QE, RES and DIS denote contributions from quasi-elastic scattering, resonance production and deep inelastic scattering, respectively. The figures are taken from [29].

## 2.5 Neutrino interactions with matter

This section explains the interaction processes relevant for neutrinos with energies of around 1 GeV and above. Neutrino-nucleon interactions dominate cross-sections in this energy range and can be divided into three types: quasi-elastic scattering, resonant production and deep inelastic scattering. Their relative contributions to the total cross-section are shown in Figure 2.2. The following sections discuss the basic properties of each process, while an in-depth review can be found in literature [5, 29].

### 2.5.1 Quasi-elastic scattering

For neutrino energies below approximately 1 GeV, the quasi-elastic (QE) scattering is the dominant process for neutrino-nucleon interactions. In QE scattering a neutrino scatters on an entire nucleon rather than individual partons. Neutrons are converted into protons in neutrino interactions and vice-versa for antineutrino interactions. The corresponding leptons are produced as follows

$$\begin{aligned} \nu_\ell + n &\to p + \ell^-, \\ \bar{\nu}_\ell + p &\to n + \ell^+. \end{aligned} \tag{2.11}$$

The differential cross-section for this process can be written as

$$\frac{\mathrm{d}\sigma}{\mathrm{d}Q^2} = \frac{G_F^2 \left|V_{ud}\right|^2 m_N^2}{8\pi E_\nu^2} \left( A(Q^2) \pm \frac{(s-u)}{m_N^2} B(Q^2) + \frac{(s-u)^2}{m_N^4} C(Q^2) \right), \tag{2.12}$$

where $Q^2 = -q^2 = (p_\nu - p_\ell)^2$ is the negative transferred four-momentum squared, $E_\nu$ is the energy of a neutrino, $G_F$ is the Fermi constant, $V_{ud}$ is the element of the Cabibbo–Kobayashi–Maskawa (CKM) matrix, $m_N$ is the nucleon mass, $u$ and $s$ are

Mandelstam kinematic variables. The form factors $A(Q^2)$, $B(Q^2)$ and $C(Q^2)$ can be parametrised as functions of just one form factor

$$G_A(Q) = \frac{g_A}{\left(1 + \frac{Q^2}{M_A^2}\right)^2}, \tag{2.13}$$

where $g_A \approx 1.2694 \pm 0.0028$ and $M_A^{QE}$ is an effective axial mass. Various experimental data suggest using the value of the axial mass between 0.65 and 1.3 GeV. The GENIE collaboration [30, 31] recommends to use the value of $0.99^{+0.25}_{-0.15}$ GeV. The total cross-sections of the CC QE scattering for neutrinos and antineutrinos are depicted as dashed lines in Figure 2.2.

### 2.5.2 Resonant production

During scattering, neutrinos can produce excited states of nucleons, such as

$$\begin{aligned} \nu_\ell + N &\to \ell^- + X^*, \\ \bar{\nu}_\ell + N &\to \ell^+ + X^*, \end{aligned} \tag{2.14}$$

where $X^*$ is an excited baryonic state (e.g. $\Delta$, $N$ or similar). The cross-section of resonant scattering is usually parametrised in a form similar to Equation (2.12). However, the form factors and axial mass $M_A$ must be determined differently. The current recommendation by the GENIE collaboration is $1.12 \pm 0.22$ GeV [30, 31]. The resonant production is the dominant process at the energy ranges approximately 1.5–5 GeV (neutrinos) and 1.5–8 GeV (antineutrinos). The contribution of the resonant production to the total cross section is depicted by the dash-dotted lines in Figure 2.2.

### 2.5.3 Deep Inelastic Scattering

Inclusive deep inelastic scattering (DIS) is the leading interaction process for neutrinos with energies above approximately 5–8 GeV [29], as shown by the dotted lines in Figure 2.2. It is the predominant detection process for IceCube and, therefore, is covered in more details. In such interactions, the neutrino momentum is large enough to resolve the internal structure of nucleons and to interact with quarks directly. Typically, nucleons are broken in DIS resulting in the production of hadrons in the final states. The DIS process can be written as

$$\begin{aligned} \nu_\ell + N \to X + \ell^-,\ \bar{\nu}_\ell + N \to X + \ell^+ \quad &\text{(charged current)}, \\ \overset{(-)}{\nu}_\ell + N \to X + \overset{(-)}{\nu}_\ell \quad &\text{(neutral current)}, \end{aligned} \tag{2.15}$$

where $N = p, n$, and $\ell = e, \mu, \tau$, and $X$ denotes the set of hadrons produced in the interaction. The Feynman diagrams of these processes are depicted in Figure 2.3.

**Kinematics of DIS**

For the CC (NC) interactions in Equation (2.15) the four-momenta of individual particles can be denoted (see Figure 2.3) by $\boldsymbol{p}_{\nu_i}$, $\boldsymbol{p}_N$, $\boldsymbol{p}_\ell$ ($\boldsymbol{p}_{\nu_f}$), and $\boldsymbol{p}_X$ for the incoming neutrino, the nucleon, the resulting lepton and total four-momenta of hadrons, respectively. The kinematics of the interaction is described using Lorenz invariant variables

$$\begin{aligned} s &\equiv (\boldsymbol{p}_\nu + \boldsymbol{p}_N)^2 && \text{(centre-of-mass energy)}, \\ Q^2 \equiv -\boldsymbol{q}^2 &\equiv -(\boldsymbol{p}_{\nu_i} - \boldsymbol{p}_{\ell,\nu_f})^2 && \text{(momentum transfer)}, \\ x &\equiv \frac{Q^2}{2\boldsymbol{p}_N \cdot \boldsymbol{q}} && \text{(Bjorken } x\text{)}, \\ y &\equiv \frac{\boldsymbol{p}_N \cdot \boldsymbol{q}}{\boldsymbol{p}_N \cdot \boldsymbol{p}_{\nu_i}} && \text{(inelasticity)}. \end{aligned} \tag{2.16}$$

The DIS process typically occurs when variables satisfy the conditions:

$$Q^2 \gg m_N^2, \quad \boldsymbol{p}_N \cdot \boldsymbol{q} \gg m_N^2. \tag{2.17}$$

For DIS the inelasticity $y$ characterises a fraction of the neutrino energy that is spent on the production of hadrons, therefore,

$$y \approx E_{hadrons}/E_\nu \approx 1 - E_\ell/E_\nu, \tag{2.18}$$

where $E_\nu$ and $E_\ell$ are energies of an interacting neutrino and an out-coming lepton, respectively.

**Charged-current DIS**

In a charged current DIS, an interacting neutrino exchanges a $W^\pm$-boson with a

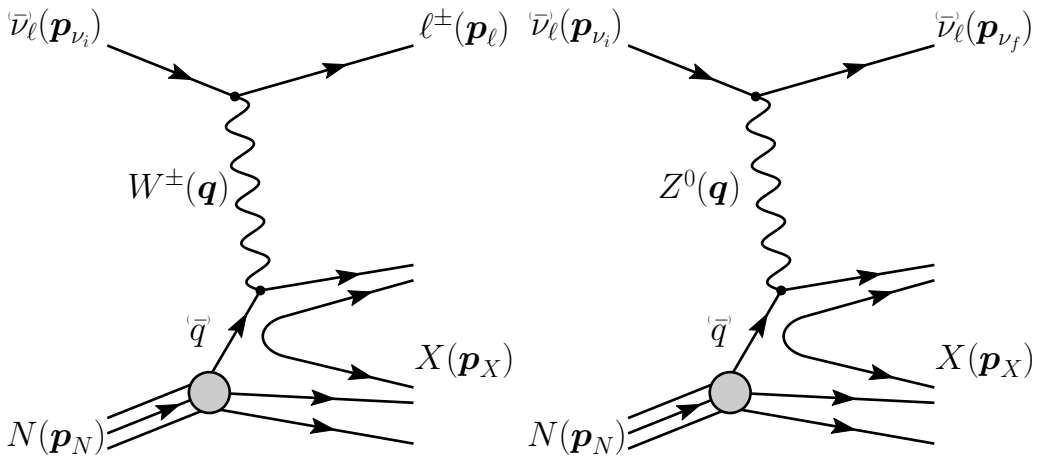


Figure 2.3: Feynman diagrams for neutrino-nucleon deep inelastic scattering (DIS) via charged (left) and neutral (right) currents. An initial nucleon is denoted as $N$, and resulting hadrons are labelled by $X$.

quark and is converted into the corresponding charged lepton. A Feynman diagram of this process is shown in the left part of Figure 2.3. The contribution of a quark $q$ or antiquark $\bar{q}$ to the total neutrino-nucleon cross section can be expressed as

$$\left(\frac{\mathrm{d}^2\sigma_{CC}^{\overset{(-)}{\nu}N}}{\mathrm{d}x\mathrm{d}y}\right)_{q,\bar{q}} = 2x\sigma_{CC}^0 g_{q,\bar{q}}^{\overset{(-)}{\nu}}(y) f_{q,\bar{q}}^N(x), \tag{2.19}$$

where $f_{q,\bar{q}}^N(x)$ is a parton distribution function (PDF) of a nucleon, and value

$$\sigma_{CC}^0 = \frac{G_F^2}{2\pi} s \left(1 + \frac{Q^2}{m_W^2}\right)^{-2}, \tag{2.20}$$

where $G_F$ is the Fermi constant, and $m_W$ is the mass of $W^{\pm}$. The factor $g(y)$ in Equation (2.19) is caused by the angular-momentum conservation.

If the helicities of the interacting (anti)neutrino and (anti)quark are opposite, their angular momenta are added, resulting in a preferred angular momentum direction. An example of such an angular momentum configuration for antineutrino-quark scattering is shown in the left part of Figure 2.4. This limits the available angular momenta phase space and leads to a reduction of the cross-section with a factor equal to $(1+\cos\theta^*)^2/4$, where $\theta^*$ is a scattering angle (see Figure 2.4) in the centre-of-mass system. The inelasticity is connected to the scattering angle with $y = (1-\cos\theta^*)/2$ and leads to a factor $g_{\bar{q}}^{\nu}(y) = g_q^{\bar{\nu}}(y) = (1-y)^2$ in Equation (2.19). For the scattering of neutrinos on quarks and antineutrinos on antiquarks, the angular momenta cancel, leading to no preferred direction and a factor $g_q^{\nu}(y) = g_{\bar{q}}^{\bar{\nu}}(y) = 1$.

The resulting cross-sections of neutrino-nucleon CC DIS interactions are

$$\begin{aligned}
\frac{\mathrm{d}^2\sigma_{CC}^{\nu N}}{\mathrm{d}x\mathrm{d}y} &= 2x\sigma_{CC}^0 \left[\sum_{q=d,s} f_q^N(x) + (1-y)^2 \sum_{\bar{q}=\bar{u},\bar{c}} f_{\bar{q}}^N(x)\right], \\
\frac{\mathrm{d}^2\sigma_{CC}^{\bar{\nu}N}}{\mathrm{d}x\mathrm{d}y} &= 2x\sigma_{CC}^0 \left[\sum_{\bar{q}=\bar{d},\bar{s}} f_{\bar{q}}^N(x) + (1-y)^2 \sum_{q=u,c} f_q^N(x)\right].
\end{aligned} \tag{2.21}$$

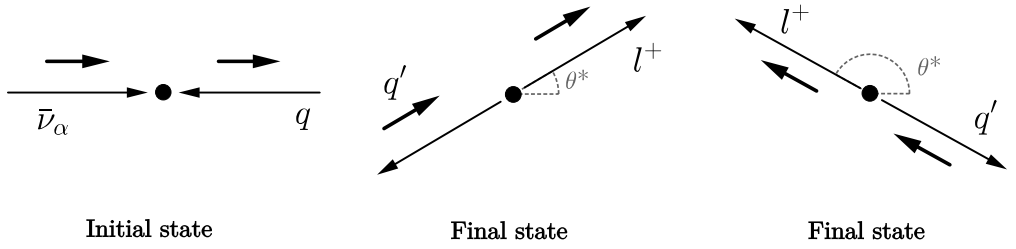


Figure 2.4: Angular momentum conservation in antineutrino-quark scattering. The configuration of particle momenta (thin arrows) and angular momenta (thick arrows) for initial state is shown in the left part, while middle and right parts depict two possible final states with different scattering angle $\theta^*$ in the centre-of-mass system. The drawing is taken from [32].

At the energies relevant to this work, nucleon PDFs are dominated by $u$ and $d$ quarks and, therefore, the cross-section can be written as

$$\begin{aligned} \frac{\mathrm{d}\sigma_{CC}^{\nu N}}{\mathrm{d}y} &\propto 2\sigma_{CC}^{0}\langle x\rangle_{d}^{N}, \\ \frac{\mathrm{d}\sigma_{CC}^{\bar{\nu} N}}{\mathrm{d}y} &\propto 2\sigma_{CC}^{0}(1-y)^{2}\langle x\rangle_{u}^{N}, \end{aligned} \tag{2.22}$$

where $\langle x\rangle_{q}^{N} = \int x f_{q}^{N}(x)\mathrm{d}x$ are the average momenta fractions carried by the corresponding quarks in the Breit frame. This means that antineutrinos are, on average, more likely to produce charged leptons with higher energies and less energetic hadrons than neutrino interactions. However, neutrino interactions have a total cross-section approximately two times higher than antineutrinos in the energy range considered in this work. Also, the cross-section dependences in Equation (2.22) result in slightly different signatures produced by muon neutrinos and antineutrinos, as discussed in Section 4.5.

**Neutral current DIS**

In neutral current interactions, neutrinos exchange $Z^0$ bosons with nuclei, without changing their flavour, as

$$\overset{(-)}{\nu}_{\ell} + N \rightarrow \overset{(-)}{\nu}_{\ell} + X. \tag{2.23}$$

The diagram for this process is shown in the right part of Figure 2.3. Neutral current interactions can be described using the same framework as for the CC interactions in the previous section. However, since NC interactions are mediated by $Z^0$ boson, Equation (2.20) has to be modified to

$$\sigma_{NC}^{0} = \frac{G_F^2}{2\pi} s \left(1 + \frac{Q^2}{m_Z^2}\right)^{-2}, \tag{2.24}$$

where $m_Z$ is the mass of $Z$-boson. The NC differential cross section then can be written as

$$\begin{aligned} \frac{\mathrm{d}\sigma_{CC}^{\nu N}}{\mathrm{d}x\mathrm{d}y} = 2x\sigma_{NC}^{0}\Big( & \left[(g_L^U)^2 + (1-y)^2(g_R^U)^2\right] \sum_{q=u,c} f_q^N(x) \\ & + \left[(g_L^D)^2 + (1-y)^2(g_R^D)^2\right] \sum_{q=d,s} f_q^N(x) \\ & + \left[(g_R^U)^2 + (1-y)^2(g_L^U)^2\right] \sum_{\bar{q}=\bar{u},\bar{c}} f_{\bar{q}}^N(x) \\ & + \left[(g_R^D)^2 + (1-y)^2(g_L^D)^2\right] \sum_{\bar{q}=\bar{d},\bar{s}} f_{\bar{q}}^N(x)\Big), \\ \frac{\mathrm{d}\sigma_{CC}^{\bar{\nu} N}}{\mathrm{d}x\mathrm{d}y} = & \left.\frac{\mathrm{d}\sigma_{CC}^{\nu N}}{\mathrm{d}x\mathrm{d}y}\right|_{L\leftrightarrow R}, \end{aligned} \tag{2.25}$$

Table 2.3: Possible neutrino sources, produced neutrino flavours and their energies.

| **Source** | **$\nu$ flavours** | **Energies** |
|---|---|---|
| The Sun | $\nu_e$ | 0.1-20 MeV |
| Nuclear reactors | $\bar{\nu}_e$ | 1–10 MeV |
| Radioactive decays and Geo-$\nu$ | $\overset{(-)}{\nu}_e$ | few MeV |
| Particle accelerators | $\overset{(-)}{\nu}_\mu, \overset{(-)}{\nu}_\tau$ | 0.1–200 GeV |
| Atmospheric production | $\overset{(-)}{\nu}_e, \overset{(-)}{\nu}_\mu$ | 0.1 MeV–100 TeV |
| The Big Bang | all | 0.17 meV |
| Supernovae | $\overset{(-)}{\nu}_e$ | 1-50 MeV |
| Astrophysical sources | all | observed above 200 TeV |

where factors $g_L^U = \frac{1}{2} - \frac{2}{3}\sin^2\theta_W$, $g_R^U = -\frac{2}{3}\sin^2\theta_W$, $g_L^D = -\frac{1}{2} + \frac{1}{3}\sin^2\theta_W$, $g_R^D = \frac{1}{3}\sin^2\theta_W$, and $f_{q,\bar{q}}^N$ are PDFs of the quarks and antiquarks of the nucleus $N$. Equation (2.25) has a more complicated structure than the equivalent expression for CC interactions, since quarks have both right and left-handed components due to the mixing between SU(2) and U(1) gauge groups for NC interactions, as for Equation (2.8).

## 2.6 Neutrino sources

Various neutrino sources played an essential role in the discovery of neutrinos and determination of their properties. The following section describes some of the available neutrino source types and their basic properties. A list of the source types, produced neutrino flavours and their approximate energy ranges are given in Table 2.3.

### 2.6.1 Nuclear reactors and radioactive decays

Historically, the first source type used in the detection of neutrinos were nuclear reactors. In nuclear reactors, a heavy nucleus (typically $^{238}$U) is split by a thermal neutron into two parts. This process creates neutron-rich nuclei that typically decay via beta decay and produce many electron antineutrinos. A typical energy of such neutrinos is between 1 and 10 MeV.

Similarly, a large quantity of an enriched radioactive isotope can be used as an artificial source of neutrinos. One of the possible neutrino sources is $^{51}$Cr, which decays via the electron capture reaction

$$^{51}\mathrm{Cr} + \mathrm{e}^- \rightarrow ^{51}\mathrm{V} + \nu_\mathrm{e}, \tag{2.26}$$

emitting neutrinos in two mono-energetic lines of 430 keV and 750 keV. Antineutrinos can be generated using $^{144}$Pr that undergoes beta-decay to $^{144}$Nd with a continuous antineutrino spectrum of energy up to 3 MeV.

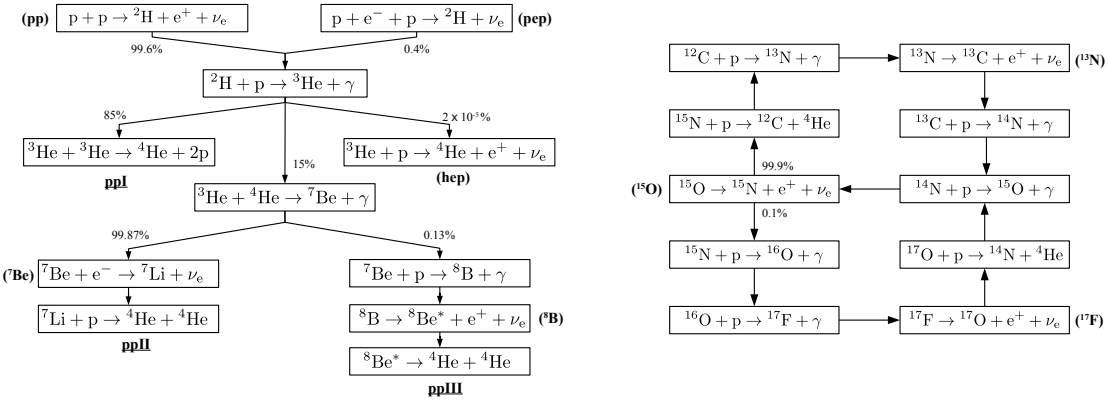


Figure 2.5: The thermonuclear processes in the Sun. The *pp* cycle is shown on the left and CNO cycle is on the right side of the drawing. The schematic is reproduced from [5].

The Earth has many radioactive isotopes. The decays of such nuclei produce a relatively large amount of neutrinos with energies similar to the ones from nuclear reactors.

### 2.6.2 Solar neutrinos

The Sun produces a large number of electron neutrinos in nuclear fusion processes. The thermonuclear processes in the Sun convert 4 protons into $^4$He as

$$4\mathrm{p} \rightarrow {}^4\mathrm{He} + 2\mathrm{e}^+ + 2\nu_\mathrm{e}. \tag{2.27}$$

This process occurs in two thermonuclear reaction chains: the *pp*-chain and the CNO cycle.

The *pp* chain starts by converting two protons into deuterium, with further production of helium and beryllium as shown in the left part of Figure 2.5. The first

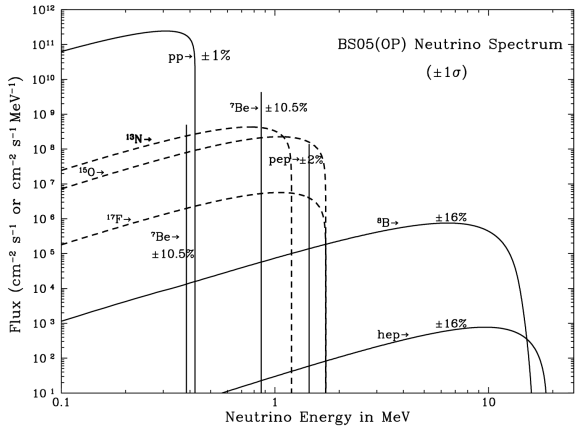


Figure 2.6: The spectrum of solar neutrinos in the Standard Solar Model [33]. For continuous flux components, the units are cm$^{-2}$ s$^{-1}$ MeV$^{-1}$. For the emission lines, the units are cm$^{-2}$ s$^{-1}$.

part of *pp* chain produces about 91% of solar neutrino flux but has a relatively low energy scale of up to 0.423 MeV. About 7.2% of neutrino flux is produced by $^{7}$Be with two neutrino lines of energies 0.39 and 0.86 MeV. Other processes contribute less than 0.3% to the total flux. Neutrinos with the highest energies are produced through *pp*-chain by the *hep* process and $^{8}$B decay, where neutrinos have energies up to 18.8 and 15 MeV, respectively.

The CNO cycle starts with $^{12}$C nuclei and converts four protons into $^{4}$He via a series of $(p, \gamma)$ processes and $\beta^{+}$-decays. The reactions occurring in the CNO cycle are shown in the right part of Figure 2.5. This chain contributes about 1.5% to the total flux.

The fluxes of different components of solar neutrinos in the Standard Solar Model [33] are shown in Figure 2.6.

### 2.6.3 Particle accelerators

Neutrinos are also produced using particle accelerators. A particle beam, typically composed of protons, is pointed towards a target, producing hadrons

$$p + N \rightarrow \pi^{\pm}, K^{\pm}, K^{0}, D^{\pm} \ldots, \tag{2.28}$$

where $N$ is a proton or neutron from the target material. Further strategies depend on the kind of neutrinos that are desired in the neutrino beam.

One of the options is to use magnetic fields to select corresponding charged particles (e.g. $\pi^{+}$ or $\pi^{-}$) and guide them into a decay tunnel, where the hadrons decay and produce neutrinos. Typically muon (anti)neutrinos are produced in this way. The selection of neutrinos or antineutrinos can be performed by changing the magnet configuration. Most of the current accelerator-based experiments, such as MINOS or T2K, use this technique. It is possible to select a narrow, low-energy range of neutrinos by placing the detector off-axis from the beam direction. The simulated change of a muon neutrino spectrum for the T2K beam at different off-axis angles is shown in the left part of Figure 2.7. This type of neutrino beams is called a *decay-in-flight* neutrino beam.

Another option is to use a low energy beam and stop hadrons in the target material before they decay. In this case, hadrons (typically charged pions) decay at rest and produce neutrinos with energies of approximately 40 MeV. This type of neutrino beams is called a *decay-at-rest* beam and was used, for example, in the LSND experiment [34].

A special neutrino beam was used in the DONUT experiment [35], where the Tevatron beam dump of 800 GeV protons was used to generate a neutrino beam enriched with tau neutrinos. In this case, most of the charged hadrons were stopped in the target material before decaying into neutrinos in a way similar to decay-at-rest beams. However, the energy of the proton beam was high enough to produce heavy hadrons that have a short lifetime and, therefore, decay before travelling even one interaction length in the material. This forms a prompt component of the neutrino spectrum. In the case of the Tevatron beam, charmed mesons, such as

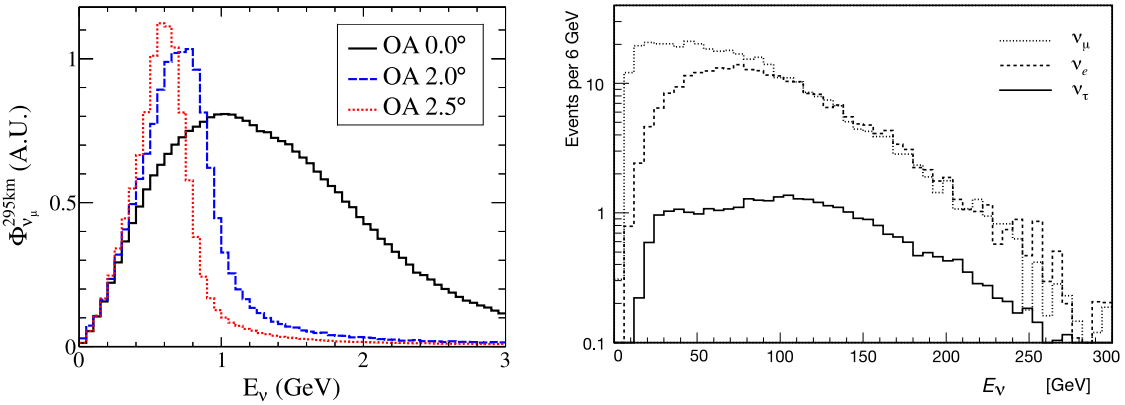


Figure 2.7: (Left) The energy spectrum of muon neutrinos for the J-PARC neutrino beam at a distance of 295 km for on axis (black) and off-axis (blue and red) locations of the detector [36]. (Right) The energy spectrum of different flavours produced by the Tevatron neutrino beam used in the DONUT experiment [35].

D-mesons, decayed to produce a neutrino beam enriched with tau neutrinos. The energy spectra of different components of the DONUT neutrino beam are shown in the right part of Figure 2.7.

### 2.6.4 Atmospheric neutrinos

Similarly to the accelerators, cosmic rays produce a lot of hadrons through interactions with nuclei in the atmosphere. They result in neutrino and muon production. Atmospheric neutrinos are used to study neutrino properties in this work. Therefore, more details about their production are given in this section.

**Cosmic rays**

The Earth's atmosphere is constantly bombarded with cosmic rays (CR). They consist mainly of protons and heavier nuclei [23]. The spectrum falls steeply with energy and has the energy dependence of approximately $E^{-2.65}$. The fluxes of the proton and heavier components of the primary cosmic ray spectrum are shown in Figure 2.8.

The CR interactions with the atmosphere produce hadrons that decay further to produce muons and neutrinos

$$\begin{aligned} \text{C.R.} + N \rightarrow X + \pi^{\pm}, K^{\pm} \\ \hookrightarrow \mu^{\pm} + \overset{(-)}{\nu}_{\mu} \\ \hookrightarrow e^{\pm} + \overset{(-)}{\nu}_{e} + \overset{(-)}{\nu}_{\mu}. \end{aligned} \tag{2.29}$$

The hadrons often have rather high energies and, therefore, produce particle cascades also known as *extensive air showers*. A typical altitude for the first interaction of cosmic rays is about 25 km.

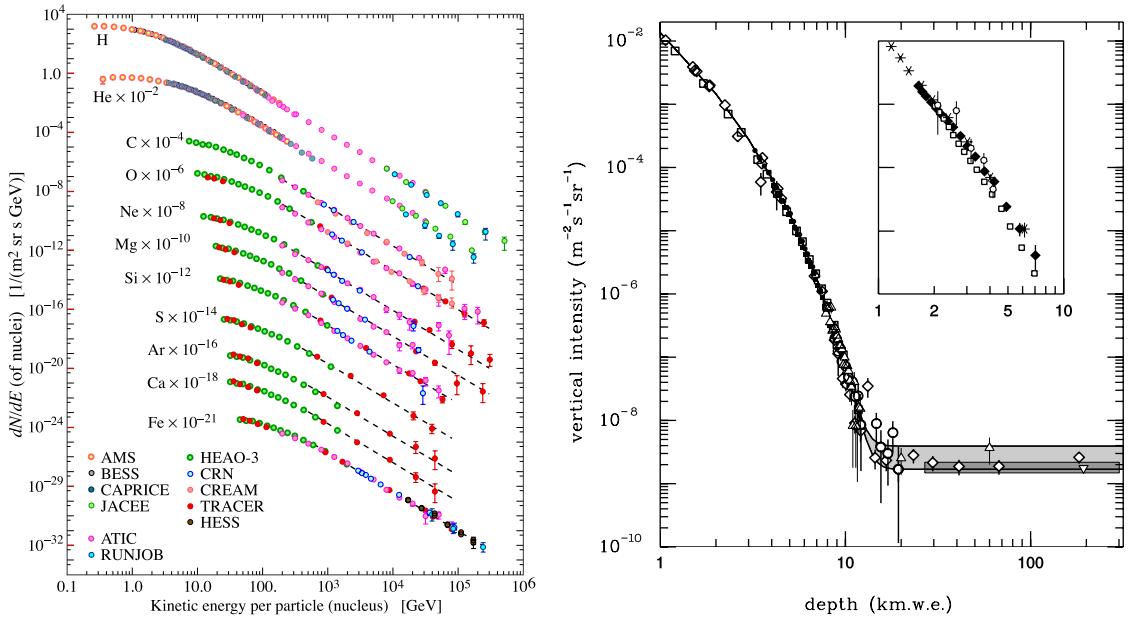


Figure 2.8: (Left) The spectrum of primary cosmic rays and its components. (Right) The intensity of muons as a function of depth in km of water equivalent (km.w.e.), the component up to 15 km.w.e. is created by CR interactions in the atmosphere and the deeper component is caused by muon neutrino interactions in the Earth. The inset compares the muon intensity for water and ice. The figures are taken from [23].

Neutrinos produced by reactions in Equation (2.29) are used in studies of atmospheric neutrino oscillations, while muons are the main background source for this work.

**Atmospheric muons**

Atmospheric muons are produced together with neutrinos in the same cosmic rays interactions. Such muons characterise CR interactions and are often used to study the corresponding hadronic processes. On the other hand, they form one of the crucial backgrounds for neutrino and low background physics. One of the ways to avoid it is to use the Earth crust as shielding and place detectors deep underground. The rate of down-going muons as a function of depth is shown in the right part of Figure 2.8. It is dominated by atmospheric muons up to a depth of approximately 10-15 km of water equivalent, and at larger depths, it is superseded by muons produced in neutrino interactions inside the Earth. This work uses the data from DeepCore, which is located only 2-2.5 km below the surface of the ice and, therefore, is heavily affected by atmospheric muons. This requires sophisticated veto techniques, which are discussed in Section 5.3.

**Atmospheric neutrinos**

Atmospheric neutrinos produced in CR interactions have a wide energy range between 100 MeV and approximately 200 TeV [37]. The muon neutrinos have an

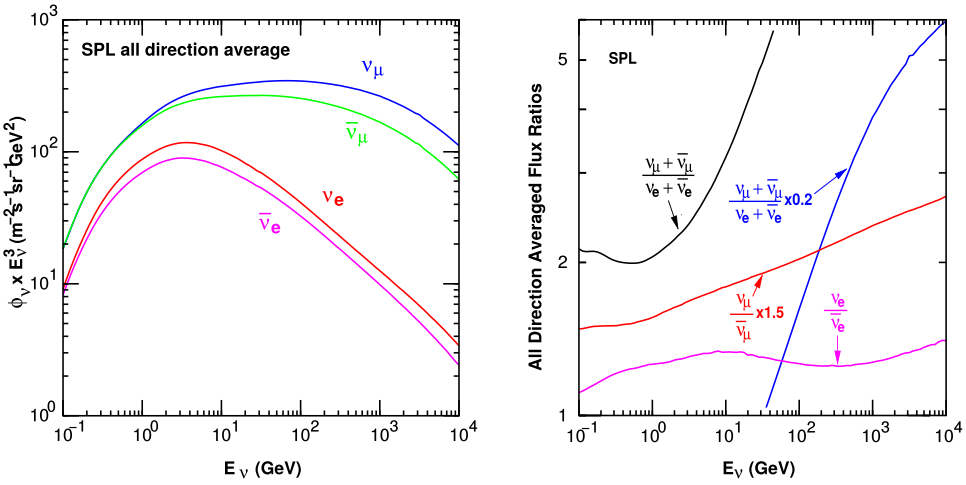


Figure 2.9: The fluxes of different neutrino flavours of atmospheric neutrinos a function of neutrino energy (left) and the ratios between them (right) calculated for the geographic South Pole. The figures are taken from [37].

energy spectrum of approximately $E^{-3}$ for energies between 10 and few hundreds GeV. The electron neutrino spectrum has a steeper energy dependence. The left part of Figure 2.9 shows atmospheric neutrino flux as a function of energy for different neutrino types as expected at the South Pole. The absolute fluxes of atmospheric neutrinos have rather large uncertainties of 20–30% at the energies used in this work.

The relative fractions of different components of the flux have an energy dependence. At low energies, almost all hadrons in Equation (2.29) decay producing neutrinos with a ratio $N_{\nu_\mu}/N_{\nu_e} \approx 2$. At higher energies, atmospheric muons can reach the Earth surface and lose their energy there. It results in very low energies of neutrinos produced by decays of such muons and suppresses the electron neutrino fraction at the energies above a few GeV. At approximately 100 GeV the muon neutrino flux is about 8 times higher than the flux of electron neutrinos.

The flux of cosmic rays is dominated by nuclei with a positive charge, while muon antineutrinos are typically produced by negatively charged hadrons or by muon decays. Therefore, the ratio of muon neutrinos to antineutrinos is equal to almost exactly 1 at the energies below 500 MeV, but rises with energy and at 1 TeV is approximately 1.6. The ratio of electron neutrinos to antineutrinos is between 1.25 and 1.35 for the energy range between 1 GeV and 1 TeV. The ratios between the fluxes of different neutrino flavours are shown in the right part of Figure 2.9.

Cosmic ray interactions can also produce charmed mesons or tau particles, resulting in the production of tau neutrinos. However, in the energy range considered in this work, the atmospheric tau neutrino flux is much smaller than 0.1% [38] and is neglected throughout this work.

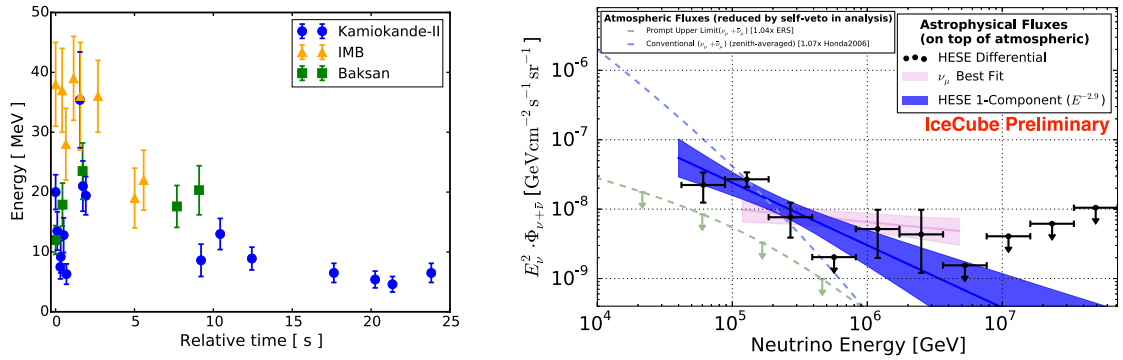


Figure 2.10: (Left) The times and energies of the neutrinos from SN1987A observed by the Kamiokande, IMB and Baksan neutrino experiments, the data are taken from [39–42]. (Right) The energy spectrum of astrophysical neutrinos observed with 6 years of IceCube data [43].

### 2.6.5 Astrophysical sources

Astrophysical processes in the Universe, such as CR interactions or supernovae explosions, can produce large quantities of neutrinos. Low energy neutrinos from supernovae explosions can be detected, if they occur sufficiently close. In 1987, the neutrinos from the supernova SN1987A were detected by Kamiokande [39], IMB [40] and Baksan [41] detectors. Their energies and arrival times after the supernova explosion are shown in the left panel of Figure 2.10.

The IceCube experiment observes neutrinos with energies up to a few PeV [44]. Such neutrinos can be produced in cosmic ray acceleration and interaction processes. They can be messengers of the most extreme processes occurring in the Universe, but their sources and generation mechanisms are not yet known. The flux of astrophysical neutrinos observed by the IceCube experiment is shown in the left part of Figure 2.10.

Another source of neutrinos is the cosmological development of the Universe. At about 379 000 years after the Big Bang, the Universe cooled down enough to allow neutrino decoupling [5]. The neutrinos had energies of about 1.3–1.5 MeV at that time. However, taking into account the expansion of the Universe, the present energy of such neutrinos is only about 0.17 meV. Neutrinos of such energies are extremely hard to detect experimentally and, thus, the cosmic neutrino background has not yet been observed.

# Chapter 3

# Neutrinos beyond the Standard Model

The properties of neutrinos in the Standard Model are discussed in Chapter 2. The existence of neutrino oscillations, discussed in this chapter, proves that neutrinos have small but non-zero masses, which are not covered by the Standard Model. First, this chapter introduces the neutrino mixing and neutrino oscillation effects, both in vacuum and matter. Then, the neutrino oscillation effects on the atmospheric neutrino flux are discussed. It is followed by information about the current status of neutrino mixing, including the recent experimental measurements and the global estimates of mixing parameters. The extension of the three-flavour paradigm, motivated by the anomalies observed at some neutrino oscillation experiments, is then discussed. Expected effects of the sterile neutrino mixing on the atmospheric neutrino flux are discussed at the end of this chapter.

## 3.1 Neutrino mixing

The properties of the weak interaction allow wave functions to enter the interaction in a form of a linear superposition of wave functions [5]. For massless particles, as for neutrinos in the SM, this does not cause any additional effects. However, the mixing of massive neutrinos results in neutrino oscillations, as discussed in the following sections.

The neutrino wave functions can be expressed [45] in two ways defined by the Hamiltonian eigenvalues. The first representation defines the *mass states* and characterises the neutrino behaviour in the absence of interactions. The mass states define the propagation of neutrinos through space. In the standard three-neutrino model, they are denoted as $\nu_1$, $\nu_2$ and $\nu_3$.

Another neutrino representation is defined by neutrino weak interactions, and the corresponding neutrino states are called the *flavour states*. These states are defined by charged leptons in the corresponding neutrino CC interactions and are denoted as $\nu_e$, $\nu_\mu$ and $\nu_\tau$.

The connection between these states is given [45] by

$$|\nu_\alpha\rangle = \sum_k U^*_{\alpha k} |\nu_k\rangle, \tag{3.1}$$

where $|\nu_\alpha\rangle$ are the flavour states with $\alpha = e, \mu, \tau$; $|\nu_k\rangle$ are the mass states with $k = 1, 2, 3$; and matrix $U_{PMNS}$ is Pontecorvo–Maki–Nakagawa–Sakata (PMNS) matrix [45, 46] that defines mixing between them. In the standard three-flavour model the mixing is parametrised as

$$U = \begin{pmatrix} 1 & 0 & 0 \\ 0 & c_{23} & s_{23} \\ 0 & -s_{23} & c_{23} \end{pmatrix} \begin{pmatrix} c_{13} & 0 & s_{13}e^{-i\delta_{CP}} \\ 0 & 1 & 0 \\ -s_{13}e^{i\delta_{CP}} & 0 & c_{13} \end{pmatrix} \begin{pmatrix} c_{12} & s_{12} & 0 \\ -s_{12} & c_{12} & 0 \\ 0 & 0 & 1 \end{pmatrix} \mathrm{diag}(1, e^{i\delta_1}, e^{i\delta_2}), \tag{3.2}$$

where $c_{ij} = \cos\theta_{ij}$ and $s_{ij} = \sin\theta_{ij}$ are cosine and sine of the mixing angle $\theta_{ij}$, respectively; $\delta_{CP}$ is the neutrino CP-violating phase. The last matrix in Equation (3.2) only applies if neutrinos are Majorana fermions and introduces two additional *Majorana* phases. These extra phases are irrelevant for neutrino oscillation effects [47], both in vacuum [48, 49] and matter [50], and are ignored in this work.

## 3.2 Neutrino oscillations in vacuum

Neutrinos are produced as a superposition of the mass states as expressed in Equation (3.1). This mixing and non-zero neutrino masses cause *neutrino oscillations*, the changes of the initial neutrino flavour after travelling some distance. This section describes the phenomenology of neutrino oscillations in vacuum using the plane wave approach from [5].

### 3.2.1 Interference of wave functions

When a neutrino of flavour state $\nu_\alpha$ is produced, it continues to travel through space as a superposition of the three mass states. Each state propagates through space as a plane wave

$$|\nu_k(t)\rangle = e^{-iE_k t} |\nu_k\rangle, \tag{3.3}$$

where $E_k = \sqrt{\vec{p}^2 + m_k^2}$ is the energy of the corresponding mass state, and $t$ is time. Since the mixing matrix in Equation (3.1) is unitary, this can be expressed as

$$|\nu_\alpha(t)\rangle = \sum_{\beta=e,\mu,\tau} \left( \sum_k U^*_{\alpha k} e^{-iE_k t} U_{\beta k} \right) |\nu_\beta\rangle. \tag{3.4}$$

Then, the probability of neutrinos to change the flavour from $\nu_\alpha$ to $\nu_\beta$ is

$$P_{\nu_\alpha \to \nu_\beta}(t) = |\langle \nu_\beta | \nu_\alpha(t) \rangle|^2 = \sum_{k,j} U^*_{\alpha k} U_{\beta k} U_{\alpha j} U^*_{\beta j} e^{-i(E_k - E_j)t}. \tag{3.5}$$

Since the neutrino masses are small compared to the kinetic energy, the energy can be expressed as

$$E_k \approx E + \frac{m_k^2}{2E}, \qquad E_k - E_j \approx \frac{\Delta m_{kj}^2}{2E}, \tag{3.6}$$

where value $\Delta m_{kj}^2 \equiv m_k^2 - m_j^2$ is called the *mass-squared splitting*. Due to ultra-relativistic neutrino speeds, the time in Equation (3.5) can be replaced with the distance travelled by neutrino as $t = L$. Then, the probability is

$$\begin{aligned} P_{\nu_\alpha \to \nu_\beta}(t) = \delta_{\alpha\beta} - 4 \sum_{k>j} \mathbf{Re}(U_{\alpha k}^* U_{\beta k} U_{\alpha j} U_{\beta j}^*) \sin^2 \left( \frac{\Delta m_{kj}^2}{4E} L \right) \\ + 2 \sum_{k>j} \mathbf{Im}(U_{\alpha k}^* U_{\beta k} U_{\alpha j} U_{\beta j}^*) \sin \left( \frac{\Delta m_{kj}^2}{2E} L \right), \end{aligned} \tag{3.7}$$

where $\alpha = \beta$ corresponds to a *survival probability*, i.e. the probability of the neutrino to keep its initial flavour, while $\alpha \neq \beta$ is a *transition probability*, i.e. probability of the initial state $\nu_\alpha$ to be detected as $\nu_\beta$.

The transition probabilities in Equation (3.7) are non-zero only if neutrino mass states have different masses and the neutrino mixing in Equation (3.2) has non-zero mixing angles. Therefore, the existence of neutrino oscillations proves that at least two neutrino mass states have non-zero masses and the existence of the neutrino mixing at the same time.

### 3.2.2 Two-neutrino approximation

The two-neutrino model is an approximation of the full three-flavour model, where only the mixing between two massive neutrinos is considered. This approximation often gives an accurate estimate of the neutrino oscillation probabilities, because the mass-squared differences $\Delta m_{21}^2$ and $\Delta m_{31}^2$ are different by about two orders of magnitude. Also, this approximation has only two parameters with intuitive physical meaning.

In this approximation, two neutrino flavours, $\nu_\alpha$ and $\nu_\beta$, are connected to two mass states, $\nu_1$ and $\nu_2$, by the rotation matrix with one mixing angle $\theta$

$$U = \begin{pmatrix} \cos\theta & \sin\theta \\ -\sin\theta & \cos\theta \end{pmatrix}. \tag{3.8}$$

This model has only one mass-squared difference $\Delta m^2 \equiv m_2^2 - m_1^2$. Using this notation, the transition probability in Equation (3.7) is expressed as

$$P_{\nu_\alpha \to \nu_\beta}(L) = \sin^2(2\theta) \sin^2 \left( \frac{\Delta m^2}{4E} L \right), \tag{3.9}$$

and the corresponding survival probability is written as

$$P_{\nu_\alpha \to \nu_\alpha}(L) = 1 - P_{\nu_\alpha \to \nu_\beta}(L) = 1 - \sin^2(2\theta) \sin^2 \left( \frac{\Delta m^2}{4E} L \right). \tag{3.10}$$

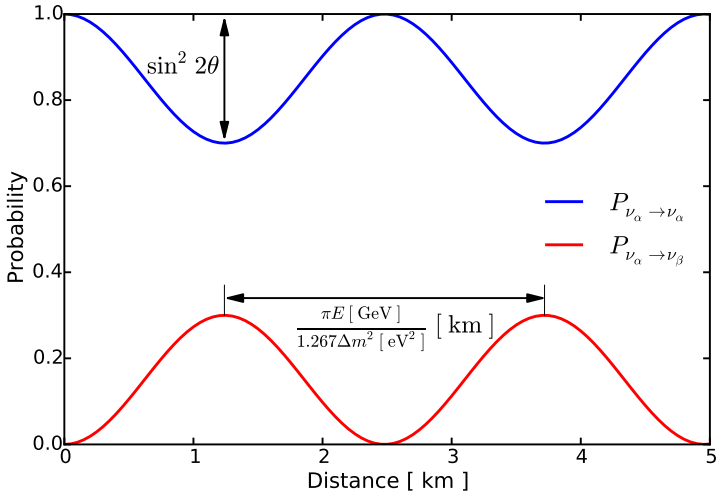


Figure 3.1: An example of the neutrino survival (blue) and transition (red) probabilities in the two-neutrino model. The physical meaning of the oscillations mixing parameters is depicted with arrows. The neutrino mixing parameters $\sin^2 2\theta = 0.3$ and $\Delta m^2 = 1$ eV$^2$ are assumed.

When converting from the natural units to the units used by experiments the neutrino oscillations phase is modified to

$$\frac{\Delta m^2 L}{4E} = 1.267 \frac{\Delta m^2\ [\ \mathrm{eV}^2\ ] \cdot \mathrm{L}\ [\ \mathrm{km}\ ]}{E\ [\ \mathrm{GeV}\ ]}. \tag{3.11}$$

The oscillation probabilities from Equations (3.9) and (3.10) as functions of the travelled distance are depicted in Figure 3.1. The amplitude of neutrino oscillations is defined by the value of $\sin^2 2\theta$, while the mass-squared splitting $\Delta m^2$ defines the total oscillation length

$$L_{osc}\ [\ \mathrm{km}\ ] = \frac{\pi E\ [\ \mathrm{GeV}\ ]}{1.267 \Delta m^2\ [\ \mathrm{eV}^2\ ]}. \tag{3.12}$$

After travelling the distance equal to $L_{osc}/2$ the neutrino has the highest probability to be detected as a different flavour state and returns to its initial state after $L_{osc}$.

## 3.3 Neutrino oscillations in matter

The previous section introduces the vacuum neutrino oscillations. The presence of matter can significantly modify the neutrino oscillation probabilities [51, 52] as discussed in this section. It starts with the introduction of the effective matter potentials, followed by the information about the effective mixing parameters and resonant matter effects. This section is based on [5].

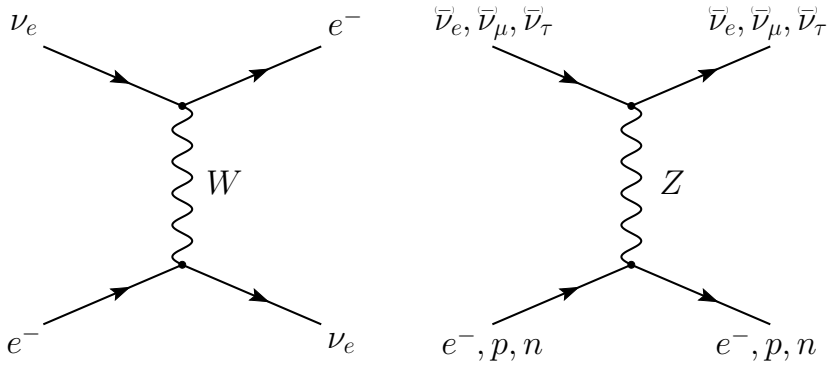


Figure 3.2: The Feynman diagrams for the elastic coherent forward scattering for charged (left) and neutral current (right) interactions. The diagram for electron antineutrino CC interactions can be obtained by the rotation of the left panel by 90°.

### 3.3.1 Effective matter potential

When neutrinos travel through matter, they experience a potential due to the coherent forward elastic weak scattering. It modifies the neutrino propagation and can change the oscillation probabilities.

Only electron neutrinos interact with electrons via the charged current elastic scattering. The Feynman diagram of this process is shown in the left part of Figure 3.2. The effective matter potential [51, 53] for this interaction is

$$V_{CC} = \sqrt{2} G_F N_e, \tag{3.13}$$

where $G_F$ is the Fermi constant and $N_e$ is the numerical density of electrons in medium. For electron antineutrinos, this potential has an opposite sign. Muon and tau neutrinos have no potential due to the CC interactions, since the ordinary matter has electrons but no muons or taus.

All neutrino flavours are equally affected by the neutral current coherent elastic scattering with electrons, protons and neutrons. The Feynman diagram for the corresponding processes is shown in the right part of Figure 3.2. The NC interaction potential is

$$V_{NC}^f = \sqrt{2} G_F N_f g_V^f, \tag{3.14}$$

where $f$ denotes a particle type with the corresponding numerical density $N_f$ and the vector coupling $g_V^f$. The $g_V^f$ values for fermions are given in Table 3.1. The

Table 3.1: The vector couplings $g_V$ for neutrinos, leptons, up and down quarks [5], $s_W$ denotes the sine of the Weinberg angle $\theta_W$.

| | $\boldsymbol{\nu_\ell}$ | $\boldsymbol{\ell}$ | $\boldsymbol{u,\ c,\ t}$ | $\boldsymbol{d,\ s,\ b}$ |
|---|---|---|---|---|
| $g_V$ | $\frac{1}{2}$ | $-\frac{1}{2} + 2s_W^2$ | $\frac{1}{2} - \frac{4}{3}s_W^2$ | $-\frac{1}{2} + \frac{2}{3}s_W^2$ |

electron is a fundamental particle; therefore, the potential is written as

$$V_{NC}^{e} = \sqrt{2} G_F N_e (-\frac{1}{2} + 2\sin^2\theta_W). \tag{3.15}$$

On the other hand, protons and neutrons consist of *uud* and *ddu* quark configurations, respectively, and their potentials are

$$\begin{aligned} V_{NC}^{p} &= \sqrt{2} G_F N_p (2g_V^u + g_V^d) = \sqrt{2} G_F N_p (\frac{1}{2} - 2\sin^2\theta_W), \\ V_{NC}^{n} &= \sqrt{2} G_F N_n (g_V^u + 2g_V^d) = -\frac{1}{2}\sqrt{2} G_F N_n. \end{aligned} \tag{3.16}$$

The potentials for protons in Equation (3.16) and electrons in Equation (3.15) have the same value, but opposite signs. Matter typically consists of atoms and is electrically neutral, what results in an equal number of protons and electrons, i.e. $N_p = N_e$. This results in the cancellation of their contributions leading to the NC potential driven only by neutrons as

$$V_{NC} \equiv V_{NC}^{n} = -\frac{1}{\sqrt{2}} G_F N_n, \tag{3.17}$$

while the potential for antineutrinos has an opposite sign.

### 3.3.2 Evolution of neutrino flavours

The evolution of neutrino flavours can be calculated from the Schödinger equation

$$i\frac{\mathrm{d}}{\mathrm{d}x}\Psi_\alpha = \hat{H}_F \Psi_\alpha, \tag{3.18}$$

where $\Psi_\alpha = (\psi_{\alpha e}, \psi_{\alpha\mu}, \psi_{\alpha\tau})^T$ define the flavour content of the wave function and $\hat{H}_F$ is the effective Hamiltonian in the flavour basis. For the three-neutrino model, it is defined as

$$\hat{H}_F = \frac{1}{2E} U \hat{\mathrm{M}}^2 U^\dagger + \hat{V}_{int}, \tag{3.19}$$

where $\hat{\mathrm{M}}^2 = \mathrm{diag}(0, \Delta m_{21}^2, \Delta m_{31}^2)$ is defined by the mass-squared splittings and $\hat{V}_{int} = \mathrm{diag}(V_{CC} + V_{NC}, V_{NC}, V_{NC})$ corresponds to the effective matter potential. Since the potential of the NC interactions is the same for all neutrino flavours and contributes only to the diagonal components of the Hamiltonian, it adds a common phase for all flavours and can be ignored. Then, the interaction part of Equation (3.19) can be replaced with $\hat{V}_{int} = \mathrm{diag}(V_{CC}, 0, 0)$. For neutrino with the initial flavour $\nu_\alpha$, the wave function is defined as $\Psi_\alpha(0) = \mathrm{diag}(\delta_{\alpha e}, \delta_{\alpha\mu}, \delta_{\alpha\tau})$ at the neutrino production point. Using this notation, the transition or survival probabilities are calculated as

$$P_{\nu_\alpha \to \nu_\beta}(x) = |\psi_{\alpha\beta}(x)|^2. \tag{3.20}$$

For vacuum this solution coincides with the probabilities in Equation (3.7). A full solution of Equation (3.18) with matter is complicated and typically performed numerically.

### 3.3.3 Effective mixing parameters and the MSW effect

Similarly to the vacuum oscillations discussed in Section 3.2.2, the two-flavour approximation simplifies the explanation of the matter effects. When the common phase is ignored, the evolution Equation (3.18) can be rewritten as

$$i\frac{\mathrm{d}}{\mathrm{d}x}\begin{pmatrix}\psi_\alpha\\ \psi_\beta\end{pmatrix} = \frac{1}{4E}\begin{pmatrix}-\Delta m^2\cos 2\theta + 2EV_{CC} & \Delta m^2\sin 2\theta\\ \Delta m^2\sin 2\theta & \Delta m^2\cos 2\theta - 2EV_{CC}\end{pmatrix}\begin{pmatrix}\psi_\alpha\\ \psi_\beta\end{pmatrix}. \quad (3.21)$$

This equation can be diagonalised by the transformation

$$U_M^T\hat{\mathrm{H}}_F U_M = \hat{\mathrm{H}}_M, \quad (3.22)$$

with

$$\hat{\mathrm{H}}_M = \mathrm{diag}(-\Delta m_M^2, \Delta m_M^2), \qquad U_M = \begin{pmatrix}\cos\theta_M & \sin\theta_M\\ -\sin\theta_M & \cos\theta_M\end{pmatrix}, \quad (3.23)$$

where $\Delta m_M^2$ and $\theta_M$ are the effective mass-squared splitting and the effective mixing angle, respectively. Then, the evolution equation is written as

$$i\frac{\mathrm{d}}{\mathrm{d}x}\begin{pmatrix}\psi_\alpha\\ \psi_\beta\end{pmatrix} = \frac{1}{4E}\begin{pmatrix}-\Delta m_M^2\cos 2\theta_M & \Delta m_M^2\sin 2\theta_M\\ \Delta m_M^2\sin 2\theta_M & \Delta m_M^2\cos 2\theta_M\end{pmatrix}\begin{pmatrix}\psi_\alpha\\ \psi_\beta\end{pmatrix}. \quad (3.24)$$

This equation coincides with the Equation (3.21) with $V_{CC} = 0$ but has modified mixing parameters. Therefore, the probabilities have the same form as for the vacuum oscillations

$$\begin{aligned} P_{\nu_\alpha\to\nu_\alpha} &= 1 - \sin^2 2\theta_M \sin\left(\frac{\Delta m_M^2 L}{4E}\right),\\ P_{\nu_\alpha\to\nu_\beta} &= \sin^2 2\theta_M \sin\left(\frac{\Delta m_M^2 L}{4E}\right). \end{aligned} \quad (3.25)$$

The effective mass-squared splitting value can be expressed using the vacuum mixing parameters and the matter potential as

$$\Delta m_M^2 = \sqrt{\left(\Delta m^2\cos 2\theta - 2EV_{CC}\right)^2 + \left(\Delta m^2\sin 2\theta\right)^2}, \quad (3.26)$$

while the effective mixing angle is

$$\tan 2\theta_M = \frac{\tan 2\theta}{1 - \frac{2EV_{CC}}{\Delta m^2\cos 2\theta}}. \quad (3.27)$$

Equations (3.26) and (3.27) have the resonance when the electron density is

$$N_e^R = \frac{\Delta m^2\cos 2\theta}{2\sqrt{2}EG_F}, \quad (3.28)$$

where even small mixing angles are enhanced to the maximal value $\theta_M|_R = \pi/4$. In this case, the effective mass-squared splitting has the minimal value

$$\Delta m_M^2|_R = \Delta m^2\sin 2\theta. \quad (3.29)$$

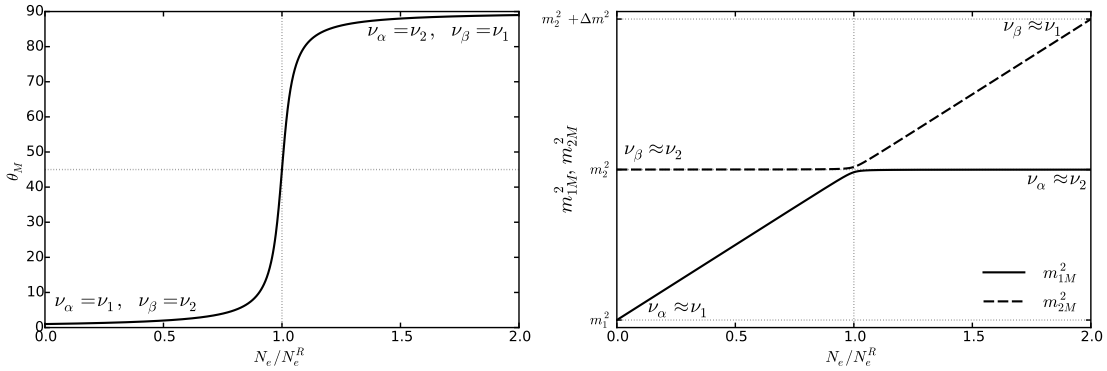


Figure 3.3: The effective mixing angle (left) and mass-squared splitting (right) for the two-flavour model as a function of the electron density $N_e/N_e^R$ for the vacuum mixing angle $\theta = 1°$.

This matter enhancement effect is called the *Mikheyev–Smirnov–Wolfenstein* (MSW) effect [51, 54]. The resonant condition can be satisfied only for neutrinos or antineutrinos separately, since they have opposite signs for the matter potentials $V_{int}^{\nu} = -V_{int}^{\bar{\nu}}$.

The behaviour of the effective mixing angle as a function of the electron density $N_e/N_e^R$ for a small vacuum angle is shown in the left panel of Figure 3.3. For $N_e \to 0$ the effective matter mixing angle is $\theta_M \approx \theta$. In this particular case, this means that the state $\nu_\alpha$ consists almost entirely of the mass state $\nu_1$ and $\nu_\beta$ of the state $\nu_2$. The $\theta_M$ reaches the maximal mixing value of 45° for the resonant density and leads to the maximal neutrino oscillation amplitude. When the density is much larger than the resonant value, the effective mixing angle is $\theta_M \to 90°$, resulting in $\nu_\beta \approx \nu_1$ and $\nu_\alpha \approx \nu_2$, what is opposite to the vacuum mixing. This condition is realised for $\nu_e - \nu_\mu$ mixing in the Sun, where electron neutrinos with energies above approximately 10 MeV are produced almost exclusively as the state $\nu_2$.

The effective mass-squared values for $\nu_1$ and $\nu_2$ are given by the expression

$$m_{M2,1}^2 = \frac{1}{2}\left(m_1^2 + m_2^2 + 2EV_{CC} \pm \Delta m_M^2\right). \tag{3.30}$$

Their behaviour is depicted in the right part of Figure 3.3. At densities $N_e \to 0$ the masses coincide with vacuum masses. The effective mass-squared splitting is minimal around $N_e \sim N_e^R$ and is given by Equation (3.29). At $N_e = 2N_e^R$ the mass-squared splitting is equal to $\Delta m^2$ and rises linearly as a function of density for larger values.

### 3.3.4 Mantle-core-mantle enhancement

An important resonant effect can happen when neutrino travels through matter of changing density. A particularly interesting effect happens when neutrino crosses a one-and-half period of the castle wall matter profile [55–59] shown in Figure 3.4.

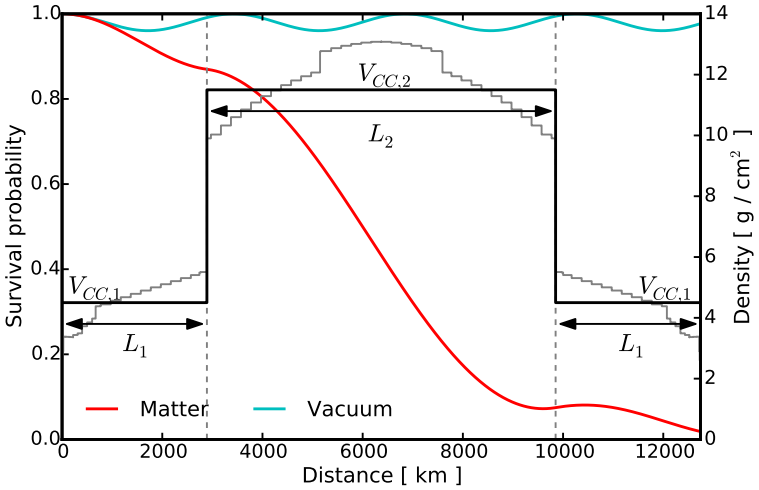


Figure 3.4: The Preliminary Earth Model (PREM) density profile (grey) and its one-and-half period of the castle wall parametrisation (black) for the diametral trajectory of the Earth. The effective potential and the length of mantle layers are denoted as $V_{CC,1}$ and $L_1$, respectively. The values $L_2$ and $V_{CC,2}$ correspond to the Earth's core. The survival probability in the two-flavour model in vacuum is shown in cyan, while the enhanced probability for the mantle-core-mantle effect is depicted in red. The mixing parameters are $\sin^2\theta = 0.01$ and $\Delta m^2 = 10^{-3}$ eV$^2$, while the neutrino energy is $E = 1.37$ GeV.

This profile corresponds to atmospheric neutrinos travelling through the mantle, crossing the Earth's core and travelling through mantle again.

In this case, the transition probability is given [5] by the relation

$$P_{\nu_\alpha\to\nu_\beta} = \left[2s_1\sin^2\theta_{M,1}(c_1c_2 - s_1s_2\cos 2(\theta_{M,1}-\theta_{M,2})) + s_2\sin 2\theta_{M,2}\right]^2, \qquad (3.31)$$

where $c_i = \cos\phi_i$ and $s_i = \sin\phi_i$ with $\phi_i = \Delta m^2_{M,i}L_i/4E$; $\theta_{M,i}$ and $\Delta m^2_{M,i}$ are the effective mixing angle and the mass-squared splitting in the corresponding layer of matter. This profile can result in a drastic increase of the oscillation amplitude as shown in Figure 3.4. It is important to note that this effect is not caused by the MSW effect described in Section 3.3.3, but is a result of the constructive parametric enhancement of the transition probabilities in consecutive layers of matter.

## 3.4 Standard atmospheric neutrino oscillations

Atmospheric neutrinos are of particular interest in this work. The production mechanism and properties of neutrinos are covered in Section 2.6.4, while this section discusses the neutrino oscillation effects.

For atmospheric neutrinos with energies above approximately 10-15 GeV, the neutrino oscillations are driven by the transition of muon neutrinos into tau neutrinos with the probabilities

$$P_{\nu_\mu\to\nu_\tau} \approx \sin^2 2\theta_{23}\sin^2\left(1.27\frac{\Delta m^2_{32}[\text{ eV}^2\text{ }]L[\text{ km }]}{E[\text{ GeV }]}\right), \quad P_{\nu_\mu\to\nu_\mu} \approx 1 - P_{\nu_\mu\to\nu_\tau}. \qquad (3.32)$$

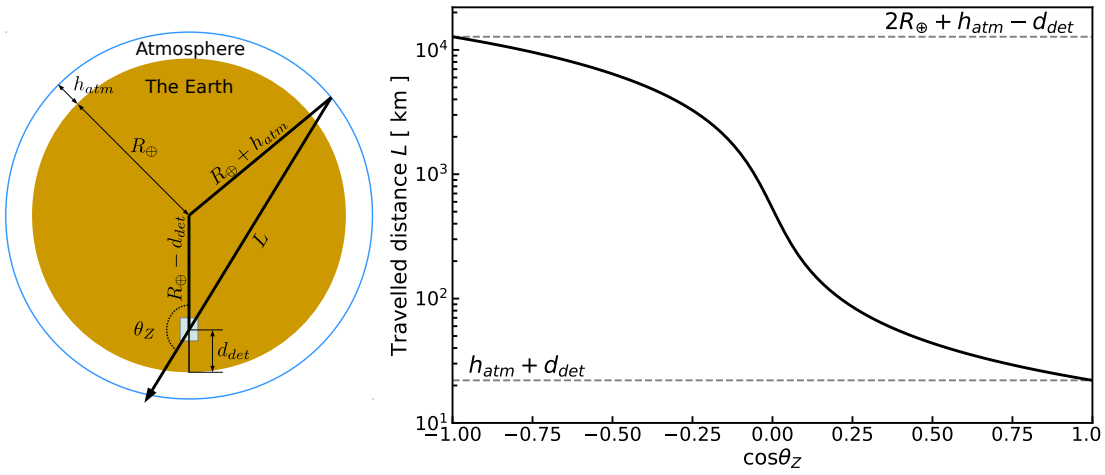


Figure 3.5: The geometry for the atmospheric neutrino oscillations (left) and the distance travelled by neutrino as a function of the cosine of the neutrino zenith angle (right).

The travelled distance $L$ is calculated using the Earth's geometry as

$$L = (R_\oplus - d_{det})\cos(\pi - \theta_Z) + \sqrt{(R_\oplus + h_{atm})^2 - (R_\oplus - d_{det})^2(1 - \cos^2(\pi - \theta_Z))}, \tag{3.33}$$

where $R_\oplus \approx 6371$ km is the Earth's radius; $d_{det}$ is the detector depth under the Earth's surface; $h_{atm} \sim 20$ km is the average altitude for the neutrino production in the atmosphere; and $\theta_Z$ is the neutrino zenith angle. The geometric representation of these values is shown in the left panel of Figure 3.5. The travelled distance $L$ as a function of the neutrino zenith angle is shown in the right panel of Figure 3.5. For IceCube, the *directly upgoing* neutrinos with $\cos\theta_Z = -1$ correspond to the maximal distance of $L \approx 12760$ km; the *horizontal* neutrinos with $\cos\theta_Z = 0$ have $L \approx 530$ km; while the directly *downgoing* neutrinos travel only the distance of $L \approx 22$ km.

The survival probabilities for muon neutrinos and antineutrinos as functions of the neutrino energy and zenith angle are depicted in Figure 3.6. The method described in [60, 61] is used for the calculations of the oscillation probabilities in the three-neutrino model including the matter effects. The probabilities above $\sim 15$ GeV are driven by Equation (3.32), while at energies below 10–15 GeV the matter effects start to play a significant role. As discussed in the next section, the neutrino mass ordering is currently unknown. For the normal neutrino mass ordering ($m_3 > m_2 > m_1$) muon neutrinos experience the matter effects, while antineutrinos are almost not affected. A change to the inverted ordering ($m_2 > m_1 > m_3$) results in the flip between probabilities for neutrinos and antineutrinos.

The neutrino oscillations result in an almost complete disappearance of the directly upgoing muon neutrinos and antineutrinos with energies of about 25 GeV. The energy of the minimum is proportional to the value of $\Delta m^2_{32}$, while its depth is defined by $\sin^2 2\theta_{23}$. The measurement of $\Delta m^2_{32}$ and $\sin^2\theta_{23}$ in the muon neutrino disappearance channel is one of the primary goals of this work and is presented in Chapter 6.

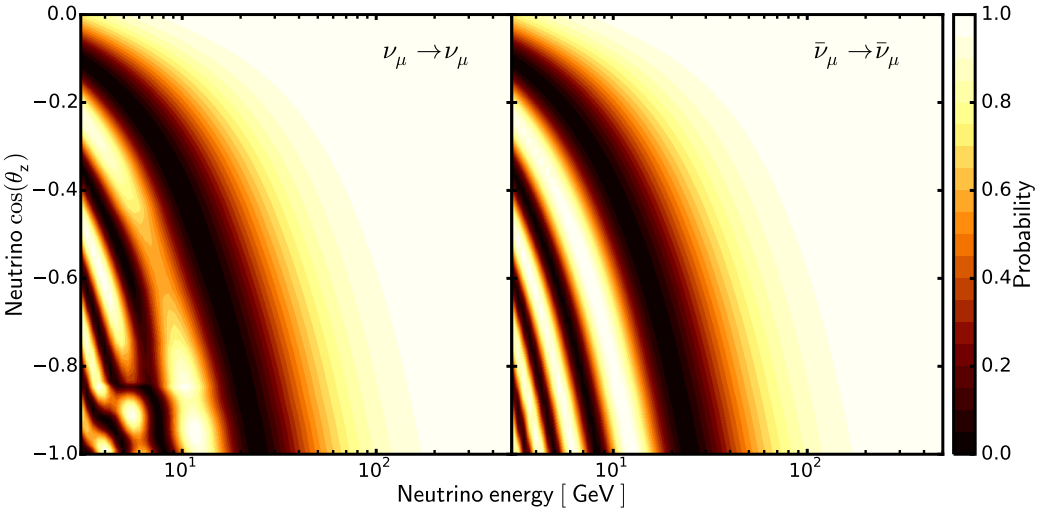


Figure 3.6: The muon neutrino (left) and antineutrino (right) survival probability as a function of the neutrino energy and cosine of the zenith angle. The normal neutrino mass ordering with $\Delta m^2_{31} = 2.515 \cdot 10^{-3}$ eV$^2$ and $\sin^2 \theta_{23} = 0.565$ is assumed. The distortions of the probabilities for muon neutrinos with $\cos \theta_z < -0.85$ are caused by the matter effects.

## 3.5 Current status of the three-neutrino model

This section discusses the current status of the neutrino oscillation experiments. First, selected experimental measurements are presented and are followed by the global estimates of the oscillations parameters. Finally, still unknown properties of the neutrino mixing are discussed.

### 3.5.1 Selected experimental results

A biased selection of the most important neutrino oscillation results is discussed in this section. It starts with atmospheric neutrino oscillation measurements, followed by the results obtained with accelerator neutrinos. Finally, the results of the reactor and solar neutrino experiments are discussed.

**Atmospheric neutrinos**

As stated earlier, the atmospheric neutrino oscillations are driven by the mass-squared splitting $\Delta m^2_{32}$ and the mixing angle $\theta_{23}$. In 1998, Super-Kamiokande was the first experiment [4, 64] to discover such oscillations by observing a deficit of muon neutrinos crossing the Earth.

The Super-Kamiokande experiment, shown in the left part of Figure 3.7, is a water Cherenkov detector located in the Kamioka mine, Japan. It consists of a steel tank with the height and the diameter of approximately 40 m containing 50 kton of water overlooked by about 13000 PMTs, which detect the Cherenkov light produced by neutrino interactions. The latest Super-Kamiokande measurement [63] of the atmospheric neutrino mixing is shown in the right panel of Figure 3.7.

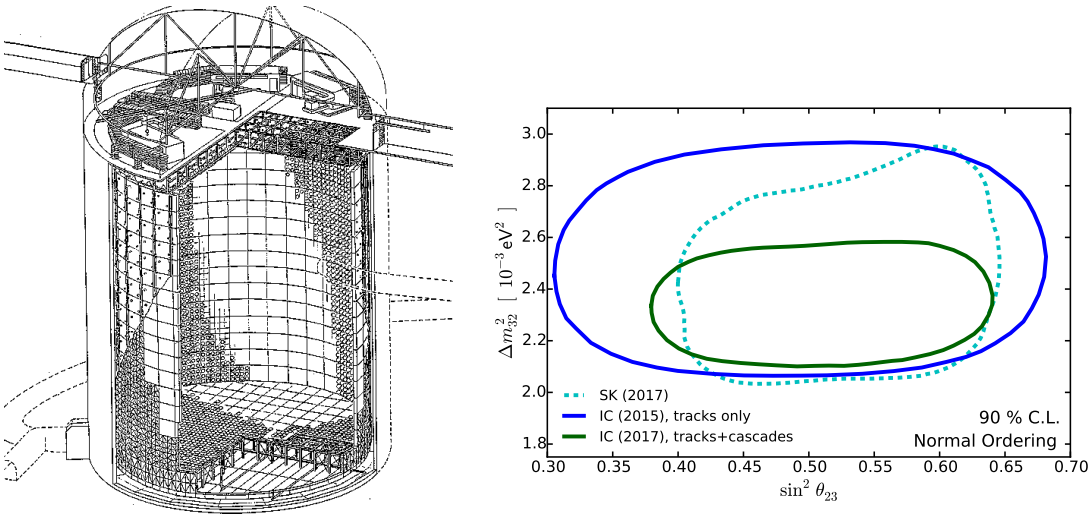


Figure 3.7: (Left) A schematic view of the Super-Kamiokande (SK) experiment [62]. (Right) The results for atmospheric neutrino mixing parameters at 90% C.L. obtained by SK (cyan) [63] and two studies performed by IceCube (blue and green) [7, 8]. The results shown in blue serve as the basis for this work.

Currently, IceCube [7, 8] provides some of the most precise measurements of the atmospheric neutrino oscillations. The design of the detector and its performance are discussed in Chapter 4. The results of two independent measurements from the IceCube experiment are depicted in the right part of Figure 3.7. The first study [7] is performed on three years of data taken between 2011 and 2013 and serves as the base for the study presented in this work. The second analysis [8] uses a broader event selection and more sophisticated reconstruction techniques with the data taken between 2012 and 2014.

**Accelerator neutrinos**

Currently, the most precise measurements of the mixing parameters $\Delta m^2_{32}$ and $\theta_{23}$ are obtained using accelerator neutrinos. Such experiments typically consist of two detectors: one near the neutrino beam site and another at a certain distance. This is done to use rate ratios in neutrino oscillation measurements and eliminate some of the systematic uncertainties. The neutrino beams are typically dominated by muon neutrinos and can operate in neutrino or antineutrino modes. As of now, the most precise results are coming from the MINOS/MINOS+ [65], T2K [66] and NOvA [67, 68] experiments.

The T2K experiment uses the neutrino beam produced at J-PARC in Tokai, Japan. The ND280 detector is used as the near detector, while Super-Kamiokande serves as the far detector. The energy spectrum peaks at approximately 0.6 GeV leading the maximal neutrino oscillation effect in the far detector, which is located at a distance of 295 km.

Two other experiments, NOvA and MINOS/MINOS+, use the NuMI beam [69] produced at Fermilab, the USA. MINOS uses the magnetised near and far detectors

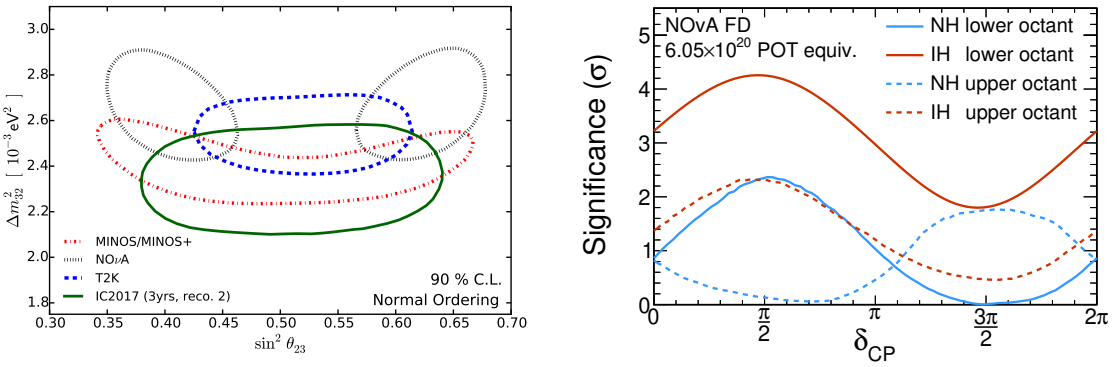


Figure 3.8: (Left) The measurements of the atmospheric mixing parameters provided by MINOS/MINOS+ [65] (red), T2K [66] (blue) and NOvA (black) [67] experiments. The most precise measurement from the IceCube experiment is shown in green for comparison. (Right) The $\delta_{CP}$ measurement provided by the NOvA experiment [68].

with the target masses of 1 and 5.4 kton, respectively. The far detector is located at the distance of approximately 735 km. The detectors consist of a steel and plastic scintillator layers. The scintillator strips have alternating orientations in different layers to allow the 3D event reconstruction. The NuMI beam was configured to produce neutrinos with the spectrum peaking at approximately 4 GeV during the MINOS experiment, while during the MINOS+ phase the energy was increased to about 7 GeV, as required for the NOvA experiment.

The NOvA experiment is located at approximately 14 mrad from the axis of the NuMI beam. This results in the neutrino energy spectrum peaking at approximately 2 GeV. The far detector is located approximately 810 km from Fermilab and consists of layers composed by cells filled with liquid scintillator. The consecutive layers have alternating orientations for the 3D event reconstruction. The near and far detectors use the identical design and have the target masses 0.3 and 14 ktons, respectively.

The accelerator experiments measure the $\nu_\mu$ disappearance as well as the appearance of $\nu_e$ in $\nu_\mu$ beams. The recent measurements of $\Delta m^2_{32}$ and $\theta_{23}$ provided by the aforementioned experiments are shown in the left panel of Figure 3.8. It is also possible to constrain $\delta_{CP}$ with the accelerator experiments and the recent results can be found in [66, 68, 70]. The example of such measurement obtained by the NOvA experiment is depicted in the right panel of Figure 3.8.

It is important to mention the results obtained by the OPERA experiment [71, 72], which confirmed the transition of muon neutrinos into the tau neutrino state using the CNGS beam at CERN. It used the detection system consisting of nuclear emulsion films interlined with lead plates and plastic scintillator strips. The tau neutrinos were identified by the kink produced by tau decays. Five tau neutrinos were observed in total, and one of such events is shown in Figure 3.9.

### Solar neutrinos

Historically, the first signs of neutrino oscillations were observed with solar neutrinos.

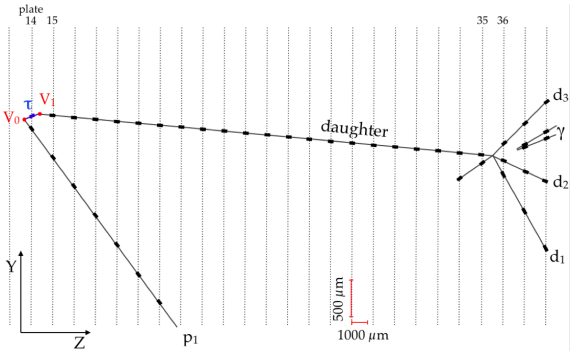


Figure 3.9: The 5th tau neutrino event observed by the OPERA experiment [71]. The dotted lines show the emulsion plates with found signals, and the lines represent the reconstructed particle trajectories, where the reconstructed $\tau$ is shown in blue.

At the end of 1960s, the Homestake experiment [73] started measurements using the neutrino capture reaction on $^{37}$Cl with the energy threshold of 0.814 MeV. The observed solar neutrino flux was only 30% of the predictions from the Standard Solar Model (SSM) [33]. A similar deficit was also observed by GALLEX / GNO [74, 75], SAGE [76] using Gallium as the target; Kamiokande [77] and Super-Kamiokande [78] using water. The predicted and observed fluxes are summarised in Figure 3.10.

The existence of the solar neutrino oscillations was confirmed by the SNO experiment [3, 81], depicted in the left part of Figure 3.11. It uses one kiloton of heavy water in 12-m diameter vessel as the target, which is overlooked by 9456 PMTs.

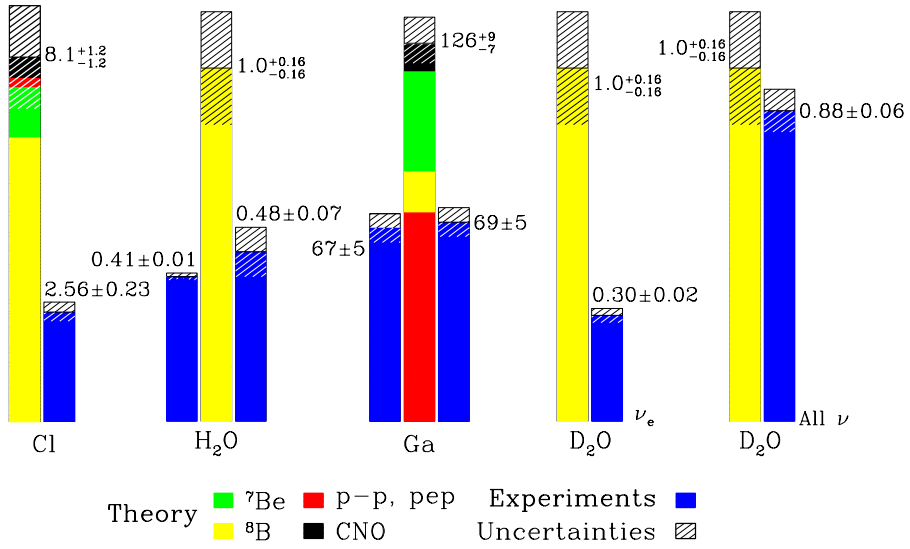


Figure 3.10: The standard solar model predictions (coloured bars) and the observed rates (blue bars) for experiments using chlorine (Cl), water ($H_2O$), gallium (Ga) and heavy water ($D_20$). For $D_2O$ $\nu_e$ and "All $\nu$" labels depict the phases of the SNO experiment sensitive to CC and NC interactions, respectively. The figure is taken from [79, 80] .

The CC, NC and elastic (ES) scatterings are observed using the reactions

$$\begin{aligned} \text{CC}: &\quad \nu_e + d \to p + p + e^-, \\ \text{NC}: &\quad \nu_\alpha + d \to p + n + \nu_\alpha, \\ \text{ES}: &\quad \nu_\alpha + e^- \to \nu_\alpha + e^-. \end{aligned} \tag{3.34}$$

The deficit similar to other experiments is observed with the CC interaction, while the rate of NC interaction is in good agreement with the SSM predictions. It means that electron neutrinos are converted into muon neutrinos as they travel from the Sun to the Earth, while the total flux of neutrinos is constant.

The sign of $\Delta m^2_{21}$ is determined by observing the matter effects in the solar neutrino oscillations. At low energies, the electron neutrino survival probability is

$$P_{ee} \equiv P_{\nu_e \to \nu_e} = 1 - \frac{1}{2}\sin^2 2\theta_{12} \approx 0.58. \tag{3.35}$$

If $\Delta m^2_{21} > 0$, the electron neutrinos are produced as the state $\nu_2$ at energies much larger than the MSW resonant energy, leading to

$$P_{ee} = \sin^2 \theta_{12} \approx 0.3. \tag{3.36}$$

If $\Delta m^2_{21} < 0$, this effect affects antineutrinos and is not observable, since they are not produced in the Sun. The right panel of Figure 3.11 depicts $P_{\nu_e \to \nu_e}$ as a function of neutrino energy, confirming that $\Delta m^2_{21} > 0$. The combined solar neutrino measurement for $\Delta m^2_{21}$ and $\theta_{12}$ is depicted in blue in the left panel of Figure 3.12.

**Reactor neutrinos**

The experiments measuring reactor neutrinos result in the precise measurements of the mass-squared splitting $\Delta m^2_{21}$ and $\Delta m^2_{31}$, and the mixing angles $\theta_{12}$ and $\theta_{13}$.

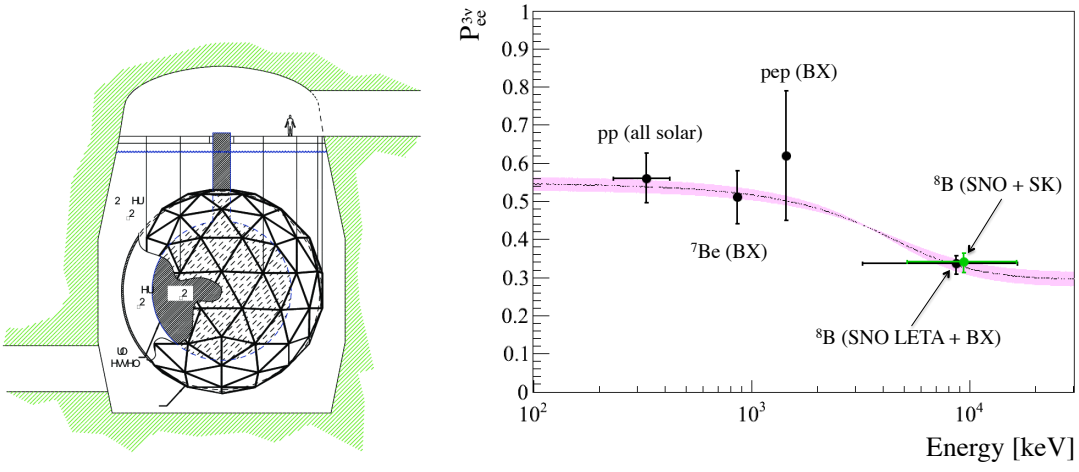


Figure 3.11: (Left) A schematic view of the SNO experiment [81]. (Right) The electron neutrino survival probability $P_{ee}$ for solar neutrinos as a function of neutrino energy [82]. The shaded band shows prediction with $\Delta m^2_{21} > 0$ and the data-points show different experimental measurements.

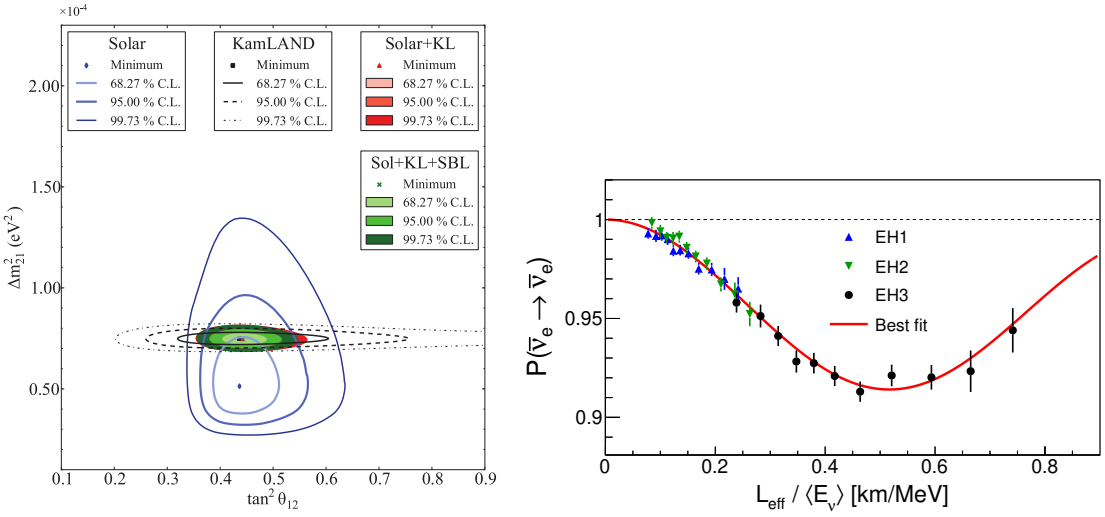


Figure 3.12: (Left) The results of KamLAND (black lines); solar neutrino experiments (blue lines), the combination between them (red shaded area); and the combination with the short baseline reactor experiments (green shaded area). The figure is taken from [81]. (Right) The observed neutrino oscillations due to $\theta_{13}$ observed by the Daya Bay experiment, where EH1, EH2 and EH3 denote the data from detectors located at different distances to the nuclear reactors [83].

The results of the KamLAND [84] experiment play an important role for the measurement of $\Delta m^2_{21}$ and $\theta_{12}$. Its detection volume consists of approximately 1 kton of the liquid scintillator in the 13-m diameter sphere, which is overlooked by approximately 1850 PMTs. It detects electron antineutrinos produced by 56 nuclear reactors with 180 km weighted average distance. The results of the KamLAND experiment are shown as black lines in the left part of Figure 3.12.

A new generation of reactor experiments typically consists of multiple identical liquid scintillator detectors located at various distances from nuclear power plants. As of now, the most precise reactor neutrino measurements are coming from the RENO [85], Double Chooz [86] and Daya Bay [83] experiments. Their data determined the non-zero value of the mixing angle $\theta_{13}$. An example of such measurement from the Daya Bay experiment is shown in the right panel of Figure 3.12.

### 3.5.2 Combined fit and unknown properties of neutrino mixing

**Global estimates of the mixing parameters**

A variety of data taken by different neutrino oscillation experiments is analysed to make global estimates of the neutrino mixing parameters. Such estimates are provided by Particle Data Group [23, 89] or NuFIT [87, 88]. The best-fit estimates for the neutrino mixing parameters from NuFIT 3.1 are listed in Table 3.2.

The value of $\sin^2\theta_{12}$ is approximately 0.3 and $\sin^2\theta_{23}$ is very close to 0.5 (the maximal mixing). On the other hand, the third mixing angle is very small with

Table 3.2: The global estimates of the three-neutrino mixing parameters from NuFIT 3.1 [87, 88] and experimental channels sensitive to these parameters. The value of $\Delta m^2_{3\ell} = \Delta m^2_{31} > 0$ for the normal ordering (NO) and $\Delta m^2_{3\ell} = \Delta m^2_{32} < 0$ for the inverted ordering (IO).

| **Parameter** | | **NuFIT 3.1** | **Experimental channel** |
|---|---|---|---|
| $\sin^2\theta_{12}$ | | $0.307^{+0.013}_{-0.012}$ | $\nu_e \to \nu_e$ (solar), |
| $\Delta m^2_{21}$ [ $10^{-5}$ eV$^2$ ] | | $7.40^{+0.21}_{-0.20}$ | $\bar{\nu}_e \to \bar{\nu}_e$ (reactor) |
| $\sin^2\theta_{23}$ | NO | $0.565^{+0.025}_{-0.120}$ | $\nu_\mu \to \nu_\mu$, $\nu_\mu \to \nu_\tau$ |
| | IO | $0.572^{+0.021}_{-0.028}$ | (atmospheric, accelerator) |
| $\Delta m^2_{3\ell}$ [ $10^{-3}$ eV$^2$ ] | NO | $2.515 \pm 0.035$ | |
| | IO | $-2.483^{+0.034}_{-0.035}$ | $\bar{\nu}_e \to \bar{\nu}_e$ (reactor) |
| $\sin^2\theta_{13}$ | NO | $0.02195^{0.00075}_{0.00074}$ | $\bar{\nu}_e \to \bar{\nu}_e$ (reactor) |
| | IO | $0.02212^{+0.00074}_{-0.00073}$ | |
| $\delta_{CP}$ [ $^\circ$ ] | NO | $228^{+51}_{-33}$ | $\nu_\mu \to \nu_e$ |
| | IO | $281^{+30}_{-31}$ | (accelerator) |

the value of $\sin^2\theta_{13} \approx 0.02$. The value of the mass splitting $\Delta m^2_{21} \approx 7.4 \cdot 10^{-5}$ eV$^2$ is approximately 30 times smaller than $|\Delta m^2_{32}| \approx 2.5 \cdot 10^{-3}$ eV$^2$. As of now, most of the neutrino mixing parameters are known with the precision better than 5%. However, some parameters are still known with poor precision and are discussed in the following paragraphs.

**Neutrino mass ordering**

As stated earlier, the sign of $\Delta m^2_{21}$ is known from the solar neutrino measurements. However, the sign of the atmospheric mass-squared splitting $\Delta m^2_{32}$ is unknown. Therefore, there are two possible neutrino mass orderings as shown in the left part of Figure 3.13. In the normal mass ordering (NO) the state $\nu_3$ is the heaviest and $m_3 > m_2 > m_1$, while for the inverted mass ordering (IO) the state $\nu_3$ is the lightest with $m_2 > m_1 > m_3$.

**Octant and value of $\theta_{23}$**

The leading effect of the three-neutrino oscillations for atmospheric and accelerator neutrinos is driven by Equation (3.32) and is proportional to $\sin^2 2\theta_{23}$. This results in the degeneracy for the mixing angle octant ($\theta_{23} \to \pi/4 - \theta_{23}$). The example of such degeneracy is shown in the right part of Figure 3.13.

**CP-violating phase $\delta_{CP}$**

There are indications that neutrinos experience a maximal CP-violation with $\delta_{CP} \approx 3\pi/2$. As of now, the no-CP-violation hypothesis with $\delta_{CP} = 0$ is disfavoured with a significance of only about $2\sigma$ and it is necessary to measure it with better precision.

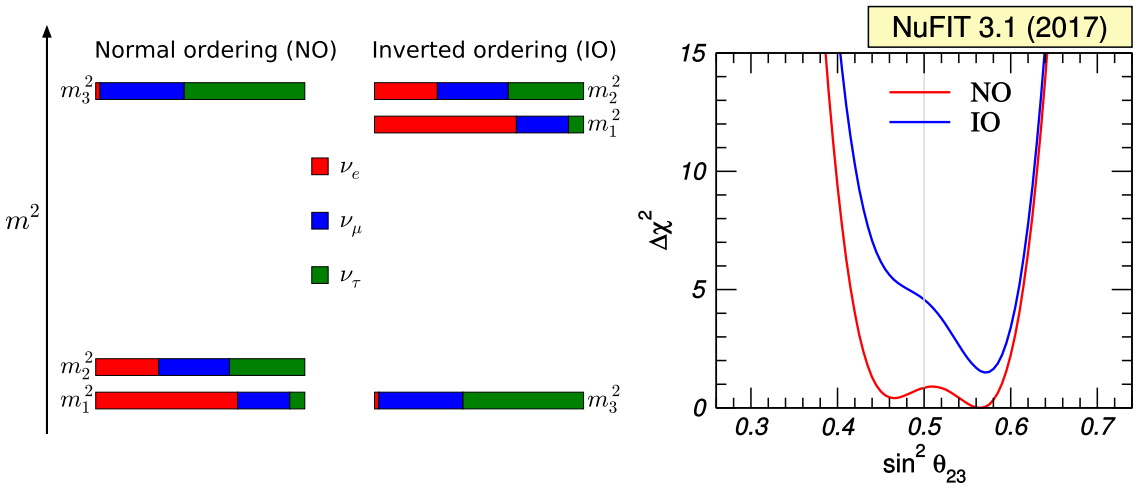


Figure 3.13: (Left) Two possible realisations of the neutrino mass ordering. (Right) The result of the combined fit for $\sin^2\theta_{23}$ from [88] that shows the $\theta_{23}$ octant degeneracy.

## 3.6 Sterile neutrinos

A number of anomalous results were observed by various neutrino oscillation experiments. Such anomalies can be explained by additional neutrinos that do not take part in the weak interactions. The following section discusses the anomalies, the phenomenology of the sterile neutrino mixing and the current experimental results relevant for atmospheric neutrinos.

### 3.6.1 Anomalies in neutrino oscillation data

**Accelerator short-baseline experiments**

Indications of neutrino oscillations at distances shorter than expected from the standard three-flavour model are observed with accelerator neutrinos. The LSND experiment measured [9] the excess of electron neutrinos in the decay-at-rest muon neutrino beam with energies between 20 and 52.8 MeV. It used a liquid scintillator detector with the effective mass of about 167 tons. The expected electron neutrino flux is about $8 \times 10^{-4}$ of the total flux. The observed excess consists of extra $(87.9 \pm 22.4 \pm 6.0)$ electron neutrinos as shown in the left part of Figure 3.14. The measured rates are consistent with a hypothesis of an extra neutrino type with a mass-squared splitting in the range of 0.2–10 $\text{eV}^2$.

The MiniBooNE experiment confirmed [10] the LSND results, but it observed the difference between neutrino and antineutrino oscillations. It requires more than one additional neutrino as an explanation. The observed event excess and fits to the various neutrino hypotheses are shown in the right panels of Figure 3.14.

**Reactor neutrinos**

Anomalies are also observed with reactor antineutrinos, where the measured flux is approximately 5% lower than the theoretical predictions. The compilation of such

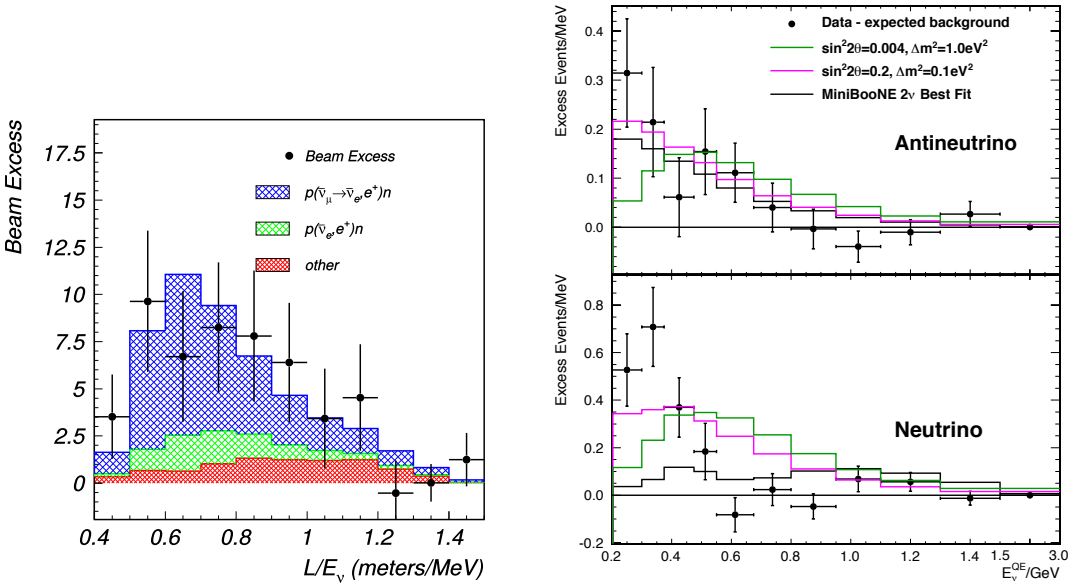


Figure 3.14: (Left) The event excess (black points) observed by the LSND experiment [9]. The expectation from $\nu_e$ contamination in the beam and other backgrounds are depicted in green and red, respectively. The expectation from $\nu_\mu \to \nu_e$ transition due to the mixing of a new neutrino state is depicted in blue. (Right) The event excess observed by the MiniBooNE experiment [10] for neutrinos (lower panel) and antineutrinos (upper panel). The lines depict expectations for the different realisations of the mixing to a new state, while black curve shows the extracted best-fit expectation for each mode.

results is shown in Figure 3.15. These results can be interpreted by oscillations of electron antineutrinos to a new neutrino type with the mass-squared splitting on the order of a few eV$^2$ [11].

However, a variety of isotopes and uncertainties in the decay branching ratios make nuclear reactor flux modelling very challenging. The distortion of the reactor antineutrino flux between 4 and 6 MeV is observed by current experiments [85, 86, 90, 91]. Also, the recent results from the Daya Bay [92] experiment show the correlation between the neutrino deficit and the nuclear reactor load, what disfavours the model with additional neutrino types. Therefore, the reactor neutrino anomaly is likely to be resolved by better reactor flux modelling rather than additional neutrino species.

### Radiochemical experiments

The radiochemical experiments measuring solar neutrinos were calibrated using $^{51}$Cr and $^{37}$Ar isotopes as neutrino sources [12]. The ratio between the observed and predicted neutrino fluxes is

$$R^{Ga} = 0.86 \pm 0.05, \tag{3.37}$$

leading to approximately $2.8\sigma$ tension [12, 13]. It can be explained by electron neutrino oscillation to a new neutrino type with the mass-squared splitting on the

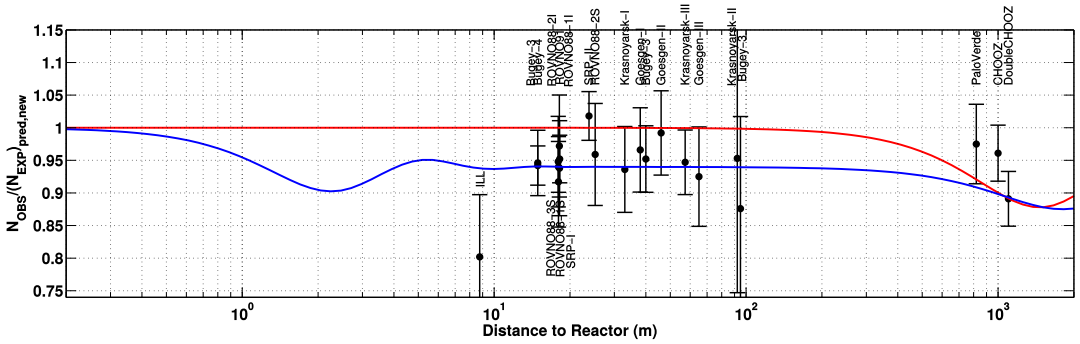


Figure 3.15: The observed fraction of the expected reactor antineutrino flux as a function of the distance to reactors, as seen by different experiments. The red line depicts the expectation without sterile neutrinos, while the blue line shows the expectation that includes the mixing to a new sterile state with $\Delta m^2 > 2$ eV$^2$ and $\sin^2 2\theta = 0.12$. The figure is taken from [93].

order of a few eV$^2$.

### 3.6.2 Sterile neutrino mixing in the "3+1" model

Some anomalies discussed in the previous section can be explained by additional neutrino species. However, the experimental data from LEP [24] limit the possibility of new neutrinos to take part in the weak interaction. Therefore, further neutrino species should be *sterile*.

The simplest extension of the three-neutrino theory is the "3+1" sterile neutrino model. It adds a single sterile neutrino $\nu_s$ with the corresponding neutrino mass state $\nu_4$. In this work, the mass $m_4$ is assumed to be the heaviest in order not to violate the cosmological limits on the sum of neutrino masses $\sum m_\nu$ (see review in [23]).

In this case, the mixing matrix from Equation (3.2) is expanded to have a $4 \times 4$ shape

$$\mathbf{U} \equiv \begin{pmatrix} U_{e1} & U_{e2} & U_{e3} & U_{e4} \\ U_{\mu 1} & U_{\mu 2} & U_{\mu 3} & U_{\mu 4} \\ U_{\tau 1} & U_{\tau 2} & U_{\tau 3} & U_{\tau 4} \\ U_{s1} & U_{s2} & U_{s3} & U_{s4} \end{pmatrix}, \tag{3.38}$$

where the last column controls the mixing between active and sterile neutrino states.

A new neutrino state adds 3 mixing angles and two CP-violating phases to the mixing matrix [94]. IceCube has no sensitivity to CP-phases and they are assumed to be zero in this work. In this case, the PMNS matrix is parametrised as

$$\mathbf{U} = \mathbf{U_{34}U_{24}U_{23}U_{14}U_{13}U_{12}}, \tag{3.39}$$

where $\mathbf{U_{ij}}$ denotes a rotation matrix in the $ij$-plane by an angle $\theta_{ij}$. The angle $\theta_{14}$ controls the mixing between $\nu_e$ and $\nu_4$ and is ignored in this work due to strict

limits from other experiments [94] and limited impact on the analysis presented in this work. Therefore, the additional elements of the mixing matrix have values

$$\begin{aligned} |U_{e4}|^2 &= 0, \\ |U_{\mu 4}|^2 &= \sin^2\theta_{24}, \\ |U_{\tau 4}|^2 &= \cos^2\theta_{24} \cdot \sin^2\theta_{34}. \end{aligned} \tag{3.40}$$

The elements $U_{\mu 4}$ and $U_{\tau 4}$ are in the focus of this work and their impact on atmospheric neutrinos is discussed in more details in Section 3.7.

It is important to note that the anomalies discussed in the previous section require a non-zero sterile neutrino mixing to electron and muon states. The reactor and radiochemical anomalies need a non-zero element $U_{e4}$, while the anomalies in the accelerator data require a non-zero combination of $U_{e4}U_{\mu 4}$.

### 3.6.3 Current limits on $|U_{\mu 4}|^2$ and $|U_{\tau 4}|^2$

Various neutrino oscillation experiments perform searches for the sterile neutrino mixing. SciBooNE/MiniBooNE [100], CDHS [99], CCFR [98], Super-Kamiokande [97], IceCube [96] and MINOS/MINOS+ [95] place limits on the allowed mixing angle $\theta_{24}$ (or mixing element $|U_{\mu 4}|^2$) in a wide range of the sterile mass-squared splitting $\Delta m^2_{41}$. These limits are shown in the left panel of Figure 3.16. In the range of masses considered in this work the strongest limits are coming from the searches

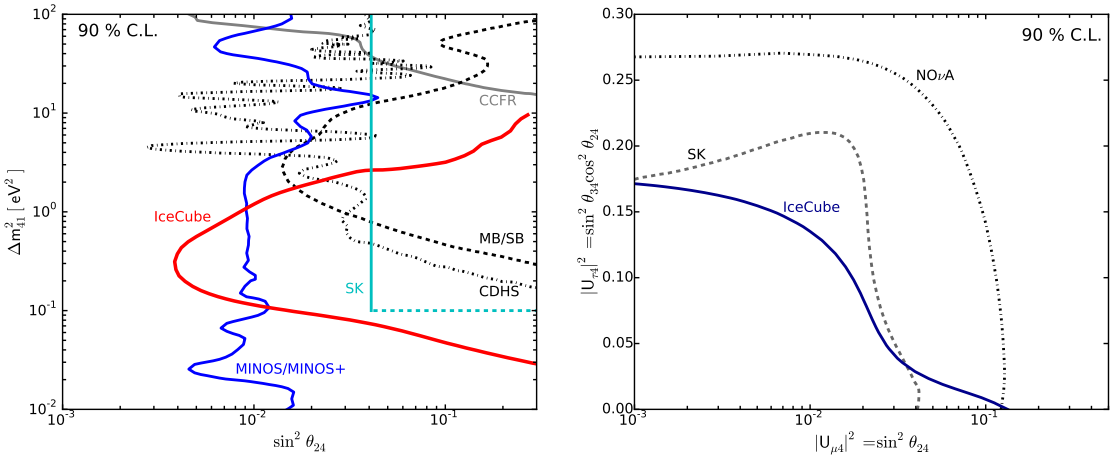


Figure 3.16: (Left) The current 90% C.L. limits on $\sin^2\theta_{24}$ obtained by MINOS/MINOS+ [95], IceCube [96], Super-Kamiokande [97], CCFR [98] , CDHS [99] and MiniBooNE/SciBooNE [100]. (Right) 90% C.L limits on $U_{\mu 4}$ and $U_{\tau 4}$ mixing elements obtained by NOvA [101], Super-Kamiokande [97] and IceCube DeepCore [102]. The MINOS collaboration does not report the limits for $U_{\tau 4}$ and $U_{\mu 4}$ at the same time and, therefore, the corresponding limit is not shown here. The analysis procedure for the IceCube DeepCore search is presented in Chapter 7.

Table 3.3: The 90% C.L. exclusion limits obtained by MINOS/MINOS+ [95], Super-Kamiokande [97], NOvA [101], IceCube [96]. The results of this work are denoted as "IceCube DeepCore" and are also published in [102].

| Experiment | $\|U_{\mu 4}\|^2$ | $\|U_{\tau 4}\|^2$ | $\Delta m^2_{41}$ |
|---|---|---|---|
| MINOS/MINOS+ | 0.005 | 0.16 | 0.5 eV$^2$ |
| Super-Kamiokande | 0.041 | 0.18 | |
| NOvA | 0.126 | 0.268 | |
| IceCube | 0.005 | – | |
| IceCube DeepCore | 0.11 | 0.15 | 1 eV$^2$ |

using the TeV atmospheric neutrinos in IceCube [96], MINOS/MINOS+ [95] and Super-Kamiokande [97].

The accelerator and atmospheric neutrinos provide limits on the mixing elements $U_{\mu 4}$ and $U_{\tau 4}$. Currently, the limits are set by Super-Kamiokande [97] and NOvA [101] experiments, as well as by the analysis in IceCube DeepCore [102] presented in Chapter 7. These results are shown in the right panel of Figure 3.16. In addition, the limits on $U_{\tau 4}$ are provided by MINOS/MINOS+ [95]. The limits on $U_{\mu 4}$ and $U_{\tau 4}$ are summarised in Table 3.3.

## 3.7 Sterile neutrino signatures in atmospheric neutrinos

This section explains the effects of the sterile neutrino mixing expected in the observed atmospheric neutrino flux. The matter potential in the case of the sterile neutrino model is presented first. It is followed by the information about the expected impact on the atmospheric neutrinos with energies of about few TeV and below 100 GeV.

### 3.7.1 Matter effects

The main effects of the sterile neutrino mixing on the atmospheric neutrino flux are caused by the propagation of neutrinos through matter. All active neutrinos participate in the NC interactions, while sterile neutrinos have zero potential. After subtracting the diagonal component that does not affect the results, the sterile neutrinos gain the effective matter potential of the NC interactions with the opposite sign. The matter potential in Equation (3.19) is thus modified to

$$\hat{V}_{int} = \mathrm{diag}(V_{CC}, 0, 0, -V_{NC}) = \frac{G_F}{\sqrt{2}}\,\mathrm{diag}(2N_e, 0, 0, N_n). \tag{3.41}$$

This effective potential leads to an enhancement of the sterile neutrino effects, as discussed in the following sections. This work uses the GLoBES package [103, 104]

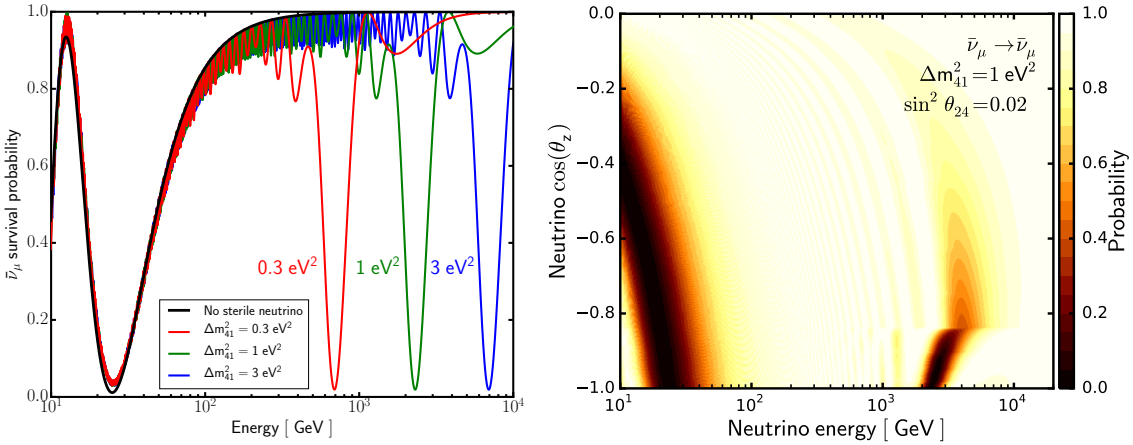


Figure 3.17: (Left) The muon antineutrino survival probability as a function of neutrino energy for the standard three-neutrino model (black) and $\sin^2\theta_{24} = 0.02$ mixing to the sterile state for different values of $\Delta m^2_{41}$ (red, green and blue). (Right) Muon antineutrino survival probability as a function of neutrino energy and zenith angle for $\Delta m^2_{41} = 1$ eV$^2$ and $\sin^2\theta_{24} = 0.02$. The dark region for $\cos\theta_z < -0.85$ and the energy range between 2 and 4 TeV is caused by the mantle-core-mantle resonant transition to the sterile state, when neutrinos travel through the Earth's core. The dark region below 50 GeV corresponds to the standard atmospheric oscillations.

with the sterile neutrino extension [105] to calculate oscillation probabilities in the presence of sterile neutrinos.

### 3.7.2 Resonant $\nu_\mu \to \nu_s$ transition

The most characteristic effect of the sterile neutrino mixing on the atmospheric neutrino flux is expected at energies above few hundreds GeV. It arises from the mantle-core-mantle parametric resonance described in Section 3.3.4. Due to this effect, the vacuum oscillations are enhanced to an almost complete transition of muon antineutrinos to the sterile state [58, 59, 106, 107].

For the sterile neutrino mixing parameters $\Delta m^2_{41} = 1$ eV$^2$ and $\sin^2\theta_{24} = 0.02$ this effect happens at the energy of about 2.4 TeV for $\cos\theta_z = -1$. The energy of the resonance is proportional to the sterile mass-squared difference $\Delta m^2_{41}$. The muon antineutrino survival probabilities for different values of $\Delta m^2_{41}$ as a function of neutrino energy are depicted in the left panel of Figure 3.17, while the right panel shows the expected survival probability as a function of the neutrino energy and arrival direction. This effect is used in the IceCube sterile neutrino searches presented in [96].

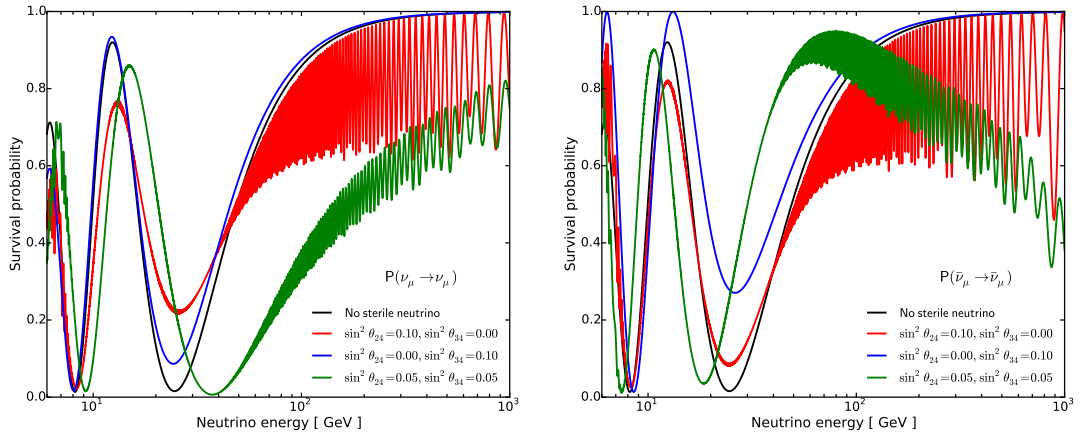


Figure 3.18: The survival probabilities for muon neutrinos (left) and antineutrinos (right) for the standard oscillations (black curve) and various realisations of the sterile neutrino mixing (coloured lines). The parameters of the standard mixing are $\Delta m^2_{31} = 2.515 \cdot 10^{-3}$ eV$^2$, $\sin^2\theta_{23} = 0.565$, while $\Delta m^2_{41} = 1$ eV$^2$. The averaging in $\pm 1\%$ window is applied to reduce the effects of the fast oscillating component caused by $\Delta m^2_{41}$.

### 3.7.3 Impact on the standard neutrino oscillations

The sterile neutrino mixing can also modify the standard atmospheric neutrino oscillations [108–110] below 100 GeV, discussed in Section 3.4. The depth and position of the minimum around 25 GeV for $\cos\theta_z = -1$ are modified as shown in Figure 3.18. This effect is sensitive to the mixing angles $\theta_{24}$ and $\theta_{34}$.

If the mixing angle $\theta_{24}$ is significantly different from zero, but the value of $\theta_{34}$ is small, the depth of the minimum is changed. Also, the normalisation of the observed flux is reduced due to the fast oscillations between muon and sterile states. If the value of $\theta_{34}$ is non-zero and $\theta_{24}$ is small, only the depth of the minimum is modified. The survival probabilities for these sterile mixing realisations are shown in red and blue in Figure 3.18.

If mixing angles $\theta_{24}$ and $\theta_{34}$ are both non-zero, the position of the minimum is shifted due to the additional oscillation phase [110]. For $\theta_{24} = \theta_{34}$ the position of the first disappearance minimum of muon neutrinos moves to higher energies, while antineutrinos experience a shift to lower energies.

The observable effects of the sterile neutrino mixing below 100 GeV are almost independent of the sterile neutrino mass. This is expected because the value of $\Delta m^2_{41}$ controls the period of the fast oscillating component, which is averaged by the detector resolutions.

A change of the standard neutrino mass ordering swaps the probabilities of neutrinos and antineutrinos [109]. For the case when only one sterile mixing angle is different from zero, this change can be compensated by the $\theta_{23}$ octant flip. This effect is shown in the left part of Figure 3.19. However, once both mixing angles are non-zero, a change of neutrino mass ordering cannot be compensated with an octant flip, as depicted in the right part of Figure 3.19.

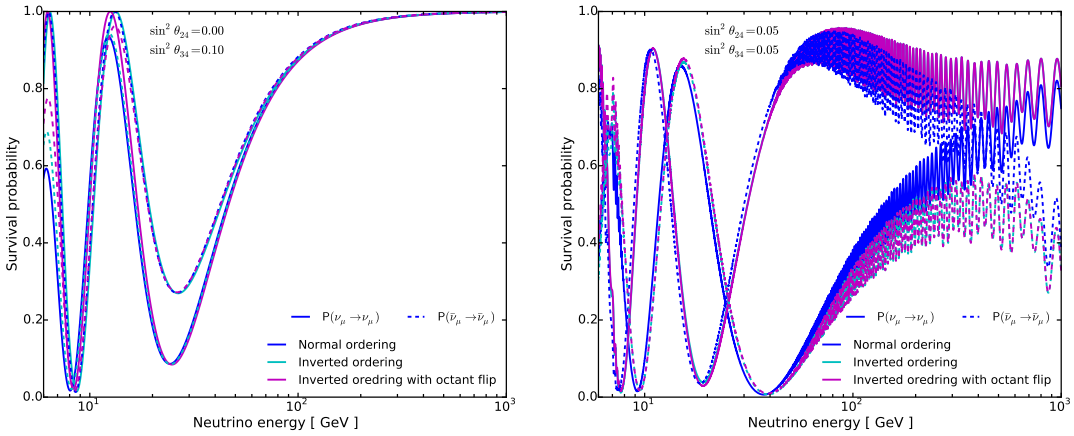


Figure 3.19: The impact of the neutrino mass ordering on the sterile mixing effects for $\sin^2\theta_{24} = 0$, $\sin^2\theta_{34} = 0.10$ (left) and $\sin^2\theta_{24} = \sin^2\theta_{34} = 0.05$ (right). The normal and inverted orderings are shown in blue and cyan, respectively. The inverted mass ordering with the flipped $\theta_{23}$ octant is shown in magenta. The mixing parameters are $\Delta m^2_{41} = 1\ \text{eV}^2$, $\Delta m^2_{31} = 2.515 \cdot 10^{-3}$ $(-2.483 \cdot 10^{-3})$ $\text{eV}^2$ for normal (inverted) ordering. The value of $\sin^2\theta_{23} = 0.565$ is used for the standard octant, while $\sin^2\theta_{23} = 0.435$ is used for the flipped octant. The probabilities are averaged with $\pm 1\%$ window.

The effects of the sterile neutrino mixing are proportional to the amount of matter along the neutrino trajectory. Therefore, the strongest deviations from the standard oscillations are expected for neutrinos crossing the Earth's core and the smallest deviations are close to the horizontal direction. Figure 3.20 shows the

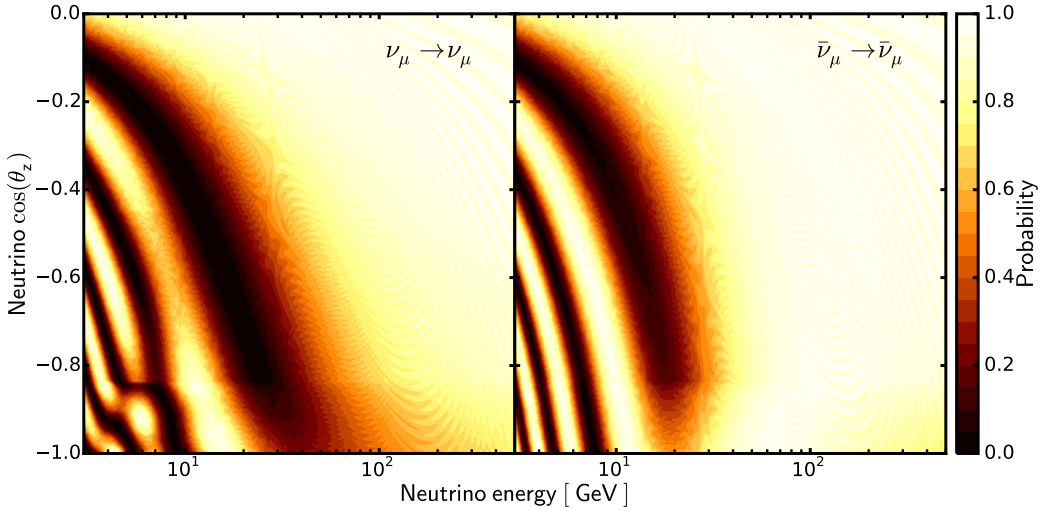


Figure 3.20: The muon neutrino (left) and antineutrino (right) survival probability as a function of neutrino energy and zenith angle for the sterile neutrino mixing with $\sin^2\theta_{24} = 0.02$ and $\sin^2\theta_{34} = 0.17$. The atmospheric mixing parameters are $\Delta m^2_{31} = 2.515 \cdot 10^{-3}$ $\text{eV}^2$ and $\sin^2\theta_{23} = 0.565$. The same probabilities for the standard three-neutrino model with the same mixing parameters are provided in Figure 3.6.

survival probability for muon neutrinos and antineutrinos as a function of neutrino energy and zenith arrival direction.

In this work, the expected impact of the sterile neutrino mixing on the standard atmospheric neutrino oscillations is used to test the standard three-flavour paradigm and limit the existence of the sterile neutrino. The results of this search are presented in Chapter 7.

# Chapter 4

# Detection of neutrinos in ice

This chapter describes the basic principles of neutrino detection in ice that are used by IceCube. It starts with a description of the neutrino interactions relevant to IceCube and is followed by the information about the Cherenkov effect and propagation of particles through the ice. Next, the design of the IceCube Neutrino Observatory and its performance are explained. Experimental signatures, which are produced by different interaction types of different neutrino flavours, are presented at the end of this chapter.

## 4.1 Neutrino interaction processes

As discussed in Section 2.5, deep inelastic scattering (DIS) is the most important interaction process for neutrinos with energies relevant for the IceCube detector. In charged current (CC) interactions an incoming neutrino is converted into a corresponding charged lepton and produces a hadronic shower. To the first order, the cross-sections of CC neutrino and antineutrino interactions from Equation (2.21) and (2.22) have the dependencies

$$\frac{\mathrm{d}\sigma_{CC}^{\nu N}}{\mathrm{d}y} \propto \text{const}, \quad \frac{\mathrm{d}\sigma_{CC}^{\bar{\nu} N}}{\mathrm{d}y} \propto (1-y)^2, \tag{4.1}$$

where $y$ is inelasticity of the interaction. Neutrinos have almost no dependence on $y$, while antineutrinos have $(1-y)^2$ factor due to the angular momentum conservation discussed in Section 2.5.3. In the laboratory frame, the inelasticity can be written as

$$y = 1 - \frac{E_\ell}{E_\nu} \approx \frac{E_{\text{hadrons}}}{E_\nu}, \tag{4.2}$$

where $E_\ell$ is the energy of an out-coming lepton, $E_{\text{hadrons}}$ is the total energy of hadrons produced in the interaction, and $E_\nu$ is the total energy of interacting neutrino. From Equations (4.1) and (4.2), it can be seen that in average antineutrinos transfer a larger fraction of their momenta to the corresponding charged leptons when compared to DIS interactions of neutrinos.

A visible part of neutral current (NC) DIS interactions consist only of hadrons, since an outcoming neutrino has a negligible probability of interacting inside the detector again.

## 4.2 Cherenkov effect

When a charged particle moves through a medium, it polarises electron clouds of the atoms that form the medium. The de-excitations lead to the emission of electromagnetic radiation, which is usually cancelled by emission from nearby atoms. But if the particle moves with speed $v$ faster than the phase velocity of light in the medium (i.e. $v > c/n$), the emission undergoes constructive interference under a specific angle as shown in Figure 4.1. The resulting emitted light is called the Cherenkov radiation, and it was first observed in 1934 [111].

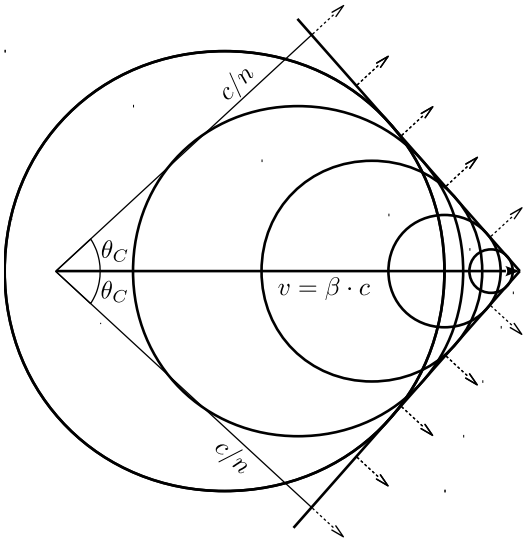


Figure 4.1: The Huygens-Fresnel principle for a charged particle moving faster than the speed of light in the medium and producing Cherenkov light.

The Cherenkov angle, the angle of emission, is defined by

$$\cos\theta_C = \frac{1}{\beta n}, \tag{4.3}$$

where $\beta = v/c$ is the speed of the particle, and $n$ is the refractive index of the medium. A typical index of refraction for Antarctic ice is $n \approx 1.32$, which corresponds to the Cherenkov angle $\theta_C \approx 41°$ for highly relativistic particles. For a particle with mass $m$, the effect has a kinetic energy threshold $K_c$, which is given by

$$K_c = mc^2 \left( \frac{1}{\sqrt{1 - \frac{1}{n^2}}} - 1 \right). \tag{4.4}$$

In ice this corresponds to the kinetic energy thresholds of about 0.270 MeV for electrons and 56.2 MeV for muons.

A number of Cherenkov photons, $\mathrm{d}N_\gamma$, emitted per wavelength, $\mathrm{d}\lambda$, by a segment of the track with length $\mathrm{d}l$ is given by the Frank-Tamm formula [112, 113]

$$\frac{\mathrm{d}^2 N_\gamma}{\mathrm{d}l\mathrm{d}\lambda} = 2\pi\alpha z^2 \frac{1}{\lambda^2}\left(1 - \frac{1}{\beta^2 n^2}\right), \tag{4.5}$$

where $\alpha \approx 1/137$ is the fine-structure constant and $z$ is the electric charge of the particle. In ice, an ultra-relativistic particle emits about 260 photons per cm in the optical part (350 nm $< \lambda <$ 650 nm) of the spectrum. The energy losses due to

Cherenkov radiation are about $10^{-3}$–$10^{-2}$ MeV/cm and are negligible compared to other energy losses, such as ionisation or radiative losses described in Section 4.3. However, this effect plays a crucial role in the detection of neutrinos by the IceCube detector.

## 4.3 Propagation of particles through the ice

### 4.3.1 Energy losses of particles

When particles travel through matter they lose their energy via various interaction processes. Ionisation, Bremsstrahlung, pair production and photo-nuclear interactions are the main contributors to the losses [114]. The total energy loss is a sum of the individual losses

$$-\frac{\mathrm{d}E}{\mathrm{d}x} = \left(\frac{\mathrm{d}E}{\mathrm{d}x}\right)_I + \left(\frac{\mathrm{d}E}{\mathrm{d}x}\right)_B + \left(\frac{\mathrm{d}E}{\mathrm{d}x}\right)_{PP} + \left(\frac{\mathrm{d}E}{\mathrm{d}x}\right)_N \tag{4.6}$$

The fraction of energy lost through each of these mechanisms depends on the particle type and its energy. The mechanisms relevant to Cherenkov neutrino detectors are presented in the following sections.

### 4.3.2 Muons in ice

For muons with energies above 1 GeV losses due to ionisation have a weak energy dependence. On the other hand, the losses due to Bremsstrahlung, pair production and photo-nuclear interactions together form radiative losses, which are rising with energy. Therefore, the energy losses can be simplified [114] as

$$-\frac{\mathrm{d}E}{\mathrm{d}x} = a_I(E) + b_R(E) \cdot E, \tag{4.7}$$

where $a_I(E)$ corresponds to ionisation losses and $b_R(E) = b_B(E) + b_P(E) + b_N(E)$ characterise radiative losses. Different components of muon energy losses as a function of its kinetic energy are depicted in Figure 4.2. Parameters $a_I$, $b_B$, $b_P$, $b_N$ have rather weak energy dependence and, therefore, can be assumed constant for the energy range relevant to this work. Then, Equation (4.7) can be simplified as

$$-\frac{\mathrm{d}E}{\mathrm{d}x} \approx a + b \cdot E, \tag{4.8}$$

where $a \approx 2$ MeV/cm and $b \approx 3.4 \cdot 10^{-6}$ cm$^{-1}$ [114]. In this way the average *range* (track length) $R$ of a muon with energy $E$ is calculated as

$$R = \frac{1}{b} \cdot \ln\left(\frac{b}{a} \cdot E + 1\right). \tag{4.9}$$

Ranges of individual muons have rather significant variations from Equation (4.9) due to the stochastic nature of radiative losses. The average distance travelled by

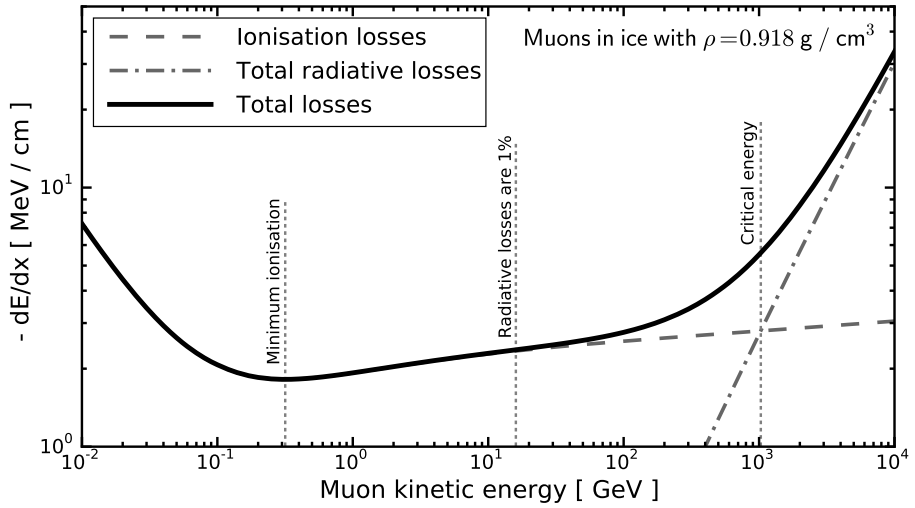


Figure 4.2: Muon energy losses in the Antarctic ice as a function of kinetic energy. The solid curve depicts total energy losses, while dashed and dash-dotted lines represent ionisation and radiative losses, respectively. Additionally, the energy of minimum ionisation, critical energy and the energy where radiative losses are 1% of the total losses are shown in the figure. The data from [114] are used for the figure.

a muon track in Antarctic ice is about 47 meters at 10 GeV and 1.6 km at 500 GeV. This length is much larger than typical sizes of cascades produced by other particles, as described in the next sections. For muons, the critical energy, where radiative losses start to dominate, is about 1.03 TeV, which is outside of the energy range considered in this work.

### 4.3.3 Electromagnetic showers

Electrons, positrons and photons can be produced directly in neutrino interactions, as well as in interactions or decays of the secondary particles. Electrons lose their energy by emission of hard photons in Bremsstrahlung processes, while photons produce $e^+e^-$ pairs when travelling through matter. These processes happen repetitively and collectively lead to the formation of electromagnetic (EM) showers. The development of EM showers stops when the energies of individual particles reach their critical energy $E_c$. Its value for water and ice is approximately 77 MeV with a slight difference for electrons and positrons [23] due to the differences in the annihilation cross-section. Another important variable that describes the development of the shower is the radiation length $X_0$, which defines the distance after which the energy of an electron or a positron is reduced by a factor of $1/e$. Also, it characterises $\frac{7}{9}$ of the mean free path for pair production of high-energy photons. For ice, the radiation length is approximately 39.3 cm [23].

The longitudinal profile of EM showers can be parametrised [23] by a gamma distribution

$$\frac{\mathrm{d}E}{\mathrm{d}t} = E \cdot b \cdot \frac{(b \cdot t)^{a-1} \exp(-b \cdot t)}{\Gamma(a)}, \tag{4.10}$$

where $t = x/X_0$, and the factors $a$ and $b$ can be fitted from direct particle propagation simulations described in [115] as

$$\begin{aligned} a &\approx 2.01 + 0.63 \ln E \text{ [ GeV ]}, \; b \approx 0.63 \qquad (e^+, e^-), \\ a &\approx 2.83 + 0.58 \ln E \text{ [ GeV ]}, \; b \approx 0.64 \qquad (\gamma). \end{aligned} \tag{4.11}$$

The value $t_{max}$ corresponding to the maximal energy deposition is given by

$$t_{max} = \frac{a-1}{b}. \tag{4.12}$$

Therefore, Equations (4.10) and (4.12) lead to a logarithmic growth of the cascade size as a function of its energy. EM showers are significantly smaller than muon tracks of comparable energy (see Section 4.3.2). For a 10 GeV photon-induced cascade, 90% of the energy is deposited within 4.2 meters, while for 500 GeV this length is only 6 meters. Electron-induced showers are slightly smaller due to differences in the point of the first interaction.

The particles in EM showers travel mainly along the direction of the initial particle, leading to the Cherenkov light emission that is peaked at the Cherenkov angle, as shown in the left part of Figure 4.3.

### 4.3.4 Hadronic showers

As discussed in Section 4.1, hadrons are almost always produced in neutrino interactions with ice at the energies relevant to this work. Hadrons interact strongly with nucleons of matter and produce secondary particles. Variability of the produced particles, their interactions and decays lead to large shower-to-shower variations in longitudinal profiles and Cherenkov light emission. For example, $\pi^0$ particles produced in the interactions decay almost immediately into a pair of photons creating

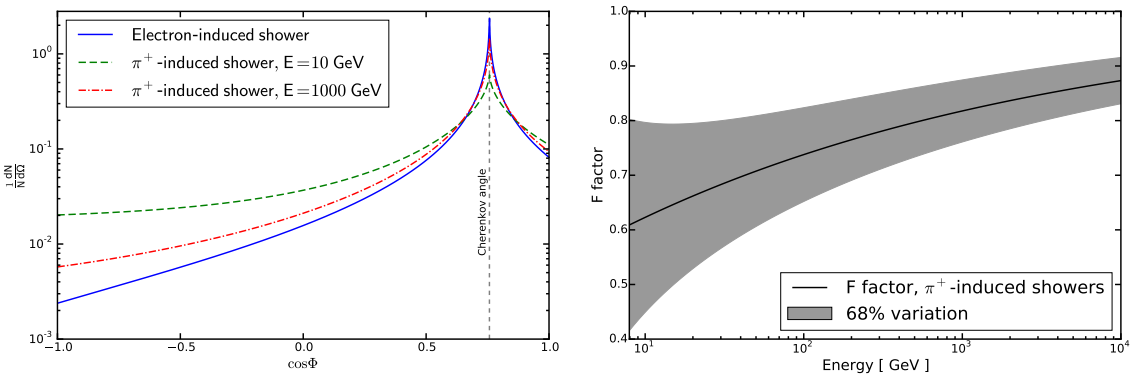


Figure 4.3: (Left) Angular distributions of Cherenkov light produced by electron- and $\pi^+$-induced showers. Two energies are depicted for $\pi^+$ showers to demonstrate the energy dependence of the angular distribution, while energies of EM showers have little impact on their Cherenkov light angular profiles. (Right) The factor $F(E)$, which describes the brightness of hadronic showers compared to EM ones, and its 68% variation for $\pi^+$-induced showers. Parametrisations from [115] are used for both figures.

Table 4.1: The values used to parametrise hadronic light output of charged pions by Equations (4.13) and (4.14). The values for other particles can be found in [115].

| **Particle** | $E_s$ [ GeV ] | $f_0$ | $m$ | $\sigma_0$ | $\gamma$ |
|---|---|---|---|---|---|
| $\pi^+$ | 0.156 | 0.273 | 0.158 | 0.406 | 1.018 |
| $\pi^-$ | 0.134 | 0.287 | 0.153 | 0.433 | 1.056 |

an electromagnetic component of hadronic showers. Charged pions decay producing muons, and produce less Cherenkov light. Also, hadronic showers can have neutral particles or heavy hadrons with energies below the Cherenkov threshold, leading to a component that does not emit any light.

On average hadronic showers have slightly larger sizes than EM cascades of the same energy. For example, a 10 GeV shower produced by $\pi^+$ deposits 90% of energy within 5.6 meters, for 500 GeV this size grows to 8 meters. Different hadrons produce showers with slightly different longitudinal and lateral distributions.

Similarly to EM showers, the light from hadronic showers is also peaked around the Cherenkov angle. However, the light is more smeared due to larger masses and the variability of individual hadrons in the showers. The angular distributions of the Cherenkov light produced by showers induced by $\pi^+$ with energies of 10 and 1000 GeV are shown in Figure 4.3. Detailed parametrisations of the shower light outputs for various types of hadrons can be found in [115, 116].

Hadrons are heavier than electrons and, therefore, have a higher energy threshold for Cherenkov light emission. The brightness of hadronic showers is given by $T_{hadron}$, a total length of all charged particles above the threshold for light emission. It is useful to introduce a factor $F(E)$, which defines a relative brightness of hadronic showers compared to EM cascades. This factor can be parametrised [115, 116] as

$$F(E) = \frac{T_{hadron}}{T_{EM}} = 1 - (1 - f_0)\left(\frac{E}{E_s}\right)^{-m} \tag{4.13}$$

with a variance given by

$$\sigma_F(E) = \sigma_0(\ln E)^{-\gamma}. \tag{4.14}$$

Values of parameters $E_s$,$f_0$, $m$, $\sigma_0$ and $\gamma$ are different for hadronic showers initiated by different particles. The corresponding values for charged pions are given in Table 4.1, while parametrisations for other particles can be found in [115]. The factor $F$ and its variation as a function of energy for showers induced by $\pi^+$ are shown in the left part of Figure 4.3.

## 4.4 The IceCube Neutrino Observatory

The effects discussed in Sections 4.2–4.3 are used to detect neutrinos in IceCube. The IceCube Neutrino Observatory [6] is located at the geographic South Pole. It consists of the on-surface cosmic ray detector, IceTop, and an in-ice counterpart. The in-ice

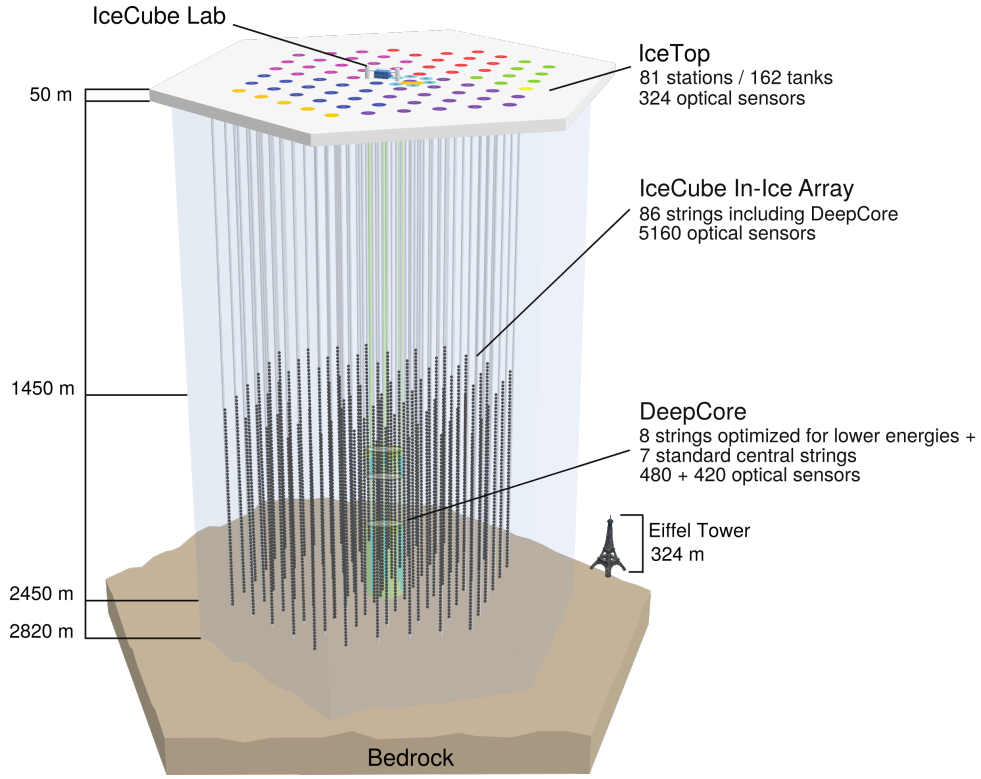


Figure 4.4: The IceCube Neutrino Observatory and its main components [6].

part, IceCube, consists of 5160 optical sensors and is designed to capture Cherenkov light from charged particles produced by neutrino interactions. A schematic view of the IceCube Neutrino Observatory and its main parts is shown in Figure 4.4. The following sections explain the design of the IceCube detector in general, as well as DeepCore, a more densely instrumented part of the array.

### 4.4.1 Digital optical module

A digital optical module (DOM) [117] is the basic detection unit of IceCube. Its purpose is to collect light, digitise resulting signals and send them to the central data acquisition system. Its schematic design is shown in Figure 4.5.

A key element of the DOM is a 10" down-looking photo-multiplier tube (PMT). The PMTs are shielded from magnetic fields by a mu-metal grid. The PMTs [118] are sensitive to photons in the wavelength range of 300 – 650 nm, with a peak efficiency of about 25% at 390 nm. High-quantum efficiency (HQE) PMTs are used in the DeepCore sub-detector, where the quantum efficiency reaches approximately 34%. The results of the laboratory measurement of the optical efficiency of several DOMs with the standard and HQE PMTs are shown in the left part of Figure 4.6. The increase of the quantum efficiency leads to about 33% increase of the noise rate, as shown in the right part of Figure 4.6. The waveforms produced by PMTs are digitised by the onboard electronics.

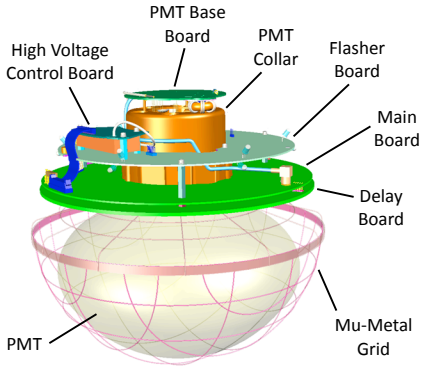


Figure 4.5: The basic design and key elements of a digital optical module (DOM) [6].

DOMs electronics include the capability to determine a local coincidence condition. The *hard local coincidence* (HLC) condition is satisfied when at least one of the nearest or next-to-nearest modules on the same string detects any signals within $\pm 1$ $\mu$s. The HLC hits often have more complicated waveforms corresponding to multiple photons. Therefore, the HLC signals are saved in a more detailed way, which uses the ATWD digitisation with 300 Msps sampling. For hits not meeting the HLC criteria, or *soft local coincidence* (SLC) hits, the basic FADC digitisation with 40 Msps sampling is used. The signals are sent to the surface using the cable connected inside the glass sphere through a specially designed penetrator. The power is supplied in the same way and converted to the high voltage for the PMTs by onboard electronics.

A very important part of the DOM is the flasher board. It consists of LEDs that are designed to emit known quantities of light to perform *in situ* calibration

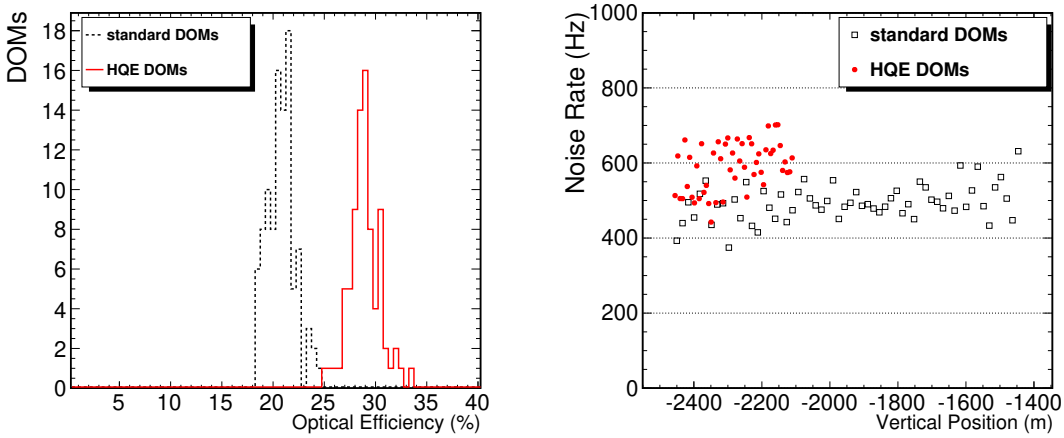


Figure 4.6: (Left) Laboratory measurement of the DOM optical efficiency at –45°C and $\lambda = 405$ nm for standard (black) and HQE (red) DOMs. (Right) The results of the *in situ* measurement of the noise rate of HLC hits for IceCube standard and DeepCore HQE DOMs. The figures are taken from [119].

of the detector. Each DOM has 12 LEDs combined in 6 pairs separated by 60° in azimuth. One LED of every pair shines light horizontally into the ice, while the second one is tilted to emit the light at 48° to emulate the Cherenkov angle of up-going particles. This light provides valuable data for calibration of local ice properties, DOM efficiency and angular acceptance. More information about design and readout of DOMs can be found in [6].

### 4.4.2 Detector layout

In IceCube the modules are arranged in 86 vertical strings that consist of 60 DOMs each. They were deployed into the ice by melting the ice using the hot water drilling technology [120]. The main part of the IceCube detector consists of 78 strings arranged on a hexagonal grid with the average horizontal spacing of 125 meters as depicted in Figure 4.7. It instruments the region between 1450 and 2450 meters below the ice surface with 17 meters vertical spacing between the DOMs, as shown in Figure 4.8.

IceCube uses the SMT8 (Simple Majority Trigger) requiring that at least 8 DOMs meet the HLC condition in a 5 $\mu s$ time window to trigger an event. The spacing between the sensors and trigger techniques lead to a neutrino detection energy threshold of approximately 100 GeV. The performance of neutrino detectors is often given in the form of an effective area, the effective size of the surface, where all crossing neutrinos would be detected with 100% efficiency. The effective area of the IceCube detector for muon neutrino detection is shown in black in Figure 4.9.

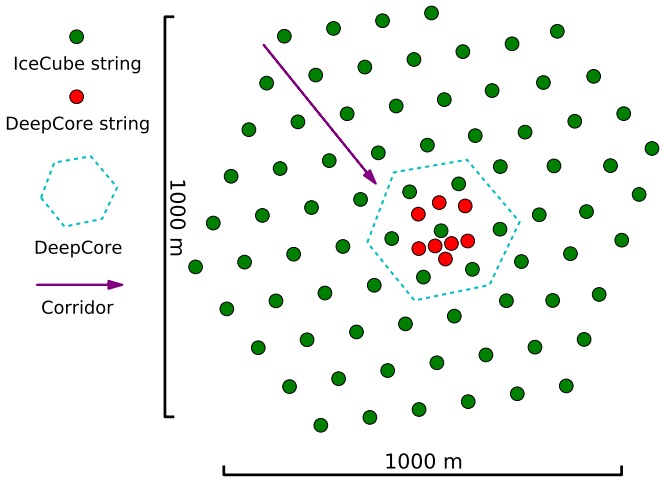


Figure 4.7: The top view of IceCube. The green and red circles depict IceCube and DeepCore strings, respectively. The cyan line shows the approximate location of the DeepCore fiducial volume. The violet arrow depicts an example of the corridors formed by the IceCube geometry, where atmospheric muons can penetrate through outer regions of IceCube leaving almost no signals.

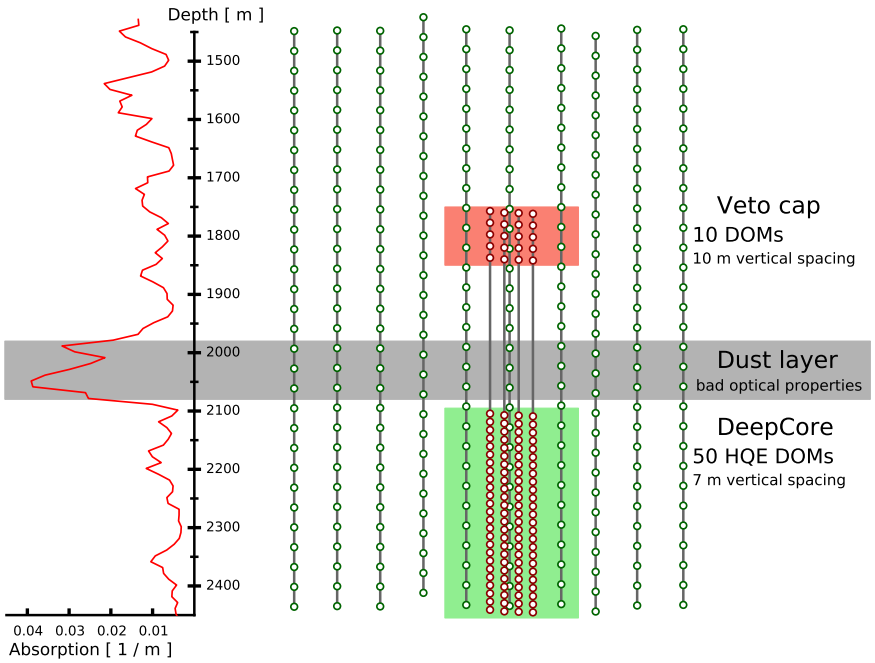


Figure 4.8: The side view of IceCube. IceCube DOMs are shown by green circles and DeepCore DOMs are depicted by red circles. The green area shows an approximate location of the DeepCore fiducial volume and red area shows the veto cap. The side panel shows the ice absorption coefficient (transparency) of the current ice model [121] as a function of depth. The dust layer, a region with short optical photon absorption length, is shown in grey.

### 4.4.3 DeepCore sub-detector

DeepCore is a more densely instrumented part of the IceCube detector [119]. It is designed to lower the neutrino detection energy threshold. DeepCore is located in the bottom-centre of the main IceCube array. The ice has the best optical properties in this region, which helps to reduce the energy threshold.

The DeepCore fiducial volume is outlined in cyan in Figure 4.7. It consists of 8 special DeepCore strings, which are shown in red in Figure 4.7, as well as 7 nearest IceCube strings. The average horizontal spacing between the strings is approximately 72 meters. Each DeepCore string consists of 60 HQE DOMs, which are grouped into two regions, each with different vertical spacing. Fifty modules are placed with 7 meters vertical spacing and instrument the depth range between 2100 and 2450 meters below the ice surface. These modules, together with 18 lowest DOMs of the 7 standard IceCube strings, are considered the DeepCore fiducial volume. Additional 10 DOMs form a veto cap and are deployed with 10 meters spacing at depths between 1750 and 1850 meters. DeepCore uses a separate SMT3 condition requiring 3 HLC hits in a 2.5 $\mu$s time window in addition to the standard IceCube SMT8 trigger.

Better ice properties, denser instrumentation, a higher quantum efficiency of the PMTs and the modified trigger lower the neutrino detection energy threshold to

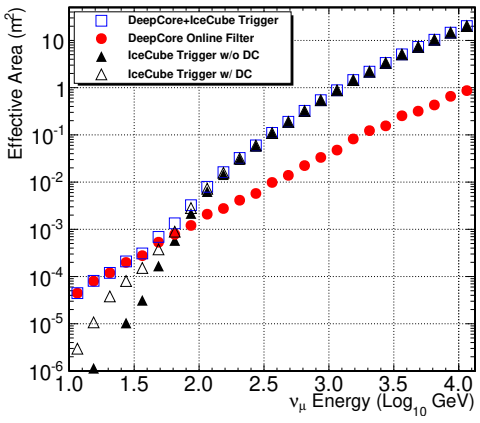


Figure 4.9: The effective area of IceCube and DeepCore for a muon neutrino detection. The filled triangles show the effective area using IceCube SMT8 trigger excluding DeepCore strings; the open triangles show the effect of inclusion of DeepCore into the SMT8 trigger. The blue squares depict the effective area when both IceCube SMT8 and DeepCore SMT3 triggers are used. The red circles show the effective area after DeepCore on-line filter. The figure is taken from [119].

approximately 5 GeV. The impact of DeepCore with and without dedicated trigger on the effective area of muon neutrino detection is depicted in Figure 4.9.

DeepCore uses the outer parts of IceCube to reject the background from muons that originate from the cosmic ray interactions with the atmosphere. The veto cap, shown in light red in Figure 4.8, helps to tag directly down-going muons, while the outer IceCube strings help against inclined muons. More details about muon rejection techniques are given in Section 5.3.

### 4.4.4 Optical properties of the ice

**Bulk ice model**

Optical properties of the ice affect the propagation of Cherenkov photons. These properties together form a *bulk ice model* in IceCube. They are characterised by the absorption coefficient $a(d)$ and effective scattering coefficient $b_e(d)$ as a function of depth, as well as *anisotropy* and *tilt*.

The absorption coefficient defines the average distance travelled by an optical photon before it is absorbed. Changes of photon direction are defined by the average distance between scatterings $b^{-1}$ and mean scattering angle $\langle \cos\theta_{sc} \rangle$. The effective scattering coefficient is defined as $b_e = b \cdot (1 - \langle \cos\theta_{sc} \rangle)$ and characterises the average distance $b_e^{-1}$ travelled by photons after which they lose information about their initial direction. Figure 4.10 shows the absorption and effective scattering coefficients as a function of the depth under the ice surface.

The bedrock under IceCube has uneven depth causing a "flow" of the glacier with a speed of approximately 10 meters per year [122]. The shape of the bedrock causes the tilt of the layers of constant optical properties. The ice flow causes the

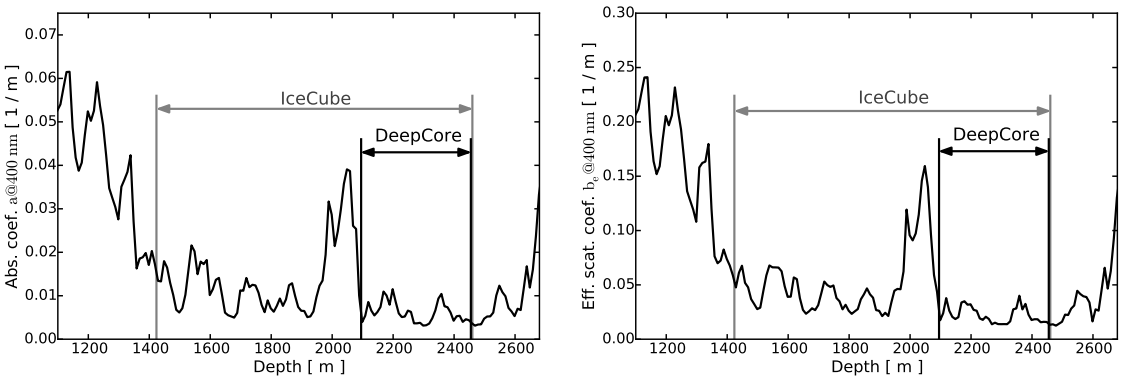


Figure 4.10: The absorption (left) and effective scattering (right) coefficients for photons with wavelength $\lambda = 400$ nm as functions of the depths below the ice surface. Instrumented regions of IceCube and DeepCore are marked by grey and black arrows, respectively.

reorientation of ice crystals along the direction of the flow. It leads to 8.2% smaller (4.2% larger) scattering coefficient than the average $b_e$ for photons travelling along (perpendicularly) to the flow direction.

The bulk ice model used in this work has 171 layers covering the depths between approximately 1100 and 2800 meters. The properties of the ice are extracted using the light from the LED calibration sources mounted in DOMs [121, 123]. The data from specially designed devices that measured the concentration of dust particles during the deployment of the detector are used to estimate tilt direction and extrapolate the optical coefficients to depths not instrumented by DOMs. More information about this process can be found in [121–124].

**Hole ice**

Deployment of the IceCube detector requires melting the ice along locations of the strings. This process frees dust particles and air bubbles from the ice. During the refreezing process, impurities tend to concentrate around the centres of the holes and form *bubble columns*. These regions have optical properties that are much worse than other parts of the bulk ice. The main effect caused by the bubble columns is a modification of the angular acceptance of the DOMs and are shown in Section 5.1.5.

## 4.5 Event topologies

A signal observed by IceCube can be different depending on the flavour of the interacting neutrino and the interaction type. Tracks and cascades are created by secondary particles produced in neutrino interactions and are the signatures distinguished by IceCube.

Track signatures are created by muons passing through the detector. At the energies considered in this work, muon track lengths are typically larger than the spacing between the modules and, therefore, the IceCube can resolve them. They result in more elongated signal patterns.

Table 4.2: The neutrino interaction types, their secondary particles and corresponding experimental signature in the IceCube detector. In the schematic drawings, black dashed lines represent neutrinos. Green lines show muons, particles of hadronic and electromagnetic showers are depicted by red and blue lines, respectively. Orange lines show tau leptons produced in CC interactions of tau neutrinos.

| **Interaction** | **Secondary particles** | **Signature** |
|---|---|---|
| CC $\overset{(-)}{\nu}_\mu$ |  $\mu^\pm$ track | Track-only |
| | 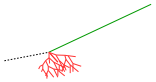 $\mu^\pm$ track and hadrons | Track with cascade |
| CC $\overset{(-)}{\nu}_\tau$ | 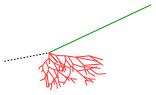 $\tau^\pm$ decaying into $\mu^\pm$ (∼17% B.R.), hadrons | |
| | 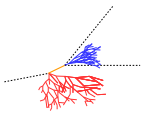 $\tau^\pm$ decaying into $e^\pm$ or hadrons (∼83% B.R.) | |
| CC $\overset{(-)}{\nu}_e$ | 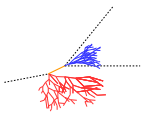 $e^\pm$, hadrons | Cascade-only |
| NC $\overset{(-)}{\nu}_\ell$ | 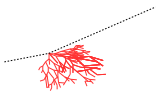 hadrons | |

On the other hand, typical sizes of EM and hadronic showers are smaller than the spacing between the modules. This means that the Cherenkov emission from the showers is seen as almost a point-like light source. In addition, the effective scattering length of the Antarctic ice is relatively short, between 20 and 50 meters, leading to almost isotropic light emission by the showers.

Three classes of experimental events can be defined: track-only, cascade-only and mixture of track and cascade. Table 4.2 lists the interactions of neutrinos and the corresponding detector signatures.

The track-only signature is possible when muon neutrinos interact via charged currents with rather low energy transfer to hadrons (inelasticity $y \sim 0$), so they emit almost no light and cannot be detected. An example of such an event produced by a $\bar{\nu}_\mu$ CC interaction is shown in the left part of Figure 4.11. As discussed in Section 2.5, muon antineutrinos are more likely to produce such events. This signature also appears when an interaction vertex is far outside of the detector and

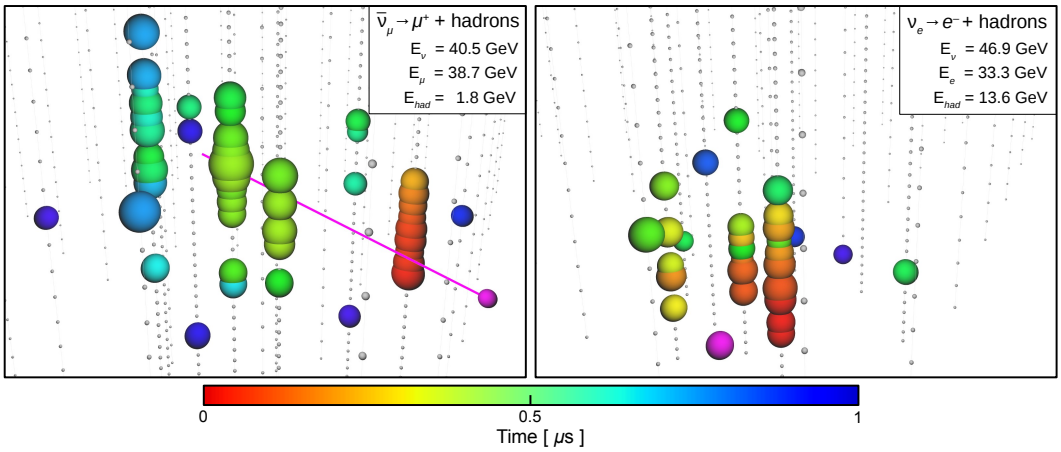


Figure 4.11: Examples of the track (left) and cascade (right) events in IceCube DeepCore. The magenta circle and line show the vertex of the neutrino interaction and produced muon track. The coloured circles depict the signal times, while their sizes show the integrated charges in the DOMs. The modules without signals are shown by grey circles.

the resulting muon track enters the detector. Similar signatures can be produced by atmospheric muons entering the detector. Other possibilities are elastic scattering on electrons or quasi-elastic scattering on nucleons. However, their cross-sections are small compared to deep inelastic scattering at energies above 10 GeV.

A track with cascade signature is produced by muon neutrino CC interactions, where part of the neutrino momentum is transferred to the resulting muon, while another part of the energy goes into a production of the hadronic shower. Energies of hadronic showers in neutrino interactions are slightly higher compared to antineutrinos due to angular momentum conservation discussed in Section 2.5. Also, this signature can be produced in some CC interactions of tau neutrinos. Tau leptons are produced in such interactions, and in approximately 17% of the cases they decay to muons, which can produce tracks in the detector. However, such muons have rather low energies and often are not bright enough to be distinguishable.

The cascade-only signature is always produced by $\nu_e$ CC interactions, and in 83% of $\nu_\tau$ CC interactions where tau leptons decay into electrons or hadrons. An example of the cascade event produced by a $\nu_e$ CC interaction is shown in the right part of Figure 4.11. In addition, this signature is produced by NC interactions of all neutrino flavours, since only hadronic showers are visible in such interaction. Different cascade types leave very similar signals in the detector. Therefore, IceCube has little power distinguish cascades produced by different neutrino interactions.

As seen from Table 4.2 muons are produced mainly in $\nu_\mu$ CC interactions, so a presence of a muon track is an important signature for the flavour identification. Also, in such interactions the out-going muon direction is strongly correlated with the direction of interacting neutrino and can be used as a proxy for the neutrino arrival direction.

# Chapter 5

# Data analysis techniques

This chapter describes techniques used to extract the parameters of neutrino mixing from the IceCube data. It starts with an explanation of the framework and tools used for the simulations of neutrino interactions with the ice, propagation of the secondary particles, Cherenkov light production, propagation and detection. The next part of this chapter describes the techniques used for reconstruction and event selection. Finally, the statistical approach used for the parameter extraction and treatment of systematic uncertainties are explained.

## 5.1 Simulation of neutrino events

The physics analysis performed in this work relies on Monte Carlo (MC) simulations. The simulation chain used in this work is described in this section. It starts with a basic overview of the simulations, followed by details about the tools used in each step of the simulation production.

### 5.1.1 Overview

The simulation chain in this work is designed to save time and computational resources. It is divided into three *steps*:

- Step 1: simulation of neutrino interactions and propagation of muons.
- Step 2: propagation of other particles, production of Cherenkov light and tracking of photons to the locations of the DOMs.
- Step 3: simulation of the PMT responses, readout electronics, trigger and basic data processing.

This split is done to minimise the usage of computational resources by utilizing the results of one step in the following steps independently. In particular, the output of Step 2 is reused to simulate sets of different detector parameters. This results in a lower usage of GPUs, which are less abundant on the computer clusters.

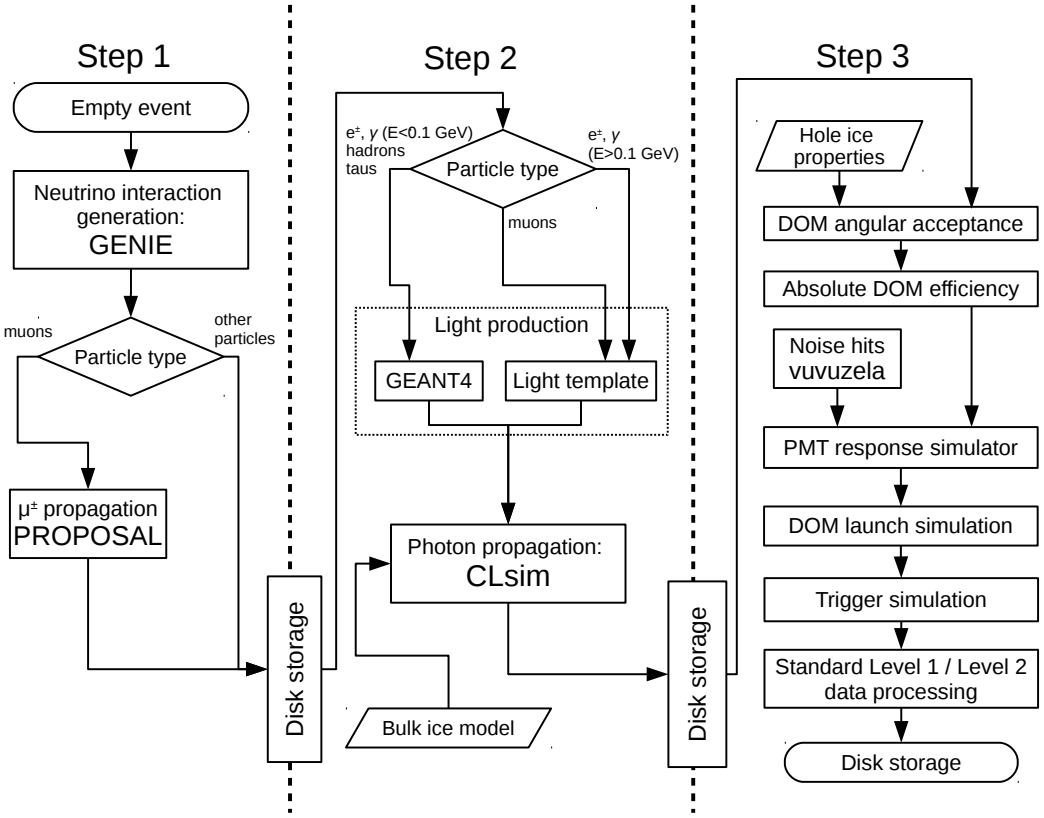


Figure 5.1: A schematic overview of the simulation chain that was developed for the studies presented in this work.

A general overview of the steps, software projects and data flow between them is shown in Figure 5.1. These steps and projects are covered in more details in the following sections.

### 5.1.2 Neutrino interactions

The first part of the simulation chain is the generation of neutrino interactions. These simulations are performed using the GENIE [30, 31] software package. It simulates the interactions of neutrinos and corresponding hadronic processes. In this work, the neutrinos are produced with a power-law energy spectrum. The simulated arrival directions are distributed isotropically in zenith and azimuth angles. The simulation volume for neutrino interactions is a cylinder aligned along the simulated neutrino direction and centred approximately in the middle of DeepCore, as shown in the right part of Figure 5.2.

The size of the cylinder is chosen depending on the energy and neutrino flavour. Each flavour of neutrinos is split into three energy ranges: low, middle and high. The energy spectrum and size of the cylinder are optimised for each range, to cover the full volume of DeepCore. Events located in IceCube, but outside of the DeepCore volume, are lost due to the background rejection criteria during the later steps of

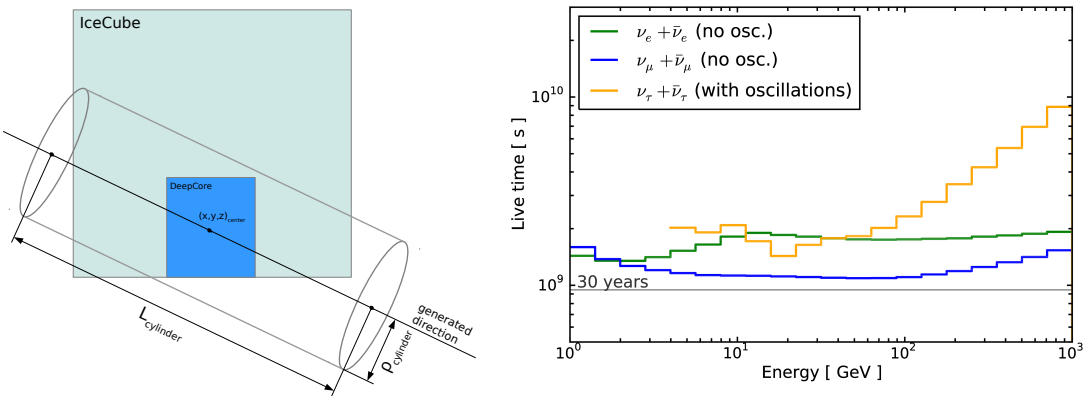


Figure 5.2: (Left) A schematic drawing of the GENIE generation volume. (Right) The live time of the neutrino simulations for electron (green), muon (blue) and tau (orange) neutrinos. For electron and muon neutrinos the live time is estimated for the atmospheric neutrino flux without oscillations, while for tau neutrinos a simple two-neutrino oscillation probability is applied.

event selection, as described in Section 5.3. Therefore, the cylinders have relatively small sizes, to minimise computational time and storage space requirements. The generation volume at high energies has to be larger to account for longer muon tracks produced in neutrino interactions. The cylinder sizes, energy distributions and a total number of events produced for every energy range and neutrino flavour are listed in Table 5.1.

The energy distributions for every energy range were chosen to produce approximately flat effective live times across the full energy range. An equivalent of at least 30 years of the detector live time were simulated for each neutrino type. The

Table 5.1: The energy distributions, dimensions of the generation cylinder and number of events produced per energy range and neutrino type.

| $\nu$ type | $E_\nu$ range | $E_\nu$ spectrum | $L_{cylinder}$ | $\rho_{cylinder}$ | $N_{events}$ |
|---|---|---|---|---|---|
| $\overset{(-)}{\nu}_e$ | 1–4 GeV | $E_\nu^{-1.9}$ | 500 m | 250 m | $1.35 \cdot 10^8$ |
| | 4–12 GeV | $E_\nu^{-2.0}$ | | | $3.3 \cdot 10^7$ |
| | 12–1000 GeV | $E_\nu^{-2.5}$ | | | $1.2 \cdot 10^7$ |
| $\overset{(-)}{\nu}_\mu$ | 1–5 GeV | $E_\nu^{-2.0}$ | 500 m | 250 m | $3.06 \cdot 10^8$ |
| | 5–80 GeV | | 900 m | | $2.25 \cdot 10^8$ |
| | 80–1000 GeV | | 1500 m | 330 m | $2.3 \cdot 10^7$ |
| $\overset{(-)}{\nu}_\tau$ | 4-10 GeV | $E_\nu^{-1.5}$ | 500 m | 250 m | $1.8 \cdot 10^7$ |
| | 10–30 GeV | $E_\nu^{-2.0}$ | | | $9.9 \cdot 10^6$ |
| | 30–1000 GeV | $E_\nu^{-3.5}$ | 1000 m | | $4.2 \cdot 10^6$ |

effective live times as a function of the neutrino energy are shown in the right part of Figure 5.2.

### 5.1.3 Cherenkov light production

This part of the simulation chain estimates the amount of produced Cherenkov light, as well as its longitudinal and angular profile. It is performed individually for each particle produced in the neutrino interactions. Different approaches are used for particles of different types and energies.

The first step is to simulate the propagation of particles through the ice or bedrock (if the neutrino interaction occurs deep enough below the surface). The PROPOSAL software package [125] is used in Step 1 for the propagation of muons. It calculates the ionisation and stochastic losses during the passage of muons through matter. The amount of Cherenkov light produced by a muon and its individual losses with energies below 500 MeV are summed together. A total light output from such a *dressed muon* is then generated using the analytic parametrisations [125].

Muon stochastic losses with energies above 500 MeV are simulated as individual particles. The amount of light produced by electrons, positrons and gamma rays (including muon stochastic losses) with energies above 100 MeV is stable and has low variability. Therefore, a direct propagation of such particles is not necessary and their Cherenkov light is estimated by analytic light templates from [115].

The properties of Cherenkov light produced by hadrons and tau leptons is estimated using the GEANT4 [126] propagation simulation through the ice. It is also used for electrons, positrons and gamma rays with energies below 100 MeV, since analytic templates cannot be used at such energies. The GEANT4 propagation is performed during Step 2 of the simulation chain.

Table 5.2 shows a summary of the simulation tools used for the particle propagation and the Cherenkov light production for different energy ranges and particle types.

### 5.1.4 Light propagation

The Cherenkov light produced by charged particles is propagated through the ice in Step 2. This process includes simulation of absorption and scattering processes in

Table 5.2: The summary of the tools used for Cherenkov light simulation.

| **Particle type** | **Energies** | **Light creation** |
|---|---|---|
| Muons (incl. losses with $E < 0.5$ GeV) | all | Template |
| $e^{\pm}$, $\gamma$ (incl. muon losses with $E > 0.5$ GeV) | $E \geqslant 0.1$ GeV | Template |
| $e^{\pm}$, $\gamma$ | $E < 0.1$ GeV | GEANT4 |
| hadrons | all | GEANT4 |
| tau leptons | all | GEANT4 |

the IceCube ice. This propagation is very efficiently parallelised to run on GPUs and, in this work, it is performed by the CLsim software package [127]. The Cherenkov photons are traced through the ice up to the spheres encompassing the DOM surfaces and are stored to be used in the following steps of the simulation chain. In order to save computational resources, a total number of produced photons is down-sampled according to the nominal PMT efficiency increased by about 48%. This increase is added in order to simulate HQE PMTs, variations of DOM efficiency and DOM angular acceptance, as explained in the following section.

### 5.1.5 Detector simulation

Step 3 of the simulation chain models the detector response to the photons that arrived at the DOMs after Step 2.

**DOM angular acceptance and efficiency**

The first part of the detector simulation concerns the DOM angular acceptance curve and the total collection efficiency of the DOMs. The total efficiency includes the effects of the DOM glass, PMT quantum and photoelectron collection efficiencies.

The bubble columns, or *hole ice*, mentioned in Section 4.4.4, affect the photon acceptance as a function of the photon arrival direction. In particular, the scattering and absorption processes can block the photons travelling through the ice along the IceCube strings, but increase the efficiency of photon detection for other angles. In this work, the impact of the hole ice is simulated by effective angular acceptance curves, which are parametrised as

$$g(x) = A \cdot \left[ 0.34 \cdot (1 + \frac{3}{2}x - \frac{1}{2}x^3) + p_1 \cdot x \cdot (x^2 - 1)^3 + p_2 \cdot e^{10 \cdot (x - 1.2)} \right], \tag{5.1}$$

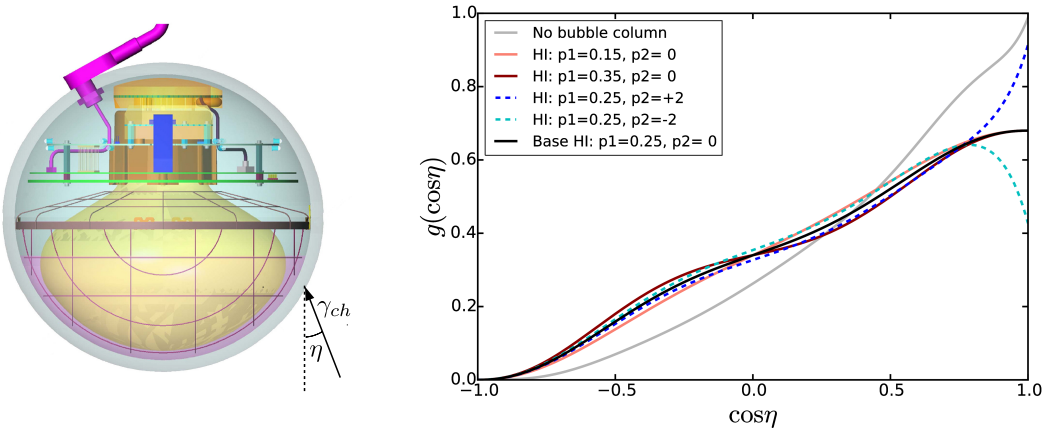


Figure 5.3: (Left) A schematic depiction of the angle used for DOM angular acceptance simulations. (Right) DOM angular acceptance models used in this work, the laboratory measurement of the angular acceptance is depicted in grey for comparison.

where $x = \cos\eta$ is connected to the photon direction as shown in the left part of Figure 5.3, factor $A$ corresponds to the total efficiency of the DOM. Parameter $p_1$ in Equation (5.1) is obtained from LED calibration studies. Parameter $p_2$ is added to cover the uncertainties of the angular acceptance in the face of the PMT, since this region is not well constrained by the current LED calibration studies.

The baseline model used in this work has $p_1 = 0.25$ and $p_2 = 0$. Models with $p_1$ in the range [0.15, 0.35] and $p_2$ in the range [–5, +2] are simulated to estimate the impact of the detector description uncertainties. The curves are renormalised to the same integral efficiency (area) by changing the parameter $A$ in Equation (5.1). The photon propagation results from Step 2 are reused for different detector parameters, because the impact of the angular acceptance modifications is much larger than variations in the light propagation. The baseline model and its variations are depicted in the right part of Figure 5.3.

Variations of the overall DOM efficiency are simulated by scaling factor $A$ in Equation (5.1) to achieve a desired efficiency. The DOM efficiency is known with the precision of about 10%. Therefore, the efficiencies between 88% and 112% of the nominal value are simulated to cover the full uncertainty range.

### Noise

The DeepCore DOMs have a noise rate of approximately 600 Hz, which has both Poisson and non-Poisson (also called *correlated*) components. Every DOM has its own noise rate from both components, which are measured during the special noise data-taking phases in IceCube. Noise is typically caused by photons produced by low energy neutrino interactions, radioactive decays in the ice and DOM, scintillation and electronic noise. The detector noise is generated by the *vuvuzela* package [128].

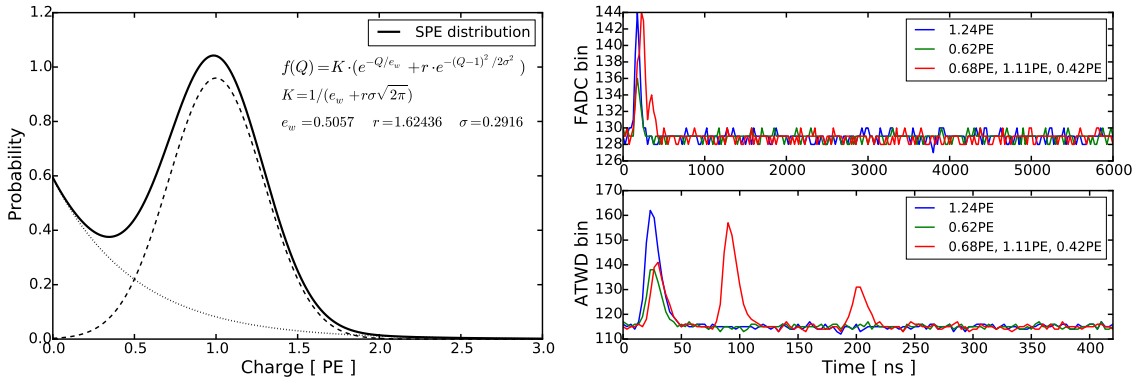


Figure 5.4: (Left) The single photoelectron (SPE) charge distribution. The full distribution is shown by the solid line, while the exponential and Gaussian components are shown by the dotted and dashed lines, respectively. (Right) The simulated waveforms for DOM 29 on string 83 for two pulses with different charges. The FADC and ATWD samplings are depicted in upper and lower panels, respectively. Blue and green lines show examples of single photons, while red lines depict the simulated response to 3 photons arriving within the 200 ns time window.

**PMT response and DOM simulation**
This step simulates the DOM responses for the photons generated and accepted in the previous steps. The response of PMTs is characterised by the single photo-electron (SPE) distribution, which defines the amplitude of the signal caused by one photon hitting the photocathode. This study uses an averaged SPE distribution that consists of the Gaussian centred at 1 PE and the exponential part [118] as shown in Figure 5.4. The response of the DOM electronics is simulated afterwards. This includes simulations of the HLC criteria and waveforms for the ATWD and FADC readouts. Examples of the simulated waveforms are shown in the right part of Figure 5.4.

**Trigger simulation and basic processing**
The DOM responses from the previous step are used to simulate the detector trigger explained in Section 4.4. The trigger time is set to the beginning of the detector readout interval, which is defined as $\pm 10$ $\mu$s from the first HLC pulse triggering the detector. This assures that times of the neutrino interactions are randomised in the way expected in the data. The further processing is performed using the same basic processing chain as is applied to the detector data. After this step, the simulations and data have identical formats, except that the simulation retains the information necessary for event weighting.

## 5.2 Event reconstruction

The following section describes the methods used for event reconstruction in IceCube DeepCore. A staged approach is used in this work. First, the particle direction is reconstructed and interaction type is identified, as discussed in Sections 5.2.1–5.2.2. Then the energy is estimated using the method described in Section 5.2.3.

### 5.2.1 Directional reconstruction

In this work, the direction of the interacting neutrino is estimated using the direction of a muon produced in a $\nu_\mu$ CC interaction. The average distance between strings in DeepCore is approximately 72 meters, while the effective scattering length is about 50 meters [121]. This means that there is a significant portion of photons that are *direct*, i.e. experience minimal scattering before hitting the PMT. The directional reconstruction algorithm uses direct photons to avoid systematic biases caused by the uncertainties in the bulk ice optical properties.

When a minimum ionising muon passes close to the strings, its non-scattered photons leave a specific hyperbolic pattern as a function of the photon arrival time $t_\gamma$ and the DOM depth $z$. It can be expressed [32, 129] as

$$t_\gamma(z) = (t_c - t_0) + \frac{1}{c}\left((z - z_c)u_z + \sqrt{n^2 - 1}\sqrt{d_c^2 + (z - z_c)^2(1 - u_z^2)}\right), \qquad (5.2)$$

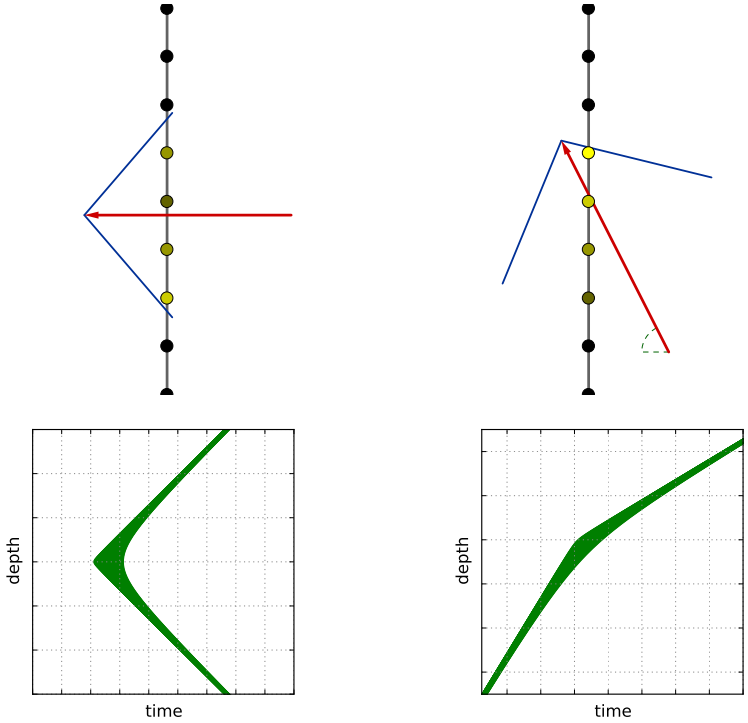


Figure 5.5: Expected direct light time patterns as a function of the depth for a minimum ionising muon passing close to a string. The illustrations are taken from [32].

where $u_z \equiv \cos\theta_z$ characterises the muon zenith angle $\theta_Z$; $t_c$, $z_c$ and $d_c$ are the time, depth and distance of the point of the closest approach between the muon track and the string, respectively; $t_0$ is the time of the muon track starting point; and $c$ is the speed of light. Figure 5.5 depicts schematic drawings of this pattern for two different muon directions.

The direct hit selection is performed using the procedure from [32]. Only the strings where at least 3 DOMs have been hit, and DOMs with the first pulse in a time window [–1, +2] $\mu$s from the median arrival time of the signals in the string are considered. The selection starts with the DOM with the highest integral signal and checks the nearest module above on the same string for signal in the time window

$$\left[ t_0 - \frac{d_{0,+1}}{c_{ice}} - t_{delay}, t_0 + \frac{d_{0,+1}}{c_{ice}} + t_{delay} \right], \tag{5.3}$$

where $t_0$ is the time of the first pulse, $d_{0,+1}$ is the distance between DOMs, $c_{ice}$ is the speed of light in ice and $t_{delay}$ is the allowed time delay. The time delay of 20 ns is used in this work to select photons experiencing little scattering and avoid contamination from scattered photons or the detector noise.

The next DOMs are selected in a similar way; however, the time window is set to

$$\left[ t_i - \frac{d_{i,i+1}}{c_{ice}} - t_{delay}, t_i + \frac{d_{i,i+1}}{v_{eff}} + t_{delay} \right], \tag{5.4}$$

where $v_{eff}$ is the effective speed defined as the slowest speed between any of the three previous DOMs. If a new signal is accepted, all previously accepted DOMs are checked to match the hyperbolic pattern. The signals are rejected if they have a delay larger than $t_{delay}/2$ from the line connecting the first and the last accepted DOMs. This procedure is repeated until either 8 consecutive DOMs are rejected, or until the end of the string is reached. The same procedure is repeated for DOMs located below the initial one. The string is used for the reconstruction if at least 3 DOMs are identified to detect direct photons.

The muon direction is fit minimising a modified chi-squared value $\chi^2_{mod}$, calculated using the DOMs with direct hits as

$$\chi^2_{mod} = \sum_i \left[ \frac{(t^{exp}_\gamma(z_i) - t^{obs}_\gamma(z_i))^2}{\sigma^2_\gamma} + \frac{2 \cdot q(z_i) \cdot \sqrt{r^2_{DOM} + d^2_\gamma}}{(\cos\phi_\gamma + 1) \cdot \bar{q} \cdot d_0} \right], \tag{5.5}$$

where $t^{obs}_\gamma(z_i)$ is the time of the observed signal in the $i$th DOM with depth $z_i$; $t^{exp}_\gamma(z_i)$ is the expected photon arrival time given by Equation (5.2); and $\sigma_\gamma = 3$ ns corresponds to the DOM timing resolution [117]. The second term in Equation (5.5) is a penalisation term that accounts for the probability of observing a charge $q(z_i)$ far from the production point, where $\bar{q}$ is the average charge over all selected DOMs, $d_\gamma$ is the distance travelled by the photon, $r_{DOM}$ is the module radius, and $\cos\phi_\gamma$ is the projected photon arrival angle on the DOM. The distance $d_0 = 10$ m defines the strength of the penalisation and can be interpreted as the distance where 1 PE signal is expected in the PMT.

The expression in Equation (5.2) defines the hyperbola for one string, but it can be extended for multiple strings as discussed in [32, 129]. Only the zenith angle can be reconstructed for the *single-string* (SS) events, where only one string has direct light. For such events, the azimuth direction is reconstructed by the LineFit reconstruction algorithm [130]. The azimuth angle is reconstructed for the *multi-string* (MS) events, which have two or more string with direct photons. It is important to mention that the neutrino oscillation effects probed in this work have no dependence on the azimuth angle due to the Earth symmetry.

The median neutrino zenith resolutions for events with and without identified tracks as a function of the deposited energy and the neutrino arrival direction are depicted in Figure 5.6. The criteria for track identification is discussed in Section 5.2.2. The median zenith angle resolution for $\nu_\mu$ CC events with identified muon tracks is approximately 12° at 10 GeV and 5° at 100 GeV. For events without identified tracks, the resolution is approximately 13°, almost independent of energy. The median resolution for NC interactions, $\nu_e$ and $\nu_\tau$ CC interactions is between 18 and 23°. The events originating from upgoing neutrinos typically have a better angular resolution, while the down-going events have rather poor resolution due to the PMT orientation in the DOMs.

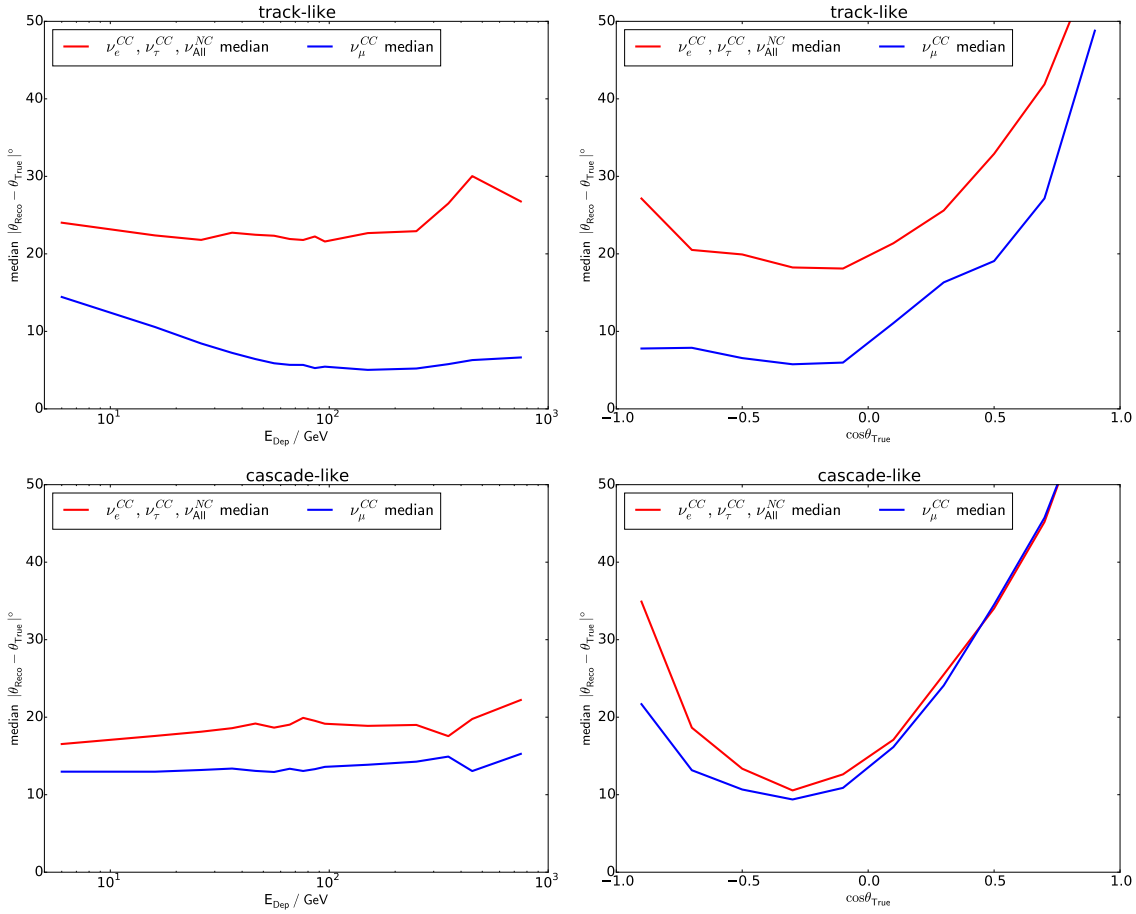


Figure 5.6: The median neutrino zenith resolutions for track-like (upper panels) and cascade-like (lower panels) events as a function of deposited energy (left) and neutrino arrival zenith direction (right). The deposited energy is defined as the full neutrino energy for CC interactions or as the hadronic cascade energy for NC interactions. The resolutions for $\nu_\mu$ CC interactions are depicted in blue, while $\nu_e$, $\nu_\tau$ CC interactions and all NC interactions are depicted in red.

### 5.2.2 Particle identification

The event topology is identified using information from the directional reconstruction. For this purpose, the isotropic point-like emission pattern mimicking the particle shower is fit by modifying the Equation (5.2) as

$$t_\gamma(z) = t_0 + \frac{n}{c}\sqrt{d_c^2 + (z - z_c)^2}, \tag{5.6}$$

where $z_c$ and $d_c$ are the depth of and the distance to the point-like source, respectively. The track and cascade hypotheses are fit to estimate $\chi^2_{track}$ and $\chi^2_{cascade}$, which are used to calculate the particle identification score as

$$\text{PID} = \frac{\chi^2_{track}/(N_{DOMs} - 3)}{\chi^2_{cascade}/(N_{DOMs} - 4)}, \tag{5.7}$$

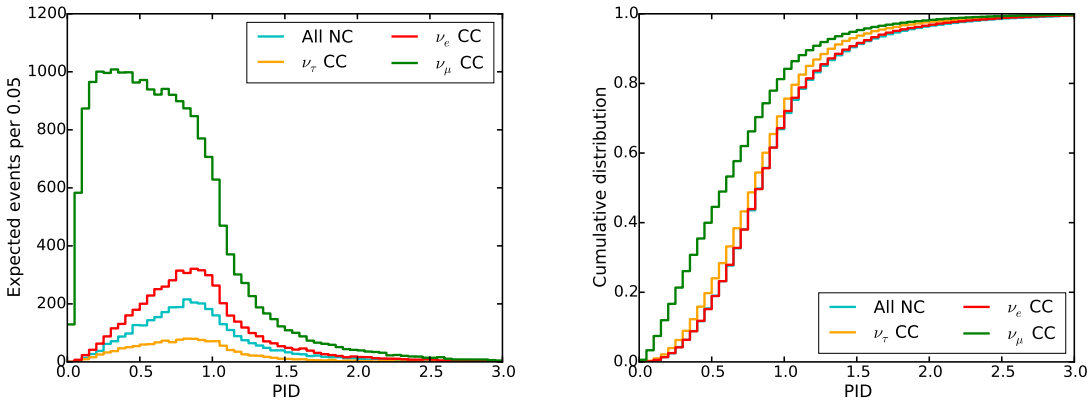


Figure 5.7: The expected PID score distribution (left) and cumulative distribution (right) for different interaction types for approximately 6 years of the detector live time with $\Delta m^2_{32} = 2.515 \cdot 10^{-3}$ eV$^2$ and $\sin^2\theta_{23} = 0.565$. The distributions for CC interactions of $\nu_\mu$, $\nu_e$ and $\nu_\tau$ are depicted in green, red and orange, respectively, while NC interactions of all flavours are depicted in cyan.

where $N_{DOMs}$ is a number of DOMs with direct photons. The quantities $(N_{DOMs}-3)$ and $(N_{DOMs}-4)$ correspond to the number of degrees of freedom for the track-like and point-like hypotheses. Small values of the PID correspond to events identified as tracks, while large values are likely to be cascades. Using this metric the events are split into the *track-like* with PID $< 0.7$ and *cascade-like* events with PID $\geq 0.7$. The expected PID distributions for different neutrino interactions are depicted in Figure 5.7.

### 5.2.3 Energy reconstruction

The full energy of the neutrino interaction is estimated after the muon direction is known. The methods used in this work are designed for $\nu_\mu$ CC interactions and reconstruct neutrino energies in steps.

First, the muon track endpoint is identified along the reconstructed direction using the method described in [131]. It uses the logarithm of the likelihood ratio

$$LLHR = \log \frac{\prod_i^{DOMs} p_i(\text{noHit}|\text{track})}{\prod_i^{DOMs} p_i(\text{noHit}|\text{noTrack})} \tag{5.8}$$

where $p_i(\text{noHit}|\text{track})$ is the probability to observe no signal in DOMs with an assumption of an infinite muon track, while $p_i(\text{noHit}|\text{noTrack})$ is the probability for a finite track with a given vertex and endpoint along the reconstructed direction. These probabilities are illustrated graphically in Figure 5.8. The value from Equation (5.8) is minimised to find the muon track endpoint, while a different algorithm is used for the vertex reconstruction

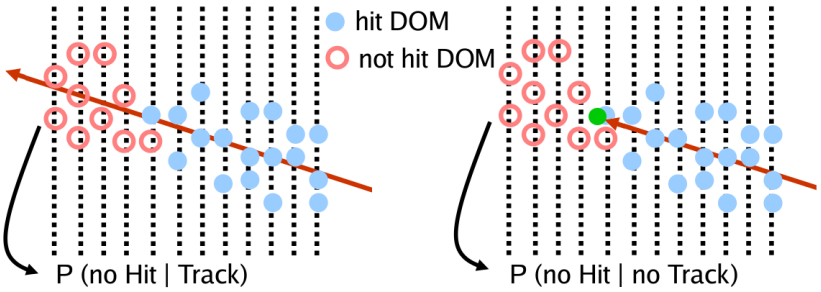


Figure 5.8: A schematic view of muon track endpoint reconstruction. The red line represents infinite (left) or ending (right) muon track with endpoints shown in green, and blue and red circles represent DOMs with and without a signal, respectively. $P$(no Hit|Track) shows the probability of having no signal in a given DOM with an infinite track and $P$(no Hit|no Track) is the probability of having no signal for muon track that ended in the detector.

The vertex position is measured using the *hit-no hit* likelihood with the method from [132, 133]. All DOMs within a 200 m cylinder along the infinite track hypothesis are considered. For each module, the probability of having or not having a signal is calculated from the Poisson distribution as

$$\begin{aligned} p_{\text{no hit}}(\lambda) &= p_0(\lambda) = e^{-\lambda}, \\ p_{\text{hit}}(\lambda) &= 1 - p_0(\lambda) = 1 - e^{-\lambda}, \end{aligned} \tag{5.9}$$

where $\lambda$ is the light expectation estimated as

$$\lambda = \lambda_{track} + E^{EM}_{cascade} \cdot \lambda^{1\text{GeV}}_{cascade} + \nu \cdot \Delta T_{event}, \tag{5.10}$$

where $\lambda_{track}$ and $\lambda^{1\text{GeV}}_{cascade}$ are the expected number of photons arriving from the track and 1 GeV EM cascade, respectively; $E^{EM}_{cascade}$ is the EM-equivalent energy for the hadronic shower; $\nu$ is the noise rate in the DOM; and $\Delta T_{event}$ is the time extent of the pulses in the event. The track and cascade light expectations are taken from the *photorec* lookup tables [134]. These tables contain the tabulated observed DOM signals obtained from the simulations of tracks and electromagnetic cascades located throughout the detector. The total negative log-likelihood

$$LLH = -\sum_{i}^{DOMs} \log p_i(\lambda_i) \tag{5.11}$$

is minimised to obtain the vertex position along the reconstructed direction and the cascade energy, as depicted the left part of Figure 5.9. The total energy of the event is calculated as

$$E_\nu = \frac{b}{a}\left(e^{b \cdot L_\mu} - 1\right) + F^{-1}(E^{EM}_{cascade}), \tag{5.12}$$

where $a = 0.226$ GeV/m, $b = 4.6 \cdot 10^{-4}$ m$^{-1}$ are the properties of the muon energy losses estimated for the energy range between 10 and 100 GeV [114]; $L_\mu$ is the reconstructed track length; and $F^{-1}$ is the factor from Equation (4.13) that accounts for

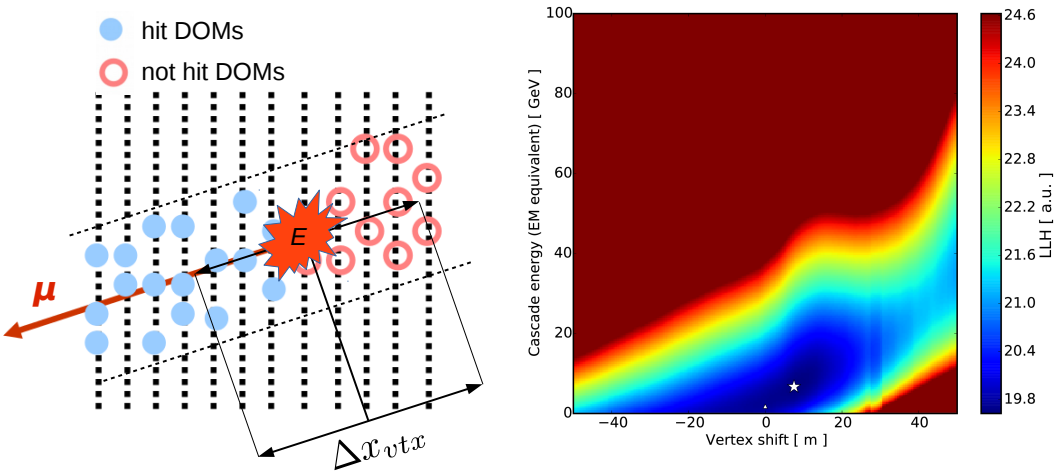


Figure 5.9: (Left) The variables reconstructed by the vertex reconstruction algorithm, with $\Delta x_{vtx}$ showing the vertex shift with respect to an arbitrary seed position and $E$ is the energy of the hadronic shower. (Right) The example of the likelihood as a function of the vertex shift and the cascade energy. The elongation of the minimum (blue region) demonstrates the correlation between the vertex position and the energy of the hadronic shower.

a smaller amount of Cherenkov light produced by hadronic cascades when compared to the electromagnetic showers.

An example of the likelihood landscape is depicted in the right panel of Figure 5.9. The shower energy and vertex position are correlated, since the amount of light is constant for each event. The length of the track is shortened when the vertex position is shifted to the front, resulting in a higher cascade energy compensating the lower muon light expectation. The shift in the opposite direction results in a lower reconstructed cascade energy. Any estimation of the inelasticity is complicated by this correlation, though the total neutrino energy can still be reconstructed with adequate precision.

The median energy resolution for events with and without a clearly identified muon track is shown in Figure 5.10. This method reconstructs energy with a median resolution of 30% at 10 GeV. The resolution for $\nu_\mu$ CC interactions improves with increasing energy to the values of about 20% and 25% at 40 GeV for the track-like and cascade-like events, respectively. For the interactions producing cascades the median resolution is between 25 and 30%.

## 5.3 Event selection

The event selection used in this work is nearly identical to that described in [32]. Therefore, only a general summary is presented at the beginning of this section. It is followed by the information about the data-driven atmospheric muon template.

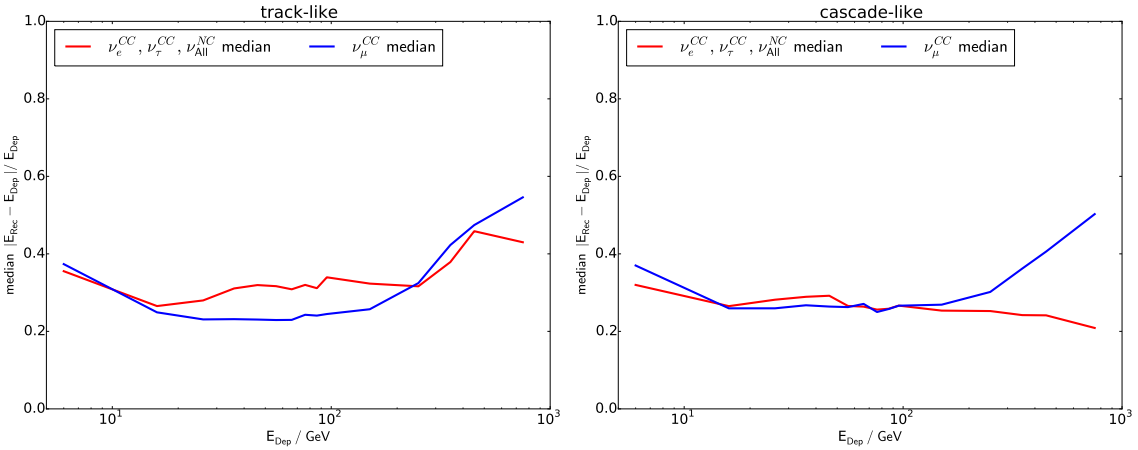


Figure 5.10: The median energy resolutions for the track-like ($PID < 0.7$) and the cascade-like ($PID \geq 0.7$) events. The $\nu_\mu$ CC interactions are depicted in blue and events producing showers ($\nu_e$, $\nu_\tau$ CC and NC interactions of all flavours) are shown in red.

A few minor changes in the event selection, when compared to [32], are discussed in the final part of this section.

### 5.3.1 General overview

In this work, the event selection is designed to reduce the background from atmospheric muons and to select events caused by $\nu_\mu$ CC interactions. The key cuts used in the analysis are summarised in this section.

**DeepCore trigger and filter**

First, an event must satisfy conditions of the DeepCore trigger and online filter [119]. These conditions guarantee that an event passes through the DeepCore volume. Also, it applies loose criteria to reject events created by down-going atmospheric muons. The filter rejects approximately 96% of atmospheric muons and keeps more than 99% of atmospheric neutrinos [119]. At this stage, approximately 99.97% of all events in the sample are still the background events.

**DeepCore Level 3**

An event should pass the standard DeepCore Level 3 cuts. Their main purpose is to reject events originating from the noise and atmospheric muons. Events originating from neutrino interactions typically produce relatively large signals within a short time window after the trigger and are localised in DeepCore. On the other hand, atmospheric muons create hits over longer time windows during their propagation through the whole detector.

Two of the cuts at this level are used to reject events originating from the pure DOM noise:

- An integrated charge larger than 2 PEs and more than 2 pulses in a 200 ns sliding time window are required.
- An event should show signs of directionality. This algorithm searches for pairs of DOM pulses in a sliding 750 ns time window for 48 directional configurations. An event is accepted if there is at least one directional configuration with 3 pulses having apparent velocities in the range of $[0.1, 1.0]$ m/ns.

The extra criteria analyse the DOM signals in the fiducial volume and the veto region (see Section 4.4.3) to reject atmospheric muons:

- The requirements of the DeepCore online filter from [119] are applied to all pulses (rather than just HLC pulses).
- There should be not more than 12 hits above a depth of 2148 m before the trigger time.
- The position of the first pulse after the seeded R-T cleaning [135] procedure should be deeper than 2068 m.
- An event is rejected if there is a clustering of signals in the veto region before the trigger time. The algorithm rejects an event if the veto region has a cylinder with 250 m height and 150 m radius with integrated charge of more than 4 PE before the trigger time.
- More than 40% of the charge should be detected within the first 600 ns after the trigger time; the first two pulses in an event are excluded for this criterion.
- The ratio of charges in the veto region to the fiducial volume must be smaller than 1.5 after the seeded R-T signal cleaning procedure.

The DeepCore Level 3 cuts keep approximately 80% of neutrino events while rejecting about 92 % of the background events. After this level, the background events still account for 99.5% of the total event count.

**Minimal number of hit DOMs**

An event must have a sufficient amount of light for energy and zenith reconstruction. Therefore, the following criteria are applied:

- At least 5 DOMs with the HLC criteria
- At least 8 DOMs after the seeded R-T cleaning
- At least 5 DOMs need pulses with timing consistent with the direct photon hypothesis, as discussed in Section 5.2.1.

Approximately 25% of neutrino events and 33% of the background events accepted by the DeepCore Level 3 pass these conditions.

**Atmospheric muon rejection**
The data sample is dominated by atmospheric muons after applying the cuts from the previous sections. Therefore, more sophisticated background rejection techniques are applied to increase the purity of the sample:

- The first HLC pulse triggering the detector must be less than 200 m away from the central IceCube string and must have a depth between approximately 2158 and 2445 m.
- There must be less than 5 PE of charge that can be causally connected to the hypothesis of a down-going muon track. This criterion is further discussed in Section 5.3.2.
- The requirement on the clustering of signals before the trigger time from the DeepCore Level 3 is strengthened to 3 PE.
- There must be not more than 1 hit consistent with the hypothesis of an atmospheric muon travelling through the corridors formed by the detector geometry. This criterion is further discussed in Section 5.3.2.
- The LineFit [130] and SPEFit [136] fast directional reconstruction algorithms should reconstruct an event as up-going with $\cos\theta_z < 0$.

These criteria result in approximately 99.92% reduction of the background rate after the previous step, while keeping approximately 35% of the neutrino-induced events. After applying these criteria, the event sample has a background contamination of approximately 35%.

**Reconstruction quality**
Another important part of the event selection is identification of the events with a good fit quality for the directional reconstruction, discussed in Section 5.2.1. The fit quality is defined as

$$Q_{fit} = \chi^2_{mod}/(N_{DOMs} - P), \tag{5.13}$$

where $\chi^2_{mod}$ is given by Equation (5.5); $N_{DOMs}$ represents the number of DOMs with direct photons and $P$ is the number of fit parameters in Equation (5.5). This value should be smaller than 20 for single-string events and less than 60 for multi-string events to ensure a good directional reconstruction. In addition, the background events typically have a worse fit quality. This results in an acceptance of about 60% of neutrino events, while only 20% of the remaining background events are accepted. After this step, the event sample has approximately 15% contamination from background events.

**Usage of the upgoing region**
After the previous steps of the event selection, about 15% of the sample is atmospheric muons. Most of the remaining background events are reconstructed as

down-going by the algorithm discussed in Section 5.2.1, while neutrino events are typically up-going. Therefore, the analysis is performed in the up-going region, with $\cos\theta_z < 0$. This results in a rejection of more than 85% of the remaining atmospheric muon events while keeping about 90% of neutrino events. At this level, the final contamination is expected to be smaller than a few percent of the total event rate. However, a sufficient quantity of atmospheric muon simulations is not available for use in the analysis due to computational limitations. Therefore, a data-driven template is fit in the analysis to account for the remaining background, and its selection is discussed in the next section.

### 5.3.2 Atmospheric muon template

As stated in the previous section, sufficient atmospheric muon simulations were not available at the time of the studies presented in this work. Therefore, a data-driven template is used to estimate the impact of the atmospheric muon background. The criteria used for its selection are discussed below.

**Causally connected pulses**
This criterion identifies the pulses that are causally connected, and could, therefore, be caused by a background muon. If an atmospheric muon arrives to DeepCore, it typically leaves signals in the region

$$\begin{aligned} \Delta r_i/c &< 2.5\ \mu\text{s}, \\ -0.15\ \mu\text{s} - \Delta t_i < \Delta r_i/c &< 1.85\ \mu\text{s} - \Delta t_i, \end{aligned} \tag{5.14}$$

where $\Delta t_i = t_i - t_{trig}$ and $\Delta r_i = |\vec{r}_i - \vec{r}_{trig}|$ are the time difference and the distance between $i$th DOM and the first pulse triggering the detector, respectively. The requirement

$$\Delta r_i/c > \frac{2}{3}\Delta t_i + \frac{1}{3}\ \mu\text{s} \tag{5.15}$$

is applied to avoid counting the light originating from neutrino events in DeepCore. The requirements given by Equations (5.14) and (5.15) define a veto region shown in red in the left part of Figure 5.11. The total charge observed in this region is used as a cut parameter. Its distributions for neutrinos and atmospheric muons are shown in the right part of Figure 5.11. The event is rejected if a total charge of 5 PE or more is found. More information about the optimisation of this event criteria can be found in [131].

**Corridor cut**
The IceCube strings are placed on a regular triangular grid. Such a geometry results in the existence of the *corridors*, through which muons can penetrate to DeepCore leaving only a few weak signals in the outer layers of IceCube. Examples of such corridors are shown in the left part of Figure 5.12. This algorithm catches the dimmest light produced by such muons. It searches for hits in the time window $[t_\mu - 150\ \text{ns}, t_\mu + 250\ \text{ns}]$, where $t_\mu$ is the expected photon arrival time for a muon

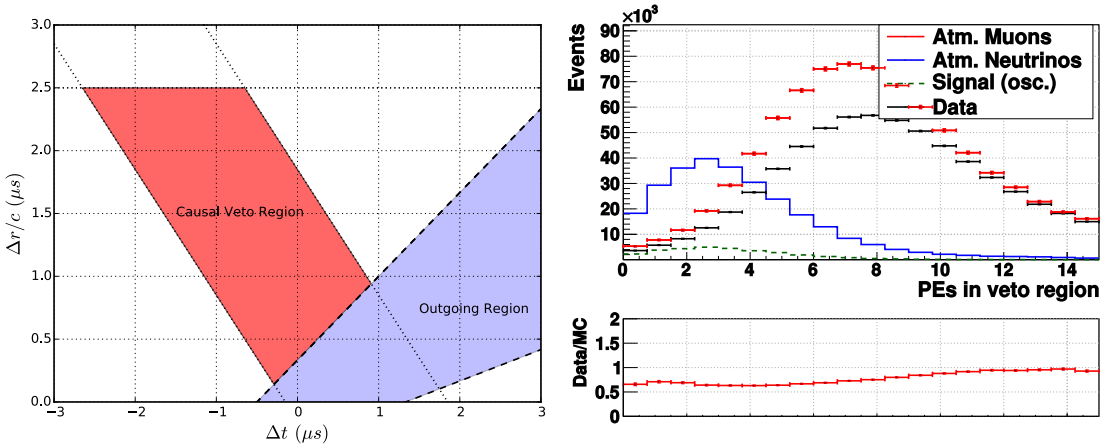


Figure 5.11: (Left) Graphical representation of the cut on the causally connected hits, where $\Delta t$ and $\Delta r/c$ are the time difference and the distance between the probed DOM and the first HLC signal triggering the detector, respectively. The red shaded area shows the veto region, while the blue region demonstrates the expected location for neutrino events. The figure is taken from [137]. (Right) The expected distribution of all neutrinos (blue), oscillated muon neutrinos (green), simulated atmospheric muons (red) and data (black) as a function of the total charge in the veto region. The figure is taken from [32].

going through such a corridor. The zenith direction is varied with a 0.02-radian step for each corridor. The largest number of hit DOMs found among all corridors and zenith directions is used as the cut variable. Events with 0 or 1 hits are accepted, while all other events are rejected. The performance of this method is shown in the right part of Figure 5.12. More details about this criterion and its optimisation can be found in [32].

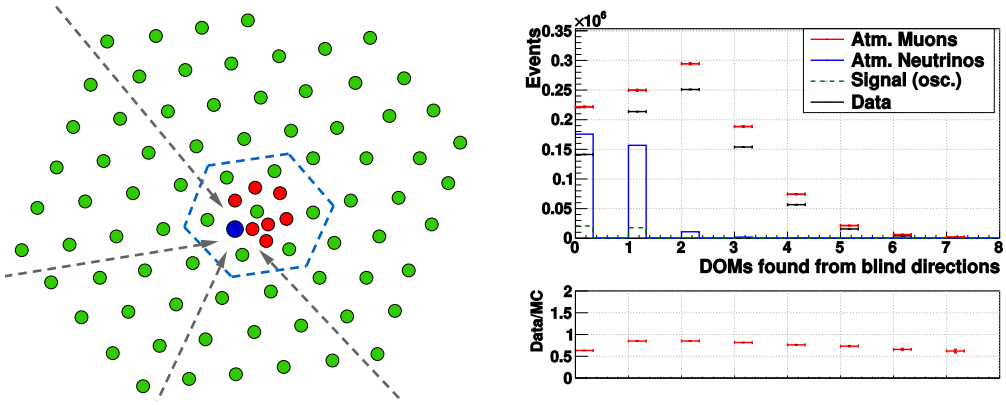


Figure 5.12: (Left) Examples of the corridors (grey arrows) formed by the detector geometry. (Right) The distribution of the number of hit DOMs in a coincidence with the hypothesis of a track coming through the detector corridors for all neutrinos (blue), oscillated muon neutrinos (green), simulated atmospheric muons (red) and data (black). Both panels are taken from [32].

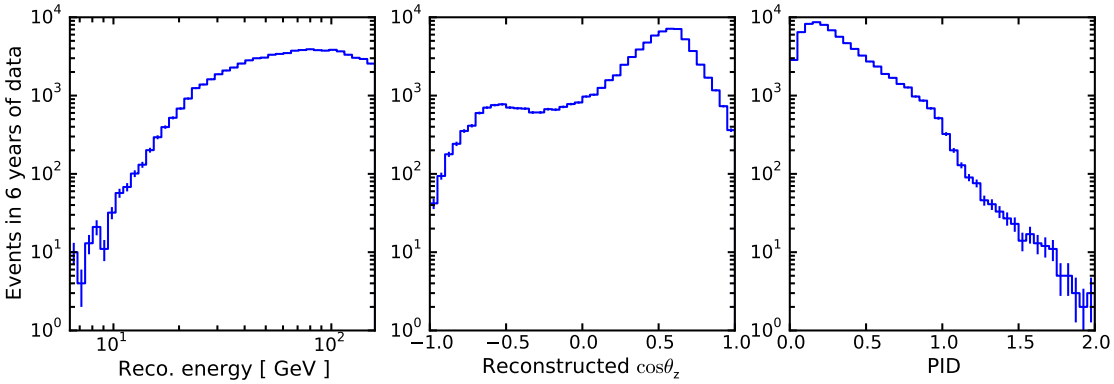


Figure 5.13: The energy (left), reconstructed zenith (middle) and PID (right) distributions of the events in the muon template obtained by the inverted cuts from 6 years of IceCube DeepCore data.

**Inverted cut criteria**

Simulations of the atmospheric muons require a large amount of computational resources. Currently, sufficient live time is not available to estimate the background contamination. The two criteria presented in the previous paragraphs are modified to select a data-driven atmospheric muon template. First, the corridor cut is changed to require 3 or more hits in order to achieve a high purity muon sample. The cut on the causally connected hits is then removed. The energy, zenith and PID distribution of the events in the muon template are shown in Figure 5.13. It is assumed that these distributions are a good approximation of the muons that pass the standard event selection criteria.

### 5.3.3 Modifications of the selection

Minor modifications are introduced to the event selection, when compared to [32], to avoid additional background and extend the event selection. Those differences are discussed here.

**Position of the first HLC pulse**

The excess of events in the upper part of the detector was found during the sterile neutrino search described in Chapter 7. The predicted depth distribution in the data and simulations is shown in Figure 5.14. The data have approximately 30% more events than predicted in the region above –250 m in the $z$ direction (approximately 2198 m in depth). These events are likely caused by atmospheric muons penetrating to the DeepCore fiducial volume via the dust layer that is found approximately 80 meters above DeepCore. Such muons leave almost no signals in the outer veto regions of IceCube and are thus not tagged by background rejection cuts. Therefore, the muon template does not cover this region appropriately. To avoid a contamination from such muons, the events are rejected if the first HLC DOM triggering the detector has $z$ above –250 m.

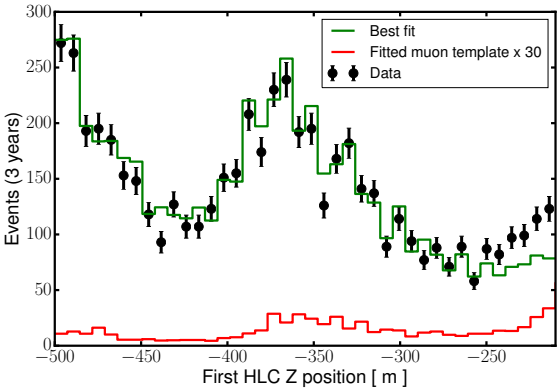


Figure 5.14: The distribution of the first HLC $z$ positions for data (black points) and expectation that includes the data-driven atmospheric muon template (green). The fitted muon template is shown in red; it was multiplied by 30 to be visible on the figure. The disagreement between the data and simulations above –250 m is likely to be caused by atmospheric muons penetrating through the dust layer.

**Identification of muon tracks**

The initial event selection used only events with a clearly visible muon track, identified by the PID score

$$PID < 0.6\ (0.8) \qquad \text{for SS (MS) events .} \tag{5.16}$$

The sterile neutrino search presented in Chapter 7 uses the same selection criteria. The PID score is used as the observable parameter for the measurement of the standard atmospheric mixing discussed in Chapter 6.

### 5.3.4 Observables at the final level

The event selection described in the previous sections retains approximately 6000 events per year in the energy range considered for this work. Figure 5.15 shows the distribution of the reconstructed variables obtained with 6 years of IceCube DeepCore data and the prediction from the simulations. Approximately 67% of events at this level originate from $\nu_\mu$ CC interactions. The contributions from different interactions and the distribution of events in the analysis binning are discussed in Chapter 6.

After the data are selected, statistical methods are applied to extract physics parameters, as discussed in the following sections of this work.

## 5.4 Parameter extraction

The extraction of the neutrino mixing parameters requires a proper statistical treatment of the data. This section discusses the statistical methods and treatment of the systematic uncertainties used in this work.

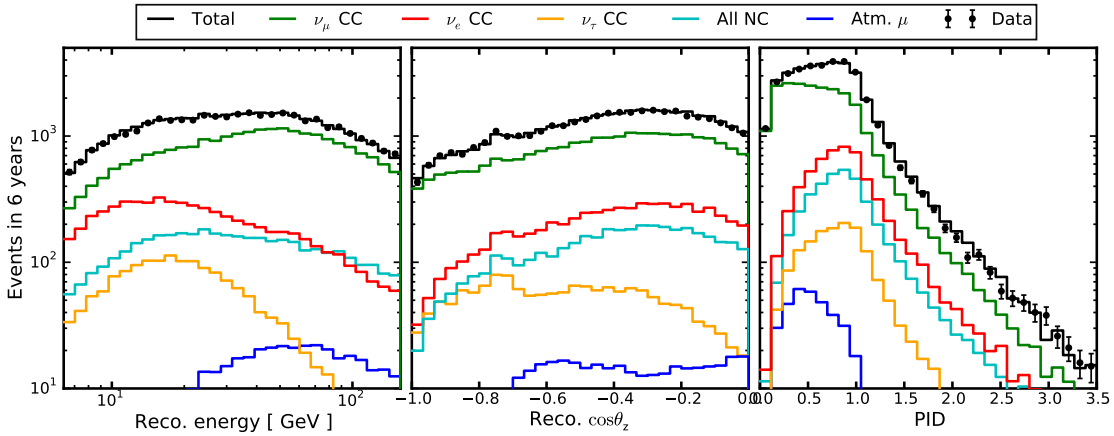


Figure 5.15: The reconstructed energy (left), zenith (middle) and PID (right) distributions of the events at the final level of the selection. The total event rates for data and simulations are shown in black, while different components are shown with coloured lines. The data are not fit in this figure, and oscillations parameters for the normal neutrino mass ordering from NuFit3.1 are used, as listed in Table 3.2 (Section 3.5.2).

### 5.4.1 Binned Poisson likelihood

The parameters are extracted using the maximal likelihood estimation. In this work, the following representation of the Poisson likelihood is minimised:

$$-\ln\mathcal{L} = \sum_i \left(\mu_i(\boldsymbol{\theta},\boldsymbol{\phi}) - n_i \ln\mu(\boldsymbol{\theta},\boldsymbol{\phi})\right) + \sum_k \frac{(\phi_k-\phi_k^0)^2}{2\sigma_{\phi_k}^2}, \tag{5.17}$$

where $n_i$ is a number of data events in the $i$th bin; $\mu_i(\boldsymbol{\theta},\boldsymbol{\phi})$ is the expectation as a function of the parameters of interest $\boldsymbol{\theta}$ and nuisance parameters $\boldsymbol{\phi}$. The second part of Equation (5.17) defines the Gaussian penalties that account for prior knowledge about nuisance parameters, where values $\phi_k^0$ and $\sigma_{\phi_k}$ are the central values and the uncertainties for the parameters $\phi_k$, respectively. The priors come from independent measurements or uncertainties in the model predictions.

### 5.4.2 Confidence level estimation

The best estimates of the parameters are obtained by minimising the expression in Equation (5.17). The uncertainty estimation is performed by profiling the likelihood with respect to the parameters of interest $\boldsymbol{\theta}$ [23]. In this work, the *test statistic* (TS) is given by the likelihood ratio

$$-2\Delta\ln\mathcal{L}(\boldsymbol{\theta}) \equiv -2\ln\frac{\mathcal{L}(\boldsymbol{\theta},\hat{\hat{\boldsymbol{\phi}}}(\boldsymbol{\theta}))}{\mathcal{L}(\hat{\boldsymbol{\theta}},\hat{\boldsymbol{\phi}})} = -2\left(\ln\mathcal{L}(\boldsymbol{\theta},\hat{\hat{\boldsymbol{\phi}}}(\boldsymbol{\theta})) - \ln\mathcal{L}(\hat{\boldsymbol{\theta}},\hat{\boldsymbol{\phi}})\right), \tag{5.18}$$

where $\mathcal{L}(\hat{\boldsymbol{\theta}},\hat{\boldsymbol{\phi}})$ is the likelihood value for the global best fit, while $\mathcal{L}(\boldsymbol{\theta},\hat{\hat{\boldsymbol{\phi}}}(\hat{\boldsymbol{\theta}}))$ is the optimal likelihood value for the probed physics parameter(s) $\boldsymbol{\theta}$. This work makes

Table 5.3: The critical values for 68%, 90% and 99% C.L. for $\chi^2$ distribution with 1 and 2 degrees of freedom (d.o.f.).

| **Confidence level** | $\boldsymbol{\Delta n = 1}$ | $\boldsymbol{\Delta n = 2}$ |
|---|---|---|
| 68% C.L. | 1.0 | 2.30 |
| 90% C.L. | 2.71 | 4.61 |
| 99% C.L. | 6.63 | 9.21 |

use of Wilks' theorem [138], stating that the TS value is approximately distributed according to a chi-squared distribution

$$-2\Delta \ln \mathcal{L} \approx \chi^2(d.o.f. = \Delta n), \tag{5.19}$$

where $\Delta n$ is a number of tested physics parameters. Parameters that result in a TS value greater than a *critical value* can be rejected with a corresponding confidence level (C.L.). The studies presented in this work are performed for one or two physics parameters, and the corresponding critical values for 68%, 90% and 99% C.L. are listed in Table 5.3.

### 5.4.3 Systematic uncertainties as nuisance parameters

Equations (5.17) and (5.22) are symmetric with respect to all parameters. Therefore, the choice of physics and nuisance parameters is made based on the needs of an individual study. For example, the mixing parameters $\Delta m^2_{32}$ and $\theta_{23}$ are physics parameters for the measurement of the standard atmospheric neutrino oscillations presented in Chapter 6. On the other hand, they are nuisance parameters in the sterile neutrino search discussed in Chapter 7, where the mixing angles $\theta_{24}$ and $\theta_{34}$ are the parameters of interest. The studies presented in this work are designed to avoid biases for the physics parameters. On the other hand, the nuisance parameters can be biased if they account for multiple or non-implemented systematic uncertainties. Therefore, the physics parameters have no priors, while nuisance parameters account for the systematic uncertainties and may have priors.

### 5.4.4 Forward folding technique

In this work, the expectations are calculated using the *forward folding* technique. It means that the expectation for a given hypothesis is obtained by reweighting the simulated MC events.

First, the *oscillated* neutrino flux is calculated for the $k$th MC event of flavour $\nu_\alpha$ as

$$\Phi^{k,osc}_{\nu_\alpha} = \Phi^k_{\nu_e} P^{osc}_{\nu_e \to \nu_\alpha} + \Phi^k_{\nu_\mu} P^{osc}_{\nu_\mu \to \nu_\alpha}, \tag{5.20}$$

where $\Phi^k_{\nu_e}$ and $\Phi^k_{\nu_\mu}$ are the atmospheric $\nu_e$ and $\nu_\mu$ fluxes corresponding to the $k$th event, respectively; and $P^{osc}_{\nu_e \to \nu_\alpha}$ and $P^{osc}_{\nu_\mu \to \nu_\alpha}$ are the oscillation transition probabilities

to flavour $\nu_\alpha$. The neutrino mixing parameters modify the probabilities $P^{osc}_{\nu_\beta \to \nu_\alpha}$, while the flux uncertainties change $\Phi_{\nu_\beta}$, as discussed in Section 5.5.2. Using the oscillated flux, the event weight is then calculated as

$$w^{k,\alpha} = w_0^{k,\alpha} \cdot \Phi^{k,osc}_{\nu_\alpha} \cdot \sigma^k, \tag{5.21}$$

where $w_0^{k,\alpha}$ is the base weight that includes the generation properties (volume, cross-section model *etc.*) from Section 5.1 and $\sigma^k$ is the modification of the weight due to the cross-section uncertainties discussed in Section 5.5.3.

The detector or cross-section uncertainties can have different impacts on the events originating from charged and neutral current neutrino interactions. In addition, the NC interactions are identical for all neutrino flavours. Therefore, the NC events are kept separate and only the flux reduction due to the transition to the sterile neutrino state is calculated for them. This means that the oscillation probabilities are not applied to the NC events in the measurement of the standard atmospheric mixing parameters. This saves computation time and helps to reduce statistical uncertainties of the MC simulations for NC events.

The total event expectation for the $i$th experimental bin is then calculated as

$$\mu_i = \sum_\alpha A_i^\alpha \left[ \sum_k w_i^{k,\alpha} \right] + N_i^{bkg}, \tag{5.22}$$

with $\alpha$ corresponding to the neutrino interaction types: CC interactions of $\nu_e$, $\nu_\mu$ and $\nu_\tau$, and all flavours NC interactions; $w_i^{k,\alpha}$ is the weight of the $k$th MC event contributing to the $i$th bin calculated from Equation (5.21). The factor $A_i^\alpha$ accounts for the impact of the detector uncertainties and it is applied as the rate modification at the histogram level for each interaction type. The detector uncertainties are further discussed in Section 5.5.4. $N_i^{bkg}$ denotes the background expectation obtained by scaling of the atmospheric muon template discussed in Section 5.3.2.

## 5.5 Systematic uncertainties

This work considers a variety of the uncertainties in the neutrino mixing, atmospheric neutrino fluxes, interaction cross-sections and background. This section discusses the systematic uncertainties considered in the measurement of the standard atmospheric neutrino mixing presented in Chapter 6. The modifications of the reconstructed energy, zenith and PID distributions by the systematic parameters discussed in the next sections can be found in Appendix A.1. A few minor differences in the treatment of the systematic uncertainties in the sterile neutrino search are discussed in Chapter 7.

### 5.5.1 Neutrino mixing

The mixing parameters $\Delta m^2_{32}$ and $\theta_{23}$ are in the focus of this work. Therefore, they do not have any priors and are freely fit. The other mixing parameters do not have

an impact on the final results presented in this work. The parameters $\Delta m^2_{21}$ and $\theta_{12}$ drive oscillations at energies well below the DeepCore energy threshold. The angle $\theta_{13}$ is known with high precision and has a small impact on the oscillation probabilities for the energy range considered in this work. Therefore, these parameters are fixed. Also, the value of the CP violating phase $\delta_{CP}$ is fixed at zero, since it has a negligible impact on the oscillation probabilities considered in this work.

### 5.5.2 Flux uncertainties

This work uses the atmospheric neutrino flux from [37] as the baseline flux model. At the energies relevant to this work, the leading uncertainties in atmospheric neutrino fluxes come from the uncertainties in the kaon production during the development of atmospheric particle showers. This work uses the flux uncertainty estimations based on [139] and they can be broken into the following classes.

**Normalisations**
The total normalisation of the neutrino fluxes is not constrained in this work and is treated as a free parameter. This means that the results obtained in this work are based on shape-only effects. Additionally, the ratio between $\nu_e$ and $\nu_\mu$ flux is fitted in this work with a 5%-width Gaussian prior centred at the nominal value.

**Spectral index**
The spectral index in this work is applied as a function $E_\nu^{\Delta\gamma}$. Unlike other parameters described in this section, it takes into account a change of neutrino spectrum due to the uncertainties of the primary cosmic ray spectrum. In this work, the spectral index is fit without a prior, since it was found to correlate with uncertainties in the properties of the bulk ice and neutrino interaction cross-sections.

**Neutrino-antineutrino flux ratio**
The uncertainties of the neutrino flux compared to antineutrino flux come from [139]. In this work, they are parametrised with analytic expressions [140] to reproduce the uncertainties for the energy range between approximately 10 and a few hundred GeV.

The standard deviation of the neutrino-antineutrino flux ratio is analytically parametrised using the expression

$$F_{\nu_\alpha/\bar{\nu}_\alpha}(E_\nu, \cos\theta_z) = A^{avg}_{\nu_\alpha/\bar{\nu}_\alpha}(E_\nu) - A^{shape}_{\nu_\alpha/\bar{\nu}_\alpha}(E_\nu)\left(\frac{k_1}{\sqrt{2\pi\sigma^2}} e^{-\frac{\cos^2\theta_z}{2\sigma^2}} - k_2\right), \qquad (5.23)$$

where $A^{avg}_{\nu_\alpha/\bar{\nu}_\alpha}$ and $A^{shape}_{\nu_\alpha/\bar{\nu}_\alpha}$ characterise the energy dependence of the average uncertainty amplitude and its $\cos\theta_z$ dependence, respectively; the parameters $k_1$ and $k_2$ are chosen individually for each neutrino flavour to reproduce the uncertainties from [139].

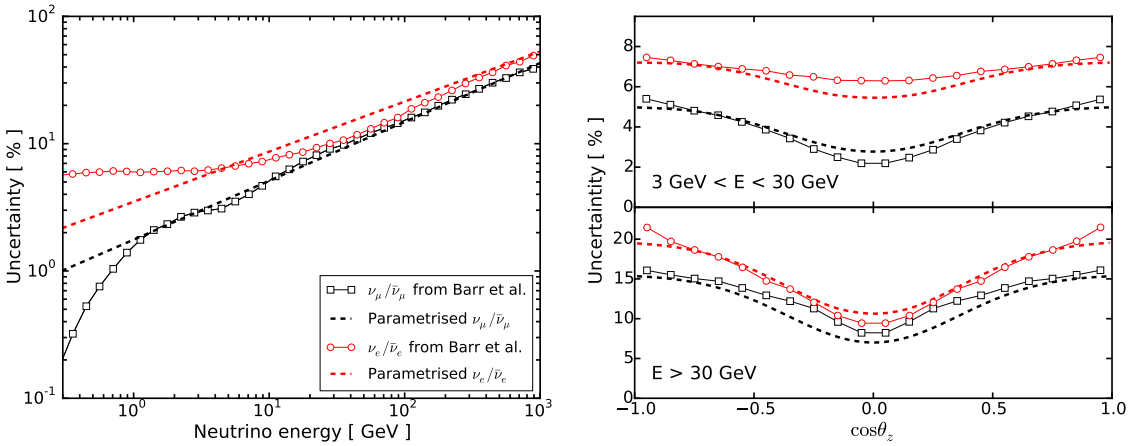


Figure 5.16: (Left) The uncertainty on the neutrino-antineutrino flux ratio for muon (black) and electron (red) neutrinos as a function of energy. The markers depict the uncertainties provided in [139], while dashed lines show the parametrisations used in this work. (Right) The zenith dependence of the neutrino-antineutrino flux ratios for energy range between 3 and 30 GeV and above 30 GeV.

The energy dependence of the uncertainties is parametrised in the form of a line in $\log_{10}$–$\log_{10}$ space as

$$A(E_\nu, E_{cutoff}) = 0.01 \cdot y_1 \cdot 10^{\left(\frac{\log_{10}(y_2/y_1)}{\log_{10}(E_2/E_1)} \log_{10}(E_\nu/E_1)\right)} \cdot \exp(-\frac{E_\nu}{E_{cutoff}}) \qquad (5.24)$$

where $y_1$, $y_2$ are the amplitudes of the uncertainties at $\log_{10} E_1$ and $\log_{10} E_2$, respectively; the exponential term corresponds to the energy cut-off $E_{cutoff}$ when it is used in the parametrisation. The numerical values used in Equations (5.23) and (5.24) for the $\nu_e$ and $\nu_\mu$ fluxes are listed in Table 5.4.

The uncertainties for the neutrino-antineutrino flux ratios arise from the same underlying hadronic processes connected to kaon production in the air showers [139]. Therefore, the $\nu_e$ and $\nu_\mu$ fluxes are modified in a correlated way. In this work, the impact is implemented through a change in neutrino weights as

$$w_k^{\nu_\alpha} = w_{k,0}^{\nu_\alpha} \cdot \left[1 + \left(\frac{\nu}{\bar{\nu}}\right) \cdot F_{\nu_\alpha/\bar{\nu}_\alpha}(E_\nu, \cos\theta_z)\right], \qquad (5.25)$$

where $w_k^{\nu_\alpha}$ is a new modified weight; $w_{k,0}^{\nu_\alpha}$ is the baseline weight; the parameter $(\nu/\bar{\nu})$ characterises the magnitude of the change and is equal 1 for $1\sigma$ deviation. The standard deviation parametrisations of the neutrino-antineutrino ratio as a function of neutrino energy and $\cos\theta_z$ are depicted in Figure 5.16.

**Upgoing-horizontal flux ratio**

The uncertainties in the neutrino-antineutrino flux ratio described in the previous paragraphs do not completely account for the $\cos\theta_z$ uncertainties of the electron neutrino flux from [139]. Therefore, an additional parameter is introduced to cover

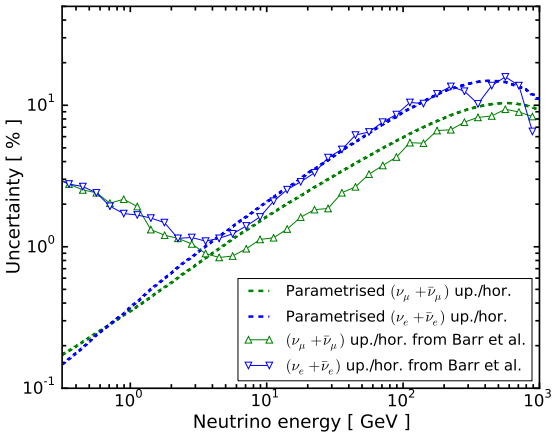


Figure 5.17: The uncertainty on the upgoing-horizontal flux ratio for $\nu_e$ (blue) and $\nu_\mu$ (green). The markers depict the uncertainties from [139], while dashed lines show the parametrisations used in this work.

it. The weight modification is applied to both neutrino and antineutrinos in a way similar to Equation (5.25):

$$w_k = w_{k,0} \cdot \left[1 + \left(\frac{up}{hor}\right) \cdot F_{up/hor}(E_\nu, \cos\theta_z)\right], \tag{5.26}$$

where $F_{up/hor}$ is parametrised in the same way as Equation (5.23). The full parametrisation of the uncertainty for the upgoing-horizontal flux ratios compared to [139] is depicted in Figure 5.17. The numerical values for the parameters are given in Table 5.4.

### 5.5.3 Cross-section uncertainties

The cross-section uncertainties in this work are mainly estimated by GENIE [31], which is used for the neutrino interaction simulation described in Section 5.1.2. They

Table 5.4: Numerical values for the parameters used to parametrise uncertainties for the neutrino-antineutrino and upgoing-horizontal flux ratios.

| Flavour | Factor | $\log_{10} E_1$ | $\log_{10} E_2$ | $y_1$ | $y_2$ | $E_{cutoff}$ | $k_1$ | $k_2$ | $\sigma$ |
|---|---|---|---|---|---|---|---|---|---|
| **Neutrino-antineutrino ratio** | | | | | | | | | |
| $\nu_e$, $\bar{\nu}_e$ | $A^{avg}_{\nu_e/\bar{\nu}_e}$ | 0.5 | 3.0 | 5.5 | 53 | – | 1.5 | 0.7 | 0.36 |
| | $A^{shape}_{\nu_e/\bar{\nu}_e}$ | 0.5 | 2.0 | 0.9 | 10 | 650 | | | |
| $\nu_\mu$, $\bar{\nu}_\mu$ | $A^{avg}_{\nu_\mu/\bar{\nu}_\mu}$ | 0.5 | 3.0 | 3 | 43 | – | 2.5 | 1.5 | 0.36 |
| | $A^{shape}_{\nu_\mu/\bar{\nu}_\mu}$ | 0.5 | 2.0 | 0.6 | 5 | 1000 | | | |
| **Upgoing-horizontal ratio** | | | | | | | | | |
| $\nu_e$, $\bar{\nu}_e$ | $A^{shape}_{up/hor,\nu_e}$ | 0.5 | 2.0 | 0.9 | 10 | 650 | 0.3 | 0 | 0.35 |

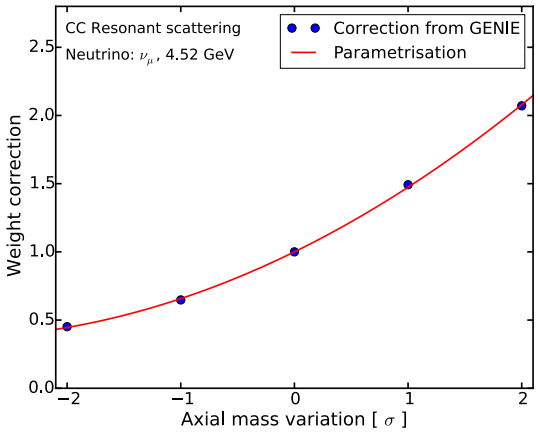


Figure 5.18: An example of the weight parametrisation (red line) for the axial mass correction factors (blue data points) from GENIE [31].

are treated in the way as discussed in this section.

**Quasi-elastic and resonant axial masses**
As discussed in Section 2.5, the quasi-elastic and resonant neutrino cross-sections can be parametrised using the axial masses. For CC quasi-elastic scattering, the axial mass has a value of $M_A^{CCQE} = 0.99$ GeV with an asymmetric uncertainty of +25%/–15%. For the CC resonant production, its value is $M_A^{CCRES} = 1.12$ GeV with an uncertainty of ±20%. In this work, the correction to the event cross-section is calculated by GENIE [31] for deviations between $-2\sigma$ and $+2\sigma$, with $1\sigma$ step. The intermediate values are obtained by fitting a second-degree polynomial through the GENIE correction coefficients, as shown in Figure 5.18.

**NC normalisation**
To take into account possible uncertainties of the hadronisation processes in the NC interactions, the normalisation of the NC events is free with a 20% Gaussian prior.

### 5.5.4 Detector uncertainties

The uncertainties in the detector properties are among the most important sources of systematic uncertainties in this work. The production of many simulations to cover all possible values of the detector parameters is not computationally feasible. Instead, their impact is estimated from a limited number of systematic simulation sets, where each set includes a full MC simulation of the given detector parameters. The procedure for the treatment of the detector uncertainties, and the corresponding parameters are discussed in this section.

**Treatment of discrete parameters**
In this work, the impact of systematic uncertainties is parametrised from the MC

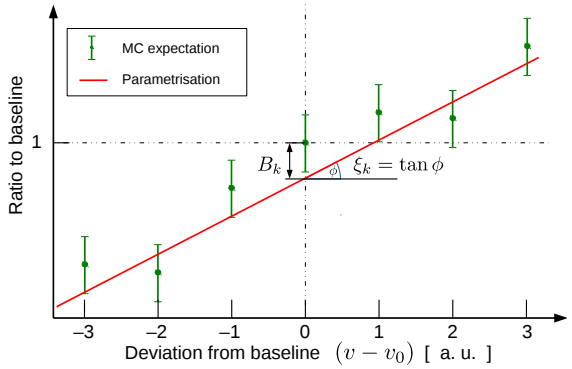


Figure 5.19: A schematic example of the parametrisation used for the treatment of discrete systematic uncertainties in the case of only one variable. The green data points represent the expected ratio of the MC prediction to the baseline MC simulation with errors coming from the MC statistics, while the red line shows the fitted parametrisation.

systematic sets, where each set simulates modified detector parameters. Unlike other parameters, the impact of a given detector systematic parameter is applied as an event rate modification at the histogram level. This means that the event expectation for each experimental bin is scaled according to the pre-calculated expected impact of the detector systematic parameter on this bin.

For each bin, the modification of the event rate is calculated for every systematic MC set. These values are then fitted for every bin using a line or multidimensional plane (depending on the number of parameters) as

$$A_k^{det}(\vec{v}) = B_k + \sum_{i=0}^{n_{par}} \xi_k^i \cdot (v^i - v_0^i), \tag{5.27}$$

where $v^i$ and $v_0^i$ is a systematic parameter and its baseline value, respectively; $B_k$ and $\xi_k^i$ are the fitted coefficients for $k$th experimental bin. The parameter $B_k$ accounts for the finite statistics of the MC simulations and incorporates the information from the independent systematic sets. This leads to an effective decrease of the MC statistical uncertainties and an increase in precision of the extracted parametrisations. Figure 5.19 shows a schematic example of such a parametrisation for one systematic parameter and the meaning of the parameters from Equation (5.27). These parametrisations are calculated separately for 4 interaction types: $\nu_e$, $\nu_\mu$, $\nu_\tau$ CC interactions and NC interactions of all flavours. Figure 5.20 shows the examples of the parametrisation projections for the parameters discussed in the following paragraphs.

**DOM efficiency**

Recent calibration studies have constrained the DOM optical efficiency with a precision of approximately 10%. Therefore, seven MC sets with 88, 94, 97, 100, 103, 106, 112% of the nominal DOM efficiency are used in this work to estimate the impact of this parameter. The example projections of the multiplane parametrisations for 4 experimental bins of $\nu_\mu$ CC interactions are shown in the top left part of Figure 5.20.

**Hole ice properties**

The properties of the hole ice, discussed in Sections 4.4.4 and 5.1.5, change the DOM acceptance as a function of the photon arrival direction. In this work, its impact is simulated by the effective DOM angular acceptance curves defined in Equation (5.1) and discussed in Section 5.1.5. It has two free parameters, which are denoted as $p_1$ and $p_2$ and have the baseline values of $p_1 = 0.25$ and $p_2 = 0$. Five values of $p_1$ in the range [0.15, 0.35] cover the expected uncertainty range for this parameter. The uncertainties of the forward acceptance parameter $p_2$ are estimated from 6 MC sets covering the values –5, –3, –1, 0, 1 and 2. The examples of the hole ice parametrisations are shown in the top right and bottom left parts of Figure 5.20.

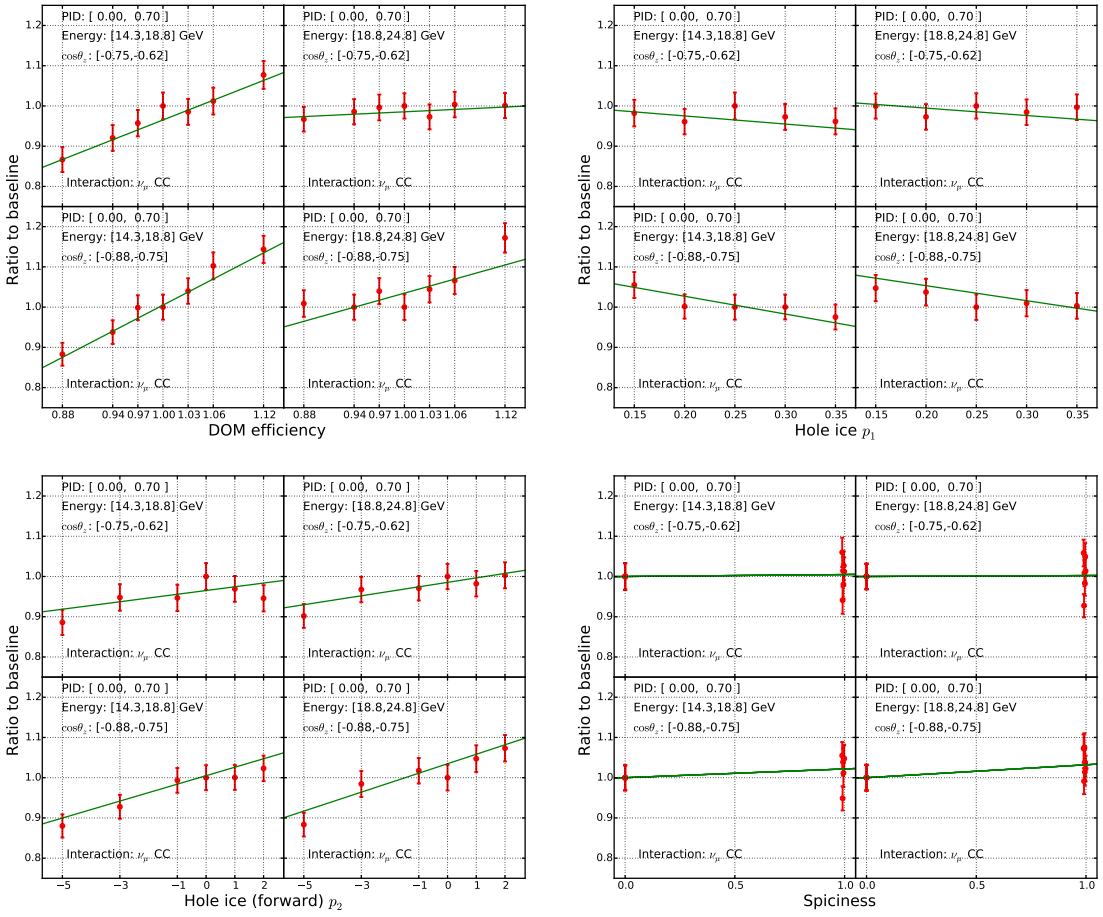


Figure 5.20: Examples of the parametrisations used to treat the impact of the discrete detector parameters for the DOM efficiency (top left), hole ice $p_1$ (top right), hole ice forward acceptance $p_2$ (bottom left) and *spiciness* (bottom right). The red circles depict the ratios of the expectation of the modified parameter, relative to the baseline MC expectation. The error bars show the MC statistical uncertainty. The green lines depict the projections of the multiplane parametrisations in Equation (5.27) on the corresponding parameter.

**Alternative hole ice modelling**
The DOM angular acceptance curves are the effective parametrisation of the hole ice impact. However, this approach simulates only the average effects and does not account for possible time and scattering differences that are expected for photons emitted at different distances from DOMs. A new simulation technique [141] is developed to directly model photon scattering in the bubble columns with variable sizes and optical properties. A new parameter with name *spiciness*[1] is introduced in this work to account for a possible impact of the mismodelling of the light propagation through the bubble columns. This parameter is designed to account only for the impact, which cannot be covered by other detector uncertainties. Therefore, the detector parameters, described in the previous paragraphs, are first estimated for the new simulation sets, and the remaining differences are then included to the parametrisations in Equation (5.27). The baseline simulation with the effective angular acceptance treatment is assigned the spiciness value of 0, while the simulations with a new hole ice treatment have the value of 1. The impact is estimated from 6 MC sets, which cover the bubble column diameters between approximately 20 cm and 1.8 m with the scattering lengths between 10 cm and 1.7 m. The bottom right panel of Figure 5.20 shows the examples of the spiciness parametrisations for 4 experimental bins for $\nu_\mu$ CC interactions.

### 5.5.5 Background

A few sources of background are considered in this work and are discussed below.

**Atmospheric muons**
The rate of atmospheric muons is many orders of magnitude higher than the rate of atmospheric neutrinos. The event selection used in this work successfully removes most of them. However, acceptance of even a small fraction of muons can result in a significant contamination of the sample. The data-driven template explained in Section 5.3.2 is used to account for a possible muon background. Its normalisation is free, since currently there are no sufficient atmospheric muon simulations available for making a reliable estimate of the background rate.

**Detector noise**
Every DOM in IceCube has a noise rate of about 600-700 $s^{-1}$ and accidental chance might trigger the detector. The strict selection of the direct photons and the event quality cuts reduce the rate from noise-only events to a negligible level. Therefore, this background is not considered any further in this work.

[1] An internal IceCube codename

# Chapter 6

# Measurement of the standard atmospheric neutrino mixing

This chapter discusses the procedure and the results of the standard atmospheric neutrino oscillation measurement. It starts with an overview of the analysis, followed by the checks performed before the data unblinding. Then the data stability and the agreement between the data and simulations are discussed. Finally, the results of the study with 6 years of data and additional checks are reported.

## 6.1 Analysis overview

This section discusses the observables, binning, expected signatures of the atmospheric neutrino oscillations and the fit parameters used in this study.

### 6.1.1 Data sample and expected signature

This analysis uses the detector data taken between May 2011 and May 2017, resulting in 35212 events at the analysis level. Only the data from the stable data-taking runs with at least 85 operating strings are used, resulting in an effective live time of about 5.8 years. The reconstructed energy ($E_{reco}$), cosine of zenith ($\cos\theta_Z$) and particle identification score (PID) are used as observables for each event.

This analysis uses the events in the energy range between approximately 6 and 158 GeV. The left part of Figure 6.1 shows the energy distribution from the data and the contributions from different interaction types. The shape of the distribution is characterised by a combination of a steeply falling power-law spectrum, the neutrino detection energy threshold and neutrino oscillation effects.

Only up-going events are used in the analysis to reduce the contamination from atmospheric muons, as discussed in Section 5.3. The reconstructed $\cos\theta_z$ distribution of the data and the contributions from different interactions are depicted in the right panel of Figure 6.1. It shows a slight increase of the data rate at $\cos\theta_Z \sim -0.75$, which is caused by a directional reconstruction algorithm failing to find a preferred direction for some events resulting in a zenith angle reconstructed

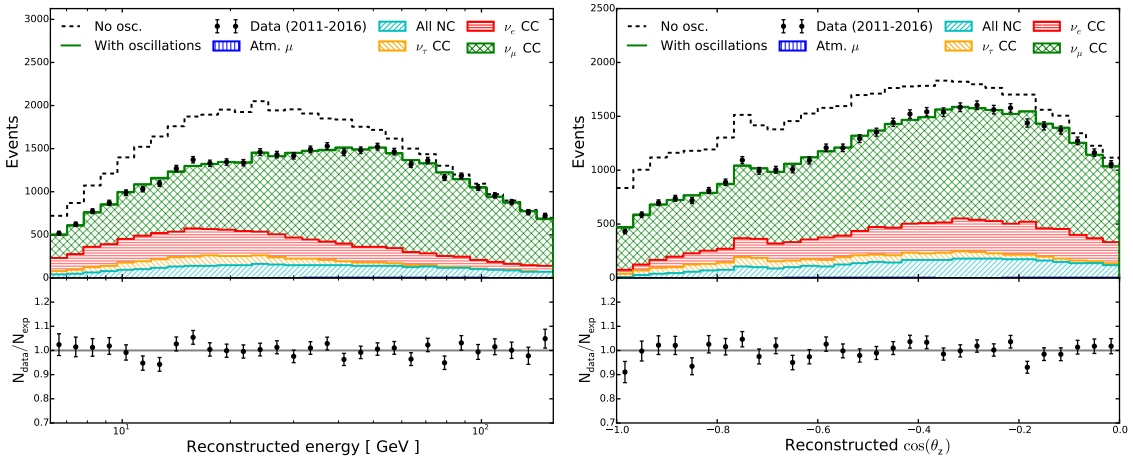


Figure 6.1: The distributions of the reconstructed energy (left) and zenith angle (right) for the no-oscillation hypothesis (dashed black line) and the best-fit of this study (green line). The filled areas show the contributions from CC interactions of $\nu_\mu$ (green), $\nu_e$ (red), $\nu_\tau$ (orange), NC interactions of all neutrinos (cyan) and atmospheric muons (blue). The bottom panels show the ratios between the data and the best-fit expectations.

close to the Cherenkov angle in ice. The neutrino oscillations result in the suppression of the rate for neutrinos crossing the Earth, while horizontal events are practically not affected.

The distributions of the PID score for the data and contributions from different interactions are shown in Figure 6.2. The data are split into the *track channel* with PID $\in [0, 0.7)$ and the *cascade channel* with PID $\in [0.7, +\infty)$. Events in the track channel are identified to have muon tracks from $\nu_\mu$ CC interactions and typically have better directional resolutions. The cascade channel has events without iden-

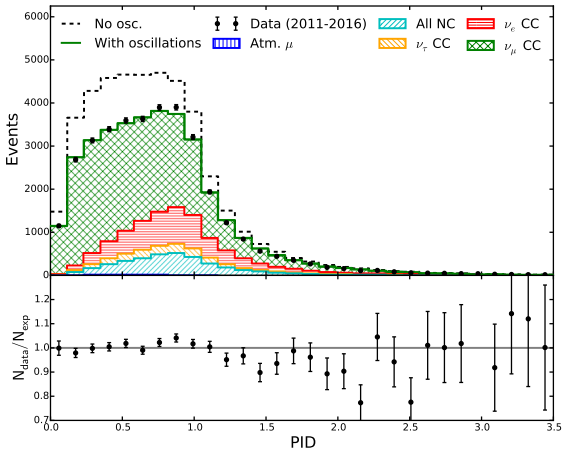


Figure 6.2: The PID distribution without oscillations (dashed black line), for the best-fit (green line) and the data. The filled areas show the contributions from CC interactions of $\nu_\mu$ (green), $\nu_e$ (red), $\nu_\tau$ (orange), NC interactions of all neutrinos (cyan) and atmospheric muons (blue). The bottom panel shows the ratio between data and the best-fit expectation.

Table 6.1: The number of events in the event sample that originate from different interaction types. The estimates are obtained from the simulations and the data-driven background template at the best-fit point of this study (see Table 6.2 and Section 6.4). The numbers in parentheses show the event expectation for the no-oscillation hypothesis.

| **Component** | **Track channel** | **Cascade channel** | **Total** |
|---|---|---|---|
| $\nu_\mu$ CC | 13680.0 (19578.3) | 9999.8 (14235.5) | 23679.8 (33813.8) |
| $\nu_e$ CC | 1992.5 (1927.2) | 4108.2 (3973.0) | 6100.7 (5900.2) |
| $\nu_\tau$ CC | 633.1 (0) | 1017.7 (0) | 1650.8 (0) |
| All $\nu$ NC | 1165.5 (1165.5) | 2434.7 (2434.7) | 3600.2 (3600.2) |
| Atm. $\mu$ | 128.5 | 52.0 | 180.5 |
| Total, sim., best fit | 17599.5 (22799.5) | 17612.5 (20695.2) | 35212.0 (43494.7) |
| Total, data | 17580 | 17632 | 35212 |

tified tracks. Such events typically have worse resolutions, but provide important information to constrain the impact of the systematic uncertainties.

The track channel comprises 17580 events, while the cascade channel has 17632 events. Table 6.1 shows the contributions of the different interaction types to the data. The track channel has approximately 78% of the events originating from $\nu_\mu$ CC interactions, while for cascade channel this fraction is only 57%. Interactions producing only showers contribute approximately 21% of the event count in the track channel and 43% in the cascade channel. These fractions are estimated for the best-fit parameters of this analysis, which are discussed in Section 6.4.

The resulting data are split in 176 bins in the reconstructed energy, zenith and PID. The reconstructed energy is split into 11 bins: the low energy part of the spectrum has 8 logarithmic bins between $10^{0.8}$ and $10^{1.75}$ GeV, while the high energy part adds 3 extra bins between $10^{1.75}$ and $10^{2.2}$ GeV. The reconstructed $\cos\theta_z$ is split

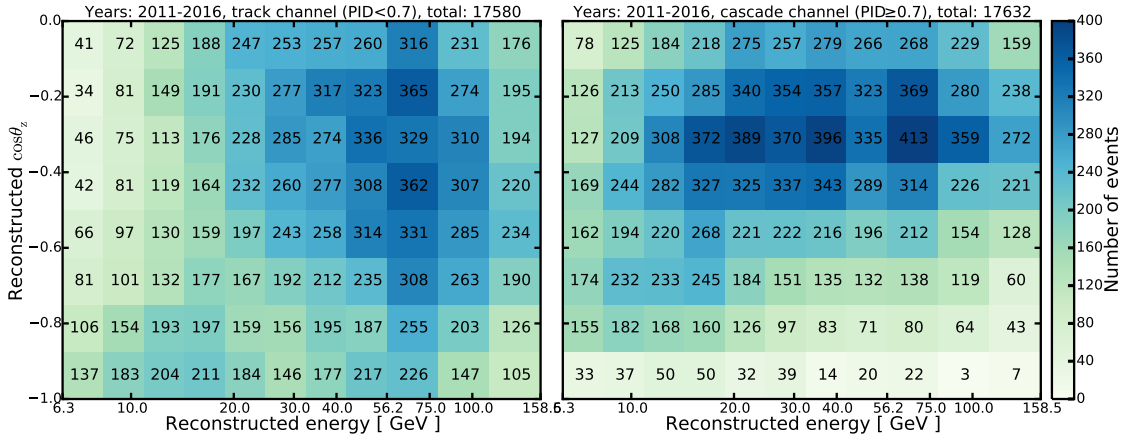


Figure 6.3: The number of events in 6 years of data in the track (left) and cascade (right) channels as used in the analysis.

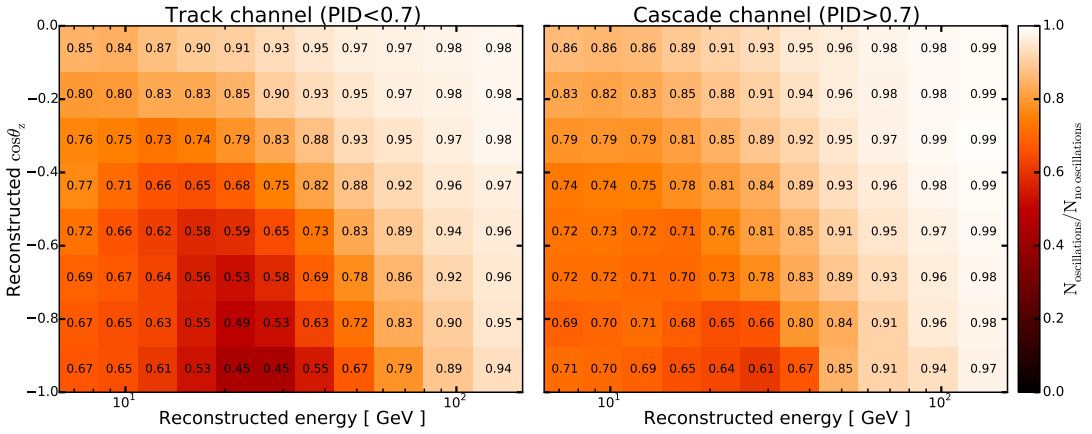


Figure 6.4: The expected neutrino oscillation effects on the track (left) and cascade (right) channels for the binning used in this analysis. The values $\Delta m^2_{32} = 2.515 \cdot 10^{-3}$ eV$^2$ and $\sin^2\theta_{23} = 0.5$ are used.

into 8 bins in the range between –1 and 0. The size of the bins is selected based on the expected energy and zenith resolutions. As stated earlier, the data are split into two channels based on the PID value. The event counts for all 176 bins used in this analysis are shown in Figure 6.3.

The effects of the atmospheric neutrino oscillations for the observables are shown in Figure 6.1 and 6.2. The expected effect in the full experimental binning is depicted in Figure 6.4. For maximal mixing ($\sin^2\theta_{23} = 0.5$), the expected reduction of the event rate in the track channel is about 55% for up-going events with energies between 20 and 30 GeV, while for the cascade channel the effect is only 40%. The oscillation minimum is better localised in the track channel due to better resolutions and a higher $\nu_\mu$ purity, while in the cascade channel it is more smeared. Only a few percent reduction of the rate is expected for horizontal events with energies above 60 GeV. As discussed in Section 3.4, the energy of the maximal muon neutrino disappearance is proportional to $\Delta m^2_{32}$, while the mixing angle $\theta_{23}$ modifies its amplitude. The impact of these parameters on the shape of the histograms can be found in Appendix A.1.

### 6.1.2 Fit parameters

This analysis has 14 free parameters listed in Table 6.2. Two of them are the neutrino mixing parameters $\Delta m^2_{32}$ and $\sin^2\theta_{23}$, which are the focus of this study. The fit is performed with the normal neutrino mass ordering $\Delta m^2_{32} > 0$ and the inverted ordering is not considered[1]. The value of the CP-violating phase $\delta_{CP}$ is fixed to zero, while other parameters are fixed to the global best-fit values from [23]. The calculation of neutrino oscillation probabilities is performed by the algorithm

[1]Based on other studies in IceCube, this analysis is expected to have no sensitivity to the neutrino mass ordering.

Table 6.2: The list of the parameters used in this study, their baseline values, priors (if applied) and the best-fit estimates (see Section 6.4). The uncertainties for the nuisance parameters are obtained from MINUIT, while the uncertainties for the atmospheric mixing parameters are calculated from the likelihood profiles.

| **Parameter** | **Baseline** | **Prior** | **Best fit $\pm 1\sigma$** |
|---|---|---|---|
| **Oscillations parameters** | | | |
| $\Delta m^2_{32}$ [ $10^{-3}$ eV$^2$ ] | none | none | $2.54^{+0.11}_{-0.12}$ |
| $\sin^2\theta_{23}$ | none | none | 0.51±0.05 |
| **Flux parameters** | | | |
| $\nu_e$ norm. | 1.0 | $1.00 \pm 0.05$ | 1.008±0.049 |
| $\Delta\gamma$ | 0.05 | none | 0.057±0.028 |
| $(\nu/\bar{\nu})$ [ $\sigma$ ] | 0 | $0 \pm 1$ | 0.64±0.51 |
| (up./hor.) [ $\sigma$ ] | 0 | $0 \pm 1$ | 0.086±0.98 |
| **Detector parameters** | | | |
| DOM eff. [ % ] | 100 | $100 \pm 10$ | 98.6±3.0 |
| Hole ice $p_1$ | 0.25 | $0.25 \pm 0.1$ | 0.265±0.039 |
| Hole ice $p_2$ | 0 | none | 0.89±0.45 |
| spiciness | 0 | none | 0.42±0.32 |
| **Cross section** | | | |
| NC norm. [ % ] | 100 | $100 \pm 20$ | 91±14 |
| $M_A^{CCQE}$ [ GeV ] | 0.99 | $0.99^{+0.25}_{-0.15}$ | $0.96^{+0.24}_{-0.14}$ |
| $M_A^{CCRES}$ [ GeV ] | 1.12 | $1.12 \pm 0.22$ | $1.07 \pm 0.17$ |
| **Background** | | | |
| Atm. $\mu$. frac. [ % ] | none | none | $0.5^{+1.2}_{-0.5}$ |

from [60, 61] in the standard three-neutrino mixing model using PREM [142] as the matter profile of the Earth.

The 12 nuisance parameters accounting for systematic uncertainties are split into 4 groups: flux, detector, cross-section and background uncertainties, as listed in Table 6.2. A detailed discussion of each parameter can be found in Section 5.4. Some of the parameters have Gaussian priors, as listed in Table 6.2. The priors come from independent measurements or uncertainties in the model predictions.

Figure 6.5 shows the correlations between the fit parameters. A large correlation of a parameter with the mixing parameters results in a larger impact of this parameter on the sensitivity. In particular, the largest correlation is observed between $\Delta m^2_{32}$ and DOM efficiency, which is the leading systematic uncertainty for this analysis, as is discussed in the next sections. The impacts of each parameter on the experimental histograms can be found in Appendix A.1.

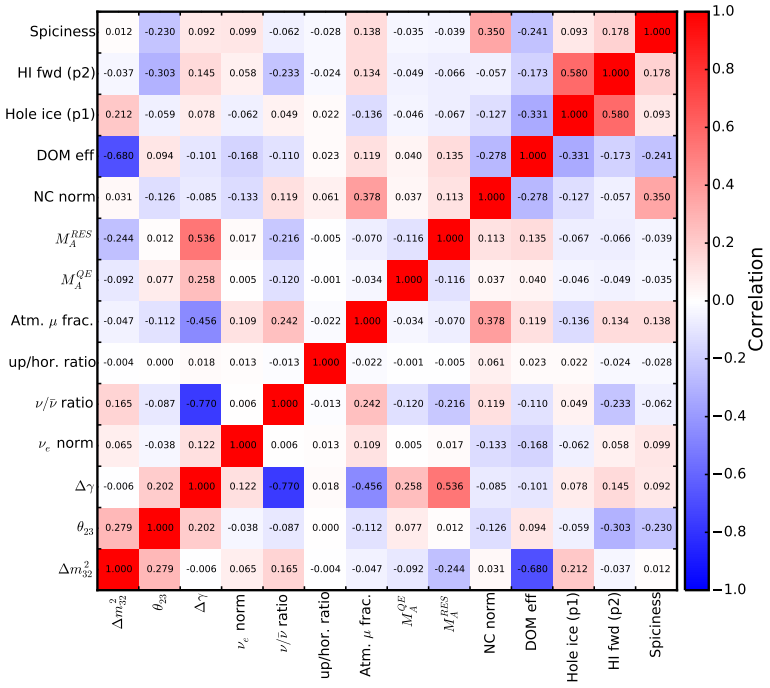


Figure 6.5: Correlations between the fit parameters in the measurement of the standard atmospheric neutrino oscillations.

## 6.2 Analysis checks

According to the IceCube internal regulations, the analysis is performed in a *blind way* to avoid biases of the final results. This means that sensitivity estimations, studies of the systematic uncertainties and other aspects of the analysis are only performed with simulations or in a way that does not reveal any of the fit parameters. The key checks and studies that were performed before the *unblinding* are presented in this section.

### 6.2.1 Minimisation performance

This work uses the MIGRAD minimisation routine from the MINUIT [143] package as implemented in [144]. One of the essential checks to perform before fitting the data is to ensure that the minimiser is capable of finding the true minimum in a complicated, multidimensional likelihood space. In this study, this was checked by injecting 143 different realisations of the physics parameters, as shown in the left part of Figure 6.6. The starting values for fit parameters are set approximately $1\sigma$ away from the injected or baseline values[2].

The minimiser successfully recovers the injected values with a precision sufficient for this work. The right part of Figure 6.6 shows the minimisation performance for

[2]For the parameters without priors, the fit started at random value corresponding to an approximately $1\sigma$ deviation expected in the analysis.

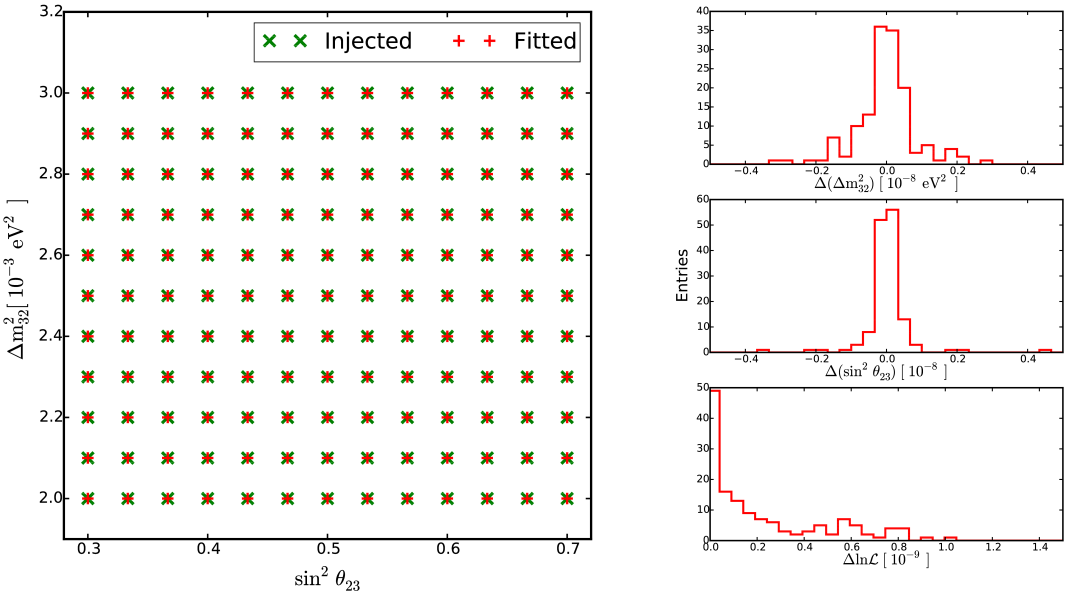


Figure 6.6: The minimisation performance in the muon neutrino disappearance analysis. The left panel depicts the injected (green) and fitted (red) values of the mixing parameters. The minimisation precisions for $\Delta m^2_{32}$ and $\sin^2\theta_{23}$ are shown in the top and middle right panels, respectively. The bottom right panel shows the difference between the minimised and true log-likelihood value.

the atmospheric mixing parameters and the precision of finding the true likelihood value. The nuisance parameters are also well recovered with deviations smaller than $10^{-6}$ from the injected values.

### 6.2.2 Test statistic distribution

The Wilks' theorem [138] is used to set the confidence levels in this work. It states that for this analysis the $-2\Delta\ln\mathcal{L}$ test statistic (TS) should follow a chi-squared distribution with 2 degrees of freedom (d.o.f.). However, the Wilks' theorem provides an accurate estimate of confidence levels only in the absence of boundaries. The effects of the atmospheric neutrino oscillations are proportional to $\sin^2 2\theta_{23}$, while the parametrisation of the PMNS matrix is done in terms of the angle $\theta_{23}$. This means that there is an effective boundary at $\theta_{23} = 45°$ ($\sin^2\theta_{23} = 0.5$), where the muon neutrino disappearance effect is maximal. The impact of this boundary is tested using statistical pseudo-trials obtained through the Poisson fluctuations of the total baseline event expectation. The standard analysis procedure is then applied to the resulting histograms. For each of the realisations discussed here at least 2000 statistical trials were created.

The pseudo-trials are generated with different injected values for $\sin^2\theta_{23}$ to study the impact of the boundary. The resulting distributions of the TS are presented in

the left panel of Figure 6.7. If the $\theta_{23}$ value is injected at maximal mixing, the TS follows $\chi^2$ with an effective number of d.o.f. closer to 1. The distribution is closer to $\chi^2$ with 2 d.o.f for values $\theta_{23}$ far from the boundary. The obtained coverage for the 90% C.L. critical value from the Wilks' theorem as a function of the injected $\sin^2\theta_{23}$ is presented in the right panel of Figure 6.7. At $\sin^2\theta_{23} = 0.5$ the coverage is almost 96% and decreases to the target coverage for $\sin^2\theta_{23} = 0.7$, if statistical uncertainties of the simulations are neglected.

This study is the first neutrino oscillation measurement that uses six years of IceCube DeepCore data. The minimal effective live time of the simulations is about 27 years and is observed in the off-signal region with horizontal, high energy $\nu_\mu$ CC interactions. For the signal region, this number is typically above 50 years. The impact of the MC statistical uncertainties is estimated using statistical pseudo-trials. The expectation for each trial is initially fluctuated according to the available statistics of the baseline MC set. The resulting expectation is then fluctuated according to the Poisson distribution. It is important to note that this procedure likely overestimates the MC statistical uncertainties, since the usage of the detector systematic sets decreases the effective statistical uncertainties of the simulations, but this effect is not trivial to quantify.

The expected impact of the MC statistical uncertainties on the neutrino mixing parameters is smaller than $0.3\sigma$, but it can affect the expected TS distribution. When MC statistical uncertainties are included, the coverage decreases by approximately 2% from the values obtained without MC statistical fluctuations.

Considering the expected value of $\sin^2\theta_{23}$, this analysis is likely to have an accurate coverage within $\pm 3\%$ for 90% C.L. It can be further improved using the Feldman-Cousins procedure [145]. However, this requires numerous statistical pseudo-trials across the full parameter space and is outside the scope of this study.

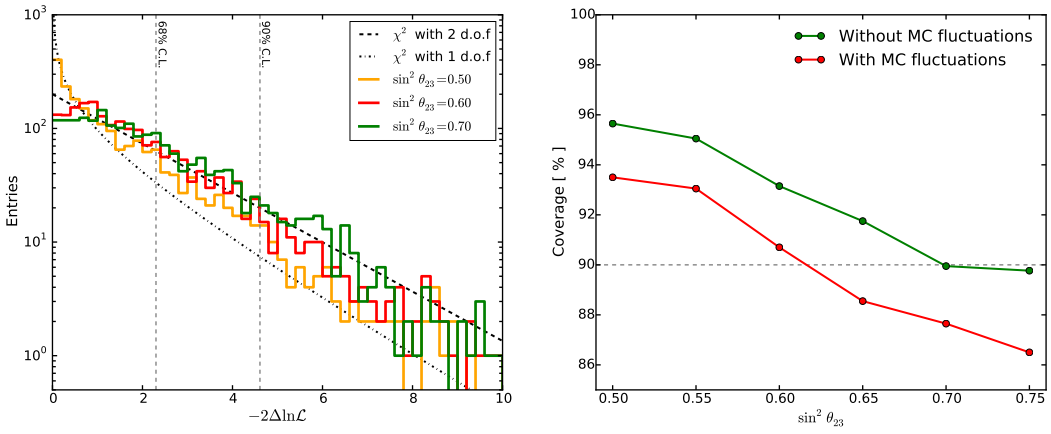


Figure 6.7: (Left) The test statistic distribution for different values of $\sin^2\theta_{23}$. (Right) The coverage from the pseudo-trials as a function of the injected $\sin^2\theta_{23}$. The green curve shows the coverage for pure Poisson fluctuations, while the red curve also includes the MC statistical fluctuations.

## 6.3 Expected sensitivity and impact of systematic uncertainties

The median sensitivity of this study is estimated using Asimov data-sets [146]. The expected sensitivity of this analysis to $\Delta m^2_{32}$ and $\sin^2\theta_{23}$ is depicted with black curves in Figure 6.8. Figure 6.8 also shows the sensitivity in the case of perfectly known systematic uncertainties.

The impact of systematic uncertainties on the sensitivity to $\Delta m^2_{32}$ is shown in the left part of Figure 6.9. The systematic uncertainties result in a 42% reduction in the sensitivity, with the detector parameters dominating this number. If the detector properties were known perfectly, the expected sensitivity would be 32% better. The DOM efficiency affects the overall energy scale of reconstructed neutrino events and, therefore, the precision of measuring the energy of the neutrino oscillation minimum. This explains a large correlation between the DOM efficiency and $\Delta m^2_{32}$, discussed in Section 6.1.2. It makes the DOM efficiency uncertainty the most important single systematic parameter, accounting for approximately 30% sensitivity degradation. The cross-section uncertainties lead to about 5% reduction of the sensitivity, and the flux uncertainties result in around 3% degradation.

The impact on the sensitivity to $\sin^2\theta_{23}$ is shown in the right panel of Figure 6.9. The systematic uncertainties lead to approximately 24% loss of sensitivity to mixing $\sin^2\theta_{23}$. Similarly to $\Delta m^2_{32}$, the leading contribution comes from the detector uncertainties, resulting in 13% degradation. The spiciness, hole ice $p_1$ and DOM efficiency account for approximately 4% degradation each. The flux and cross-section uncertainties lead to about 3% and 2% loss of the sensitivity, respectively.

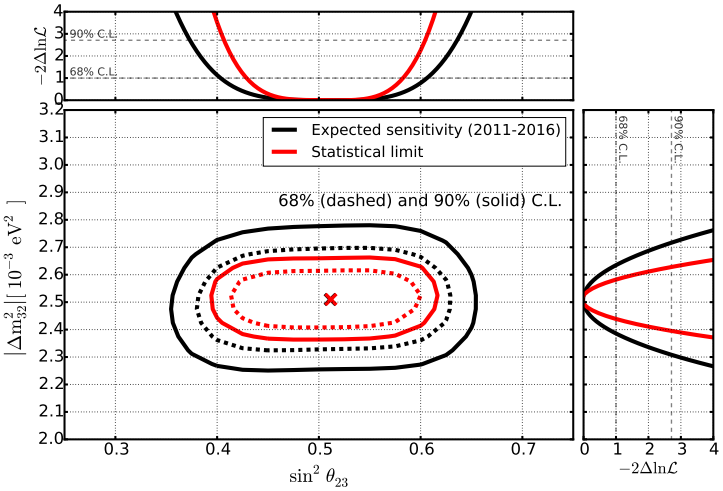


Figure 6.8: The expected sensitivity to $\Delta m^2_{32}$ and $\sin^2\theta_{23}$ of this study in case of only statistical uncertainties (red) and for the full treatment of the systematic uncertainties (black). The solid and dashed lines correspond to 90 and 68% C.L., respectively. The upper and the right panels depict the projected likelihoods for $\sin^2\theta_{23}$ and $\Delta m^2_{32}$, respectively.

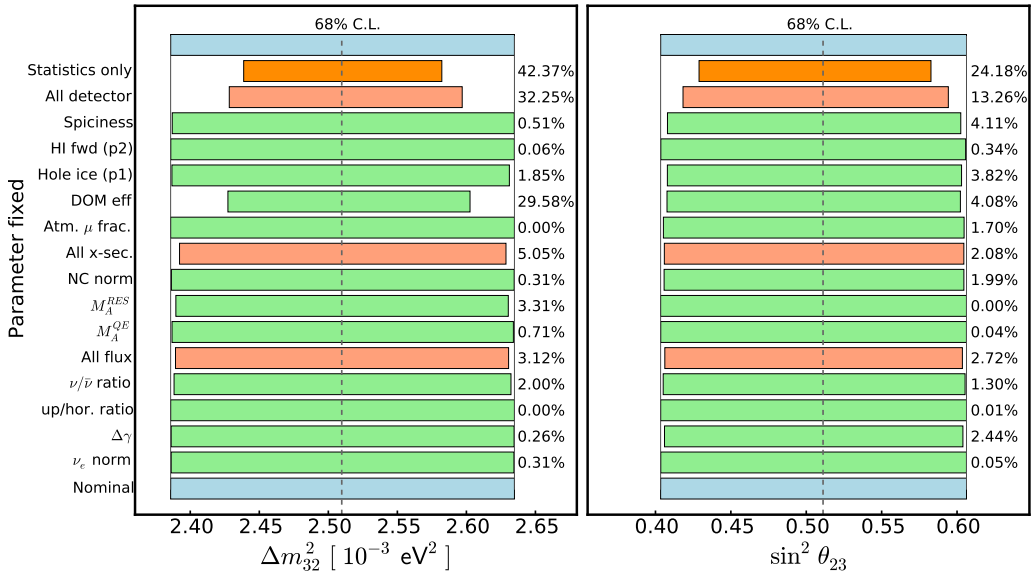


Figure 6.9: The expected 68% C.L. uncertainty (blue bars) for $\Delta m^2_{32}$ (left) and $\sin^2\theta_{23}$ (right). The orange bars depict the statistical limit, where all nuisance parameters are fixed, red and green bars show the expected uncertainty if the corresponding group or the single nuisance parameter are fixed. The percentages characterise the expected improvement of the sensitivity if the corresponding parameter is fixed.

## 6.4 Results

This section describes the results of the analysis. It starts with a discussion about the yearly stability of the data, followed by the information about the agreement between data and simulations. The best fit estimates of the atmospheric neutrino mixing parameters and obtained uncertainties are discussed at the end of this section.

### 6.4.1 Agreement between data-taking seasons

This study uses 6 years of data from the full 86-string IceCube DeepCore configuration. Each year of data taking, or *season*, starts in May. The first season used in this analysis is labelled IC86-1 and corresponds to the data taken between May 2011 and May 2012. The last season used in this work is IC86-6, which was taken between May 2016 and May 2017. The stability of the event rate as a function of time is shown in the left panel of Figure 6.10.

The rate for the IC86-5 and IC86-6 seasons is approximately 15% higher due to the updated DOM charge calibration. It affects the position of the peak in the SPE distribution (see Figure 5.4 in Section 5.1.5) resulting in approximately 4% change of an effective PMT gain. This change affects mainly the lower levels of the event selection chain, such as DeepCore Level 3 (see Section 5.3). The reconstruction algorithms used for this study rely on minimal charge information and use mainly hit or time information. The data are mostly unaffected by this calibration, except

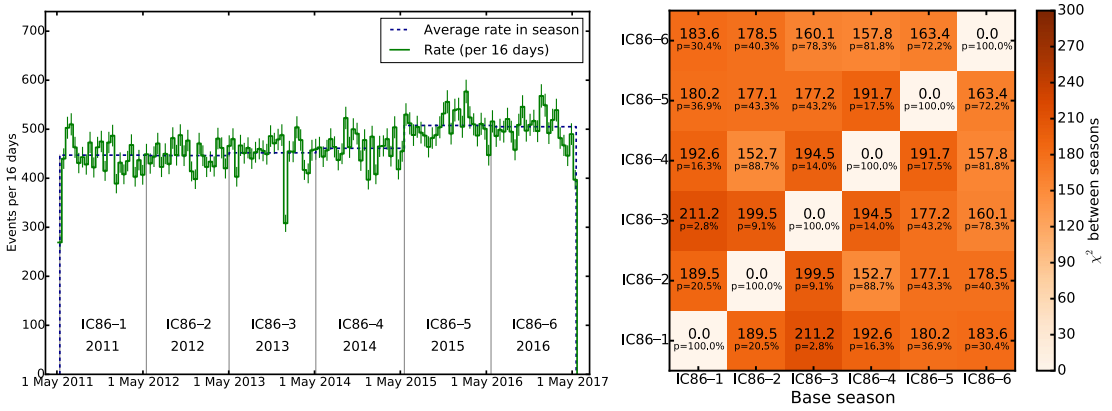


Figure 6.10: (Right) The event rate as a function of time and the average rate in the data taking seasons. (Left) The $\chi^2_{mod}$ value for the different seasons and the corresponding p-values.

for the overall scaling of the data rate. The compatibility between the seasons is estimated using the modified chi-squared value that ignores a change of the total normalisation. For example, for seasons 1 and 2, it is calculated as

$$\chi^2_{mod} = \sum_i \frac{(N_{i,1} - s \cdot N_{i,2})^2}{N_{i,1} + s^2 \cdot N_{i,2}}, \tag{6.1}$$

where $N_{i,k}$ represents the event counts in the $i$th bin of the histogram for the $k$th season. The factor $s$ renormalises the statistics to the equal event expectation, such that only the shapes are compared.

The $\chi^2_{mod}$ values between different seasons and the probabilities for such values to originate from statistical situations are shown in the right panel of Figure 6.10. The probabilities are estimated from the statistical pseudo-trials obtained from Poisson fluctuations of the averaged yearly rate. All years are found to be statistically consistent with each other. The lowest observed probability is about 2.8% and is observed between seasons IC86-1 and IC86-3. Such a value is expected considering the number of seasons compared to each other (15 realisations in total).

### 6.4.2 Agreement between data and expectations

The goodness of fit in this work is estimated using the Pearson $\chi^2$ test, defined as

$$\chi^2 = \sum_i \frac{(N_i - \mu_i)^2}{\mu_i}, \tag{6.2}$$

where $N_i$ and $\mu_i$ are the number of data events and the best-fit expectation in the $i$th bin of the histogram, respectively. There are 176 bins in the histogram and 14 fit parameters with eight priors in the analysis. Statistical pseudo-trials are used to

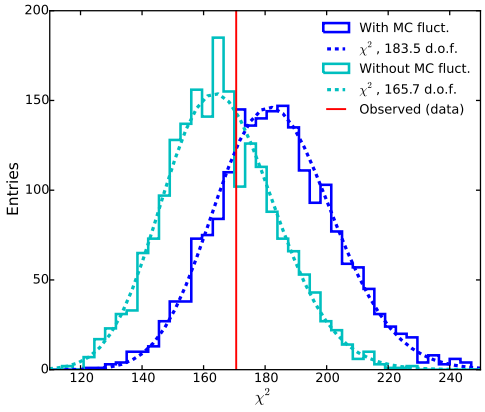


Figure 6.11: The expected Pearson $\chi^2$ distribution without (cyan) and with (blue) MC statistics taken into account. The observed value from the data is shown by the red line.

estimate the expected goodness-of-fit distribution in a way similar to Section 6.2.2. This procedure ensures that parameter correlations, boundaries and the sizes of priors are appropriately accounted to correctly estimate the effective number of d.o.f. The resulting distribution of the $\chi^2$ values is depicted in cyan in Figure 6.11. It follows the $\chi^2$ distribution with approximately 166 d.o.f..

The available live time of the simulations can result in a higher $\chi^2$ value during the fit. To estimate this impact, the expectation for each trial is initially fluctuated according to the available baseline MC statistics as explained in Section 6.2.2. The distribution of the obtained $\chi^2$ values is shown in blue in Figure 6.11. When including MC statistical uncertainties, the effective number of d.o.f. rises to the value of about 184.

The agreement between the data and expectations was checked in the *blind fit procedure*, where the data were fit with the standard fitting procedure, but the minimiser did not report the best-fit parameters. The obtained value is $\chi^2 = 170.6$. Using the $\chi^2$ distributions from Figure 6.11, the probabilities to obtain such a value from the statistical fluctuations are estimated at 36% and 74% when the MC sta-

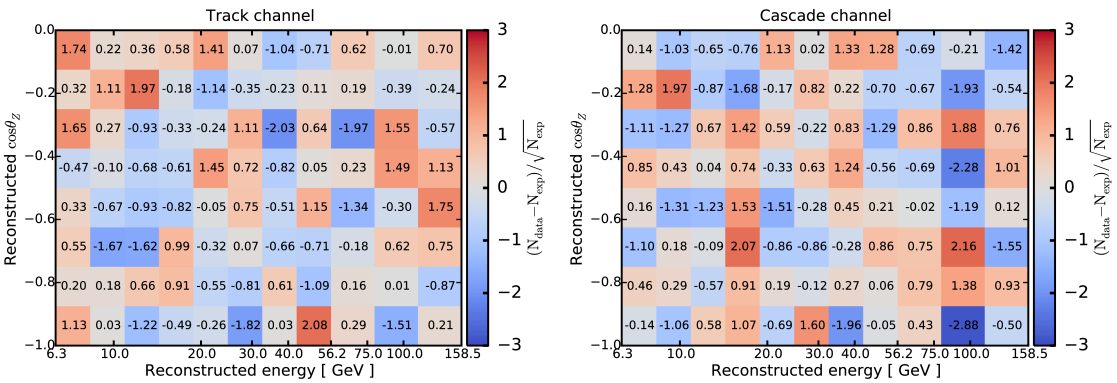


Figure 6.12: The statistical pulls between the data and the best-fit expectation for the track (left) and cascade (right) channels.

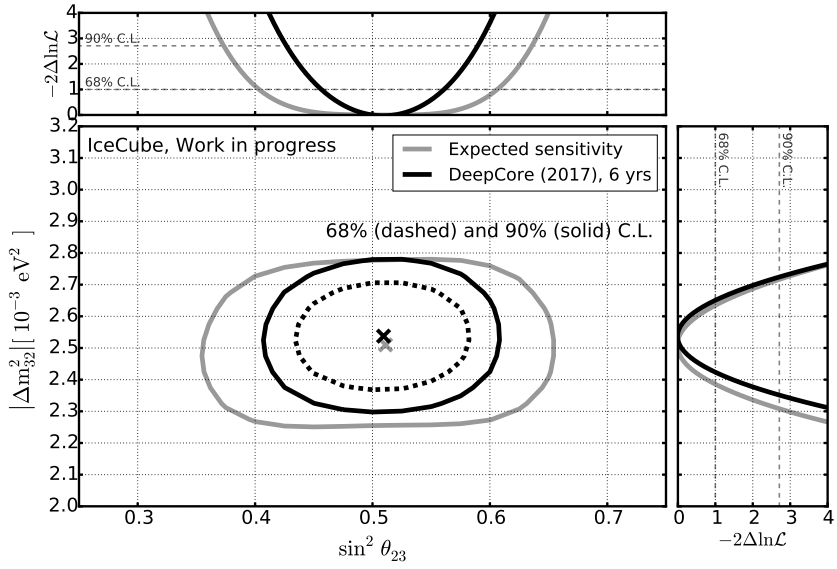


Figure 6.13: The results of the muon neutrino disappearance analysis (black). The cross shows the best fit value, while the dashed and solid lines represent 68% and 90% C.L. uncertainties, respectively. The grey lines show the expected sensitivity. The upper and right panels show the likelihood profiles for $\Delta m^2_{32}$ and $\sin^2\theta_{23}$, respectively.

tistical uncertainties are included and ignored, respectively. They demonstrate that the data and expectations are in good agreement. The statistical pulls between the data and the best-fit expectation are shown in Figure 6.12. They are distributed randomly in the experimental histograms. The agreement between the data and the best-fit expectations for each bin can be found in Appendix B.

### 6.4.3 Best-fit values and uncertainties

This study was unblinded, after the analysis procedure was checked and the agreement between the data and expectations was assured. The best estimates for the mixing parameters are

$$\begin{aligned} \Delta m^2_{32} &= 2.54^{+0.11}_{-0.12} \cdot 10^{-3}\ \text{eV}^2 \quad (68\%\ \text{C.L.}), \\ \sin^2\theta_{23} &= 0.51 \pm 0.05 \quad (68\%\ \text{C.L.}) \end{aligned} \tag{6.3}$$

where the uncertainties are obtained using the likelihood profiles, as explained in Section 5.4.2. As discussed earlier, the fit is performed in the normal ordering scenario with $m_3 > m_2 > m_1$ only. The best fit estimates for the nuisance parameters are listed in Table 6.2. The 68% and 90% C.L. allowed regions for the standard atmospheric mixing parameters are depicted in Figure 6.13. Figure 6.14 compares the observed likelihood profiles to the sensitivity and its statistical fluctuations. The observed likelihood profiles are found within the $2\sigma$ band expected from statistical fluctuations. The comparison of the obtained results to other experimental measurements of these mixing parameters is presented in Chapter 8.

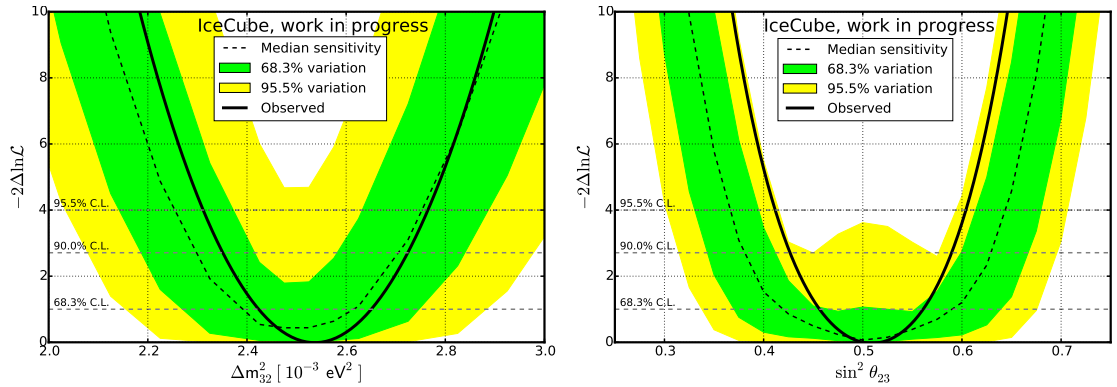


Figure 6.14: The likelihood profiles (black line) obtained for $\Delta m^2_{32}$ (left) and $\sin^2\theta_{23}$ (right). The expected median sensitivity obtained from pseudo-trials is shown with the grey dashed line, while 68.3% and 95.5% fluctuations of the sensitivity are depicted as the green and yellow bands, respectively.

## 6.5 Discussion

This section discusses the results presented in the previous section and the size of the obtained uncertainties. It starts with a discussion about the results using the two-neutrino approximation, followed by an explanation of the effects of the non-physical best-fit point on the expected $\sin^2\theta_{23}$ uncertainty. Additional systematic checks, performed after the analysis unblinding, are discussed at the end of this section.

### 6.5.1 Two-neutrino oscillation approximation

The observed uncertainty for $\sin^2\theta_{23}$ is found to be smaller than expected from the median sensitivity. This can happen when the data prefer the non-physical region requiring more disappearance than is allowed by the parametrisation of the PMNS matrix. This can be checked by fitting the data in the two-flavour model, as defined in Section 3.2.2. The parameter $\sin^2 2\theta_{23}$ is treated as the oscillation amplitude and represents non-physical mixing in the region where its value is greater than 1. Before the unblinding, this amplitude was checked to be within $2\sigma$ from the physical region, with $\sin^2 2\theta_{23} < 1.087$. After unblinding, the best estimate for this parameter is found to be

$$\sin^2 2\theta_{23} = 1.075. \tag{6.4}$$

The distribution of $\sin^2 2\theta_{23}$ obtained from the pseudo-trials and the value observed in the data are depicted in the left panel of Figure 6.15. Such a fluctuation into the non-physical region is expected from the statistical fluctuations in approximately 5.1% of the trials.

The test statistic difference, $-2\Delta\ln\mathcal{L}$, between the three-flavour fit and the non-physical two-flavour fit is 2.47, or a chi-squared difference $\Delta\chi^2$ is 2.98. This corresponds to a probability of between approximately 6% and 10%. The corresponding

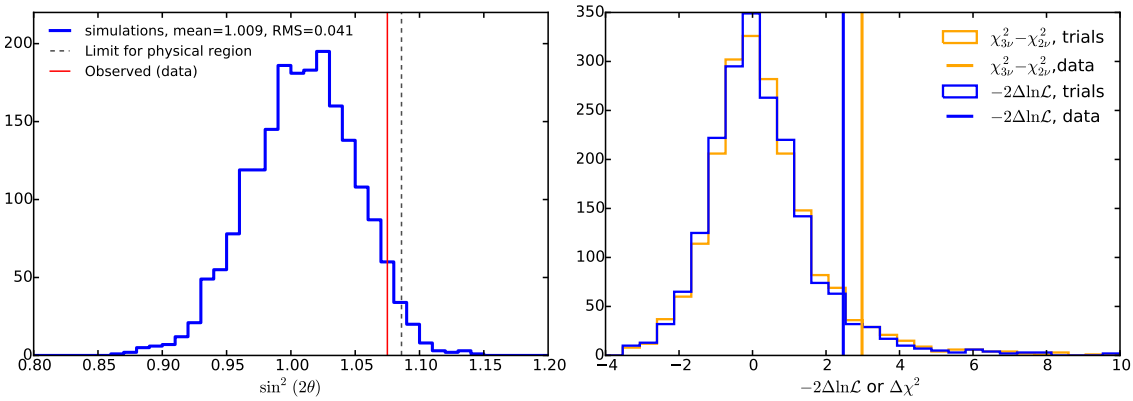


Figure 6.15: (Left) The expected distribution of $\sin^2 2\theta_{23}$ obtained from pseudo-trials. The vertical dashed line shows the $2\sigma$ boundary set in the blind fit procedure, while the red line depicts the value fit in the data. (Right) The $\chi^2$ (blue) and $-2\ln\mathcal{L}$ (yellow) difference between the fit in the three-neutrino model and two-neutrino model that allows non-physical fit. The vertical lines of the corresponding colours show the values obtained from the data.

distributions obtained from the pseudo-trials and the values observed with the data are shown in the right panel of Figure 6.15.

Figure 6.16 depicts the differences between the $\chi^2$ contributions in the physical three-flavour and the non-physical two-flavour fits for all experimental bins. More than 60% of the $\Delta\chi^2$ is coming from one bin in the track channel with $\cos\theta_z \in [-1, -0.875]$ and $E_\nu \in [24.76, 32.55]$ GeV, where the statistical pull improves from –1.82 to –1.21.

These results indicate that the non-physical best-fit value of $\sin^2 2\theta_{23}$ is likely caused by statistical fluctuations. However, more sources of systematic uncertainties

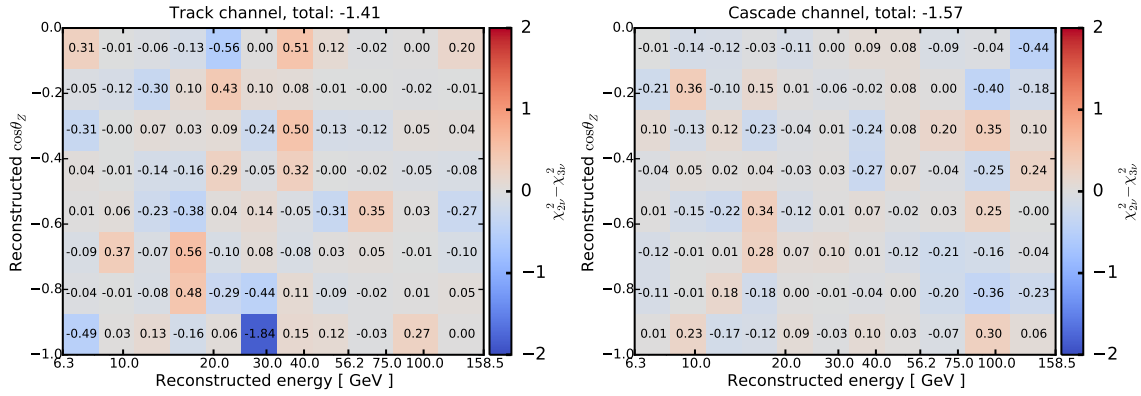


Figure 6.16: The difference between $\chi^2$ contributions for the non-physical two-flavour and the physical three-flavour fits. The left and right panels depict the track and cascade channels, respectively. Values below zero mean that the non-physical fit has a better agreement in the particular bin, while positive values indicate a worse agreement with the data.

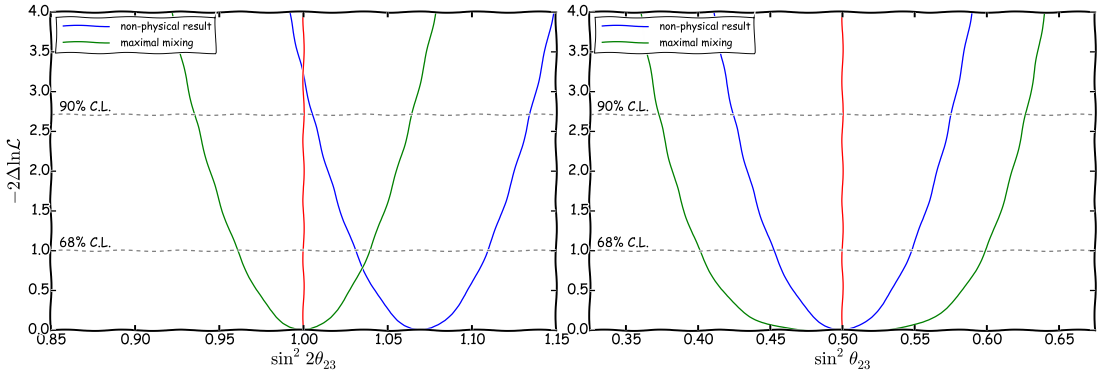


Figure 6.17: (Left) Example likelihood profiles for maximal (green) and non-physical (blue) values of $\sin^2 2\theta_{23}$. (Right) The same likelihood profiles projected on $\sin^2 \theta_{23}$.

are discussed in the next sections.

### 6.5.2 Physical and non-physical fits

The experimental resolutions, the event misidentification and the background contamination lead to a non-zero event expectation in the signal region even for the case of maximal $\theta_{23}$. Statistical underfluctuations or systematic effects can lead to a lower observed event count in the signal region or more events in the off-signal region. This forces the minimiser to compensate the observed fluctuations by pulling the value of $\sin^2 2\theta_{23}$ to the region larger than 1.

The likelihood profile, in this case, is expected to be a parabola as a function of $\sin^2 2\theta_{23}$, because the neutrino oscillation effects are proportional to this value. Examples of such profiles for the maximal and non-physical mixing are shown in the left panel of Figure 6.17. However, when this profile is recalculated to the $\sin^2 \theta_{23}$ parameter space, it changes its shape. Only the physical region is accessible by this parametrisation and both profiles are symmetric with respect to $\sin^2 \theta_{23} = 0.5$. When the data prefer the non-physical region, the likelihood rises faster than expected from the maximal mixing leading to smaller estimated uncertainties for $\sin^2 \theta_{23}$. This effect can be seen in the right panel of Figure 6.17, where the same likelihood profiles are projected onto the $\sin^2 \theta_{23}$ parameter space.

### 6.5.3 Additional systematic studies

The previous sections discussed that the fluctuation into the non-physical region can be expected from statistical fluctuations of the data. However, a variety of possible uncertainties are evaluated to check them as an explanation for the non-physical result.

#### Simulation statistics

The effect of the MC statistical uncertainties is tested using statistical pseudo-trials

obtained from the fluctuations of the maximal mixing expectation according to the available MC statistics. For 90% of the trials, the best fit lays between 0.986 and 1.024. Therefore, the expected uncertainties due to the MC statistics are not sufficient to cause any significant pull of the result into the non-physical region.

**Bulk ice model**

An improved bulk ice model is currently under development. The new model uses data obtained from all LEDs mounted in DOMs, while the current one uses the data from only one emitting string [121, 123]. An indication that the new model is a step forward in the understanding of the ice optical properties is the distribution of the reconstructed vertex $z$ positions, shown in the left part of Figure 6.18. Its impact is evaluated by injecting simulations with a new bulk ice model and fitting them with the current one. This procedure leads to the non-physical fit value of about $\sin^2 2\theta_{23} = 1.032$. The obtained value can be a partial reason for the non-physical fit, but it can account only for approximately 30% of the observed fluctuation.

**Disagreement for the single-string and multi-string fits**

The directional reconstruction algorithm used in this work can have one or multiple strings with the direct light, as discussed in Section 5.2.1. A disagreement in the number of hit DOMs after the seeded R-T pulse cleaning for the single-string and multi-string events was found after unblinding. It is shown in the right part of Figure 6.18. The impact of this disagreement is tested by reweighting simulations according to the observed shape from the data and fitting it with the original sim-

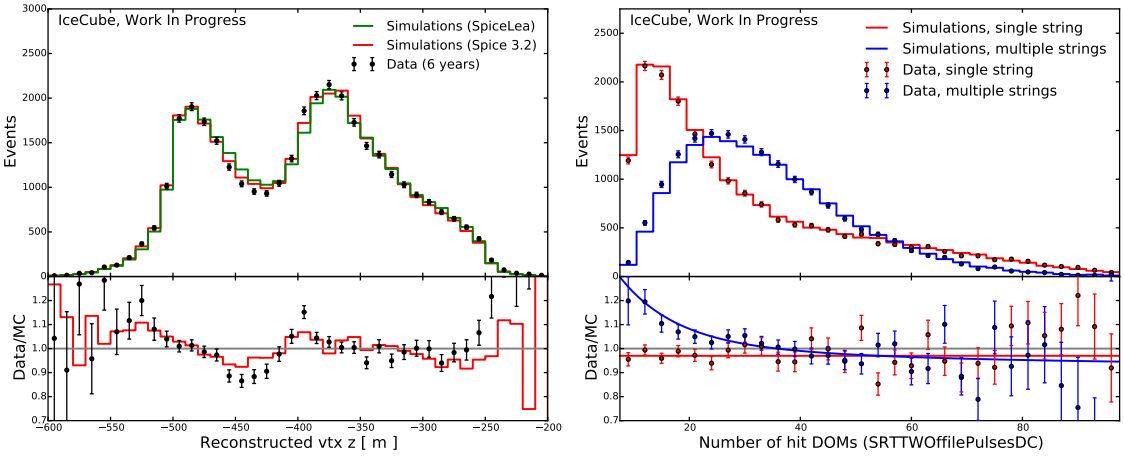


Figure 6.18: (Left) The disagreement between the data and current simulations (green, *SpiceLea*) for the reconstructed vertex $z$ position. The red line shows the expected effect of the new ice model (*Spice3.2*), which is currently under development in the IceCube collaboration. (Right) The disagreement between the data and the best-fit expectation seen for the single-string (red) and multi-string (blue) events. The bottom panel also shows the ratio between the data and expectations, where the coloured lines depict the reweighting functions applied to the simulations.

ulations. This procedure leads to $\sin^2 2\theta_{23} = 1.022$. If it is applied to the new ice model, the best fit is pulled towards 1.036, which is not still sufficient to explain the observed non-physical value.

**Hole ice properties**

A variety of realisations for the optical properties of the hole ice are probed using the direct propagation of photons through the bubble columns. These realisations are used for parametrisations of the spiciness parameter, discussed in Section 5.5.4. However, there can still be an unaccounted difference, which is quantified by fitting the corresponding simulations. The largest observed value for the mixing is $\sin^2 2\theta_{23} = 1.024$. The calibration studies to obtain precise bubble column properties are under development by the IceCube collaboration. However, the hole ice properties are unlikely to cause the non-physical result observed in this work.

**Shape of the atmospheric muon template**

The data-driven template is used to account for the atmospheric muon background. Currently, the available statistics of the atmospheric muon simulations is not sufficient to simulate the muon background directly. To test the effects of the template uncertainties, each event in the template was reweighted with the function

$$w_i^\mu = E_\mu^{\gamma_\mu} \cdot (1 - 2 \cdot t_\mu \cdot (\cos\theta_z^\mu + 0.5)) \,, \tag{6.5}$$

where $t_\mu$ is the tilt in $\cos\theta_z^\mu$; $\gamma_\mu$ is the additional muon spectral index; and $E_\mu$ and $\theta_Z^\mu$ are the reconstructed energy and zenith angle of the muon in the template, respectively.

The template is modified and then added to the neutrino simulations assuming a 5% contamination of the total sample. The resulting histograms are fit with the standard procedure using the unmodified muon template. The values of $t_\mu$ and $\gamma_\mu$ between –0.5 and +0.5 are tested. The fitted $\sin^2 2\theta_{23}$ values are depicted in Figure 6.19. The largest non-physical deviation is observed for $t_\mu = -0.5$, $\gamma_\mu = 0.25$,

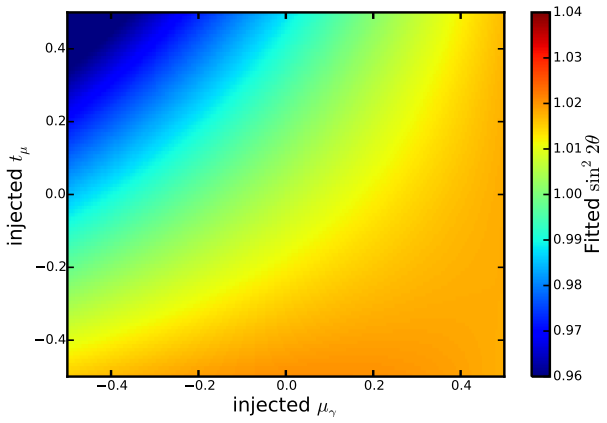


Figure 6.19: The obtained values of $\sin^2 2\theta_{23}$ as a function of injected $\cos\theta_z$ tilt and spectral index of the data-driven muon template.

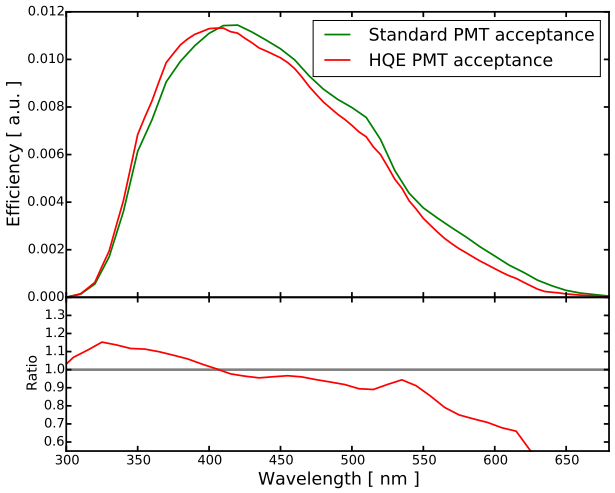


Figure 6.20: The wavelength acceptance of the standard (green) and HQE (red) DOMs. The lower panel shows the ratio between the HQE and standard efficiencies.

where $\sin^2 2\theta_{23} = 1.02$. The fitter recovers the injected muon contamination with the precision of about 20% (the reconstructed values between 4.0 and 5.8%). This means that such variations of the template cannot cause the observed non-physical result.

**Other tested hypotheses**

There are several detector features that are known to be modelled incorrectly in the current simulations used in this work. One such effect is the shadowing of PMT cathodes by the data cables. A test simulation that includes the cable shadows was created and found to have a negligible impact on the neutrino mixing parameters. Also, the HQE PMTs in DeepCore DOMs are known to have a slightly different wavelength acceptance, as shown in Figure 6.20. A baseline simulation set with the corrected acceptance was created and no significant impact on $\theta_{23}$ was found. Each module in IceCube can have a slightly different optical efficiency. Simulations with individual efficiencies for each DOM were tested. They are found to have an insignificant effect on the neutrino mixing parameters. Two different values for the bulk ice anisotropy were tested and are found to have no impact on the neutrino mixing parameters. The effects mentioned above were tested and resulted in the values of $\sin^2 2\theta_{23} < 1.02$.

**Final remarks**

All of the tested systematic uncertainties are found to have a small effect and are unlikely to cause the non-physical result. Therefore, the currently observed $\sin^2 \theta_{23}$ value is likely to be caused by statistical fluctuations. More data and improved detector modelling might be useful to further probe the origin of the non-physical result.

# Chapter 7

# The search for sterile neutrino mixing

This chapter discusses the search for sterile neutrino mixing using the data from IceCube DeepCore. It starts with a general overview of the analysis, covering the differences between this study and the one presented in Chapter 6. It is followed by information about the checks performed during the development of the analysis. Finally, the results of the search are presented. The results of this analysis are also published in [102].

## 7.1 Analysis overview

The sterile neutrino search was performed prior to the measurement of the standard atmospheric oscillations presented in the previous chapter. It relies on the same event selection and reconstruction but uses a different binning and slightly different treatment of systematic uncertainties.

### 7.1.1 Data sample and expected signal

The search for sterile neutrino mixing was developed as an extension to the measurement of the standard atmospheric neutrino oscillations published in [7]. This analysis only uses the events identified as having muon tracks by the PID score:

- single-string events: PID $< 0.6$,
- multi-string events: PID $< 0.8$.

The search uses three years of data accumulated between May 2011 and May 2014, comprising 5118 events in total. The sample is dominated by the events induced by $\nu_\mu$ CC interactions, accounting for more than 70% of the total event rate (estimated from the best-fit parameters of the analysis). The contributions of the different interaction types to the total event count are listed in Table 7.1. The reconstructed energy and zenith distributions, as well as contributions from different interaction types, are depicted in Figure 7.1.

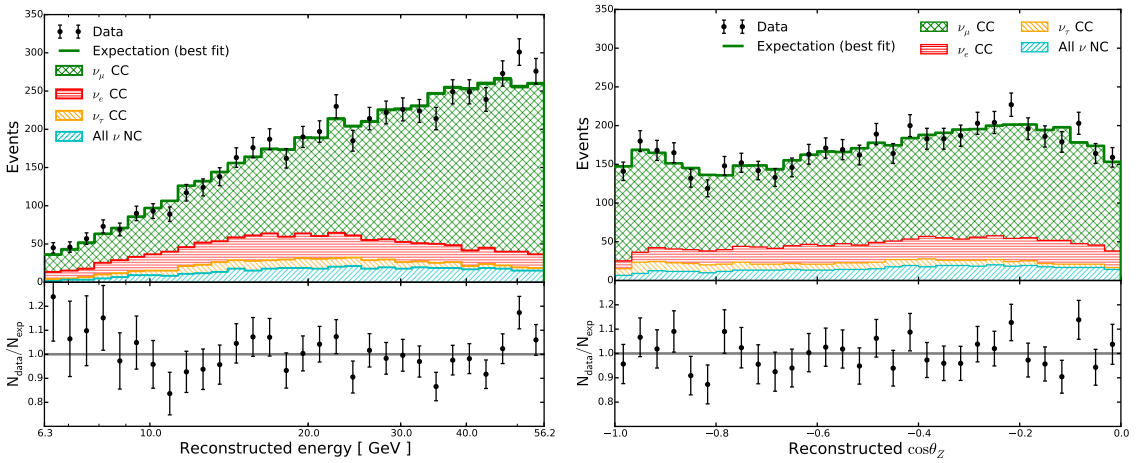


Figure 7.1: Projections of the data (black) and expectation from simulations (green line) in the sterile neutrino search for the reconstructed energy (left) and cosine of the zenith angle (right). The upper panels demonstrate the contributions from CC interactions of $\nu_\mu$ (green), $\nu_e$ (red), and $\nu_\tau$ (yellow), as well as expectation from NC interactions of all flavour (cyan). The contribution from atmospheric muons is small and is not depicted. The bottom panels show the ratios between the observed and expected number of events for each projection. The figures are also published in [102].

The data is divided into 64 bins in reconstructed energy and zenith. Only the low energy part of the data is used in this study. The reconstructed energy is split into 8 logarithmic bins between $10^{0.8}$ and $10^{1.75}$ GeV. The cosine of the reconstructed zenith angle, $\cos\theta_z$, is split into 8 bins between -1 and 0. The numbers of data events in each analysis bin are shown in Figure 7.2.

As discussed in Section 3.7.3, the strength of the sterile neutrino mixing signature is proportional to the amount of matter along a neutrino trajectory. The presence of sterile neutrinos leads to a rather large change of the overall flux normalisation. However, current flux predictions are not precise enough to incorporate this information in the fit. Therefore, the study presented here is performed in a

Table 7.1: The number of events from the different interaction types estimated from the analysis best-fit to the data.

| **Component** | **Track channel** |
|---|---|
| $\nu_\mu$ CC | 3707.5 |
| $\nu_e$ CC | 707.7 |
| $\nu_\tau$ CC | 235.3 |
| All $\nu$ NC | 446.2 |
| Atm. $\mu$ | 21.3 |
| Total (sim., best fit) | 5118.0 |
| Total (data) | 5118 |

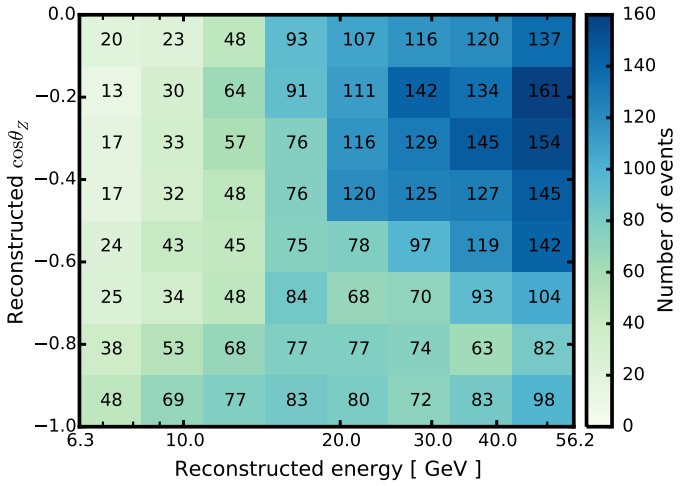


Figure 7.2: The event count from data selected for the sterile neutrino search.

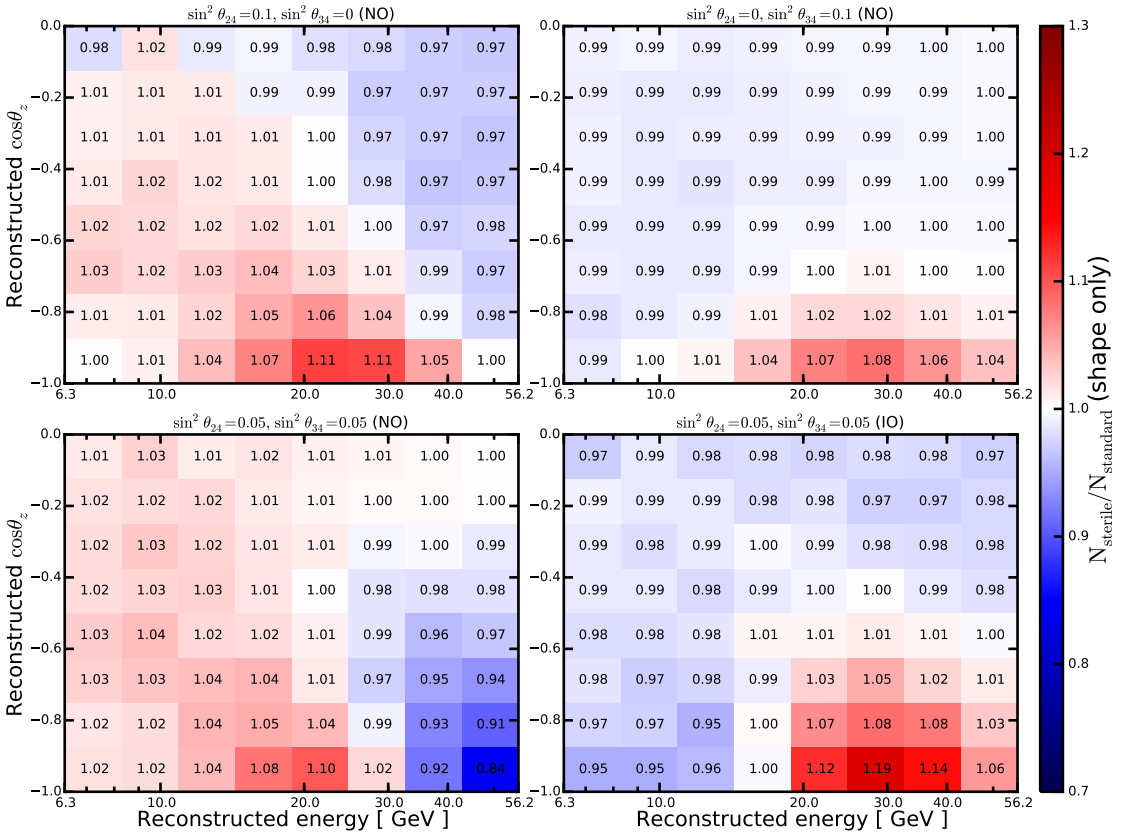


Figure 7.3: Expected changes in the observed data rate for different realisations of the sterile neutrino mixing. The bottom panels depict the same mixing for the normal ordering (NO, left panel) and the inverted ordering (IO, right panel), since for them a flip of the mass ordering cannot be compensated by a flip of the atmospheric neutrino octant, as explained in Section 3.7.3.

shape-only way, with a completely free normalisation. The sterile mixing effects are the strongest for neutrinos with $\cos\theta_z < -0.8$, where they cross the Earth's core. Two mixing angles, $\theta_{24}$ and $\theta_{34}$, are probed in this work. Figure 7.3 depicts the expected effects on the observed event rate for different realisations of the probed sterile neutrino mixing angles.

A change of the standard neutrino mass ordering results in an exchange of neutrino and antineutrino probabilities. However, if one of the sterile mixing angles is close to zero, this flip can be compensated by a $\theta_{23}$ octant flip ($\theta_{23} \to \pi/2 - \theta_{23}$), as discussed in Section 3.7.3. On the other hand, if both mixing angles are significantly non-zero, the flip of the mass ordering is not compensated and leads to differences in the observed signals, as shown in the bottom panels in Figure 7.3.

### 7.1.2 Fit parameters

This analysis has minor differences in parametrisations of some systematic uncertainties compared to the study in Chapter 6. The parameters of interest in this study are $\theta_{24}$ and $\theta_{34}$. The value of the sterile neutrino mass-squared splitting $\Delta m^2_{41}$ is fixed at 1 eV$^2$ throughout the analysis unless stated otherwise.

The standard atmospheric mixing parameters $\Delta m^2_{32}$ and $\theta_{23}$ are nuisance parameters for this study. No priors are applied to them, since a wrong selection of a prior can lead to a false positive signal with a significance of around one sigma. The normal and inverted neutrino mass ordering of the standard three-neutrino model are probed here. Other neutrino mixing parameters are fixed to the same values as in Chapter 6. In this study, the oscillation probabilities are calculated using the GLoBES project [103, 104] with the full "3+1" model [105] and PREM [142] as the Earth matter profile. Table 7.2 lists the fit parameters and the priors used in this search.

This analysis uses the spectral index $\Delta\gamma$, $\nu_e$ flux normalisation and the neutrino-antineutrino ratio to account for the impact of the flux uncertainties. Unlike the study presented in Chapter 6, the energy and zenith dependence of the neutrino-antineutrino ratio are treated as two separate fit parameters. The upgoing-horizontal flux ratio is not used in this study and it is expected to have a negligible effect on the analysis.

Two nuisance parameters account for the detector uncertainties in this study. The impact of the DOM optical efficiency is estimated from 7 systematic sets covering efficiencies between 85% and 115% of the nominal value in 5% steps. This analysis uses a different effective angular acceptance of DOMs to cover uncertainties caused by the hole ice properties. The model is varied by a single parameter, which represents the effective scattering coefficient of the hole ice column. This analysis uses a baseline value of 0.02 cm$^{-1}$ (50 cm scattering length). The impact of the uncertainty on this parameter is estimated from 10 systematic simulation sets covering the coefficient values between 0.01 and 0.033 cm$^{-1}$. The angular acceptance curves for scattering coefficients of 0.01, 0.02 and 0.033 cm$^{-1}$ are depicted in Figure 7.4.

The axial masses for quasi-elastic and resonant scattering processes are varied to

Table 7.2: A list of fit parameters in the sterile neutrino search, applied priors and the best-fit estimates for normal (NO) and inverted (IO) neutrino mass ordering. The table is also published in [102]. The uncertainties for the parameters are estimated by MINUIT or by likelihood profiling.

| Parameter | Priors | Best fit (NO) | Best fit (IO) |
|---|---|---|---|
| **Sterile mixing parameters** | | | |
| $\|U_{\mu 4}\|^2 = \sin^2\theta_{24}$ | no prior | 0.00 | 0.00 |
| $\|U_{\tau 4}\|^2 = \sin^2\theta_{34}\cos^2\theta_{24}$ | no prior | 0.08 | 0.06 |
| **Standard mixing parameters** | | | |
| $\Delta m^2_{32}$ [ $10^{-3}\mathrm{eV}^2$ ] | no prior | $2.52 \pm 0.22$ | $-2.61 \pm 0.28$ |
| $\sin^2\theta_{23}$ | no prior | $0.54^{+0.10}_{-0.12}$ | $0.47^{+0.13}_{-0.10}$ |
| **Flux parameters** | | | |
| $\nu_e$ normalisation | $1 \pm 0.05$ | $1.00 \pm 0.050$ | $1.00 \pm 0.050$ |
| $\Delta\gamma$ | no prior | $0.106 \pm 0.072$ | $0.099 \pm 0.085$ |
| $\Delta(\nu/\bar{\nu})$, energy dep. | $0 \pm 1\sigma$ | $0.19 \pm 0.96\sigma$ | $0.21 \pm 0.96\sigma$ |
| $\Delta(\nu/\bar{\nu})$, zenith dep. | $0 \pm 1\sigma$ | $0.19 \pm 0.89\sigma$ | $0.16 \pm 0.90\sigma$ |
| **Detector parameters** | | | |
| Hole ice scattering [ $\mathrm{cm}^{-1}$ ] | $0.02 \pm 0.01$ | $0.0210 \pm 0.0026$ | $0.0210 \pm 0.26$ |
| DOM efficiency [ % ] | $100 \pm 10$ | $100.8 \pm 4.5$ | $100.6 \pm 4.6$ |
| **Cross section parameters** | | | |
| $M_A$ (quasi-elastic) [ GeV ] | $0.99^{+0.25}_{-0.15}$ | $1.03^{+0.25}_{-0.15}$ | $1.03^{+0.25}_{-0.15}$ |
| $M_A$ (resonance) [ GeV ] | $1.12 \pm 0.22$ | $1.16 \pm 0.21$ | $1.14 \pm 0.21$ |
| **Background** | | | |
| Atm. $\mu$ contamination [ % ] | no prior | $0.0^{+4.0}_{-0.0}$ | $0.4^{+4.1}_{-0.4}$ |

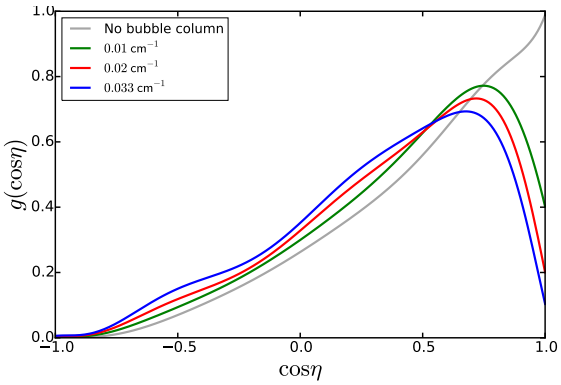


Figure 7.4: The angular acceptance curves for different scattering coefficients in the hole ice model. The value of $\cos\eta = 1$ means that that photon hist the centre of PMT, while $\cos\eta = -1$ implies that photon arrived from an opposite direction. A further explanation of the angular acceptance curve can be found in Section 5.1.

account for the cross-section uncertainties. The rate from NC interactions is fixed to the expectation from the baseline cross-section model. A data-driven template accounting for the atmospheric muon background is fit together with neutrino simulations in the same way as for the study described in Chapter 6. However, only the corresponding three years of data are used for the selection of the template. The impact of the nuisance parameters on the shape of the histograms can be found in Appendix A.2.

### 7.1.3 Minimisation performance

Similar to the measurement of the atmospheric mixing parameters presented in Chapter 6, the performance of the minimisation procedure is checked by injecting different values of the physical parameters and fitting the resulting expectation using the full analysis procedure. One hundred variations of mixing elements $|U_{\mu 4}|^2$ and $|U_{\tau 4}|^2$ were generated with the values shown in the left panel of Figure 7.5. The minimiser successfully recovers the injected values with numerical precision at the level of $10^{-4}$ or better. The differences between the injected and fitted values for $|U_{\mu 4}|^2$ and $|U_{\tau 4}|^2$ are demonstrated in the right panel of Figure 7.5. A similar performance is also observed for the nuisance parameters.

### 7.1.4 Test statistic distribution

According to Wilks' theorem [138], the test statistic (TS) should follow a chi-squared distribution with 2 degrees of freedom (d.o.f.). The parameters of interest in this study have two physical boundaries located at zero for each mixing angle, which can result in a deviation from the Wilks' theorem expectation. The coverage for different points of the parameter space is tested with statistical pseudo-trials created in the same way as described in Section 6.2.2.

Figure 7.6 depicts the distribution of the TS for three points on the parameter space. If the injected point is far from the boundaries, such as for the green curve

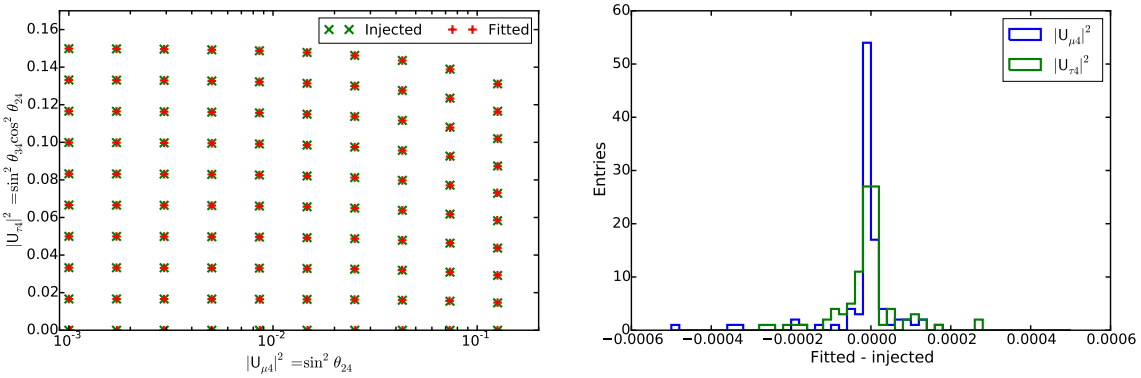


Figure 7.5: (Left) The agreement between injected and fitted values of the sterile neutrino mixing. (Right) The performance of finding the injected values of the sterile neutrino mixing $|U_{\mu 4}|^2$ and $|U_{\tau 4}|^2$.

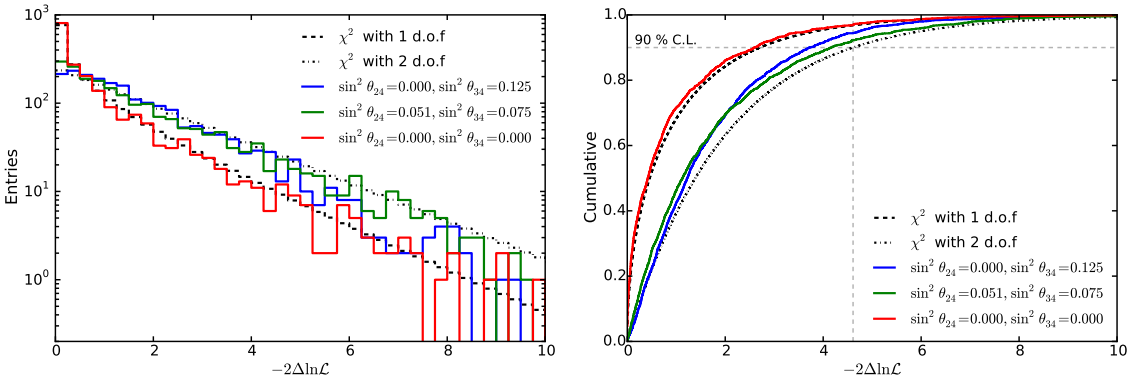


Figure 7.6: (Left) The test statistic distributions for three realisations of the sterile neutrino mixing. The black dashed and dash-dotted lines depict $\chi^2$ distribution for 1 and 2 d.o.f., respectively. (Right) The same for cumulative distributions of the test statistic.

in Figure 7.6, the TS follows a chi-squared distribution with 2 d.o.f., as predicted. However, a proximity to the boundaries results in a deviation from this number. A hypothesis without sterile neutrino mixing lies on the boundary for both parameters at the same time, leading to an effective d.o.f. close to 1, as shown by the red line in Figure 7.6. The effective d.o.f is between 1 and 2 for the realisations where only one mixing angle is close to the boundary.

The expected coverage of this study is better than the prediction from Wilks' theorem. For the expected location of the 90% confidence level (C.L.) limits, the obtained coverage is between 92% to 95%. The usage of the Feldmann-Cousins procedure [145] can improve the coverage and would improve the sensitivity by up to 10%. However, it requires large computational resources and, therefore, is out of scope for this study.

## 7.2 Expected sensitivity

The sensitivity of this study is defined by the values of the sterile neutrino mixing parameters that can be excluded in case of the null hypothesis (no sterile neutrino mixing). The median sensitivity to the mixing elements $|U_{\mu 4}|^2$ and $|U_{\tau 4}|^2$ at 90% and 99% C.L. is shown in black in Figure 7.7. The different coloured lines show the expected improvement of the sensitivity if the corresponding group of systematic uncertainties is known perfectly.

In this analysis, the most important systematic uncertainties come from the standard atmospheric mixing parameters and detector uncertainties. Each group causes a roughly 10–15% degradation of the sensitivity, as shown in Figure 7.7. The background, flux and cross-section uncertainties play a minor role and do not limit the sensitivity of this study. However, the largest limiting factor of this analysis is the available live time.

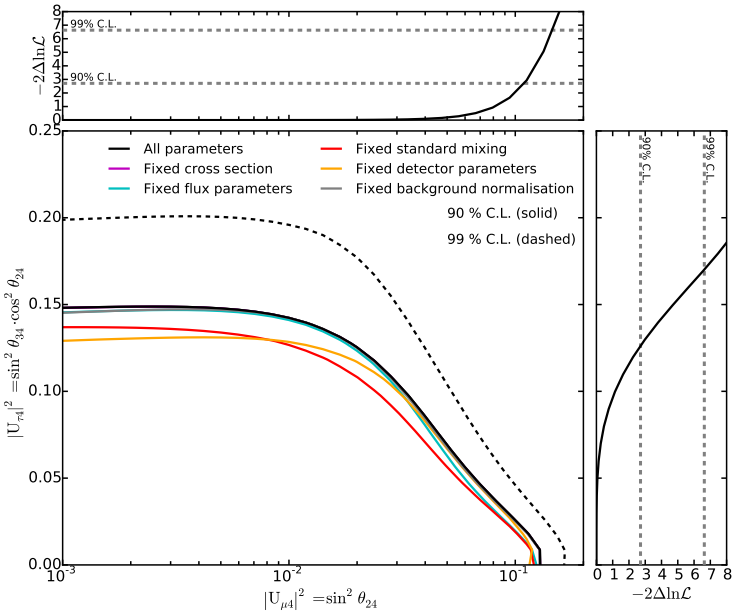


Figure 7.7: The expected sensitivity of the sterile neutrino search and the sensitivity improvement if the corresponding group of nuisance parameters is fixed. The upper and right panels show the projected sensitivities to $|U_{\mu 4}|^2$ and $|U_{\tau 4}|^2$, respectively.

## 7.3 Results

This section discusses the results of this analysis. It starts with the discussion about the agreement between data and the fitted expectations. The information about the best-fit point and obtained limits on the sterile neutrino mixing are presented at the end of the section.

### 7.3.1 Agreement between data and expectations

The value of the Pearson $\chi^2$ test is used to estimate the agreement between data and simulations in this work. The observed value of $\chi^2$ is 54.9 in this work. This analysis has 64 bins with 13 parameters and 7 priors, leading to an expected number of d.o.f. between 54 and 58. A more precise estimate of 56.3 d.o.f. is obtained from 2000 statistical pseudo-trials, with the corresponding distribution shown in the left part of Figure 7.8. The probability of observing the obtained $\chi^2$ value is approximately 53%, which indicates a good statistical agreement between the data and expectations.

Another important characteristic of the agreement is the distribution of statistical pulls between the data and the best-fit expectations. These pulls do not exhibit individually large values nor apparent clustering, as shown in the right panel of Figure 7.8. Figure 7.1 shows the agreement between the data and expectations for the reconstructed energy and zenith angle individually.

The agreement between the data and the best-fit expectations for each analysis bin can be found in Appendix B.

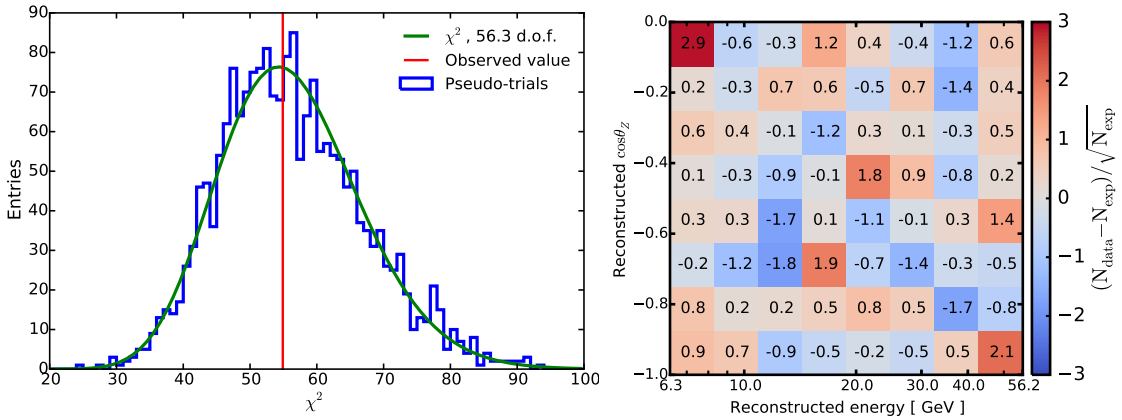


Figure 7.8: (Left) The expected $\chi^2$ test distribution obtained with pseudo-trials is shown in blue, while $\chi^2$ distribution with 56.3 d.o.f. is depicted in green. The red line shows the value observed in the data. (Right) The statistical pulls between the data and the best-fit expectation obtained in the analysis.

### 7.3.2 Best-fit values and limits

After ensuring that data are in good agreement with the expectations, the sterile mixing parameters were unblinded. The best estimate of the sterile neutrino mixing parameters in this study is

$$\begin{aligned} |U_{\mu 4}|^2 &= 0.00\ (0.00), \\ |U_{\tau 4}|^2 &= 0.08\ (0.06), \end{aligned} \tag{7.1}$$

for the normal (inverted) mass ordering of the standard neutrinos. The inverted neutrino mass ordering is marginally preferred with $\chi^2 = 54.9$, while the normal ordering has $\chi^2 = 55.2$. The fitted values for all nuisance parameters are within $1\sigma$ to their baseline expectations. The obtained best-fit values for the normal and inverted ordering are listed in Table 7.2.

The TS difference between the no-sterile-neutrino hypothesis and the best fit is $-2\Delta \ln \mathcal{L} = 0.8$. Such a value is expected from pure statistical fluctuations of the standard three-neutrino hypothesis in approximately 30% of the cases. This estimate is obtained with the 2000 aforementioned statistical trials.

Given the consistency of the results with the no-sterile-neutrino hypothesis, the limits are set on the allowed sterile mixing. The exclusion contours obtained from the profiled likelihood are depicted in Figure 7.9. The limits for the individual elements of the mixing matrix are

$$\begin{aligned} |U_{\mu 4}|^2 &< 0.11\ (90\%\ \text{C.L.}), \\ |U_{\tau 4}|^2 &< 0.15\ (90\%\ \text{C.L.}) \end{aligned} \tag{7.2}$$

for both neutrino mass ordering scenarios. The comparison of the limits obtained in this study to the limits provided by other experiments is presented in the next chapter.

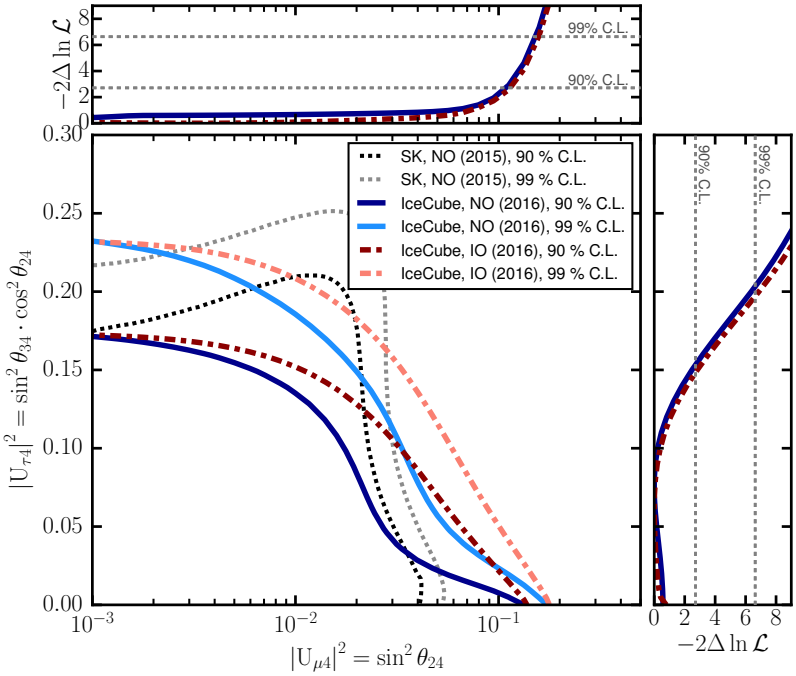


Figure 7.9: The limits on the sterile neutrino mixing obtained in this work. The dark (light) blue lines depict 90% (99%) C.L. limits for the normal mass ordering (NO). The dark (light) red lines represent the same constraints for the inverted ordering (IO). The upper and right panels show the log-likelihood profile for $|U_{\mu 4}|^2$ and $|U_{\tau 4}|^2$ mixing elements, respectively. The black and grey dashed lines depict the limits from the Super-Kamiokande experiment [97], which were the most constraining limits at the time of the analysis.

The limits in Equation (7.2) are robust against the value of $\theta_{14}$. This was tested by letting $\theta_{14}$ float during the minimisation and adding a very weak prior, which is less constraining than the results of the global fits [94]. No significant change of the best-fit parameters was observed in this procedure.

The value of the sterile mass-squared splitting, $\Delta m^2_{41}$, has no impact on the limit for $|U_{\tau 4}|^2$. The limit on $|U_{\mu 4}|^2$ has a weak dependence on $\Delta m^2_{41}$. For the value $\Delta m^2_{41} = 0.1$ eV$^2$ the limit degrades to approximately 0.12, while for 10 eV$^2$ it improves by 9% to the value of 0.10. The value of $\Delta m^2_{41}$ has a negligible effect on the best-fit parameters extracted in this analysis.

# Chapter 8

# Discussion of the results

This chapter discusses the results obtained in Chapters 6 and 7, and compares them to the other measurements done by IceCube and other experiments. The final part of this chapter shows the possible ways to improve the sensitivity of the studies presented in this work.

## 8.1 Atmospheric mixing parameters

### 8.1.1 Other measurements in IceCube

There are different approaches to study the atmospheric neutrino oscillations with IceCube DeepCore. The selection used in this work applies the most constraining criteria resulting in approximately 6000 events per year. The strict selection criteria help to reduce the impact of systematic uncertainties due to the ice optical properties, atmospheric muon contamination and pure noise events.

The second IceCube study [8] uses looser selection criteria to gain more events. It results in an atmospheric muon contamination of about 5%, ten times higher than in this work. It uses an event reconstruction that fits 8 parameters of the $\nu_\mu$ CC interaction topology using the observed charge binned in time. This reconstruction has higher efficiency but requires a large amount of computational resources. This selection results in approximately 15000 events per year but can use only data from the 2012–2014 seasons. In 2011 the detector was settling after the deployment of the last strings, resulting in an inconsistent noise rate with the later years. Since this analysis relies on charge for the reconstruction, currently it cannot use 2015 and 2016, where a new charge calibration is applied. The results that use this event selection are marked as the *medium statistics sample* in Figure 8.1.

Both analyses show comparable precision for the mass-squared splitting $\Delta m^2_{32}$. The analysis presented in this work prefers a slightly larger value for $\Delta m^2_{32}$. However, both studies are statistically consistent with each other, considering the usage of nearly independent data samples, reconstruction and selection techniques. Both of the studies prefer the $\sin^2\theta_{23}$ close to the maximal mixing. This work provides

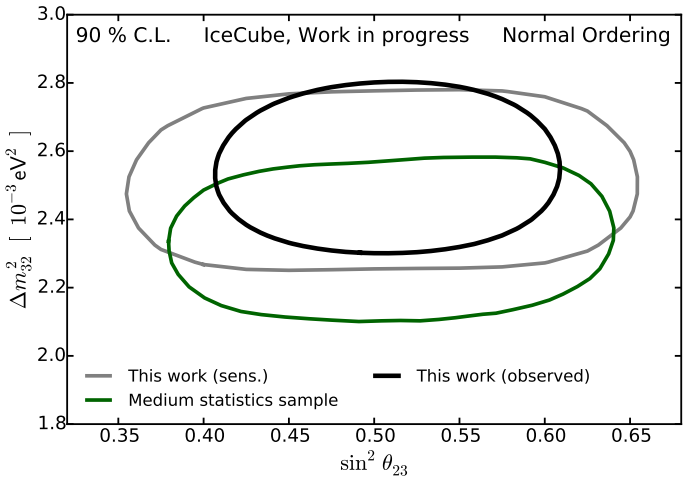


Figure 8.1: The 90% C.L. constraints on the atmospheric mixing parameters obtained by IceCube. The grey and black lines depict the sensitivity and the results of this work in Chapter 6, respectively, while the green line shows the results obtained with the medium statistics sample from [8].

approximately 20% better constraints on $\sin^2\theta_{23}$, however, this can be caused by the fluctuation into the non-physical region as discussed in Section 6.5.

Currently, there are ongoing studies to improve the sensitivity of IceCube by enhancing the efficiency for the dimmest neutrino events and improving the reconstruction techniques. The ways to improve the sensitivity of the analysis presented in this work are discussed in Section 8.3.

### 8.1.2 Comparison to other experiments

**Atmospheric neutrinos**

Currently, the atmospheric neutrino oscillations are measured by the IceCube, Super-Kamiokande [63] and ANTARES [147] experiments. Figure 8.2 compares the results of this work to the most recent measurements from these large volume water Cherenkov detectors.

IceCube DeepCore provides the most precise measurement of neutrino oscillations using atmospheric neutrinos. The uncertainty for $\Delta m^2_{32}$ is improved by approximately 40% when compared to the Super-Kamiokande results, while the precision for $\sin^2\theta_{23}$ is about 20% better. However, as discussed in Section 6.5.1, more checks are necessary to confirm these uncertainties.

**Accelerator experiments**

The experiments using accelerator neutrinos provide the most precise measurements of the atmospheric mixing parameters, as discussed in Section 3.5.1. The right panel of Figure 8.2 compares their measurements to the results obtained in this work.

The accelerator experiments benefit from controlled experimental conditions, resulting in higher precision measurements of the mixing parameters. However, a

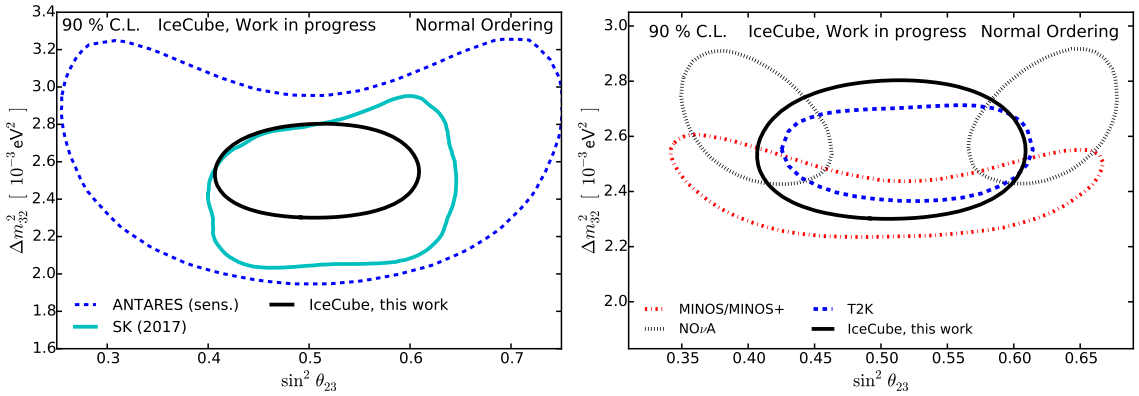


Figure 8.2: The 90% C.L. uncertainties for $\Delta m^2_{32}$ and $\sin^2\theta_{23}$ obtained in this work compared to the results obtained from the atmospheric (left) and accelerator (right) neutrino oscillation experiments [63, 65–67]. The curve for ANTARES depicts the expected sensitivity from [147].

range of possible improvements might improve the sensitivity of IceCube in future, as discussed in Section 8.3. These improvements would allow IceCube to provide the most precise measurements of $\Delta m^2_{32}$ and $\theta_{23}$ among the currently existing experiments.

## 8.2 Limits on the sterile neutrino mixing

The results of the sterile neutrino search presented in Chapter 7 provide stringent limits on the mixing elements $U_{\mu 4}$ and $U_{\tau 4}$. The comparison of the current experimental limits performed in the same parameter space is presented in Figure 8.3.

Currently, this work provides the World's strongest limit for the mixing element $|U_{\tau 4}|^2$, which is approximately 20% and 7% better than the limits from Super-Kamiokande [97] and MINOS/MINOS+ [95], respectively.

On the other hand, the best limits for the element $|U_{\mu 4}|^2$ are currently coming from the IceCube search using TeV neutrinos [96], MINOS [95] and Super-Kamiokande [97] experiment. The sensitivity of this work to $|U_{\mu 4}|^2$ is limited by insufficient resolutions and separation between neutrino events producing tracks and cascades.

The presented search for the sterile neutrino mixing uses only 3 years of data in the track channel. Preliminary studies show that the usage of the extended data sample with 6 years of data as used in Chapter 6 improves the sensitivity at $\Delta m^2_{41} = 1$ eV$^2$ by 35% and 30% for $|U_{\mu 4}|^2$ and $|U_{\tau 4}|^2$, respectively. A comparison of the current limits and the sensitivity of the extended sample is presented in Figure 8.3. The extended sample uses events with reconstructed energies of up to 158 GeV. Therefore, the impact of the sterile neutrino mass must be analysed additionally, since at such energies the frequency of the oscillations caused by $\Delta m^2_{41}$ may be resolved by the detector resolutions. Currently, those effects are under

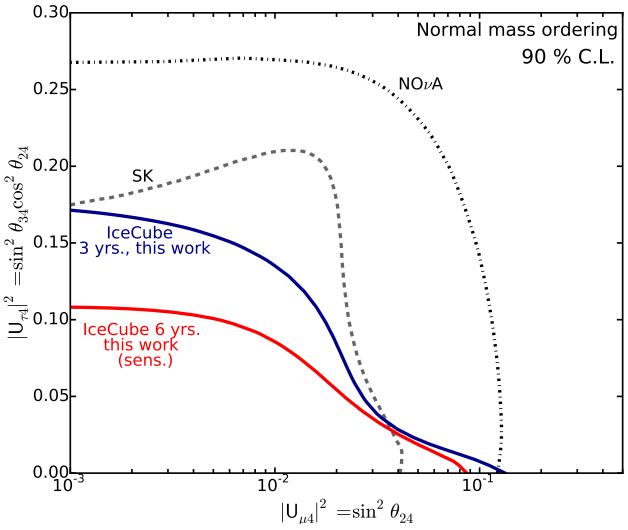


Figure 8.3: The 90% C.L. exclusion limits obtained in this work (solid blue line) and compared to the limits from Super-Kamiokande [97] (dashed black line) and NOvA [101] (dash-dotted black line). The red line depicts the sensitivity of this work with 6 years of data with the analysis procedure described in Chapter 6. Normal neutrino mass ordering is assumed for all lines.

investigation by the IceCube collaboration, but the corresponding study does not fit the time allocated for this work.

## 8.3 Possible future improvements

This section discusses possible ways to improve the results presented in this work. It focuses on the sensitivity to the standard atmospheric mixing parameters, but the discussed improvements can be also applied to the search for the sterile neutrino mixing.

### 8.3.1 Detector live time

The IceCube detector is taking data with more than 99% live time, and the detector shows no signs of ageing. Currently, six years of data with the full detector configuration are complete and the seventh year will be finished in May 2018.

The expected $1\sigma$ sensitivities to the atmospheric mixing parameters as a function of the detector live time are shown in Figure 8.4. From the left part of Figure 8.4 it can be seen that the sensitivity to $\Delta m^2_{32}$ improves almost as a $1/\sqrt{t}$ function of the detector live time. When compared to the current 6 years study, the $\Delta m^2_{32}$ sensitivity improves by 11.5% and 25% for 8 and 12 years of data, respectively.

As shown in the right part of Figure 8.4, the sensitivity to the mixing improves approximately as $1/\sqrt{t}$ for $\sin^2 2\theta_{23}$ parameter space. However, when the $\sin^2\theta_{23}$

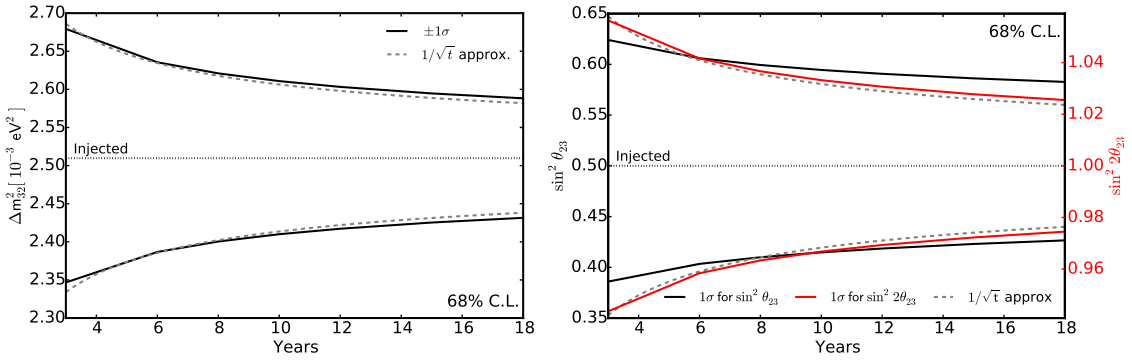


Figure 8.4: The expected size of 68% C.L. uncertainty to $\Delta m^2_{32}$ (left) and $\sin^2\theta_{23}$ (right). The $1/\sqrt{t}$ approximation is shown by the dashed lines. The red line in the right panel depicts the sensitivity to $\sin^2 2\theta_{23}$ in the two-neutrino model.

projection is considered, the improvements are only 7% and 15% for 8 and 12 years of the detector live time, respectively.

### 8.3.2 Systematic uncertainties

The sensitivity of this work is significantly affected by the systematic uncertainties. They lead to degradation of the sensitivity to $\Delta m^2_{32}$ and $\sin^2\theta_{23}$ by approximately 40% and 24%, respectively.

Better knowledge of the cross-section uncertainties may result in up to 5% improvement of the sensitivity of this study. The treatment of flux uncertainties used in this work is an approximation. It can be improved using more precise calculations that include better modelling of the cosmic ray spectrum and hadronic interactions in atmospheric showers [38, 148, 149]. This can result in an additional 3% sensitivity improvement.

The detector uncertainties have the largest effect on the sensitivity of this work. Calibration studies aim to improve the knowledge of bulk and hole ice optical properties and are expected to improve the sensitivity to $\sin^2\theta_{23}$ by about 8%.

One of the most important nuisance parameters in this work is the DOM optical efficiency. It has a 10% prior, while more precise values are expected from the ongoing calibration studies. If the DOM efficiency would be known with 3% precision, the sensitivities to $\Delta m^2_{32}$ and $\sin^2\theta_{23}$ improve by approximately 15% and 2%, respectively. The dependence of the expected $1\sigma$ sensitivity as a function of the DOM efficiency prior size is shown in Figure 8.5.

### 8.3.3 Improvements of reconstructions

Another way to improve the sensitivity of this study is to optimise the performance of the event reconstruction and the particle identification. This section evaluates an expected improvement of the sensitivity, if the reconstruction tools used in this work are improved. In this section, the expected improvements are estimated with

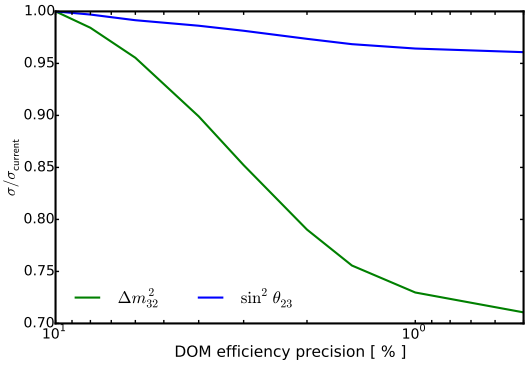


Figure 8.5: The expected improvement of the sensitivity to $\Delta m^2_{32}$ (green) and $\sin^2\theta_{23}$ (blue) as a function of the Gaussian prior size used for the DOM optical efficiency. The value of 10% is used for the results presented in this work.

simulations by reducing the differences between reconstructed and simulated values of the corresponding observable and comparing the resulting projected sensitivity with the current sensitivity.

**Energy reconstruction**

The energy reconstruction can be improved with the addition of charge information from DOMs. The improvement of the energy resolution would result in significantly better sensitivity to the mass-squared splitting, as shown in the left part of Figure 8.6. A 10% improvement of the current resolution would result in about 12% improvement in the $\Delta m^2_{32}$ sensitivity, while for $\sin^2\theta_{23}$ it is only 2%. However, a careful treatment of the charge calibration is necessary for a realistic implementation of this information into the reconstruction and analysis.

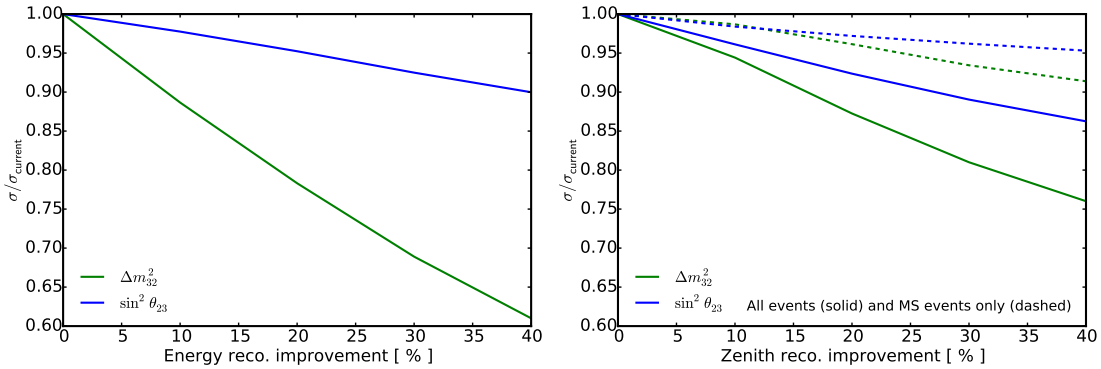


Figure 8.6: The expected sensitivity improvement for improved energy (left) and zenith (right) resolutions. The solid green and blue lines depict $\Delta m^2_{32}$ and $\sin^2\theta_{23}$, respectively. The dashed line in the right panel presents the resolution improvement applied only to the multi-string events.

**Zenith reconstruction**

The zenith angle reconstruction can be improved by the addition of partially scattered photons. The preliminary studies show that this can result in 40% to 50% better zenith angle resolution without a loss in efficiency. The expected sensitivity improvement is shown in the right part of Figure 8.6. Currently, the resolution improvement is observed predominately for the multi-string (MS) events. If the resolution for the MS events would be improved by 40%, the sensitivities to $\Delta m^2_{32}$ and $\sin^2\theta_{23}$ improve by 9% and 5%, respectively. If a 40% improvement in zenith resolution can be achieved for all events (including single-string events), the sensitivity would improve by 25% and 14%, respectively.

**PID optimisation**

The PID score used in this work was initially developed as the event fit quality. The usage of more sophisticated algorithms, such as multivariate methods, can result in a significant improvement of the $\nu_\mu$ identification. To estimate the impact of an improved $\nu_\mu$ identification, the PID values for events that produce only cascades ($\nu_e$ CC and all NC interactions) are artificially increased to achieve the desired purity of the track channel.

The current analysis has approximately 21% contamination of the track channel by the interactions producing showers. The expected sensitivity improvement as a function of the track-channel contamination is shown in Figure 8.7. If the value of 15% is achieved, the precision for $\sin^2\theta_{23}$ improves by about 6%. The sensitivity to $\Delta m^2_{32}$ slightly degrades but is within 2% of the current one. This might be caused by slightly higher resulting contamination of the cascade channel, which is also dominated by $\nu_\mu$ CC interactions and, therefore, has a sensitivity to $\Delta m^2_{32}$. It might also indicate, that the splitting between the track and cascade channels can be further optimised to maximise the sensitivity of future measurements.

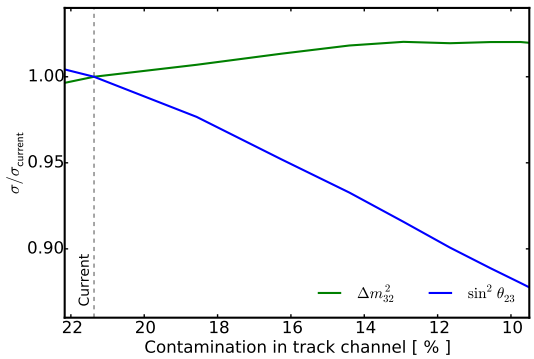


Figure 8.7: The expected change of the sensitivity as a function of the contamination of the track channel by CC interactions of $\nu_e$, $\nu_\tau$ and all NC interactions.

## 8.4 IceCube Upgrade

An upgrade of the currently existing IceCube DeepCore detector is planned in the future. It will include 7 new strings located inside the DeepCore fiducial volume with a horizontal spacing of approximately 25 m. Each string will include 125 modules with the vertical spacing of 2.4 m. New optical modules that include multiple smaller PMTs are currently under development for this project. Such a design will increase the total photo-cathode area and will provide improved photon directionality for event reconstruction algorithms. The clear ice, denser spacing and more sophisticated DOMs will result in an energy threshold of approximately 3 GeV.

In addition, the IceCube Upgrade will include improved calibration light sources. Such sources are designed to emit a known amount of isotropically distributed light. This is expected to constrain optical properties of the bulk and hole ice, as well as recalibrate the efficiencies of the IceCube and DeepCore DOMs.

The IceCube Upgrade is expected to improve the sensitivity of IceCube to the atmospheric neutrino oscillations. After running for 3 years, it is expected to lower the uncertainties for $\Delta m^2_{32}$ by more than 60% when compared to the current sensitivity. The precision for $\sin^2\theta_{23}$ is expected to improve by about 40%. The IceCube upgrade is also expected to provide a good sensitivity for other studies, for example, $\nu_\tau$ appearance in the atmospheric oscillations, searches for sterile neutrino mixing and Dark Matter. Currently, the proposal for the IceCube Upgrade has been submitted to National Science Foundation to acquire the necessary financial support.

# Chapter 9

# Conclusions

Neutrino oscillations are one of the most significant indications of new physics beyond the Standard Model. Precise measurements of the neutrino mixing parameters are expected to shine some light on a possible underlying symmetry and theory. Atmospheric neutrinos provide the possibility to study neutrino oscillations at higher energies than are accessible to anthropogenic neutrino sources. Currently, three generations of neutrinos are present in the Standard Model. Anomalous neutrino transitions are observed by some neutrino oscillation experiments, hinting towards the existence of additional sterile neutrinos. The mixing between the standard and sterile neutrinos can also be probed using atmospheric neutrinos.

The IceCube Neutrino Observatory has entered an era of precision measurements of the neutrino mixing parameters with atmospheric neutrinos. The first measurement using 6 years of the full detector configuration was presented in this work. It is the first IceCube neutrino oscillation study that used atmospheric neutrinos with energies up to 158 GeV and with an extended event selection that includes new cascade event topologies.

A wide range of improvements to the oscillation analysis were successfully developed and applied in this work. New simulation production techniques allowed for the usage of the most up-to-date knowledge of the detector and the systematic uncertainties. The event reconstruction and selection tools were also updated to include the new event topology. This work used an updated treatment of systematic uncertainties that includes a comprehensive knowledge about the IceCube detector, atmospheric neutrino fluxes and neutrino interactions. A variety of tests were performed to confirm the robustness of the presented results.

The data are found in good agreement with simulations in this work. The results of this study provide a measurement of the standard atmospheric mixing parameters

$$\begin{aligned} \Delta m^2_{32} &= 2.54^{+0.11}_{-0.12} \cdot 10^{-3}\ \text{eV}^2, \quad (68\%\ \text{C.L.}) \\ \sin^2\theta_{23} &= 0.51 \pm 0.05, \quad (68\%\ \text{C.L.}) \end{aligned} \tag{9.1}$$

which is among the most precise experimental measurements of these parameters. The results show a slight fluctuation into the non-physical region of $\sin^2 2\theta_{23}$, resulting in smaller than expected uncertainties on the atmospheric mixing angle $\theta_{23}$.

A variety of systematic uncertainties were considered and could not explain the observed deviation. The statistical fluctuations of the data are currently the most probable reason for this result with a probability between 5% and 10%.

In addition to standard oscillations, this work tests the three-neutrino paradigm by the addition of a single sterile neutrino state. Using 3 years of IceCube DeepCore data, the mixing of the sterile neutrino with muon and tau neutrinos in the "3+1" model is studied. No deviations from the standard three-flavour oscillations are observed. Therefore, this work sets the following limits on the allowed sterile mixing elements:

$$\begin{aligned} |U_{\mu 4}|^2 &< 0.11, \qquad (90\% \text{ C.L.}) \\ |U_{\tau 4}|^2 &< 0.15, \qquad (90\% \text{ C.L.}) \end{aligned} \tag{9.2}$$

for $\Delta m^2_{41} = 1$ eV$^2$. The limit for $U_{\tau 4}$ is currently the best in the World. The sensitivity to sterile neutrino mixing is expected to improve by applying the methods discussed in this work to the 6 years of data with the extended energy range.

A precise measurement of the neutrino oscillations in ice requires a careful treatment of systematic uncertainties. A limiting factor for the current studies is insufficient knowledge of the detector parameters. An ongoing calibration campaign will provide a more accurate description of the detector and is expected to result in a significant improvement of the sensitivity. More precise knowledge about the neutrino fluxes and neutrino interaction cross sections would result in further improvements in the sensitivity. Further sensitivity enhancement can be achieved through more sophisticated reconstruction and selection techniques.

The methods discussed in this work can be applied to other experiments using natural optical mediums for neutrino detection. Future upgrades of the IceCube detector are planned to lower the energy threshold, provide better calibration tools and improve event reconstructions. This would result in a higher precision for neutrino mixing within the standard three-neutrino paradigm and beyond.

# Bibliography


[1] W. Pauli, Phys. Today **31N9**, 27 (1978).

[2] C. L. Cowan, F. Reines, F. B. Harrison, H. W. Kruse, and A. D. McGuire, Science **124**, 103 (1956).

[3] Q. R. Ahmad *et al.* (SNO Collaboration), Phys. Rev. Lett. **89**, 011301 (2002), arXiv:nucl-ex/0204008 [nucl-ex] .

[4] Y. Fukuda *et al.* (Super-Kamiokande Collaboration), Phys. Rev. Lett. **81**, 1562 (1998).

[5] C. Giunti and C. W. Kim, *Fundamentals of neutrino physics and astrophysics* (Oxford University Press, 2007).

[6] M. Aartsen *et al.*, J. Instrum. **12**, P03012 (2017), arXiv:1612.05093 [astro-ph.IM] .

[7] M. G. Aartsen *et al.* (IceCube Collaboration), Phys. Rev. **D91**, 072004 (2015), arXiv:1410.7227 [hep-ex] .

[8] M. G. Aartsen *et al.* (IceCube Collaboration), Phys. Rev. Lett. **120**, 071801 (2018), arXiv:1707.07081 [hep-ex] .

[9] A. Aguilar-Arevalo *et al.* (LSND Collaboration), Phys. Rev. **D64**, 112007 (2001), arXiv:hep-ex/0104049 [hep-ex] .

[10] A. A. Aguilar-Arevalo *et al.* (MiniBooNE Collaboration), Phys. Rev. Lett. **110**, 161801 (2013), arXiv:1303.2588 [hep-ex] .

[11] G. Mention, M. Fechner, T. Lasserre, T. A. Mueller, D. Lhuillier, M. Cribier, and A. Letourneau, Phys. Rev. **D83**, 073006 (2011), arXiv:1101.2755 [hep-ex] .

[12] J. N. Abdurashitov *et al.*, Phys. Rev. C **73**, 045805 (2006).

[13] C. Giunti and M. Laveder, Phys. Rev. C **83**, 065504 (2011), arXiv:1006.3244 [hep-ph] .

[14] K. Zuber, *Neutrino Physics, Second Edition* (Taylor & Francis, 2011).

[15] E. Fermi, Z. Phys. **88**, 161 (1934).

[16] G. W. Rodeback and J. S. Allen, Phys. Rev. **86**, 446 (1952).

[17] R. Davis, Phys. Rev. **97**, 766 (1955).

[18] G. Danby, J.-M. Gaillard, K. Goulianos, L. M. Lederman, N. Mistry, M. Schwartz, and J. Steinberger, Phys. Rev. Lett. **9**, 36 (1962).

[19] K. Kodama *et al.* (DONUT Collaboration), Phys. Lett. **B504**, 218 (2001), arXiv:hep-ex/0012035 [hep-ex] .

[20] S. L. Glashow, Nucl. Phys. **22**, 579 (1961).

[21] S. Weinberg, Phys. Rev. Lett. **19**, 1264 (1967).

[22] A. Salam, *8th Nobel Symposium Lerum, Sweden, May 19-25, 1968*, Conf. Proc. **C680519**, 367 (1968).

[23] C. Patrignani *et al.* (Particle Data Group), Chin. Phys. **C40**, 100001 (2016), and 2017 update.

[24] S. Schael *et al.* (ALEPH Collaboration, DELPHI Collaboration, L3 Collaboration, OPAL Collaboration, SLD Collaboration, LEP Electroweak Working Group, SLD Electroweak Group, SLD Heavy Flavour Group), Phys. Rep. **427**, 257 (2006), arXiv:hep-ex/0509008 [hep-ex] .

[25] M. Goldhaber, L. Grodzins, and A. W. Sunyar, Phys. Rev. **109**, 1015 (1958).

[26] V. Lobashev, Nucl. Phys. A **719**, C153 (2003).

[27] C. Kraus, B. Bornschein, L. Bornschein, J. Bonn, B. Flatt, A. Kovalik, B. Ostrick, E. W. Otten, J. P. Schall, T. Thümmler, and C. Weinheimer, Eur. Phys. J C **40**, 447 (2005).

[28] L. Bornschein, B. Bornschein, S. Ebenhch, M. Hackenjos, F. Priester, M. Rllig, M. Sturm, and T. Thmmler (KATRIN Collaboration), Fusion Sci. Tech. **71**, 485 (2017), https://doi.org/10.1080/15361055.2017.1291241 .

[29] J. A. Formaggio and G. P. Zeller, Rev. Mod. Phys. **84**, 1307 (2012), arXiv:1305.7513 [hep-ex] .

[30] C. Andreopoulos *et al.*, Nucl. Instrum. Meth. **A614**, 87 (2010), arXiv:0905.2517 [hep-ph] .

[31] C. Andreopoulos, C. Barry, S. Dytman, H. Gallagher, T. Golan, R. Hatcher, G. Perdue, and J. Yarba, (2015), arXiv:1510.05494 [hep-ph] .

[32] J. P. Yáñez Garza, Ph.D. thesis, Humboldt-Universität zu Berlin, Berlin, Germany (2014).

[33] J. N. Bahcall, A. M. Serenelli, and S. Basu, Astrophys. J. Lett. **621**, L85 (2005), arXiv:astro-ph/0412440 .

[34] C. Athanassopoulos *et al.*, Nucl. Instrum. Meth. **A388**, 149 (1997).

[35] K. Kodama *et al.* (DONuT Collaboration), Phys. Rev. D **78**, 052002 (2008).

[36] K. Abe *et al.* (T2K Collaboration), Phys. Rev. D **87**, 012001 (2013).

[37] M. Honda, M. S. Athar, T. Kajita, K. Kasahara, and S. Midorikawa, Phys. Rev. D **92**, 023004 (2015), arXiv:502.03916 [astro-ph.HE] .

[38] A. Fedynitch, R. Engel, T. K. Gaisser, F. Riehn, and T. Stanev, *Proceedings, 18th International Symposium on Very High Energy Cosmic Ray Interactions (ISVHECRI 2014): Geneva, Switzerland, August 18-22, 2014*, EPJ Web Conf. **99**, 08001 (2015), arXiv:1503.00544 [hep-ph] .

[39] K. S. Hirata *et al.* (Kamiokande Collaboration), Phys. Rev. **D38**, 448 (1988).

[40] R. M. Bionta *et al.*, Phys. Rev. Lett. **58**, 1494 (1987).

[41] E. N. Alekseev, L. N. Alekseeva, I. V. Krivosheina, and V. I. Volchenko, Phys. Lett. **B205**, 209 (1988).

[42] T. J. Loredo and D. Q. Lamb, Phys. Rev. **D65**, 063002 (2002), arXiv:astro-ph/0107260 [astro-ph] .

[43] IceCube Collaboration, in *Proceedings, 35th International Cosmic Ray Conference (ICRC 2017)*, Vol. ICRC2017 (2017) p. 981.

[44] M. Aartsen *et al.* (IceCube Collaboration), Adv. Space Res. (2017), 10.1016/j.asr.2017.05.030.

[45] S. Bilenky and B. Pontecorvo, Phys. Rep. **41**, 225 (1978).

[46] Z. Maki, M. Nakagawa, and S. Sakata, Prog. Theor. Phys. **28**, 870 (1962).

[47] C. Giunti, Phys. Lett. **B686**, 41 (2010), arXiv:1001.0760 [hep-ph] .

[48] S. Bilenky, J. Hošek, and S. Petcov, Phys. Lett. B **94**, 495 (1980).

[49] M. Doi, T. Kotani, H. Nishiura, K. Okuda, and E. Takasugi, Phys. Lett. B **102**, 323 (1981).

[50] P. Langacker, S. Petcov, G. Steigman, and S. Toshev, Nucl. Phys. B **282**, 589 (1987).

[51] L. Wolfenstein, Phys. Rev. D **17**, 2369 (1978).

[52] L. Wolfenstein, Phys. Rev. D **18**, 958 (1978).

[53] H. A. Bethe, Phys. Rev. Lett. **56**, 1305 (1986).

[54] S. P. Mikheev and A. Yu. Smirnov, Sov. J. Nucl. Phys. **42**, 913 (1985), [Yad. Fiz.42,1441(1985)].

[55] E. K. Akhmedov, Sov. J. Nucl. Phys. **47**, 301 (1988), [Yad. Fiz.47,475(1988)].

[56] E. K. Akhmedov, Nucl. Phys. **B538**, 25 (1999), arXiv:hep-ph/9805272 [hep-ph] .

[57] E. K. Akhmedov, *Neutrino physics. Proceedings, Discussion Meeting, Ahmedabad, India, February 2-4, 1999*, Pramana **54**, 47 (2000), arXiv:hep-ph/9907435 [hep-ph] .

[58] M. Chizhov, M. Maris, and S. T. Petcov, (1998), arXiv:hep-ph/9810501 [hep-ph] .

[59] M. V. Chizhov and S. T. Petcov, Phys. Rev. D **63**, 073003 (2001), arXiv:hep-ph/9903424 .

[60] V. D. Barger, K. Whisnant, S. Pakvasa, and R. J. N. Phillips, Phys. Rev. **D22**, 2718 (1980).

[61] R. Wendell, (2009), `http://www.phy.duke.edu/~raw22/public/Prob3++/`.

[62] Y. Ashie *et al.* (Super-Kamiokande Collaboration), Phys. Rev. D **71**, 112005 (2005).

[63] K. Abe *et al.* (Super-Kamiokande Collaboration), (2017), arXiv:1710.09126 [hep-ex] .

[64] T. Kajita (Kamiokande, Super-Kamiokande Collaboration), *Proceedings, International Conference on Neutrino physics and astrophysics (Neutrino'98): Takayama, Japan, June 4-9, 1998*, Nucl. Phys. Proc. Suppl. **77**, 123 (1999), arXiv:hep-ex/9810001 [hep-ex] .

[65] J. Evans (MINOS+, MINOS Collaboration), *Proceedings, 27th International Conference on Neutrino Physics and Astrophysics (Neutrino 2016): London, United Kingdom, July 4-9, 2016*, J. Phys. Conf. Ser. **888**, 012017 (2017).

[66] K. Abe *et al.* (T2K Collaboration), Phys. Rev. **D96**, 092006 (2017), arXiv:1707.01048 [hep-ex] .

[67] P. Adamson *et al.* (NOvA Collaboration), Phys. Rev. Lett. **118**, 151802 (2017), arXiv:1701.05891 [hep-ex] .

[68] P. Adamson *et al.* (NOvA Collaboration), Phys. Rev. Lett. **118**, 231801 (2017), arXiv:1703.03328 [hep-ex] .

[69] P. Adamson *et al.*, Nucl. Instrum. Meth. **A806**, 279 (2016), arXiv:1507.06690 [physics.acc-ph] .

[70] P. Adamson *et al.* (MINOS Collaboration), Phys. Rev. Lett. **112**, 191801 (2014), arXiv:1403.0867 [hep-ex] .

[71] N. Agafonova *et al.* (OPERA Collaboration), Phys. Rev. Lett. **115**, 121802 (2015), arXiv:1507.01417 [hep-ex] .

[72] N. Agafonova *et al.* (OPERA Collaboration), PTEP **2014**, 101C01 (2014), arXiv:1407.3513 [hep-ex] .

[73] R. Davis, *International School on Nuclear Physics: 15th Course: Neutrinos in Cosmology, Astroparticle and Nuclear Physics Erice, Italy, September 8-17, 1993*, Prog. Part. Nucl. Phys. **32**, 13 (1994).

[74] W. Hampel *et al.* (GALLEX Collaboration), Phys. Lett. **B447**, 127 (1999).

[75] M. Altmann *et al.* (GNO Collaboration), Phys. Lett. **B616**, 174 (2005), arXiv:hep-ex/0504037 [hep-ex] .

[76] J. N. Abdurashitov *et al.* (SAGE Collaboration), J. Exp. Theor. Phys. **95**, 181 (2002), [Zh. Eksp. Teor. Fiz.122,211(2002)], arXiv:astro-ph/0204245 [astro-ph] .

[77] Y. Fukuda *et al.* (Kamiokande collaboration), Phys. Rev. Lett. **77**, 1683 (1996).

[78] K. Abe *et al.* (Super-Kamiokande Collaboration), Phys. Rev. **D83**, 052010 (2011), arXiv:1010.0118 [hep-ex] .

[79] J. Bahcall, "Solar neutrino viewgraphs," `http://www.sns.ias.edu/~jnb//`.

[80] J. N. Bahcall, Physica Scripta **2005**, 46 (2005).

[81] B. Aharmim *et al.* (SNO Collaboration), Phys. Rev. **C88**, 025501 (2013), arXiv:1109.0763 [nucl-ex] .

[82] G. Bellini *et al.* (Borexino Collaboration), Phys. Rev. **D89**, 112007 (2014), arXiv:1308.0443 [hep-ex] .

[83] F. P. An *et al.* (Daya Bay Collaboration), Phys. Rev. D **95**, 072006 (2017), arXiv:1610.04802 [hep-ex] .

[84] A. Gando *et al.* (KamLAND Collaboration), Phys. Rev. D **83**, 052002 (2011), arXiv:1009.4771 [hep-ex] .

[85] J. H. Choi *et al.* (RENO Collaboration), Phys. Rev. Lett. **116**, 211801 (2016), arXiv:1511.05849 [hep-ex] .

[86] Y. Abe *et al.* (Double Chooz Collaboration), JHEP **2016**, 163 (2016), arXiv:1510.08937 [hep-ex] .

[87] I. Esteban, M. C. Gonzalez-Garcia, M. Maltoni, I. Martinez-Soler, and T. Schwetz, JHEP **2017**, 87 (2017), arXiv:1611.01514 [hep-ph] .

[88] `http://www.nu-fit.org/`.

[89] F. Capozzi, E. Di Valentino, E. Lisi, A. Marrone, A. Melchiorri, and A. Palazzo, Phys. Rev. D **95**, 096014 (2017), arXiv:1703.04471 [hep-ph] .

[90] Y. Abe *et al.* (Double Chooz), JHEP **10**, 086 (2014), [Erratum: JHEP02,074(2015)], arXiv:1406.7763 [hep-ex] .

[91] F. P. An *et al.* (Daya Bay Collaboration), Chin. Phys. **C41**, 013002 (2017), arXiv:1607.05378 [hep-ex] .

[92] F. P. An *et al.* (Daya Bay Collaboration), Phys. Rev. Lett. **118**, 251801 (2017), arXiv:1704.01082 [hep-ex] .

[93] K. N. Abazajian *et al.*, (2012), arXiv:1204.5379 [hep-ph] .

[94] J. Kopp, P. A. N. Machado, M. Maltoni, and T. Schwetz, JHEP **2013**, 1 (2013), arXiv:1303.3011 [hep-ph] .

[95] P. Adamson *et al.* (MINOS Collaboration), Submitted to: Phys. Rev. Lett. (2017), arXiv:1710.06488 [hep-ex] .

[96] M. G. Aartsen *et al.* (IceCube Collaboration), Phys. Rev. Lett. **117**, 071801 (2016), arXiv:1605.01990 [hep-ex] .

[97] K. Abe *et al.* (Super-Kamiokande Collaboration), Phys. Rev. **D91**, 052019 (2015), arXiv:1410.2008 [hep-ex] .

[98] I. E. Stockdale *et al.*, Phys. Rev. Lett. **52**, 1384 (1984).

[99] F. Dydak *et al.*, Phys. Lett. B **134**, 281 (1984).

[100] G. Cheng *et al.* (SciBooNE, MiniBooNE Collaboration), Phys. Rev. **D86**, 052009 (2012), arXiv:1208.0322 [hep-ex] .

[101] P. Adamson *et al.* (NOvA Collaboration), Phys. Rev. **D96**, 072006 (2017), arXiv:1706.04592 [hep-ex] .

[102] M. G. Aartsen *et al.* (IceCube), Phys. Rev. **D95**, 112002 (2017), arXiv:1702.05160 [hep-ex] .

[103] P. Huber, M. Lindner, and W. Winter, Comput. Phys. Commun. **167**, 195 (2005), arXiv:hep-ph/0407333 [hep-ph] .

[104] P. Huber, J. Kopp, M. Lindner, M. Rolinec, and W. Winter, Comput. Phys. Commun. **177**, 432 (2007), arXiv:hep-ph/0701187 [hep-ph] .

[105] J. Kopp, "Sterile neutrinos and non-standard interactions (v1.1)," (2011), `https://www.mpi-hd.mpg.de/personalhomes/globes/tools.html`.

[106] Q. Y. Liu and A. Yu. Smirnov, Nucl. Phys. **B524**, 505 (1998), arXiv:hep-ph/9712493 [hep-ph] .

[107] Q. Y. Liu, S. P. Mikheyev, and A. Yu. Smirnov, Phys. Lett. **B440**, 319 (1998), arXiv:hep-ph/9803415 [hep-ph] .

[108] S. Razzaque and A. Y. Smirnov, JHEP **2011**, 84 (2011), arXiv:1104.1390 [hep-ph] .

[109] H. Nunokawa, O. Peres, and R. Zukanovich Funchal, Phys. Lett. B **562**, 279 (2003), arXiv:hep-ph/0302039 .

[110] S. Razzaque and A. Y. Smirnov, Phys. Rev. D **85**, 093010 (2012), arXiv:1203.5406 [hep-ph] .

[111] P. A. Čerenkov, Phys. Rev. **52**, 378 (1937).

[112] I. Frank and T. Ig, C.R. Acad. Sci. U.S.S.R. **14**, 109 (1937).

[113] I. Tamm, J. Phys. U.S.S.R. **1** (1939).

[114] D. E. Groom, N. V. Mokhov, and S. I. Striganov, At. Data Nucl. Data Tables **78**, 183 (2001).

[115] L. Rädel, Master's thesis, Rheinisch-Westflischen Technischen Hochschule, Aachen, Germany (2012).

[116] C. Wiebusch, Ph.D. thesis, Rheinisch-Westflischen Technischen Hochschule, Aachen, Germany (1995).

[117] R. Abbasi *et al.* (IceCube Collaboration), Nucl. Instrum. Meth. **A601**, 294 (2009), arXiv:0810.4930 [physics.ins-det] .

[118] R. Abbasi *et al.* (IceCube Collaboration), Nucl. Instrum. Meth. **A618**, 139 (2010), arXiv:1002.2442 [astro-ph.IM] .

[119] R. Abbasi *et al.* (IceCube Collaboration), Astropart. Phys. **35**, 615 (2012), arXiv:1109.6096 [astro-ph.IM] .

[120] T. Benson, J. Cherwinka, M. Duvernois, A. Elcheikh, F. Feyzi, L. Greenler, J. Haugen, A. Karle, M. Mulligan, and P. R., Ann. Glaciol. **55(68)**, 105 (2014).

[121] D. Chirkin (IceCube Collaboration), in *Proc 33rd International Cosmic Ray Conference (ICRC2013): Rio de Janeiro, Brazil, July 2-9, 2013* (2013) p. 0580.

[122] R. C. Bay, R. A. Rohde, P. B. Price, and N. E. Bramall, J. Geophys. Res. **115**, n/a (2010), d14126.

[123] M. G. Aartsen *et al.* (IceCube), Nucl. Instrum. Meth. **A711**, 73 (2013), arXiv:1301.5361 [astro-ph.IM] .

[124] M. G. Aartsen *et al.* (IceCube collaboration), *Journal of Glaciology*, **59**, 1117 (2013).

[125] J.-H. Koehne, K. Frantzen, M. Schmitz, T. Fuchs, W. Rhode, D. Chirkin, and J. B. Tjus, Comput. Phys. Commun. **184**, 2070 (2013).

[126] S. Agostinelli *et al.* (GEANT4), Nucl. Instrum. Meth. **A506**, 250 (2003).

[127] `https://github.com/claudiok/clsim`.

[128] M. Larson, Master's thesis, University of Alabama, Tuscaloosa, AL, USA (2013).

[129] J. A. Aguilar *et al.*, Astropart. Phys/ **34**, 652 (2011), arXiv:1105.4116 [astro-ph.IM] .

[130] M. Aartsen *et al.* (IceCube collaboration), Nucl. Instrum. Meth. **A736**, 143 (2014).

[131] S. Euler, Ph.D. thesis, Rheinisch-Westflischen Technischen Hochschule, Aachen, Germany (2014).

[132] A. Terliuk, *Energy reconstruction of $\nu_\mu$ events in DeepCore*, Master's thesis, Taras Shevchenko National University of Kyiv, Ukraine (2014), defended in Ukrainian, english version available from `andrey.terlyuk@gmail.com`.

[133] R. Nahnhauer, A. Terliuk, and J. P. Yanez, IceCube Internal Report **201304001-v2** (2013), available upon request from members of IceCube Collaboration.

[134] J. Lundberg, P. Miocinovic, T. Burgess, J. Adams, S. Hundertmark, P. Desiati, K. Woschnagg, and P. Niessen, Nucl. Instrum. Meth. **A581**, 619 (2007), arXiv:astro-ph/0702108 [ASTRO-PH] .

[135] O. Schulz, *The design study of IceCube DeepCore: Characterization and veto studies*, Ph.D. thesis, Max-Plank Institüt für Kernphysik, Heidelbeg, Germany (2010).

[136] J. Ahrens *et al.* (AMANDA Collaboration), Nucl. Instrum. Meth. **A524**, 169 (2004).

[137] M. Dunkman, Ph.D. thesis, The Pennsylvania State University, State College, PA, USA (2015).

[138] S. S. Wilks, Ann. Math. Statist. **9**, 60 (1938).

[139] G. D. Barr, T. K. Gaisser, S. Robbins, and T. Stanev, Phys. Rev. **D74**, 094009 (2006), arXiv:astro-ph/0611266 [astro-ph] .

[140] J. P. Yáñez Garza, Communication inside the IceCube Collaboration.

[141] D. Chirkin and M. Rongen, Communication inside the IceCube Collaboration.

[142] A. M. Dziewonski and D. L. Anderson, Phys. Earth Planet. In. **25**, 297 (1981).

[143] F. James and M. Roos, Comput. Phys. Commun. **10**, 343 (1975).

[144] `https://github.com/iminuit/iminuit`.

[145] G. J. Feldman and R. D. Cousins, Phys. Rev. **D57**, 3873 (1998), arXiv:physics/9711021 [physics.data-an] .

[146] G. Cowan, K. Cranmer, E. Gross, and O. Vitells, Eur. Phys. J. **C71**, 1554 (2011), [Erratum: Eur. Phys. J.C73,2501(2013)], arXiv:1007.1727 [physics.data-an] .

[147] I. Salvadori (ANTARES collaboration), in *Proceedings, 35th International Cosmic Ray Conference (ICRC 2017)*, Vol. ICRC2017, p. 1026.

[148] A. Fedynitch, J. Becker Tjus, and P. Desiati, Phys. Rev. D **86**, 114024 (2012), arXiv:1206.6710 [astro-ph.HE] .

[149] `https://github.com/afedynitch/MCEq`.

# Appendices

# Appendix A

# Impact of fit parameters

This section shows the impact of each fit parameters on the data rate for the studies presented in this work. The impact on the measurement of the standard neutrino oscillations is discussed in Section A.1. Section A.2 discusses the impact in the sterile neutrino search.

## A.1 Measurement of standard neutrino mixing

This section discusses the impact of the fit parameters on the reconstructed variables as used in the atmospheric neutrino mixing measurement, discussed in Chapter 6. The baseline values and probed points for each fit parameter can be found in Table A.1.

Figures A.1-A.14 demonstrate the impact of each fit parameter on the reconstructed variables. Each of the figures is split into sub-panels. The upper panel row depicts the energy, zenith and PID distributions for the baseline values and their modifications by a probed fit parameter. Other four panels show the impact of the parameter on the event rate for the track (middle row) and cascade (bottom row) channels as used in the analysis. The figures depict only the effects on the shape of the distributions, while the total event count is renormalised to the same number. The captions of each figure discuss the characteristic effects caused by the corresponding parameter.

Table A.1: The list of the parameters used in the standard atmospheric mixing measurement, their baseline and probed values, and the corresponding figure numbers.

| Parameter | Baseline value | Probed values | Figure |
|---|---|---|---|
| **Oscillations parameters** | | | |
| $\Delta m^2_{32}$ [ $10^{-3}$ eV$^2$ ] | 2.44 | 2.29, 2.59 | A.1 |
| $\sin^2\theta_{23}$ | 0.565 | 0.5, 0.65 | A.2 |
| **Flux parameters** | | | |
| $\nu_e$ norm. [ % ] | 100 | 95, 105 | A.3 |
| $\Delta\gamma$ | 0.05 | 0.0, 0.1 | A.4 |
| $(\nu/\bar{\nu})$ [ $\sigma$ ] | 0 | –1, +1 | A.5 |
| (up./hor.) [ $\sigma$ ] | 0 | –1, +1 | A.6 |
| **Detector parameters** | | | |
| DOM eff. [ % ] | 100 | 90, 110 | A.7 |
| Hole ice $p_1$ | 0.25 | 0.15, 0.35 | A.8 |
| Hole ice $p_2$ | 0 | –1, +1 | A.9 |
| spiciness | 0 | –0.5, +0.5 | A.10 |
| **Cross section** | | | |
| NC norm. [ % ] | 100 | –20, +20 | A.11 |
| $M_A^{CCQE}$ [ $\sigma$ ] | 0 | –1, +1 | A.12 |
| $M_A^{CCRES}$ [ $\sigma$ ] | 0 | –1, +1 | A.13 |
| **Background** | | | |
| Atm. $\mu$. frac. [ % ] | 1 | 0, 5 | A.14 |

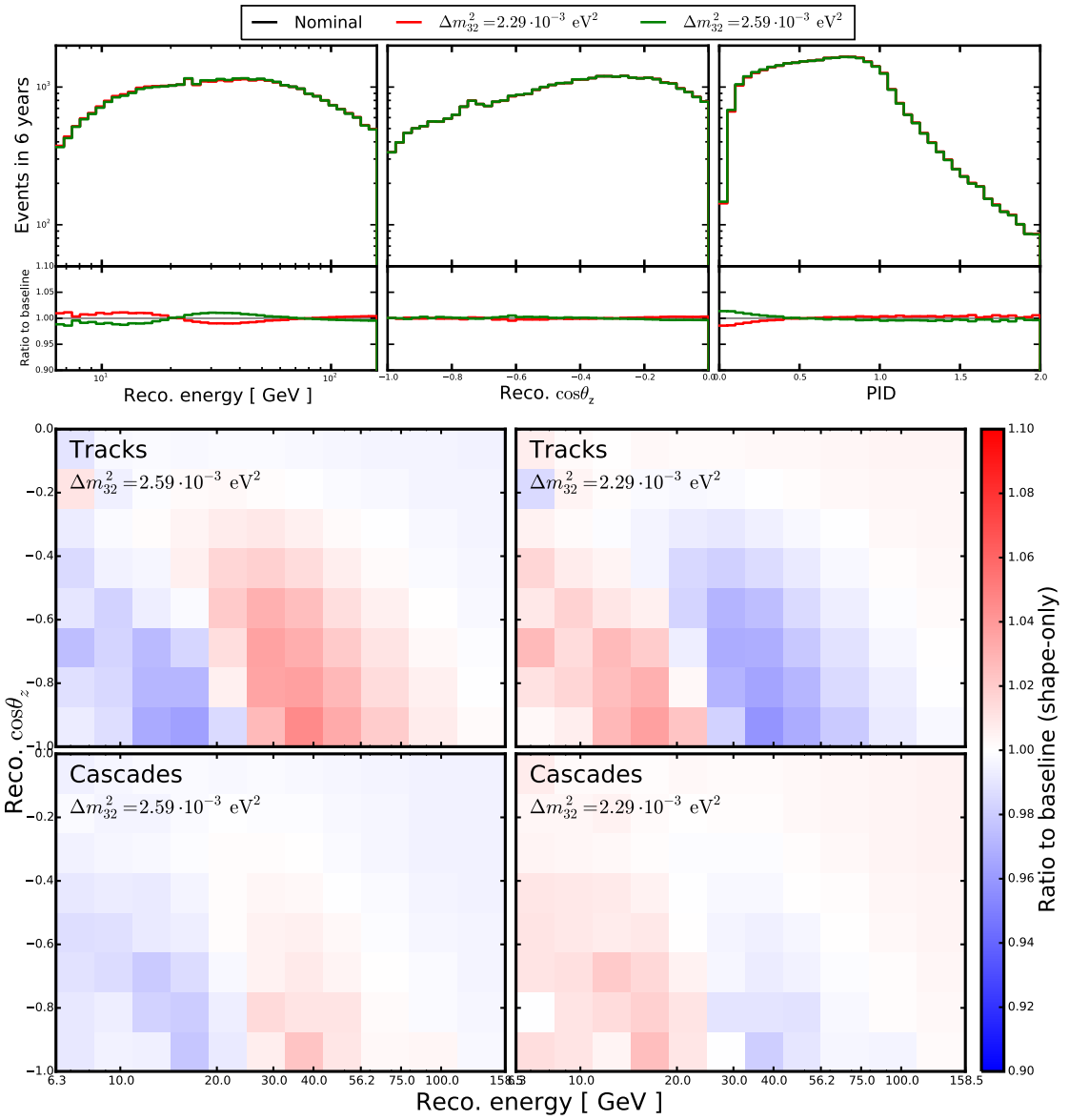


Figure A.1: The impact of $\Delta m^2_{32}$ in the standard atmospheric oscillation study. Its change shifts the energy of the oscillations minimum, what results in the wave-like shape that can be seen for the energy projection, as well as on 2D distributions.

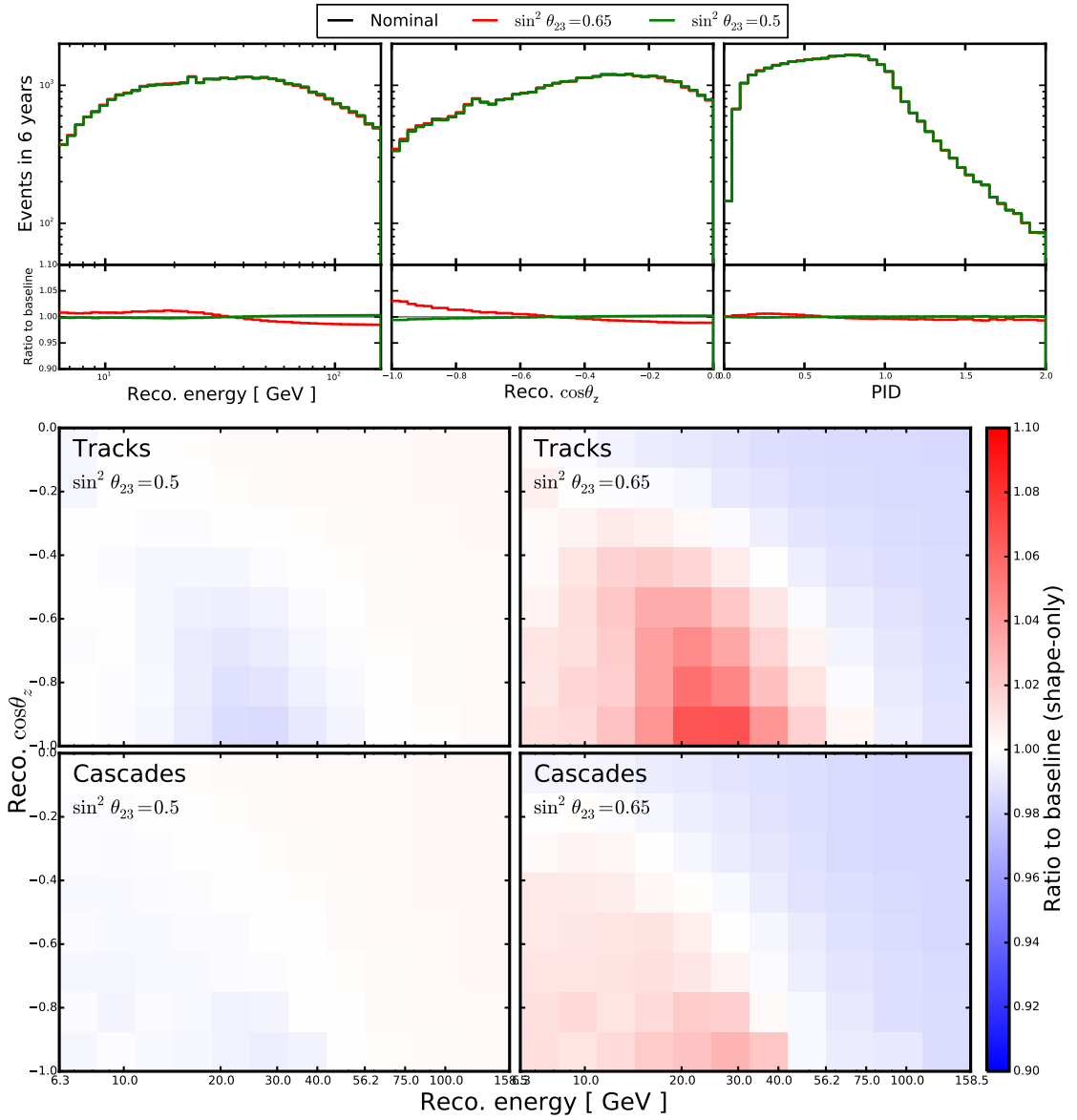


Figure A.2: The impact of $\sin^2\theta_{23}$ in the standard atmospheric mixing study. It changes the depth of the oscillation minimum resulting in a modification of the magnitude of $\nu_\mu$ disappearance effects.

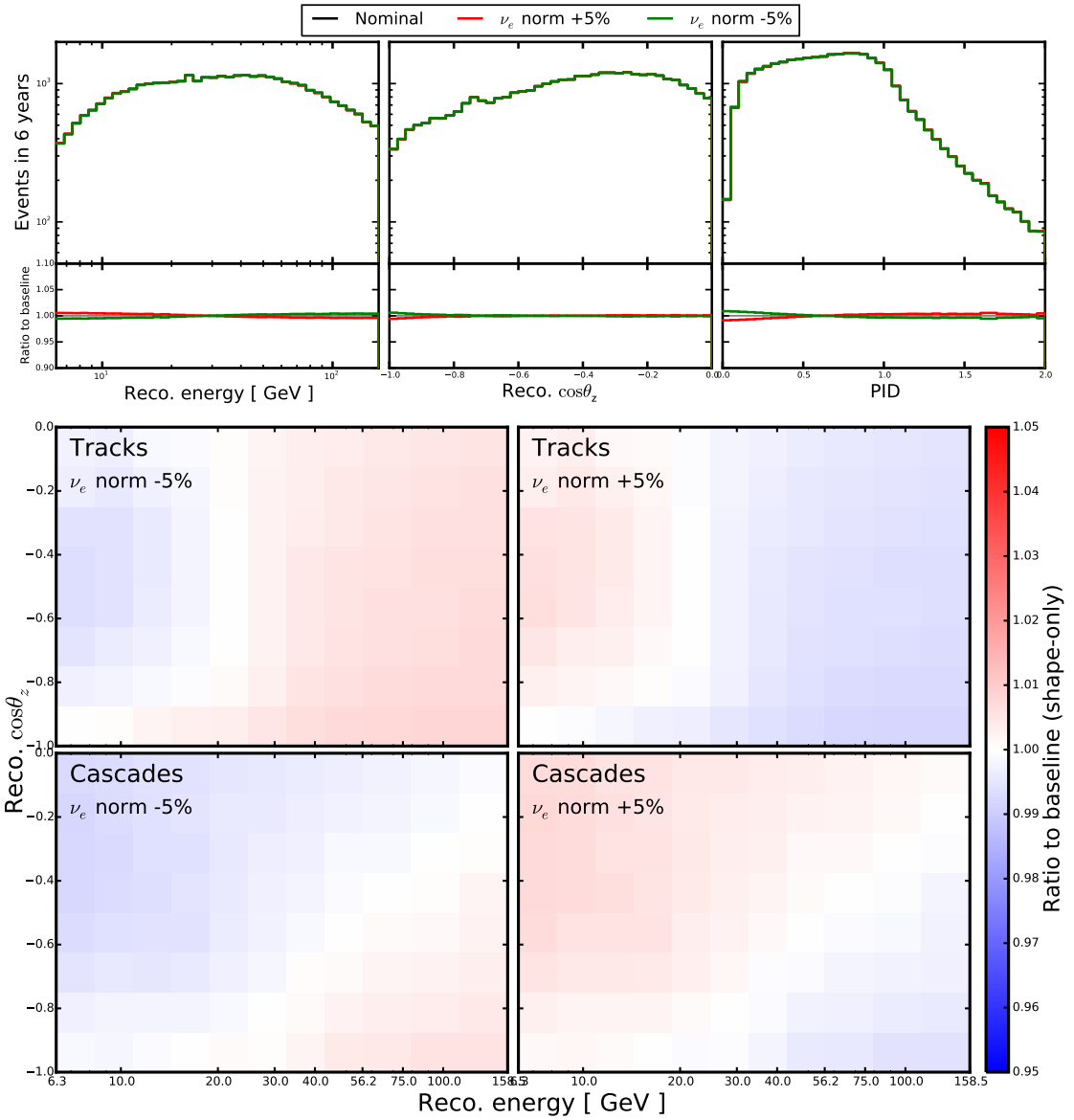


Figure A.3: The impact of the electron neutrino normalisation in the standard atmospheric oscillations study. Its effects are caused by the distribution of electron neutrino events in the final sample.

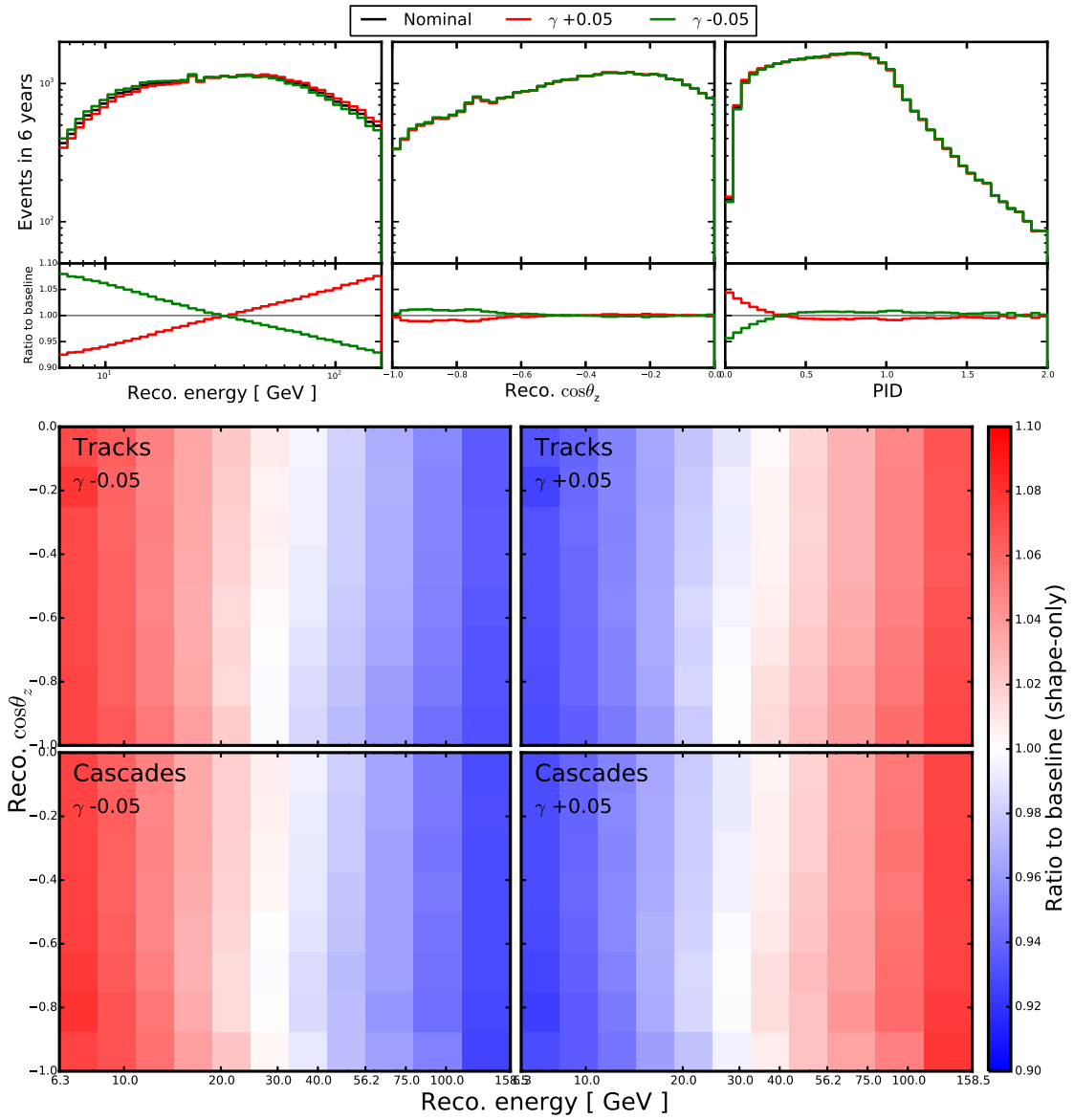


Figure A.4: The impacts of the spectral index in the standard atmospheric mixing study. The main effect is a change of the slope of the energy distribution.

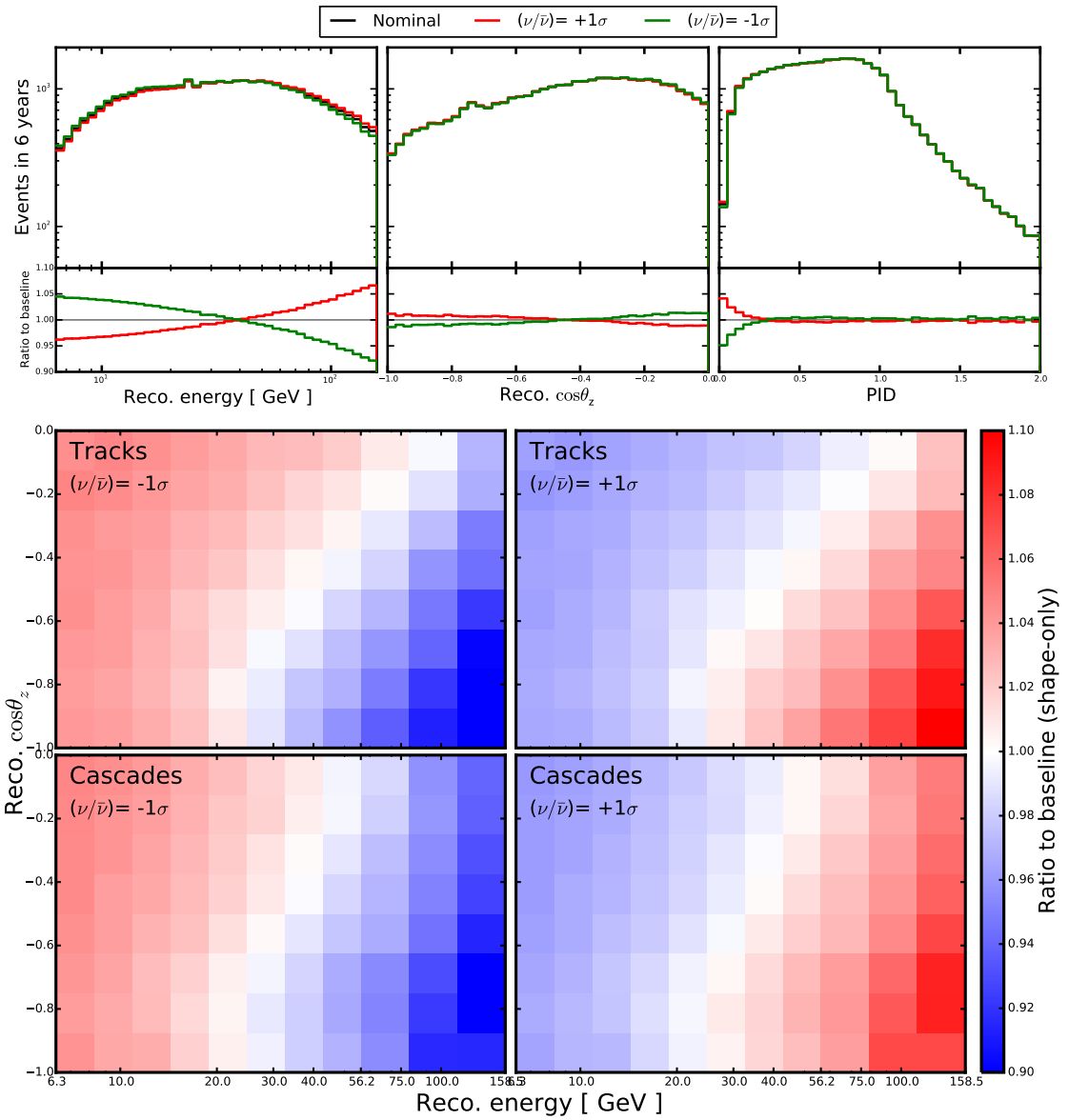


Figure A.5: The impact of the neutrino-antineutrino flux ratio in the standard atmospheric oscillation study. For energy the impact is similar to the spectral index. However, this parameter also results in additional modification of the zenith distribution.

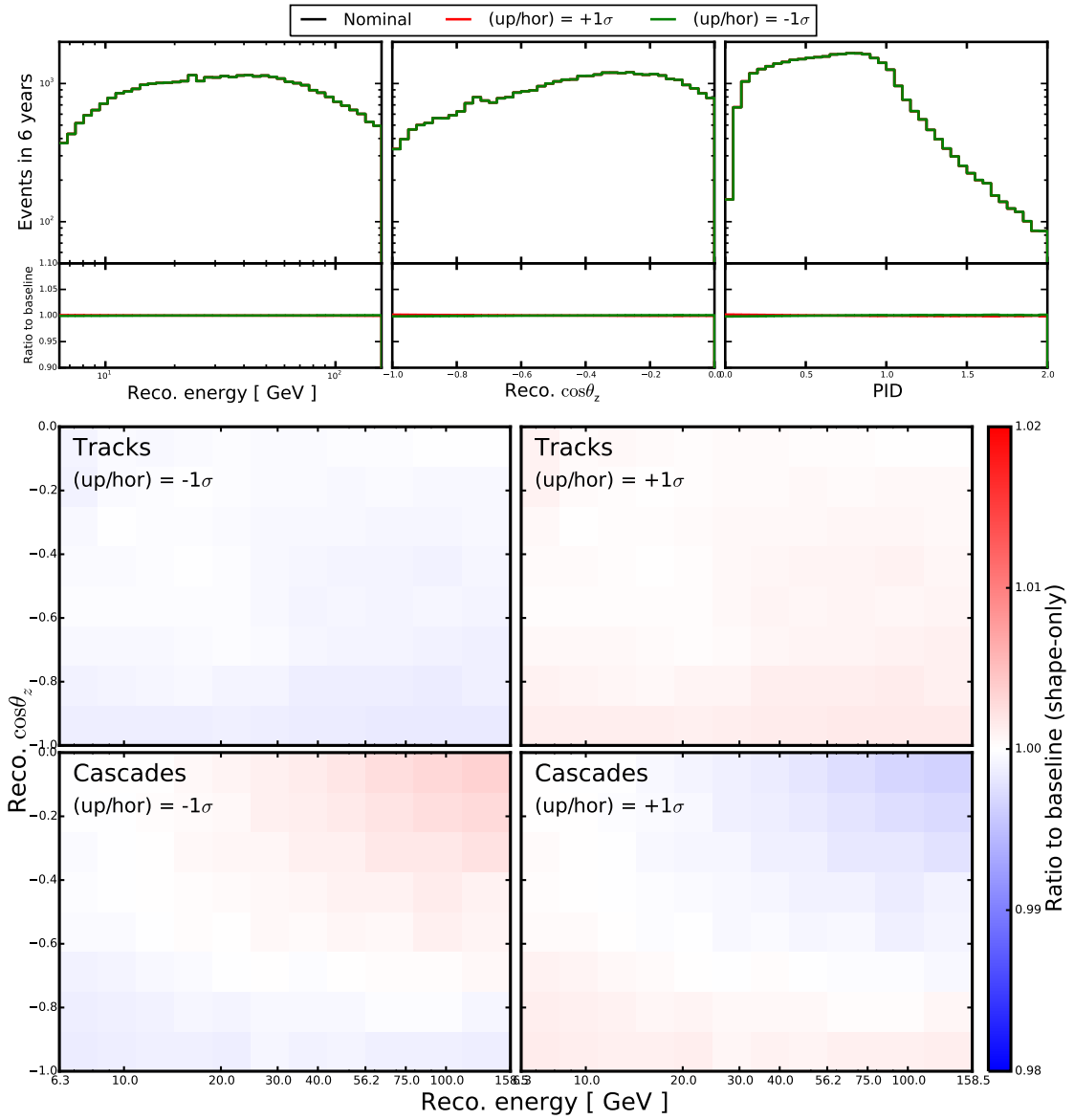


Figure A.6: The impact of the upgoing-horizontal flux ratio in the standard atmospheric oscillations study. It has a relatively small impact, since the main effects are already taken into account by the neutrino-antineutrino flux ratio.

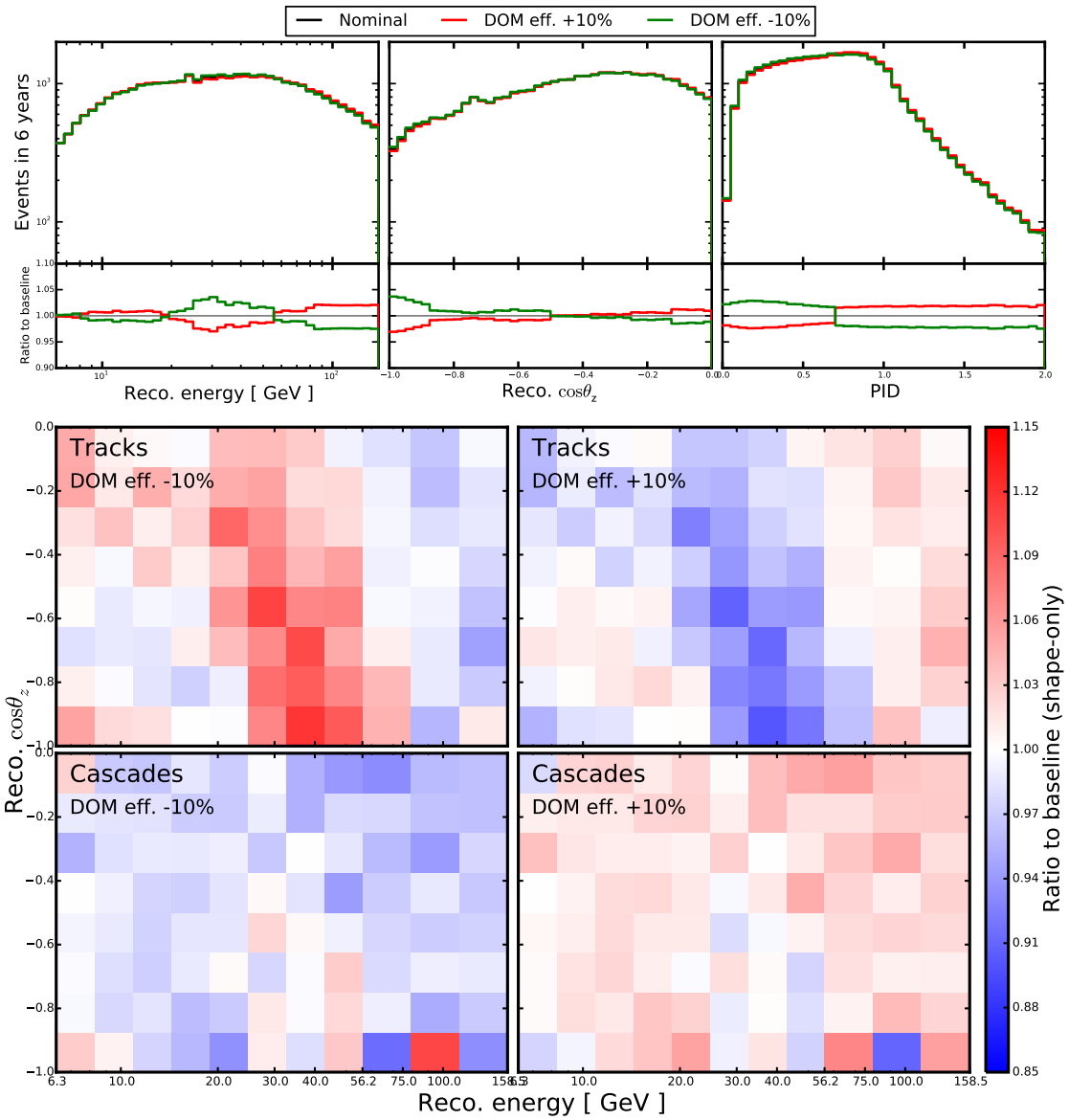


Figure A.7: The impact of the DOM efficiency in the standard atmospheric mixing study. This parameter changes the effective reconstructed energy scale and has effects similar to $\Delta m^2_{32}$. The sharp changes of the rate that can be seen in some projections are caused by the impact of MC statistical fluctuations on the parametrisations of the detector uncertainties. Their locations coincide with the analysis bin edges, which are used for the bin-by-bin parametrizations. This effect is especially pronounced for the PID distribution, which is split only into 2 bins in the analysis. The "noise" that can be seen in the 2D distributions has the same nature and is visually magnified by renormalisation of the histograms to show the shape-only effects. Similar effects can be also seen for the other detector parameters.

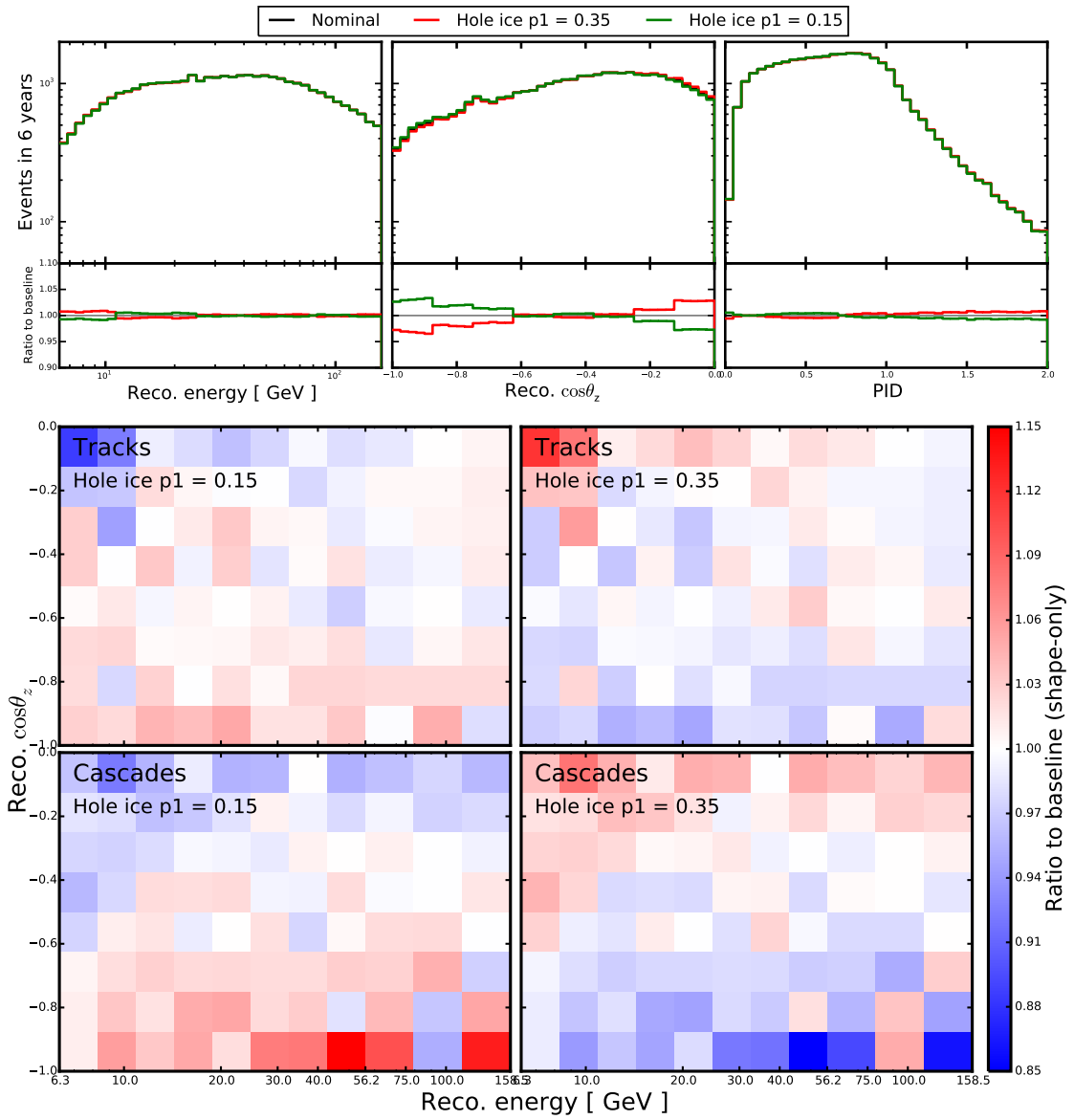


Figure A.8: The impact of the hole ice $p_1$ parameter in the standard atmospheric mixing measurement. It mainly affects the reconstructed zenith distribution. The projections and 2D distributions show the same artefacts inherent for all detector parameters (see caption of Figure A.7).

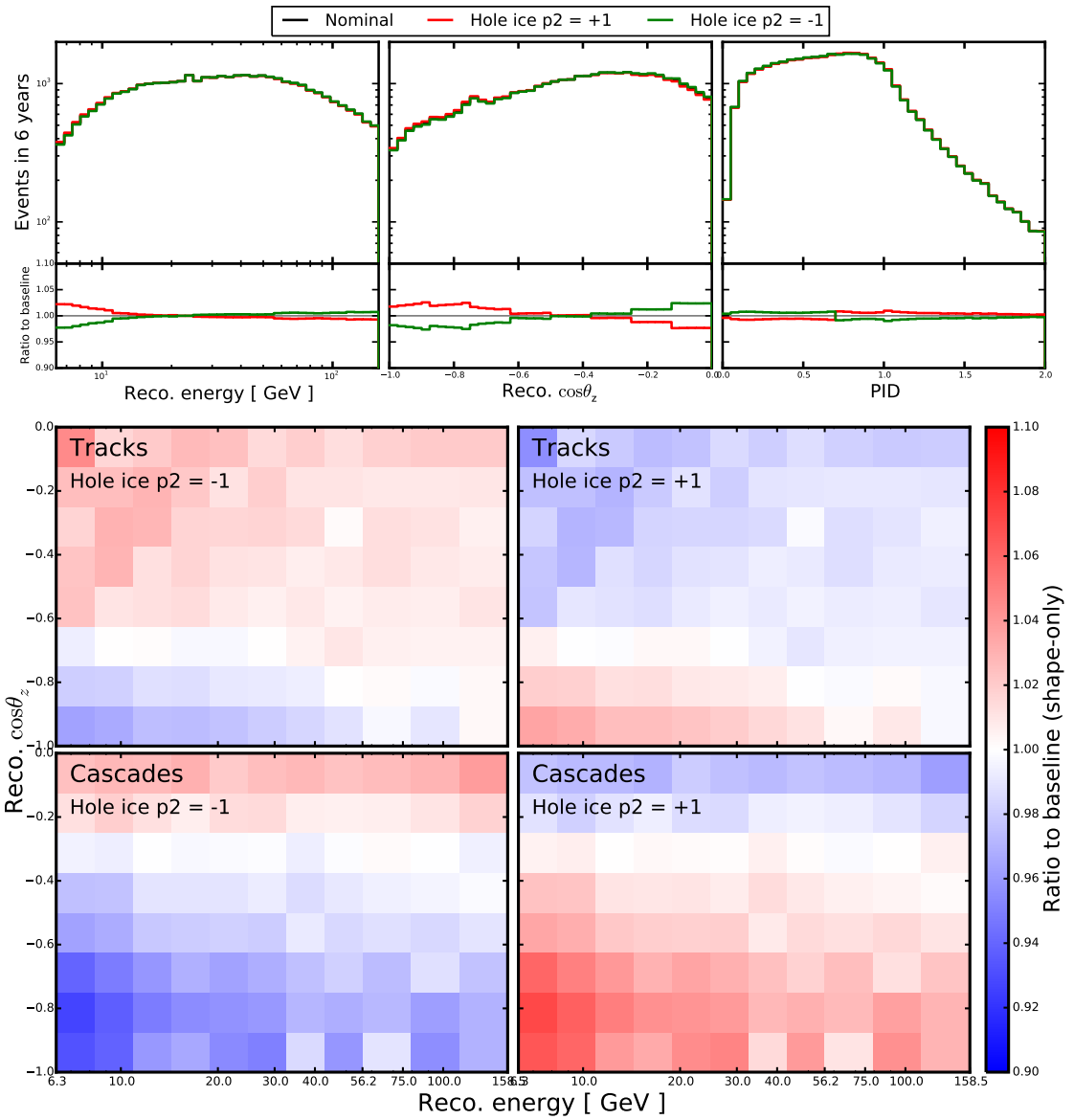


Figure A.9: The impact of the hole ice $p_2$ parameter in the standard oscillations measurement. The impact has similarities to the hole ice $p_1$ parameter, what explains a rather large correlation between these parameters in the analysis. The projections and 2D distributions show the same artefacts that can be seen for all detector parameters (see caption of Figure A.7).

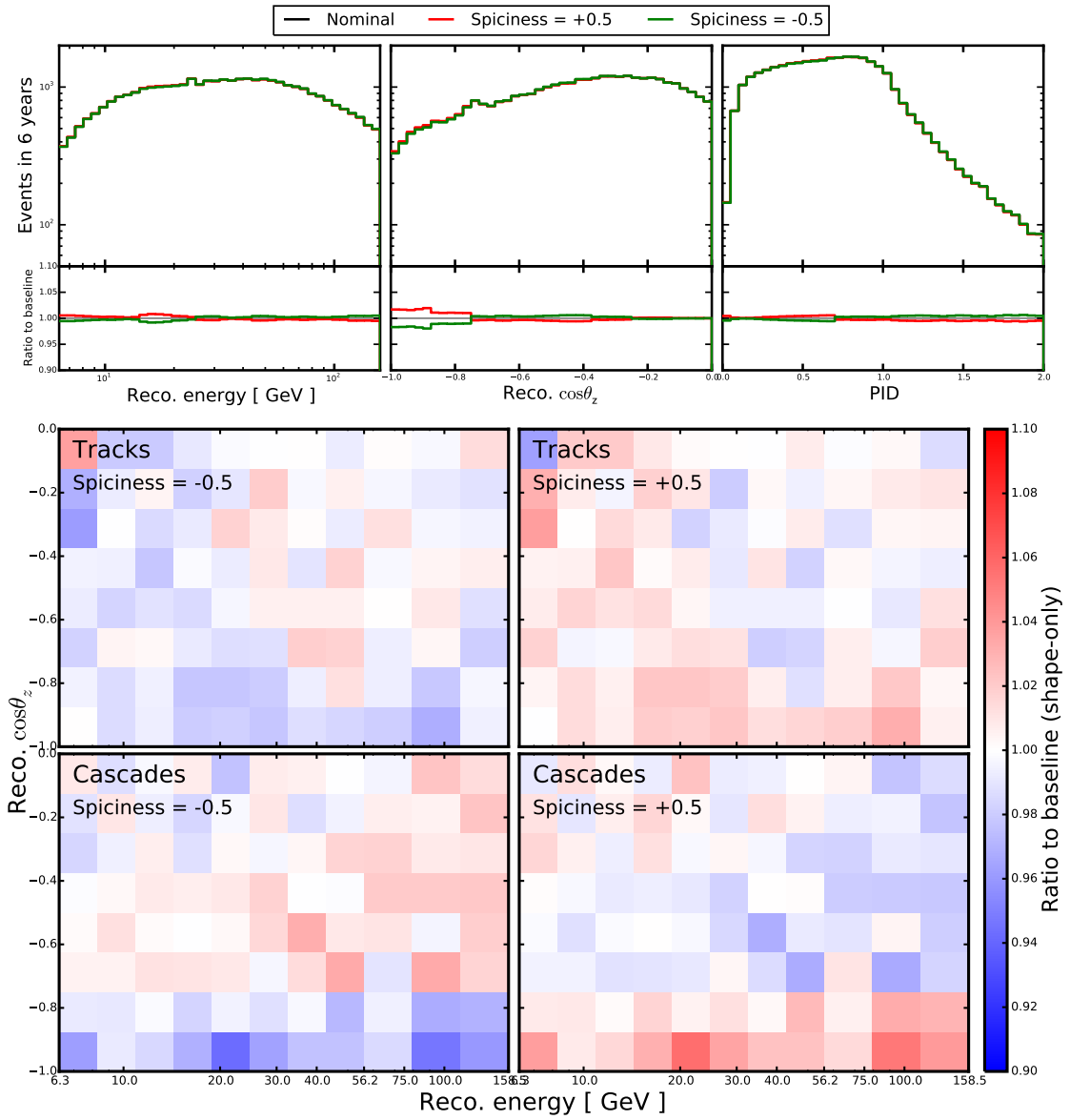


Figure A.10: The impact of the *spiciness* parameter. The impact is relatively small but is located in the signal region, leading to a possible impact on the mixing angle. The projections and 2D distributions show the artefacts that can be seen for all detector parameters (see caption of Figure A.7).

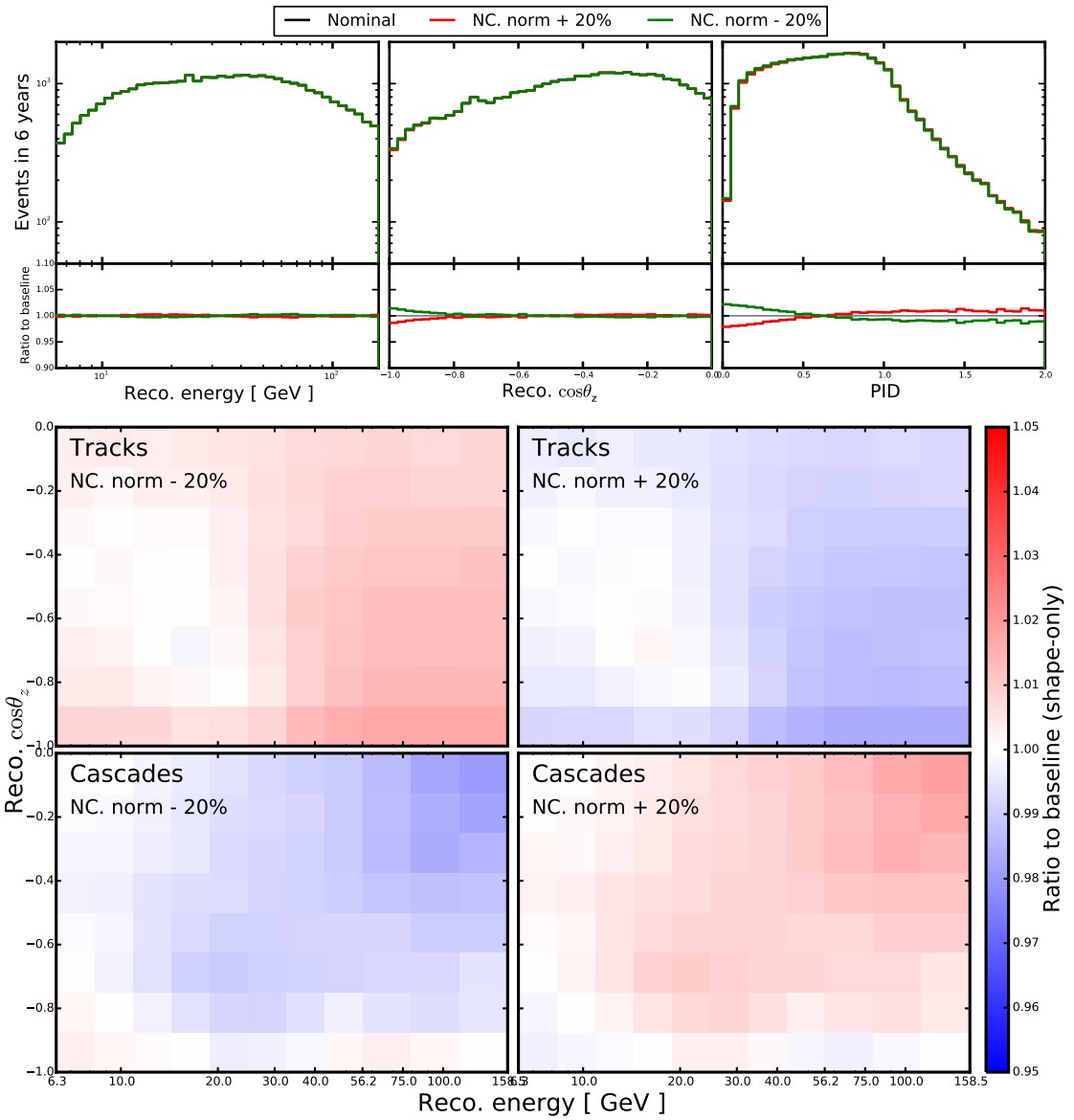


Figure A.11: The impact of the NC event normalisation in the standard neutrino oscillations study. The effects are caused by the energy, zenith and PID distribution of the NC events in the final sample.

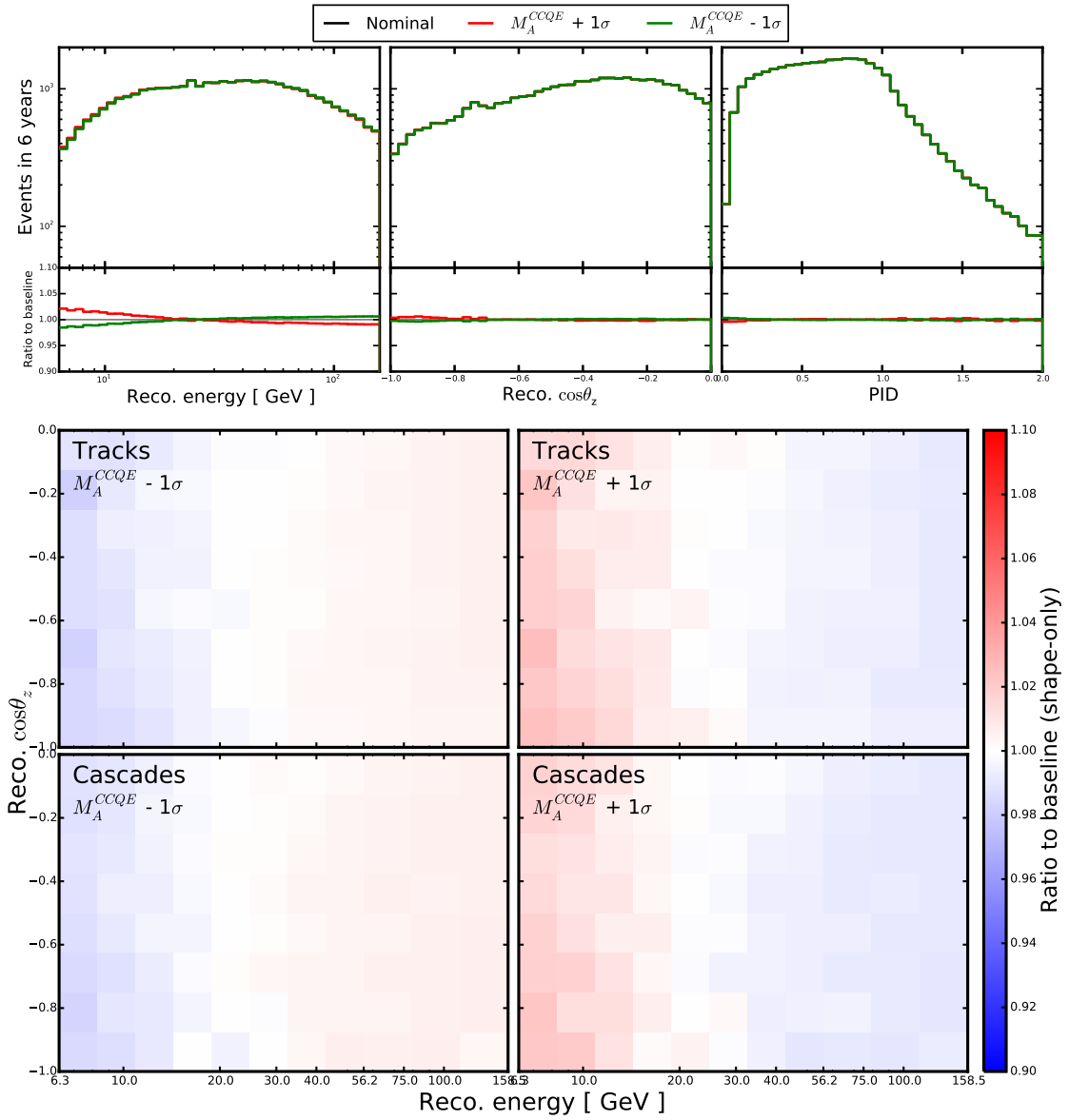


Figure A.12: The impact of the axial mass for the quasi-elastic scattering in the standard atmospheric mixing measurement. The impact is maximal at the energies below 10 GeV, where the cross-section for QE scattering is comparable with the DIS cross-section.

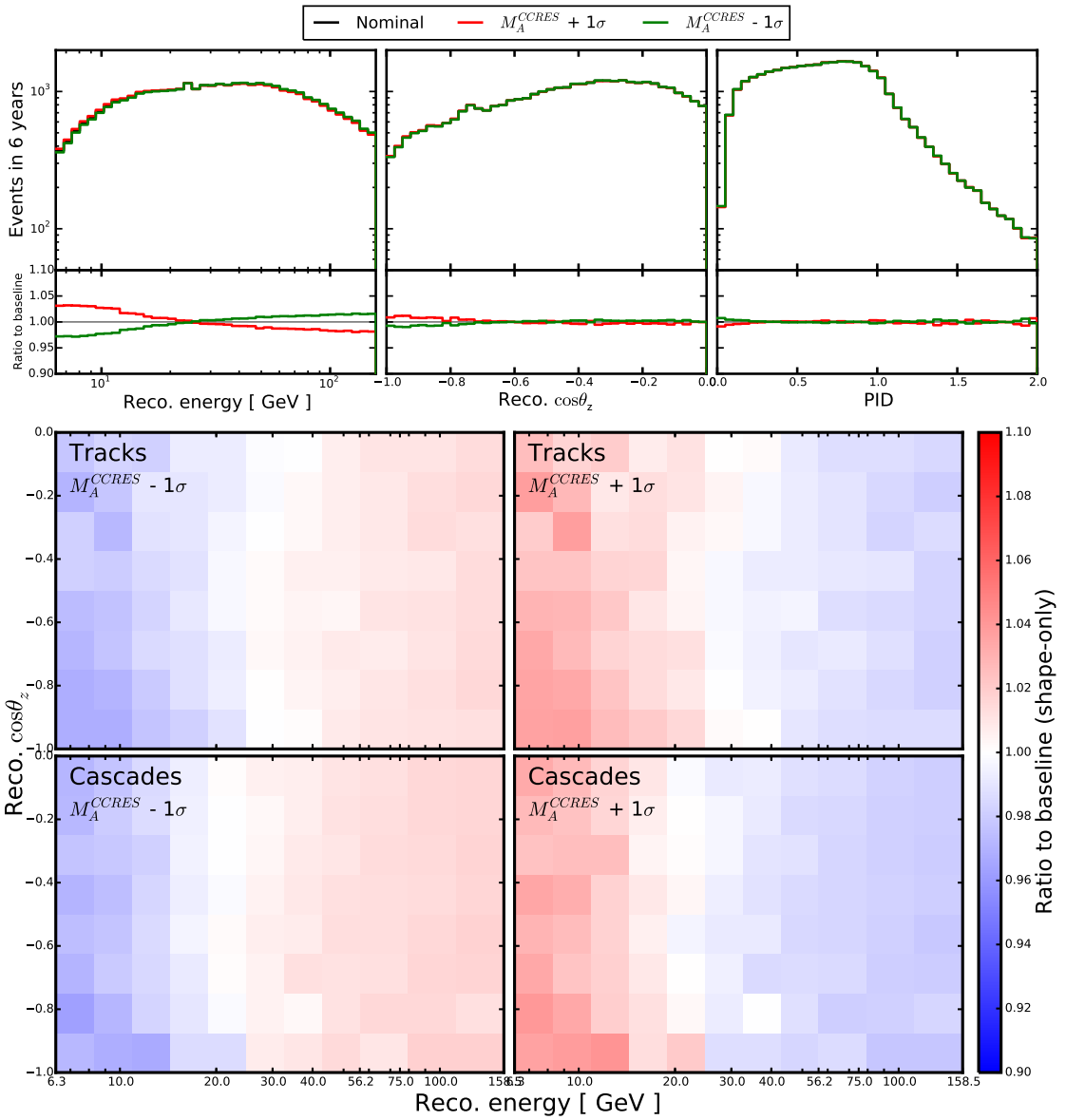


Figure A.13: The impact of the axial mass for the resonant production in the standard atmospheric mixing measurement. Its impact is located at the energies of up to 20GeV, higher than for the QE scattering.

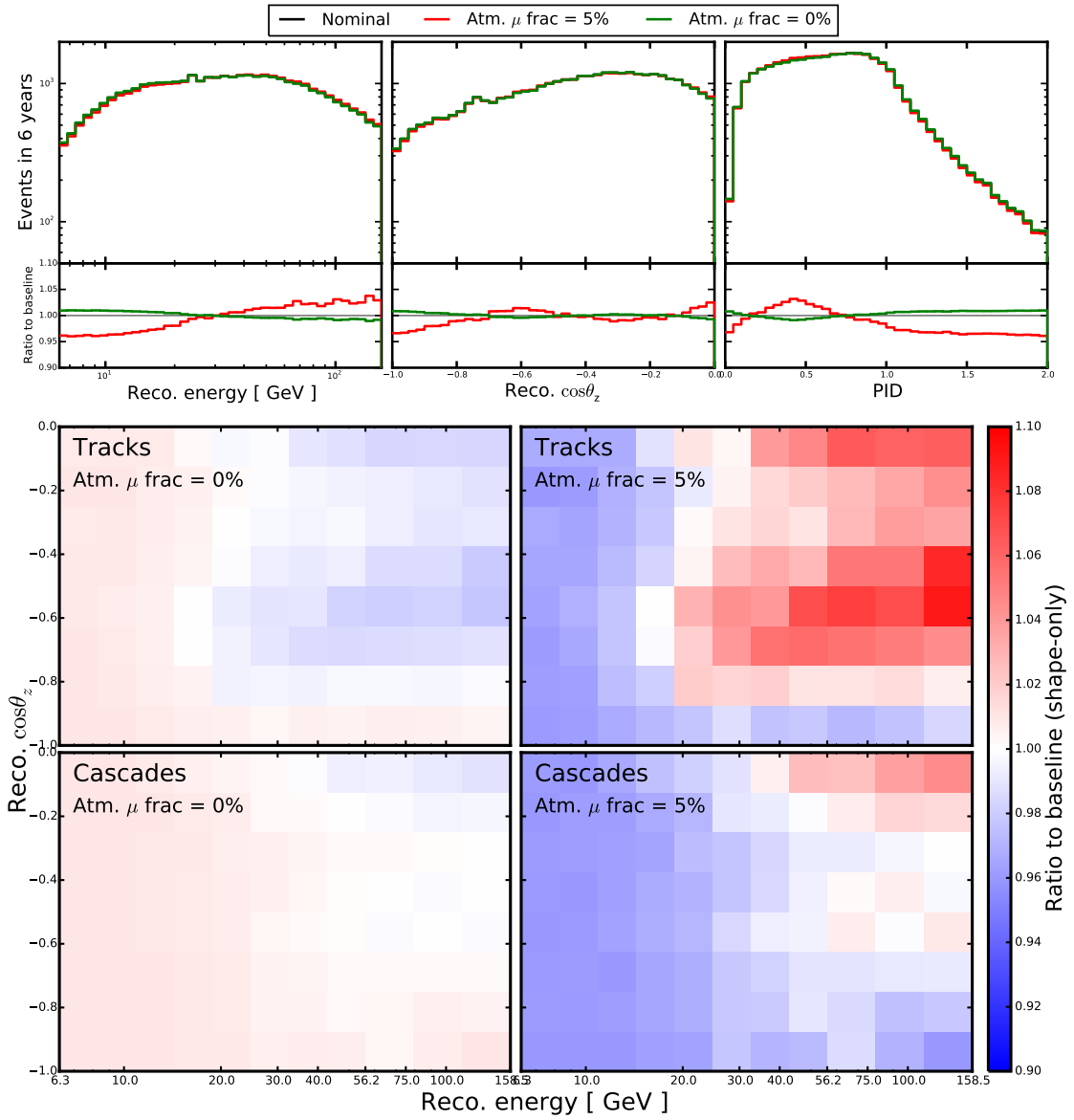


Figure A.14: The impact of the atmospheric muon contamination in the standard atmospheric mixing measurement. It is caused by the distribution of the atmospheric muons in the data-driven template.

## A.2 Search for sterile neutrinos

This section shows the impact of the nuisance parameters on the sterile neutrino search, presented in Chapter 7. The impact of the sterile neutrino mixing angles can be found in Section 7.3. The baseline values and probed points for each parameter can be found in Table A.2.

Figures A.15–A.25 depict the impact of each fit parameter. The upper panels of each figure show the impact of the parameter on the projected energy and zenith distributions, while bottom panels depict the impact on the event count in the experimental binning. This work uses the shape-only effects in the analysis. Therefore, the event count in each histogram is renormalised to show only the change of shape and not the general normalisation. The figure captions discuss the most characteristic effects caused by each parameter.

Table A.2: The list of the nuisance parameters used in the sterile neutrino search, their baseline values and points probed in Figures A.15–A.25.

| Parameter | Baseline value | Probed values | Figure |
|---|---|---|---|
| **Oscillations parameters** | | | |
| $\Delta m^2_{32}$ [ $10^{-3}$ eV$^2$ ] | 2.44 | 2.29, 2.59 | A.15 |
| $\sin^2\theta_{23}$ | 0.565 | 0.5, 0.65 | A.16 |
| **Flux parameters** | | | |
| $\nu_e$ norm. [ % ] | 100 | 95, 105 | A.17 |
| $\Delta\gamma$ | 0.05 | 0.0, 0.1 | A.18 |
| $(\nu/\bar{\nu})$, energy [ $\sigma$ ] | 0 | –1, +1 | A.19 |
| $(\nu/\bar{\nu})$, zenith [ $\sigma$ ] | 0 | –1, +1 | A.20 |
| **Detector parameters** | | | |
| DOM eff. [ % ] | 100 | 90, 110 | A.21 |
| Hole ice scattering [ cm$^{-1}$ ] | 0.02 | 0.01, 0.03 | A.22 |
| **Cross section** | | | |
| $M_A^{CCQE}$ [ $\sigma$ ] | 0 | –1, +1 | A.23 |
| $M_A^{CCRES}$ [ $\sigma$ ] | 0 | –1, +1 | A.24 |
| **Background** | | | |
| Atm. $\mu$. frac. [ % ] | 1 | 0, 5 | A.25 |

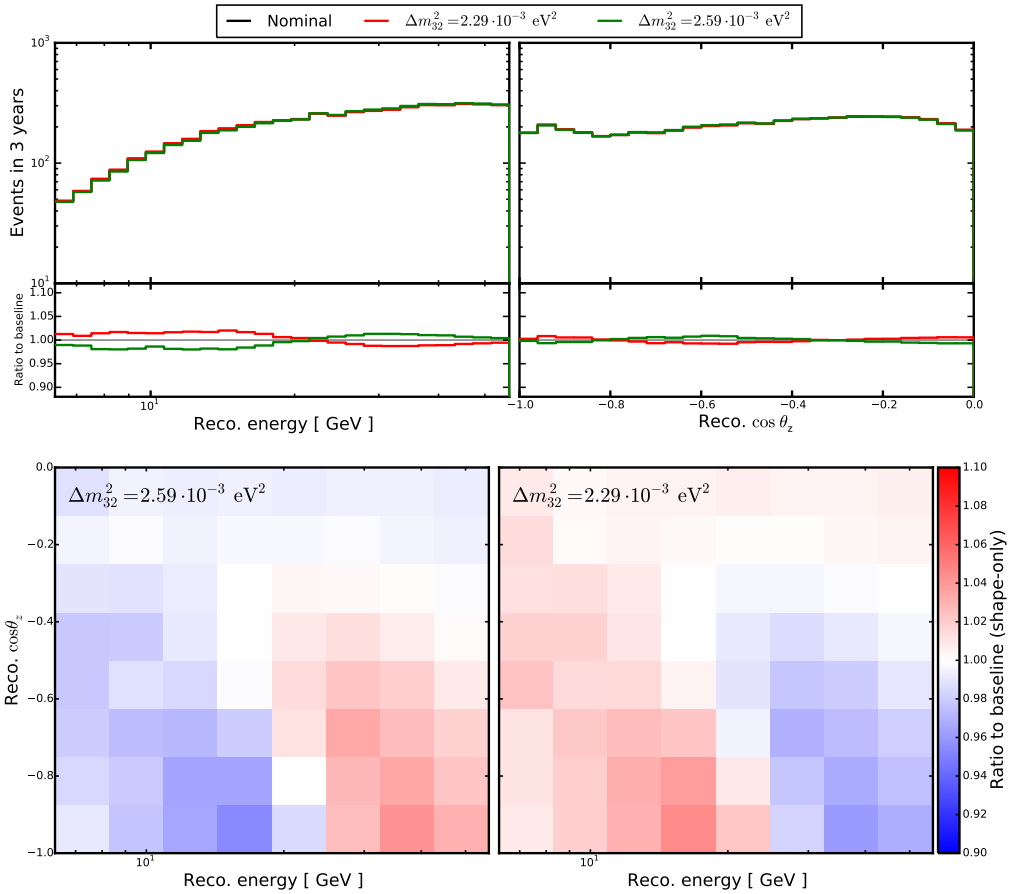


Figure A.15: The impact of $\Delta m^2_{32}$ in the sterile neutrino search. This parameter results in the energy shift of the standard oscillation minimum. This results in the wave-like signatures that can be seen in the energy projection and in the 2D distributions.

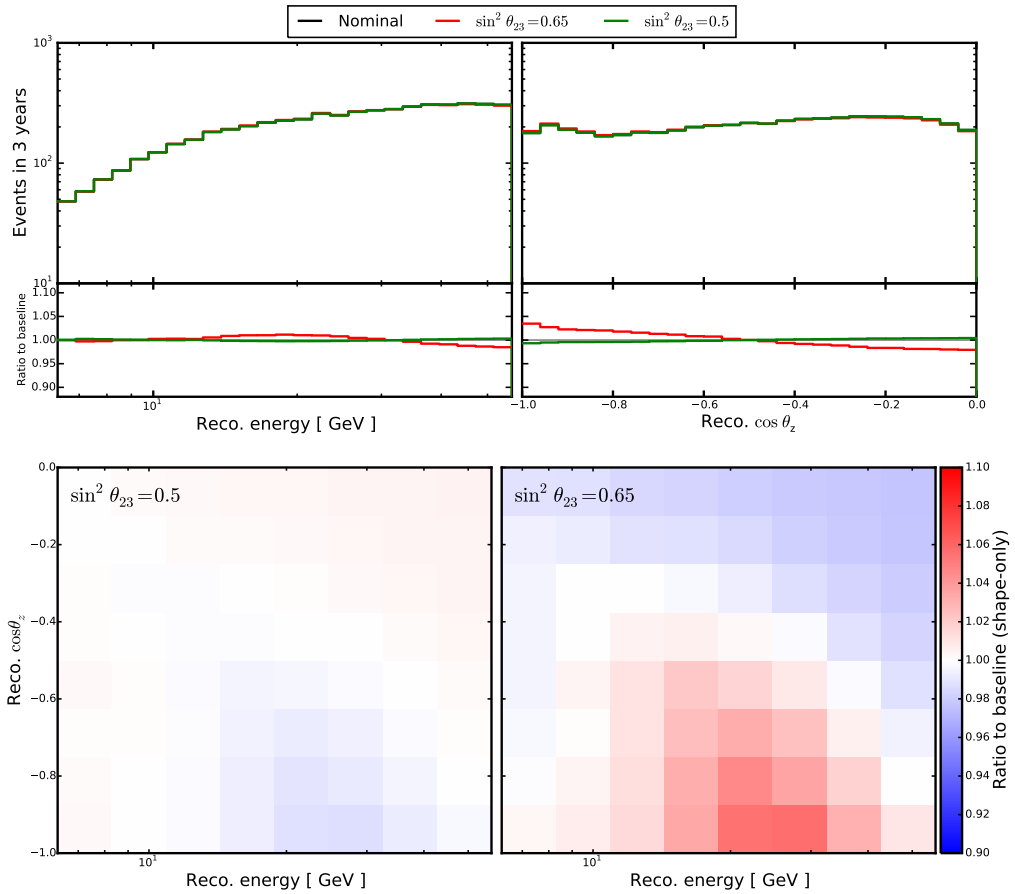


Figure A.16: The impact of $\sin^2\theta_{23}$ in the sterile neutrino search.

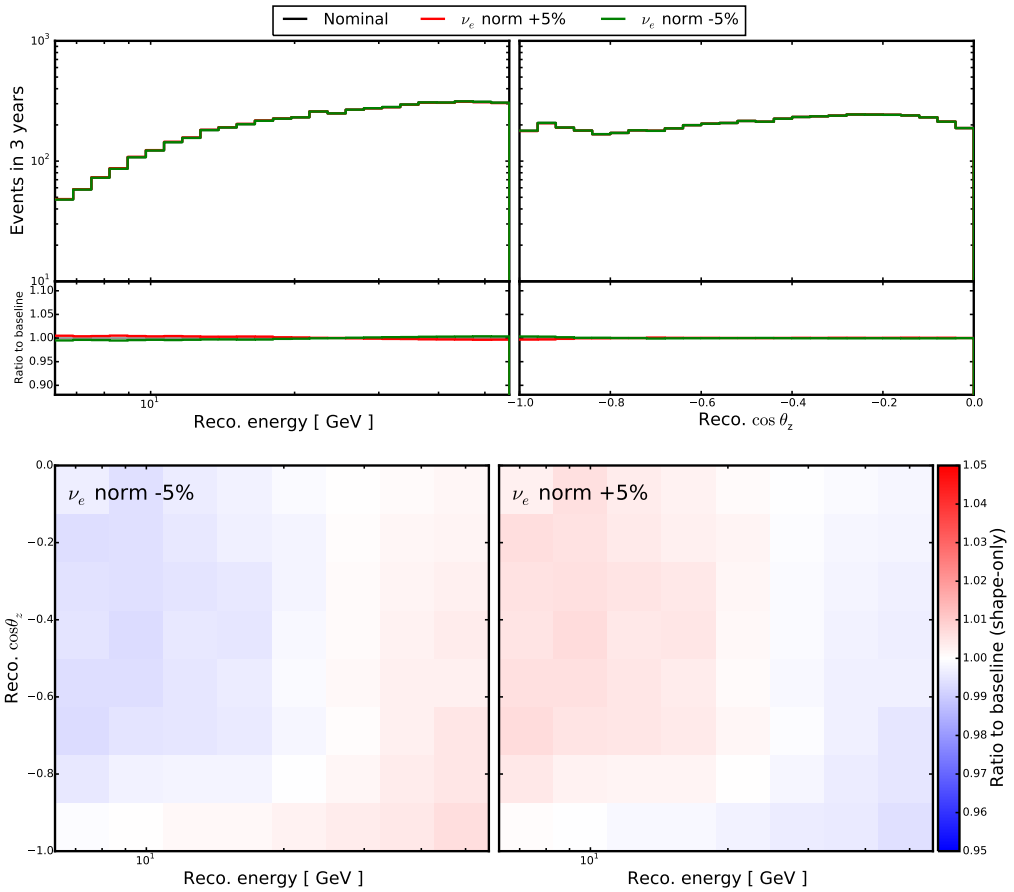


Figure A.17: The impact of the electron neutrino normalisation in the sterile neutrino search. The relatively small impact of the electron neutrino normalisation is caused by a relatively low fraction of electron neutrinos in the final sample.

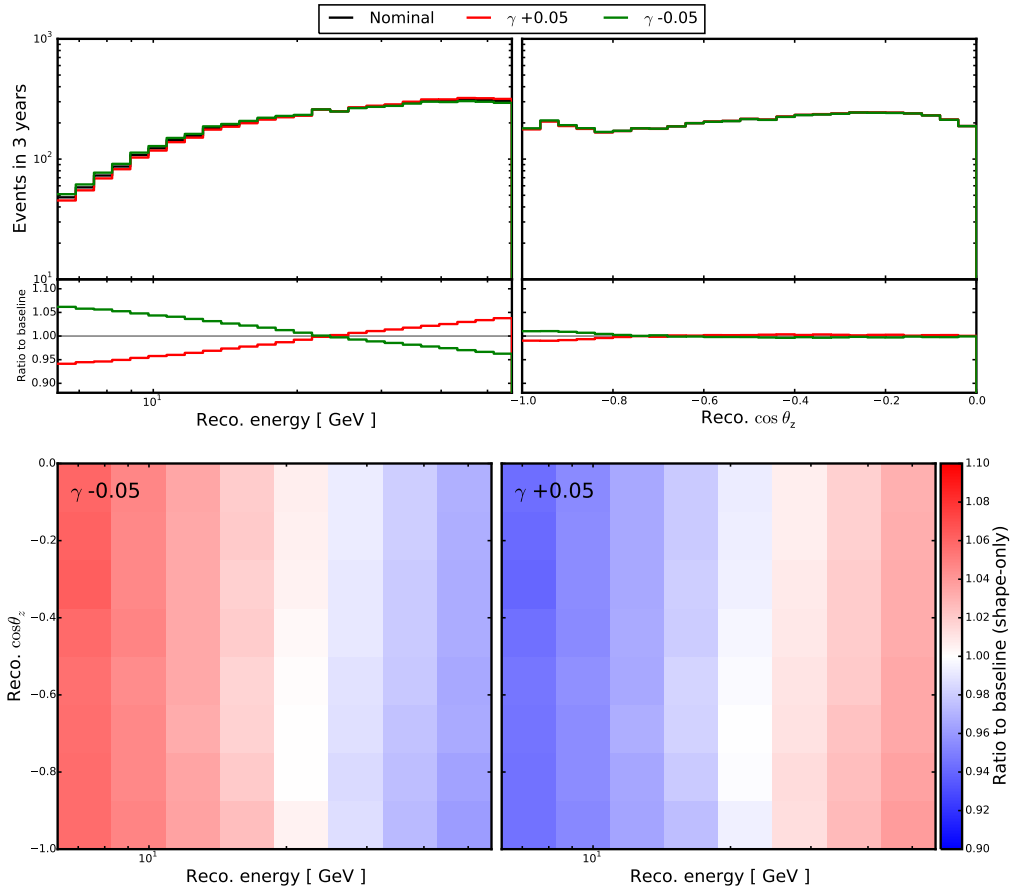


Figure A.18: The impact of the spectral index in the sterile neutrino search. It results in the change of the slope of the energy distribution.

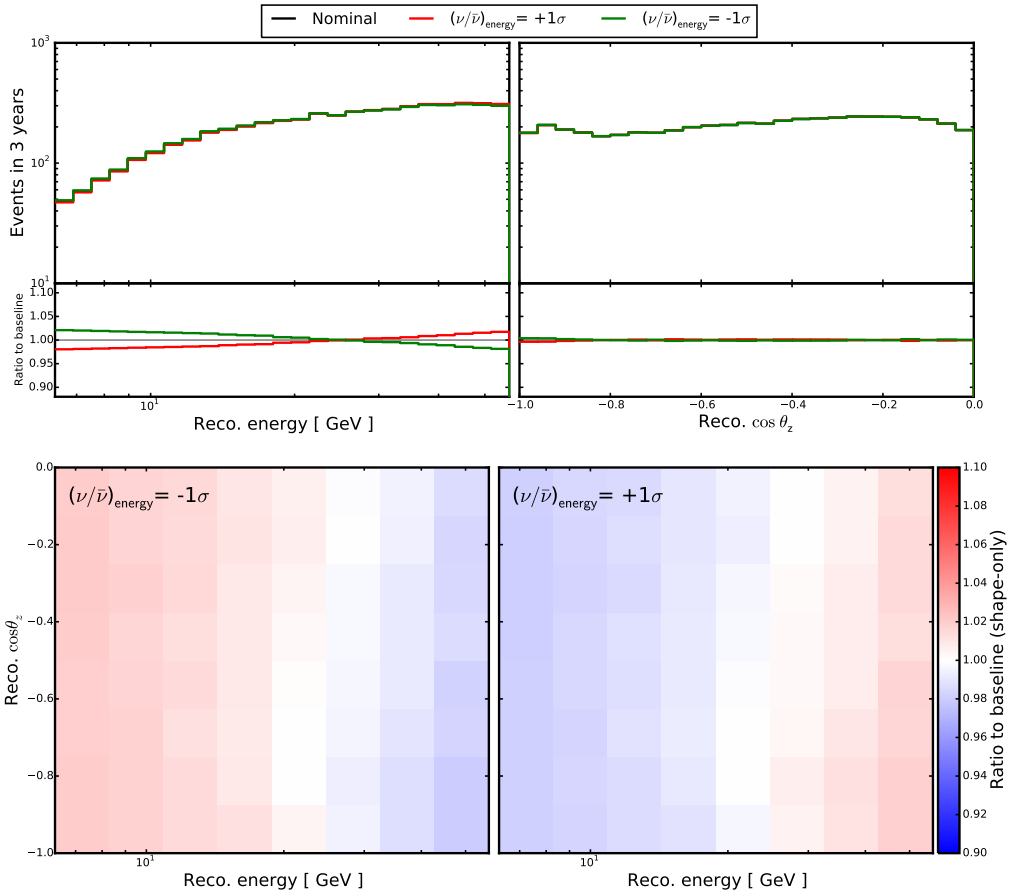


Figure A.19: The impact of the energy dependent $\nu/\bar{\nu}$ flux ratio. The effect is similar the spectral index and has no large impact on the zenith distribution.

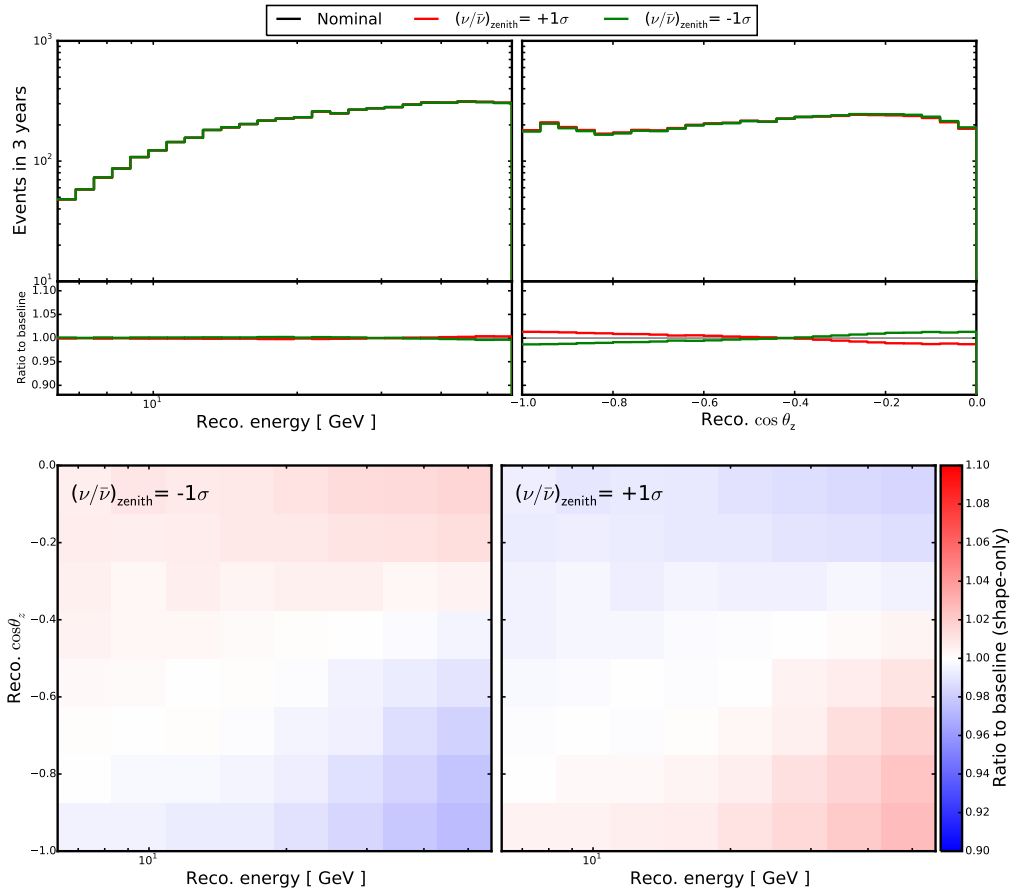


Figure A.20: The impact of the zenith dependent $\nu/\bar{\nu}$ flux ratio. As expected, it affects mainly zenith distribution, while no large effects are seen for the energy distribution.

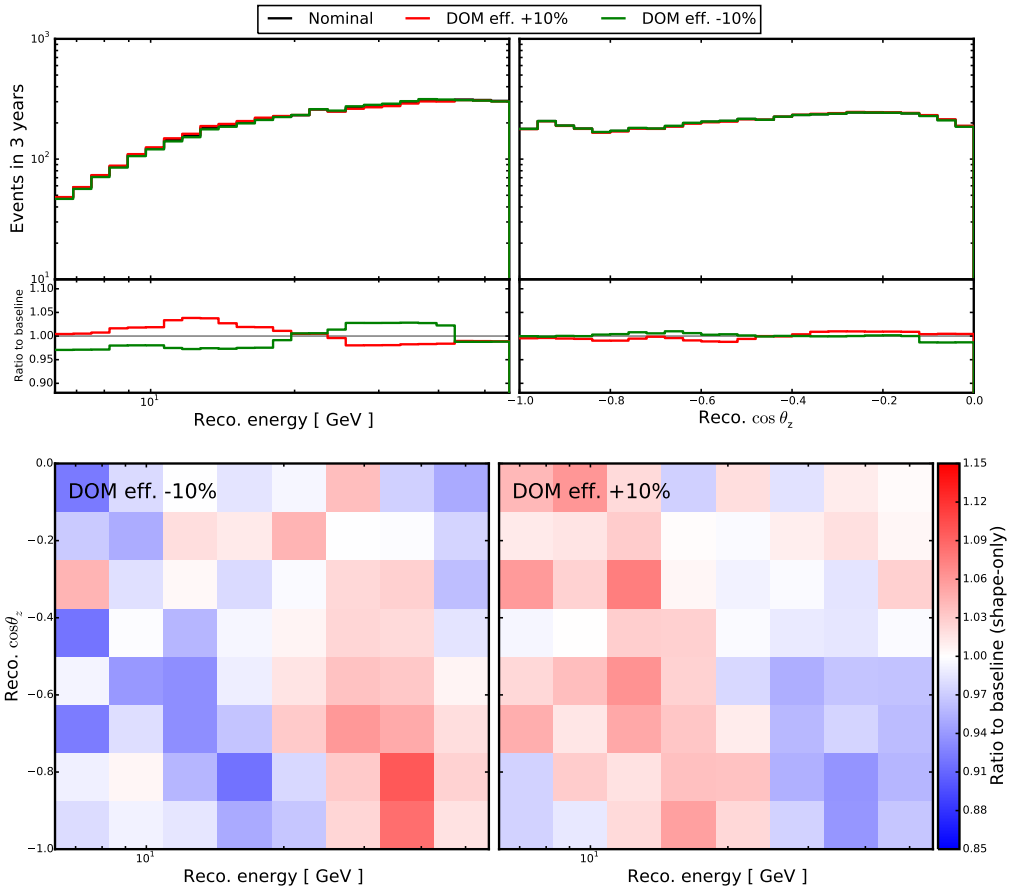


Figure A.21: The impact of the DOM efficiency in the sterile neutrino search. The DOM efficiency affects mainly the energy scale of the events, leading to an energy shift of the oscillations minimum and resulting in the "wave"-like signature. The distributions show the features inherent to all detector parameters (see caption of Figure A.7).

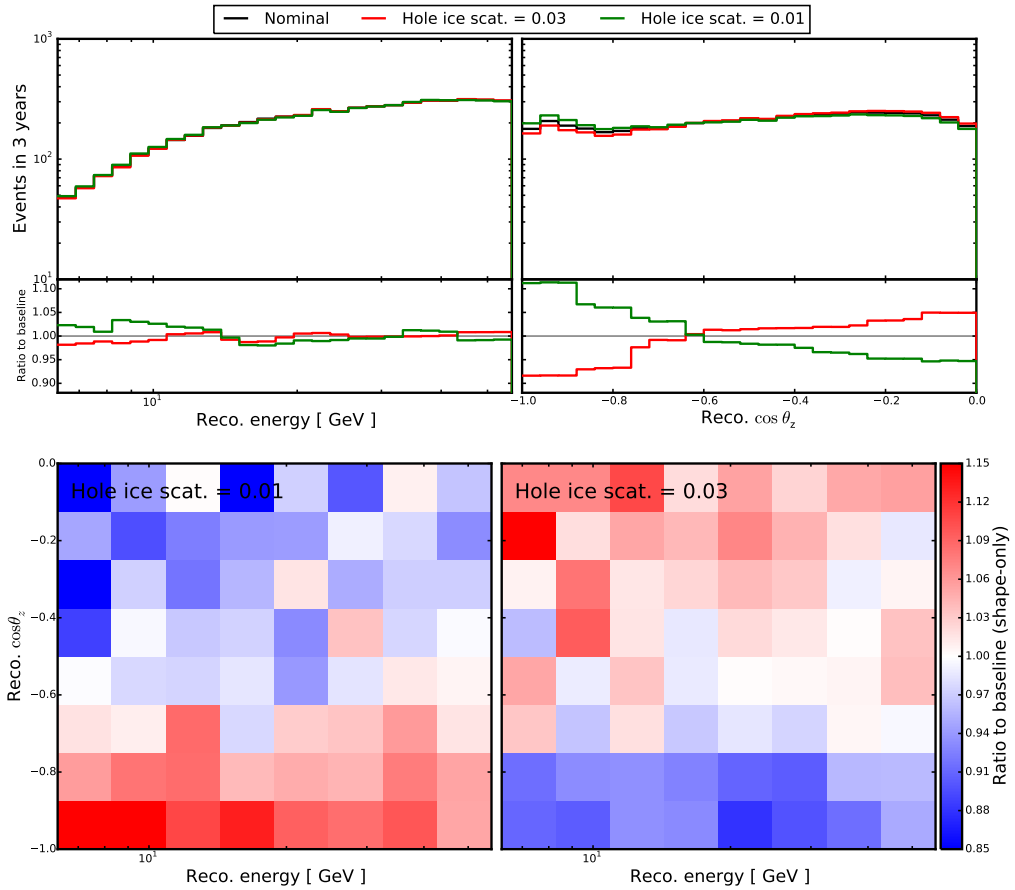


Figure A.22: The impact of the hole ice scattering in the sterile neutrino search. It affects the angular acceptance of the DOMs, resulting in the modifications of the zenith distributions. This parameter plays a larger role for the events that produce less light, resulting in a larger impact on the low energy events. The distributions also show the features inherent to all detector parameters (see caption of Figure A.7).

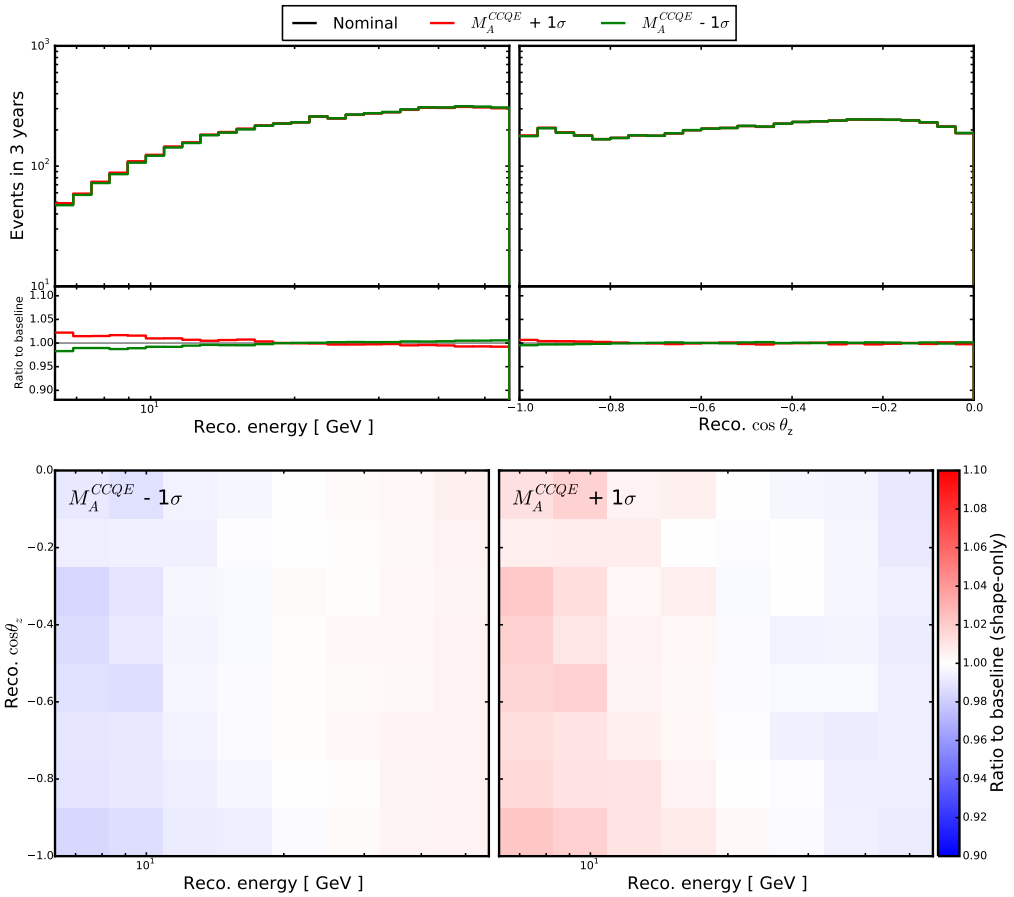


Figure A.23: The impact of the axial mass for quasi-elastic scattering in the sterile neutrino search. The QE scattering cross-section plays a larger role at the lowest energies, therefore the QE axial mass affects mainly events at the lowest reconstructed energies.

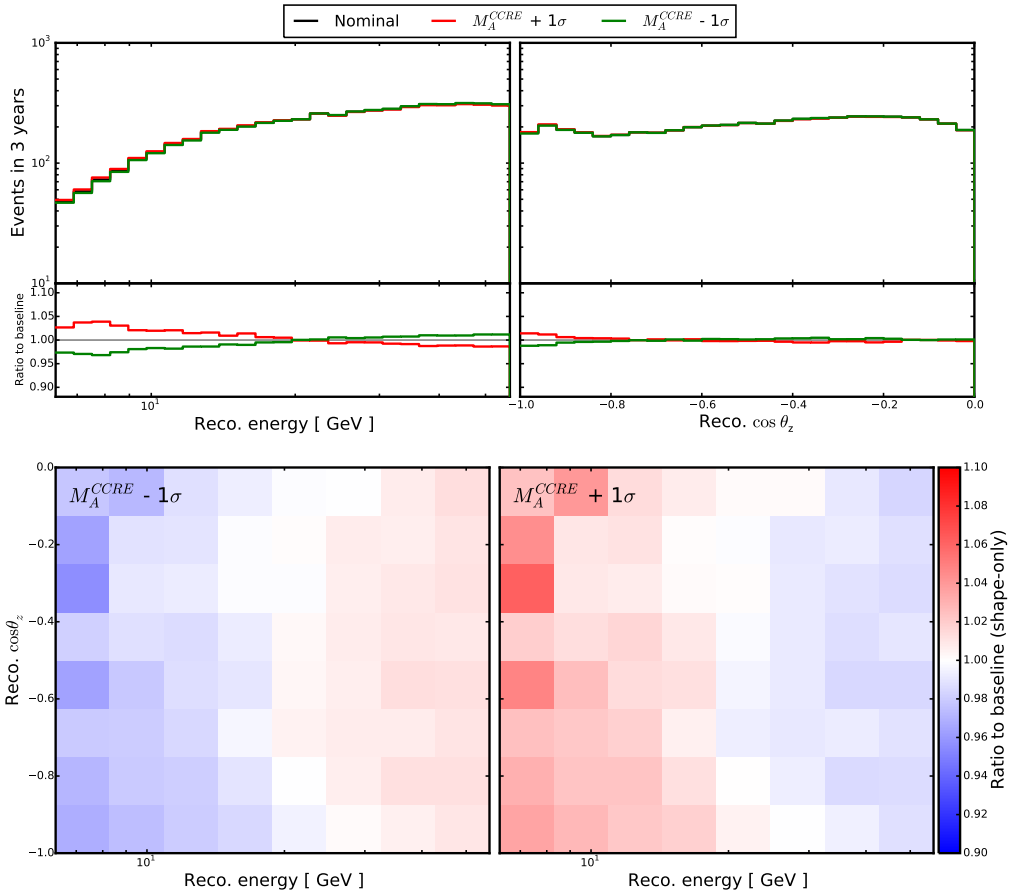


Figure A.24: The impact of the axial mass for the resonant production in the sterile neutrino search. It affects the energies up to 20 GeV, higher than for the QE axial mass.

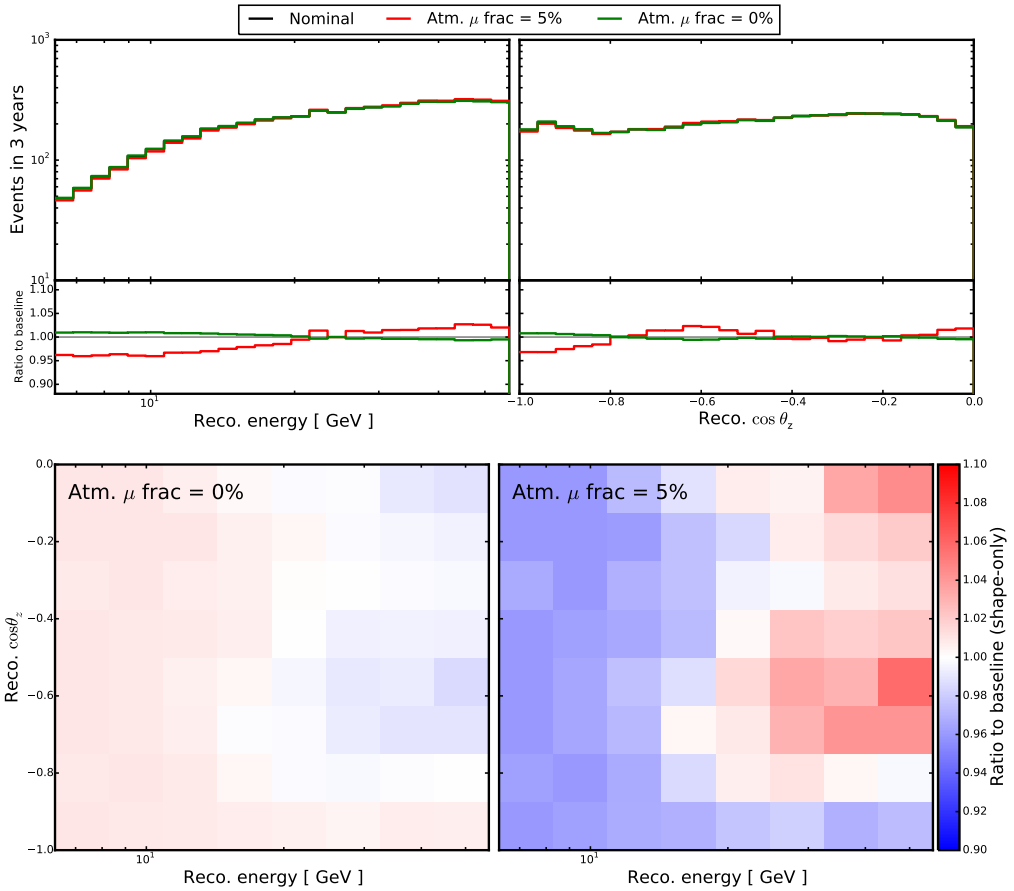


Figure A.25: The impact of the atmospheric muon contamination in the sterile neutrino search. The effect shows the distribution of events in the data-driven template.

# Appendix B

# Data and expectations for analysis bins

This Chapter shows the agreement between data and best-fit expectations for every experimental bin used in the analyses presented in Chapters 6 and 7.

Figures B.1 and B.2 show the event expectation and data for the track and cascade channels, as used in the measurement of the standard atmospheric neutrino oscillations, presented in Chapter 6. Figure B.3 shows the agreement for the sterile neutrino search, discussed in Chapter 7.

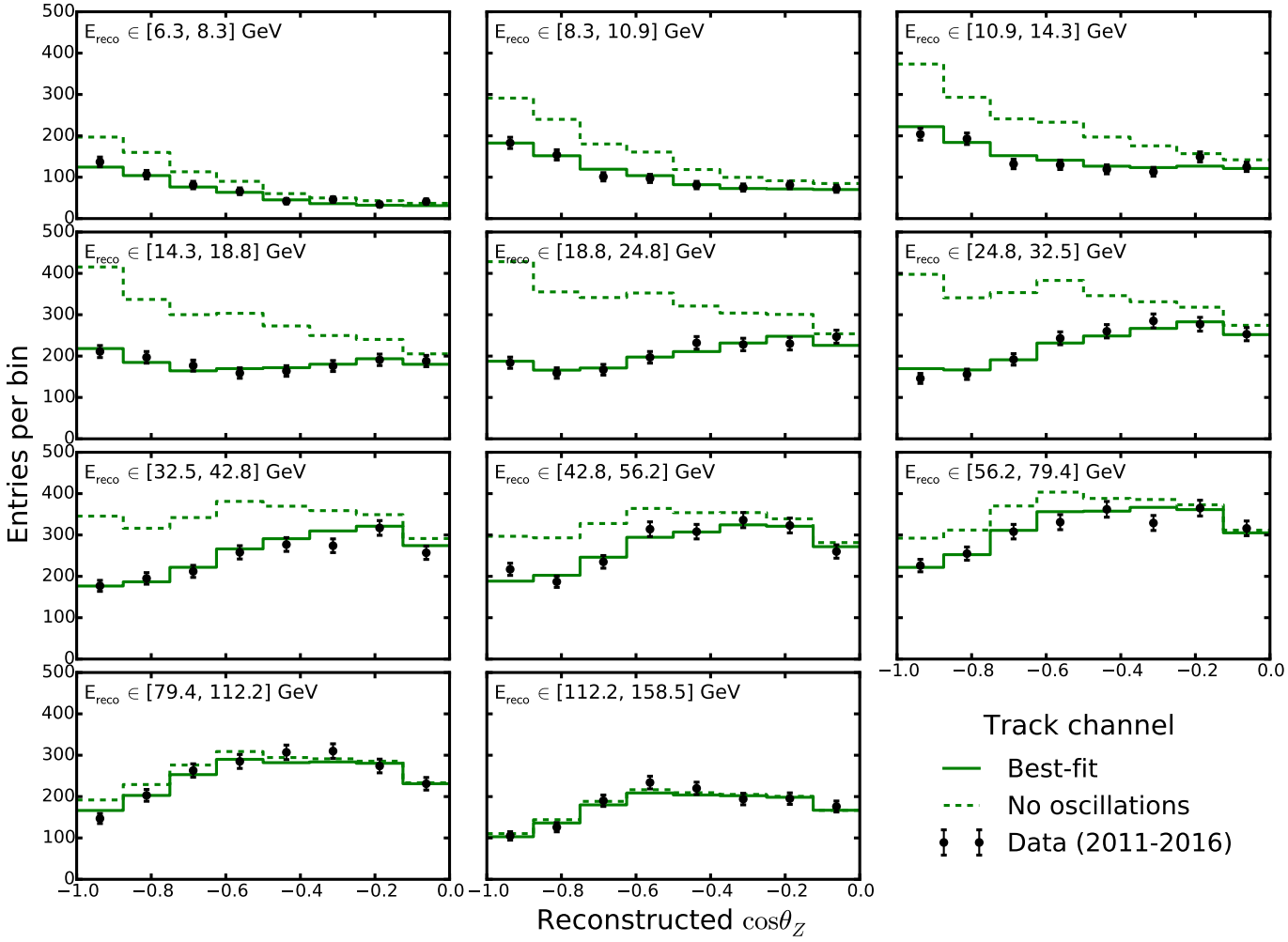


Figure B.1: The agreement between the data and the best-fit expectation for the track channel in the measurement of the standard atmospheric neutrino mixing. The no-oscillation expectation is shown for comparison and is calculated assuming the same nuisance parameters as obtained in the analysis.

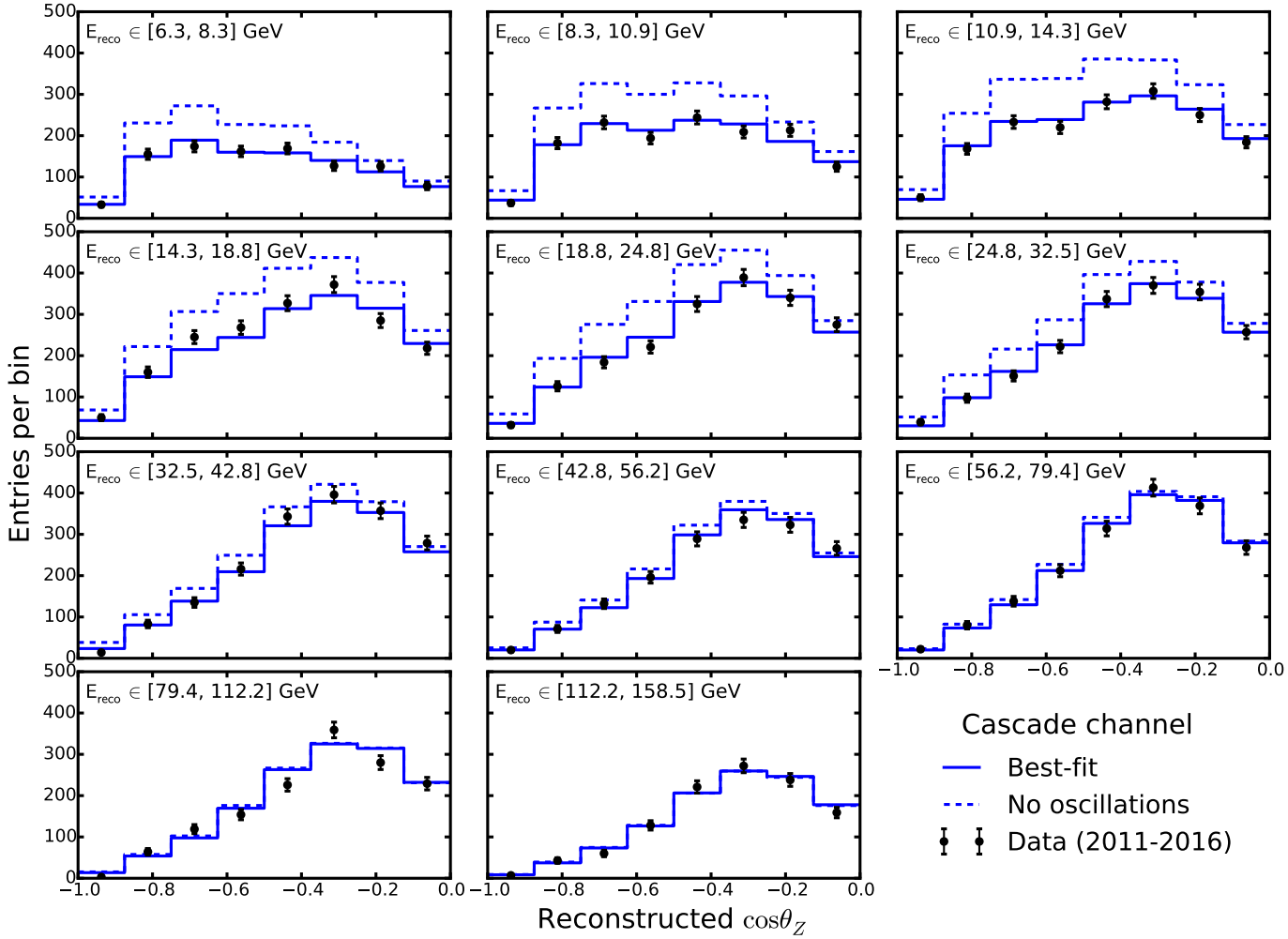


Figure B.2: The agreement between the data and the best-fit expectation for the cascade channel in the measurement of the standard atmospheric neutrino mixing. The no-oscillation expectation is shown for comparison and is calculated assuming the same nuisance parameters as obtained in the analysis.

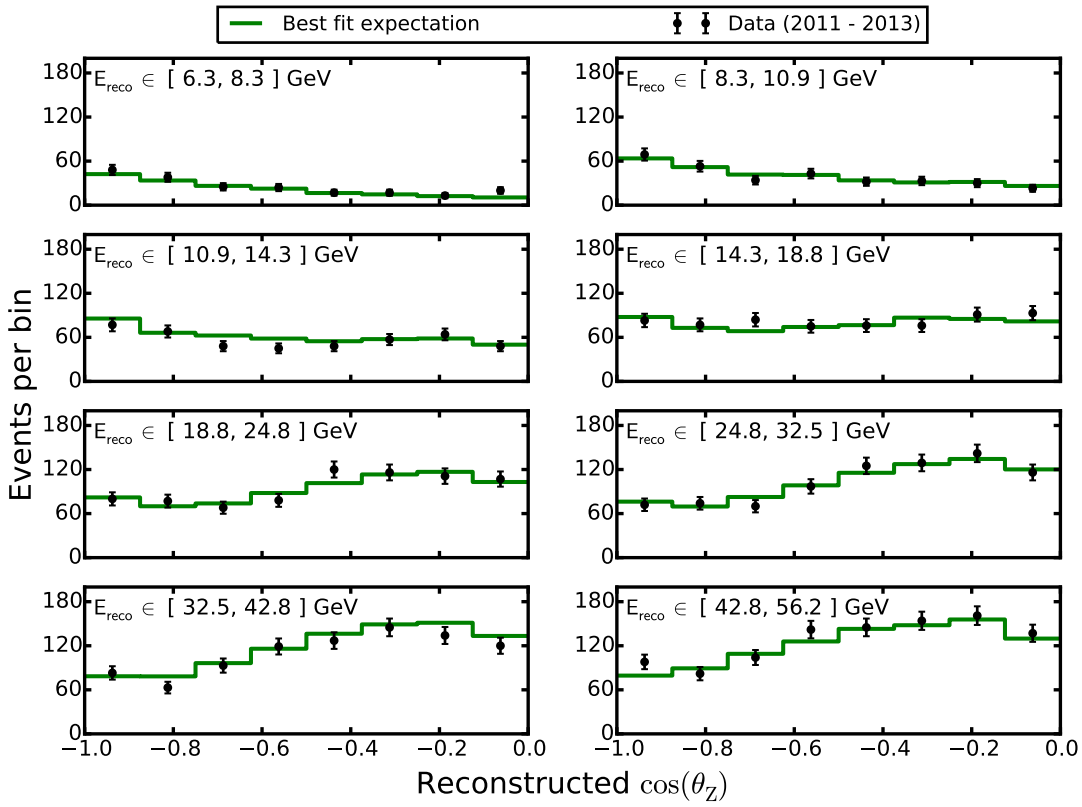


Figure B.3: The agreement between the data and the best-fit expectation in the sterile neutrino search.

# List of Figures

# List of Tables

# Acknowledgements

The results presented in this work would be impossible without the support of many people. I would like to thank Rolf Nahnhauer and Juan Pablo Yáñez for their supervision during the first half of my PhD program. It is important to note the role in this work Summer Blot in this work: our disputes about physics and analysis definitely improved the results presented here, but also were a great source of annoyance for the people sitting across the corridor. I am grateful for supervision and support of this work by Marek Kowalski.

I am thankful to Marek Kowalski, Walter Winter, Stefan Söldner-Rembold, Heiko Lacker and Kurt Busch for participation in the doctoral review committee and going through the inconvenience of reviewing and judging of this work.

I am grateful to many members of the IceCube collaboration for meaningful comments during the development of the analyses presented in this work. I would like to thank the members of the Low Energy and Neutrino Oscillations working group for their help with the analyses. It is important to note the participation of Carlos de los Heros, Joshua Hignight, João Pedro (a.k.a. "J-P") AM de Andrè, Delia Tosi in reviewing the studies presented in this work. I am thankful to Jason Koskinen, Michael Larson, Martin Leuermann for their advises and help with the analysis. I would like to mention Philipp Eller, who introduced name "spiciness" and made writing of the corresponding section rather awkward experience.

I would like to thank the people who helped me during writing, editing and proofreading of this work. They include Summer Blot, Juliana Stachurska, Robert Stein, Federica Bradascio, Simone Garrappa, Nora Linn Strotjohann, Jakob van Santen and others. Their comments and suggestions definitely made writing and editing process longer, but drastically improved the clarity and quality of this thesis and, at least partially, saved the readers from a poorly phrased content.

I would like to thank my wife, Iryna Lypova, who bravely stood and supported me during a very stressful time period, especially during the final phase of this work. I thank my friends, especially Alina Wilhelm and Igor Isaev, for very important moral support and final checks of this work. Last but not least, it is extremely to mention my family and relatives, who morally supported me despite thousands kilometres of separation.

# Selbständigkeitserklärung

Ich erkläre, dass ich die vorliegende Arbeit selbständig und nur unter Verwendung der angegebenen Literatur und Hilfsmittel angefertigt habe.

Berlin, den 22.03.2018 Andrii Terliuk